Tunneling spectroscopy of the Andreev Bound States in a Carbon Nanotube

Jean-Damien Pillet

To cite this version:

Jean-Damien Pillet. Tunneling spectroscopy of the Andreev Bound States in a Carbon Nanotube. Mesoscopic Systems and Quantum Hall Effect [cond-mat.mes-hall]. Université Pierre et Marie Curie - Paris VI, 2011. English. NNT : . tel-00833472

HAL Id: tel-00833472
https://theses.hal.science/tel-00833472v1
Submitted on 12 Jun 2013

Superconductivity is a fascinating electronic order in which electrons pair up due to an attractive interaction and condense in a macroscopic quantum state that can carry dissipationless currents, *i.e. super*currents. In hybrid structures where superconductors (S) are put in contact with non-superconducting material (X), electronic pairs propagating from the superconductor “contaminate” the non-superconducting material conferring it superconducting-like properties close to the interface, among which the ability to carry *super*current. This “contamination”, known as the superconducting proximity effect is a truly generic phenomenon.

The transmission of a supercurrent through any S-X-S structure is explained by the constructive interference of pairs of electrons traversing X. Indeed, much as in an optical Fabry-Perot resonator, such constructive interference of electronic pairs occurs only for special resonant electronic states in X, known as the Andreev Bound States (ABS). In the recent years it has been possible to fabricate a variety of nanostructures in which X could be for instance nanowires, carbon nanotubes or even molecules. Such devices have in common that their X contains only few conduction electrons which implies that ABS are also in small number. In this case, if one wants to quantitatively understand proximity effect in these systems, it is necessary to understand in detail how individual ABS form. This can be seen as a central question in the development of nanoscale superconducting electronics.

In this thesis, we observed individual ABS by tunneling spectroscopy in a carbon nanotube.

2011

Tunneling spectroscopy of the
Andreev Bound States in a Carbon Nanotube

Jean-Damien Pillet

Tunneling spectroscopy of the Andreev Bound States in a Carbon Nanotube

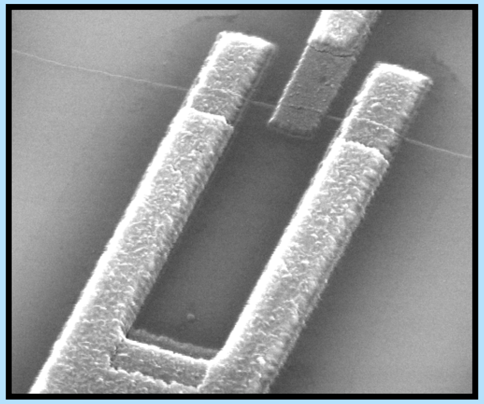

Jean-Damien Pillet
Quantronics Group
SPEC - CEA Saclay

THÈSE DE DOCTORAT DE
L'UNIVERSITÉ PARIS VI – PIERRE ET MARIE CURIE

ÉCOLE DOCTORALE DE PHYSIQUE DE LA REGION PARISIENNE - ED107

Spécialité :
Physique de la matière condensée

Présentée par Jean-Damien Pillet

Pour obtenir le grade de
DOCTEUR de l'UNIVERSITÉ PIERRE ET MARIE CURIE

Sujet de la thèse :

SPECTROSCOPIE TUNNEL DES ETATS LIES D'ANDREEV DANS UN NANOTUBE DE CARBONE

soutenue le 14 décembre 2011

devant un jury composé de :

Vincent Bouchiat (Rapporteur)
Juan Carlos Cuevas (Rapporteur)
Benoit Douçot (Président du jury)
Silvano de Franceschi
Francesco Giazotto
Philippe Joyez (Directeur de thèse)

Thèse préparée au sein du Service de Physique de l'Etat Condensé,
CEA-Saclay

Remerciements

N'étant pas de nature particulièrement éloquente, l'écriture de ces remerciements représente pour moi un exercice difficile. Néanmoins, je sais à quel point ils sont importants car je dois beaucoup aux personnes qui apparaissent dans ces quelques lignes, et je souhaite leur témoigner la reconnaissance que j'ai pour elles.

La première d'entre elles est bien sûr Philippe. Merci de m'avoir pris en thèse, de m'avoir encadré avec patience et de m'avoir tant appris. Je mesure la chance que j'ai eu de travailler avec un physicien aussi talentueux et passionné. Tu m'as donné l'opportunité de participer à une manip magnifique, et j'ai adoré. Je dois également une fière chandelle à Charis. Ses éclats de rire, sa bonne humeur, sa pêche ont énormément contribué à notre bon travail. Je me rappelle avec beaucoup de plaisir ces longues heures de salle blanche où tu m'expliquais avec pédagogie tes astuces de nano-fabrication. Je m'amusais bien, et je t'en remercie. Lors de ma dernière année de thèse, Marcelo s'est aussi beaucoup occupé de moi, en chantant, en jurant (¡Qué Boludo!), et c'était cool. Tes futur(e)s thésard(e)s ont beaucoup de chance.

Le groupe Quantronique est une grande famille et tous ses membres ont participé à l'agréable déroulement de cette thèse. Je veux les remercier également. Daniel, tu as toujours su me rappeler avec beaucoup de tact qu'il fallait bosser lors d'une thèse, et ce dès le premier jour (ce qui n'avait pas manqué de m'intimider, mais fut certainement pour le mieux). Merci également à Hugues dont le second degré m'a souvent décontenancé et également fait beaucoup rire. Ton honnêteté intellectuelle, ta clarté m'ont impressionné et guidé dans ma manière d'aborder la physique. Merci à Cristian qui a plusieurs fois su me redonner du peps à certains moments où je perdais confiance, c'était important pour moi et je t'en remercie. Merci à Denis pour ton enthousiasme extrêmement communicatif, et pour tout le temps que tu voulais bien passer avec moi quand je sollicitais ton aide, merci pour ta gentillesse. Merci à Patrice (Bertet) pour tes conseils et ton aide. Merci à Pief, pour avoir toujours répondu avec bienveillance à mes questions. Merci à Pascal pour les agréables brins de causette que l'on avait parfois. Merci à

Thomas pour ces moments sympas passés autour d'un café.

Merci aux post-docs du groupe Quantronique que j'ai croisés pendant cette belle aventure doctorale. Francois (Mallet) que j'ai rencontré au début de ma thèse et que j'ai appris à mieux connaitre depuis, avec beaucoup de plaisir. Maciej, you make me discover polish cheese and sausage, I will never forget it. Yui, merci pour les excellents sakés que tu nous ramenais du Japon. Merci Florian, pour toutes ces fois où tu m'as épargné de traverser la forêt pour rejoindre le RER et pour cette sympathique soirée à Dallas. Merci Max de t'être moqué de moi après chaque pot de thèse pour me rappeler la bonne conduite à suivre. Merci Carles, pour ta manière si singulière de parler bonne bouffe et le jabugo de mon pot de thèse. Merci Çağlar pour ta gnac lors de nos parties de foot. Merci également à Romain et Michael. Merci aux thésards avec qui c'était vraiment chouette de vivre cette aventure commune: François (Nguyen), Quentin, Augustin, Andreas, Vivien, Cécile, Olivier... Merci Hélène, tu m'avais transmis l'envie de prendre ta suite lors de ma première visite du SPEC, quel beau cadeau! Landry, tu es bien sûr à part dans cette catégorie puisqu'on est ami depuis longtemps. Je ne saurais pas exprimer ici à quel point j'étais content de te voir arriver dans le groupe. Aussi, j'écrirais simplement que partager avec toi cet intérêt pour la physique c'est énorme.

J'aimerais ajouter à cette liste Fabien pour toutes les heures de Stevie Wonder que j'écoute maintenant grâce à toi, Patrice (Roche) pour m'avoir dit un jour que je n'avais du con que l'air. Thank you Alfredo and Cristina, not only for what you brought to my thesis as theorists, but also because it was really nice learning some physics with you. Thank you Juan Carlos for making us discover, with Landry, the best places to have some tapas in Madrid.

Je remercie aussi tous les autres membres du SPEC qui ont contribué de près ou de loin à cette thèse. Mentionnons Eric Vincent pour son accueil au sein du service, Nathalie Royer, Corinne Kopec-Coelho pour leur aide dans les démarches administratives, et Jean-Michel Richomme pour avoir sauvé mon parquet grâce à sa cire d'abeille.

I would like also to thank the members of my thesis comitee: Benoit Douçot, Vincent Bouchiat, Juan Carlos Cuevas, Silvano de Franceschi and Francesco Giazotto.

Merci aux membres du groupe Qélec du LPA de m'avoir accueilli dans leur groupe après cette thèse pour mon premier post-doc : Philippe, Manu, Nico, François, Benjamin et Michel. C'est une expérience géniale de faire de la physique avec vous, et les lundredi n'ont rien gâché.

Merci à mes potes rencontrés pendant la période de Master car, d'une certaine manière, j'ai fait cette thèse avec eux. Merci Xavier pour ces heures passées au soleil autour d'une bière, David pour ta méchanceté et ton humour qui ne font qu'un, Philippe d'être un écureuil et pour ces matchs avec le Dynam'eaux, Ludivine pour ces apéros magiques dans ton ancien studio bancale, Loïg d'avoir souffert avec moi aux Buttes et ailleurs, Juliana d'avoir amené la chaleur colombienne à Paris, Yannis de m'avoir emmené parfois au bout de la nuit, Keyan pour ces discussions nocturnes autour d'un bon verre de Bordeaux. Merci à mes potes de l'ENS trop nombreux pour être tous mentionnés mais que je porte dans mon cœur et qui ont vécu cette thèse par procuration : Jérem hockeyeur acquatique, Raph mentor footbalistique, Yo camarade de traquenard, Laura qui illumina la yourte, Romain victime de l'ours blanc, Elsa neo-californienne, Sarah reine du Requin Chagrin, François le petit et le grand, Hélène globe-trotteuse, Oskar toujours chaud pour le ski, Sylvain éleveur d'escargot dans l'âme...

Pour finir, je veux remercier les membres de ma famille. En particulier, mes parents, mon frère et mes deux sœurs, mes grands-parents parce que leur soutien permanent et leur compréhension n'avaient pas de prix. Merci à Jacqueline Campagne pour ton aide lors de la préparation du pot, et pour tes tricots magnifiques. Merci à Cécile parce que tu partages ma vie et que tu me rends heureux.

Contents

Chapter 1

Introduction

Superconductivity is a fascinating electronic order in which electrons pair up due to an effective attractive interaction and condense into a state, characterized by a macroscopic phase, that can carry dissipationless currents, *i.e.* *super*currents. It was observed and understood for a long time that in hybrid structures where superconductors (S) are put in contact with non-superconducting materials (X), electronic pairs propagating from the superconductor "contaminate" the non-superconducting material conferring it superconducting-like properties close to the interface, among which notably the ability to transmit supercurrent. This "contamination", known as the superconducting proximity effect was gradually understood to be truly generic: whatever the electronics properties of X, proximity effect will occur, albeit possibly only on a range of the order of the interatomic distance in unfavorable cases.

The transmission of a supercurrent through any S-X-S hybrid structure is explained by the constructive interference of pairs of electrons traversing X. Indeed, much as in an optical Fabry-Perot resonator, such constructive interference of electronic pairs occurs only for special resonant electronic states confined inside X, known as the Andreev Bound States (ABS). Reciprocally, knowing the properties of the ABS is enough to characterize the superconducting properties of the S-X-S structure.

In hybrid nanostructures containing many ABSs, a statistical knowledge about the ABSs provided by quasiclassical theories suffices to predict the supercurrent in the structure. This is the case for instance in Superconductor-Normal metal-Superconductor (S-N-S) microbridges. However, in the recent years its has been possible to fabricate a variety of hybrid nanostructures in which X could be for instance semiconducting nanowires [1, 2, 3], carbon nanotubes [4, 5, 6, 7, 8, 9, 10, 11], aggregates [12, 13, 14] or even molecules [15]. Such devices have in common that their X contains only few conduction electrons which implies that ABS are also in small number. In this case, if one wants to quantitatively understand proximity effect in these systems, it is necessary to understand in detail how the individual ABS form in such device for which quasiclassical methods are ineffective. This can be seen as a central question in the development of nanoscale or molecular superconducting electronics.

In a first step to address this question, the initial goal of this thesis work was to observe individual ABSs in a system expected to contain only a few of them. To do so, we have set up an experiment with an hybrid device in which X was a carbon nanotube (CNT). In such a structure, it was indeed expected that there would be only a small number of ABS that one could resolve individually by performing tunneling spectroscopy directly on the CNT.

When wanting to understand the formation of ABS in systems with few electrons, one is rapidly faced with the question of Coulomb interaction: in contrast to the (quasi-)electrons of the superconductor that experience an effective attractive interaction, in a nanoscale X with few electrons, Coulombian repulsion is expected to play a large role. Hence a second question one has to address is: how do ABSs form in a system with Coulomb repulsion (obviously opposing superconducting pairing)? Prior to this thesis work, many theoretical works had addressed this point, but there had been no experimental counterpart taking the point of view of the ABS formation. Our experimental results shed light on the effect of Coulomb repulsion on ABSs.

1.1 Observation of the ABSs

The concept of ABSs has been widely used to understand a large panel of experiments in hybrid nanostructures. Yet, no experiment had so far allowed a detailed and direct spectroscopy of the ABSs. In this thesis work, we report the first spectroscopy of individually resolved ABSs, in a CNT-based hybrid device.

CNTs are suitable to perform the spectroscopy of ABSs, first, because as already mentioned they should host only a reduced number of ABSs when contacted to Ss. Also, establishing good contacts to superconducting leads has already been demonstrated [4, 7, 8], and they have a favorable elongated geometry providing an easy access to a tunnel probe. In our setup the CNT is contacted to aluminum electrodes distant of 0.7 μm. These electrodes become superconducting below $\sim$ 1K and “contaminate” the CNT. As electrodes are reconnected, they form a loop. This geometry permits to impose a superconducting phase difference δ across the CNT by threading a mag-

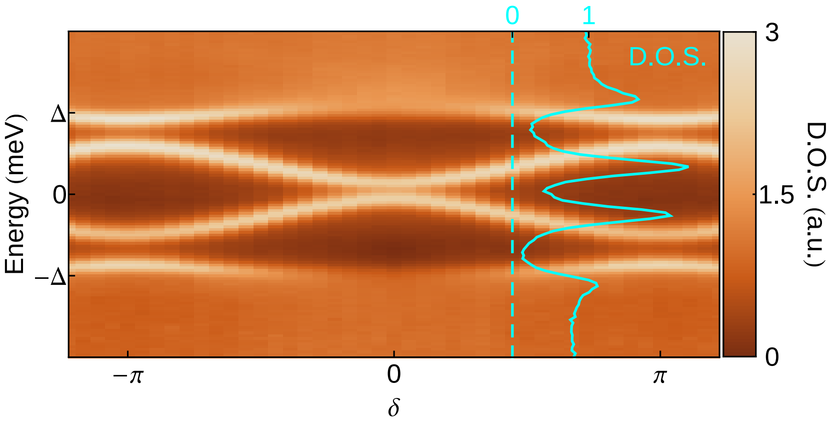

Spectroscopy of the Andreev Bound States

Figure 1.1: Colorplot of the density of states (D.O.S.) of a CNT measured as a function of the superconducting phase difference δ between electrodes. Andreev Bound States appear as resonances (bright lines on this graph) whose energies depend periodically on δ. The solid trace corresponds to a cross-section of the data at the phase indicated by the dashed line.

netic flux in the loop. In between these electrodes, a tunnel probe is weakly contacted to the CNT in order to measure its density of states by tunneling spectroscopy. The detailed description of our process of fabrication is exposed in part IV.

In part II, we present a first experiment realized on such structure in which we have successfully observed individual ABSs in the CNT. They appear as resonances in the density of states of the CNT within a gap of width 2Δ where Δ is the amplitude of the order parameter of the superconducting electrodes (see Fig. 1.1). We were also able to measure the 2π-periodic dependence with δ of the ABSs' energies. This phase dependence is a signature of the ABSs and is intimately related to their role in the transport of supercurrent in the CNT, even though that current was not actually measured in the experiment. The supercurrent carried by an ABS is indeed given by the derivative if its energy with respect to δ. In chapter 6, based on this behaviour, we evaluate the performance of our device as a SQUID-magnetometer.

1.2 ABSs in Quantum Dots

Trying to interpret this first experiment has led us to address the question of the formation of ABSs in Quantum Dots (QDs). This is because, most experiments involving electronic transport through CNTs can be interpreted

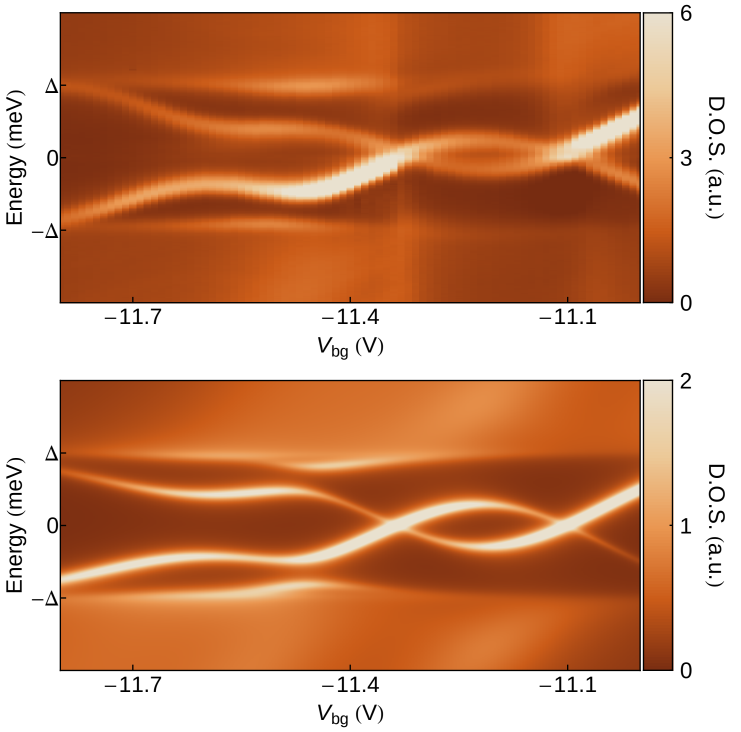

Figure 1.2: Experimental (upper graph) and theoretical (lower graph) dependence of the Andreev Bound States spectra with the voltage applied on a back gate. Comparison of our experimental results and calculations performed within the phenomenological approach of Ref. [16] yields a very good agreement. In this model, ABSs appear as facing bell-shaped resonances with their bases resting against opposite edges of the superconducting gap. For large enough Coulomb repulsion these resonances may form a loop. The features observed in experimental data can be identified as such bell-shaped resonances corresponding thus to different orbitals in the nanotube. Closer inspection reveals however that adjacent resonances are sometimes coupled, forming avoided crossings, so that we need to consider the case where two orbitals contribute simultaneously to the spectral properties within the superconducting gap. For this, we extend the model to two serially-connected QD each containing an orbital, with a significant hopping term in between. This model is fairly natural, given that the centre tunnel probe electrode is likely to act as an efficient scatterer.

in terms of QD, and ours in no exception. In QDs, the electronic structure, prior to the connection to superconducting leads, is quantized in orbitals that can each contain two electrons of opposite spin, and a gate electrode allows to control the filling of these orbitals. Moreover, due to Coulomb repulsion, the energy necessary to add an electron to the QD - the charging energy - is one of the biggest energy scale of the system. In our experiments it is ten times larger than the characteristic energy of superconductivity Δ.

Our experiment showed that by applying a voltage on a capacitively coupled gate, one can tune the ABSs' energies. The observations were consistent with ABSs arising from the hybridization of levels of opposite spin belonging to orbitals of the CNT behaving as a double quantum dot. In part I, we introduce the theoretical approaches which allow to describe these experimental results. A first approach is based on an effective non-interacting model developed in Ref. [16] by Vecino *et al.* It consists in a phenomenological treatment - Hartree-Fock like - of the Coulomb repulsion in the CNT. Though based on rough approximations, this approach yields a rather good agreement with experimental results (see Fig. 1.2) allowing to extract detailed information on our sample: couplings between CNT and the leads or strength of Coulomb repulsion. Spectra of ABSs constitute thus a powerful spectroscopic tool for QDs. We validate this phenomenological approach, for the parameters range of our experiment, by comparison with exact numerical renormalization group (NRG) calculations.

In part III, we report on a second experiment that aimed at filling the gaps left in the analysis of the first experiment. In particular we wanted to check the double-dot analysis that we had used for the first experiment. A second goal of this experiment was to investigate the possible interplay between the PE in a QD and the Kondo effect. The Kondo effect is complex many-body phenomenon which arises in a QD connected to normal leads (*i.e.* non superconducting). When the QD contains, in its last occupied orbital, a single electron, its spin degree of freedom interacts with conduction seas of the electrodes. Virtual charge fluctuations, in which an electron briefly migrates off, or into the QD lead to spin-exchange between the local moment and the conduction sea [17]. This spin-exchange gives rise to the formation of a many-body spin-singlet state characterized by an energy scale T_K: its Kondo temperature. This state manifests by a peak at the Fermi level in the density of states of the CNT. Its interplay with superconductivity has been the subject of numerous experimental [5, 9, 14, 18, 19, 20, 21] and theoretical works (see for example [22, 23, 24, 25]). There are however still few quantitative experimental investigations leaving many open questions, like: is there an interplay between Kondo effect and superconductivity ruled by the ratio T_K/Δ? We explored this interplay through the spectroscopy of

ABSs by comparing normal state and superconducting state measurements of the CNT's density of states (see Fig. 1.3). Our experimental results show that, within the parameters range of our experiment, Kondo effect observed in the normal state induces no qualitative change in the behaviour of ABSs. The behaviour that we observe experimentally is well described by NRG calculations which can capture both the Kondo effect and the formation of ABSs in QDs, as is shown in Fig. 1.3. We also discuss the quantum transition between a spin-singlet and a spin-1/2 ground state of the QD in the superconducting state when the gate voltage is varied. The most spectacular effect of such transition is the reversal of the supercurrent by adding a single extra electron in the QD. This is directly visible in our spectroscopy by an ABS that crosses the Fermi level in forming a loop pattern as a function of the gate voltage in an odd valley of the QD. A second signature of this transition is a phase shift of π in the phase-dependence of the ABSs, indicating that the CNT goes from a zero to a pi-junction behaviour. Finally in this second experiment we show some spectroscopic features that are specific of double-QD physics.

1.3 Perspectives

Our observation of the ABSs in a CNT constitutes an important step forward in the exploration of PE in nanostructure. This experiment is not just the confirmation of a fifty years old prediction [26, 27, 28], but is at the heart of modern issues on hybrid nanostructure with superconducting leads. This field is presently very active. People are considering all sorts of S-X-S devices with all possible electronic properties for X, and some of them are very promising. For instance, if X is a topological insulator (or a semiconductor with strong spin-orbit coupling and Zeeman splitting), it is predicted that - under appropriate circumstances - some ABSs should take the appearance of Majorana fermions which could be a basis for the implementation of topological quantum information processing. But so far, only a limited number of predictions have considered the effect of interactions [29]. Our work should give some insight in order to picture the influence of interaction on the formation of Majorana fermions. Apart from this exciting perspective, other cornerstone experiments could extend the present work.

Semiconducting nanowires (NW) are characterized by a large spin-orbit interaction and can be contacted to Ss. Since they share similar geometry than CNTs, the spectroscopy of ABSs could, in principle, be realized in the same way than in our experiment. Such spectroscopy would open exciting perspective for the understanding of the interplay between superconductivity

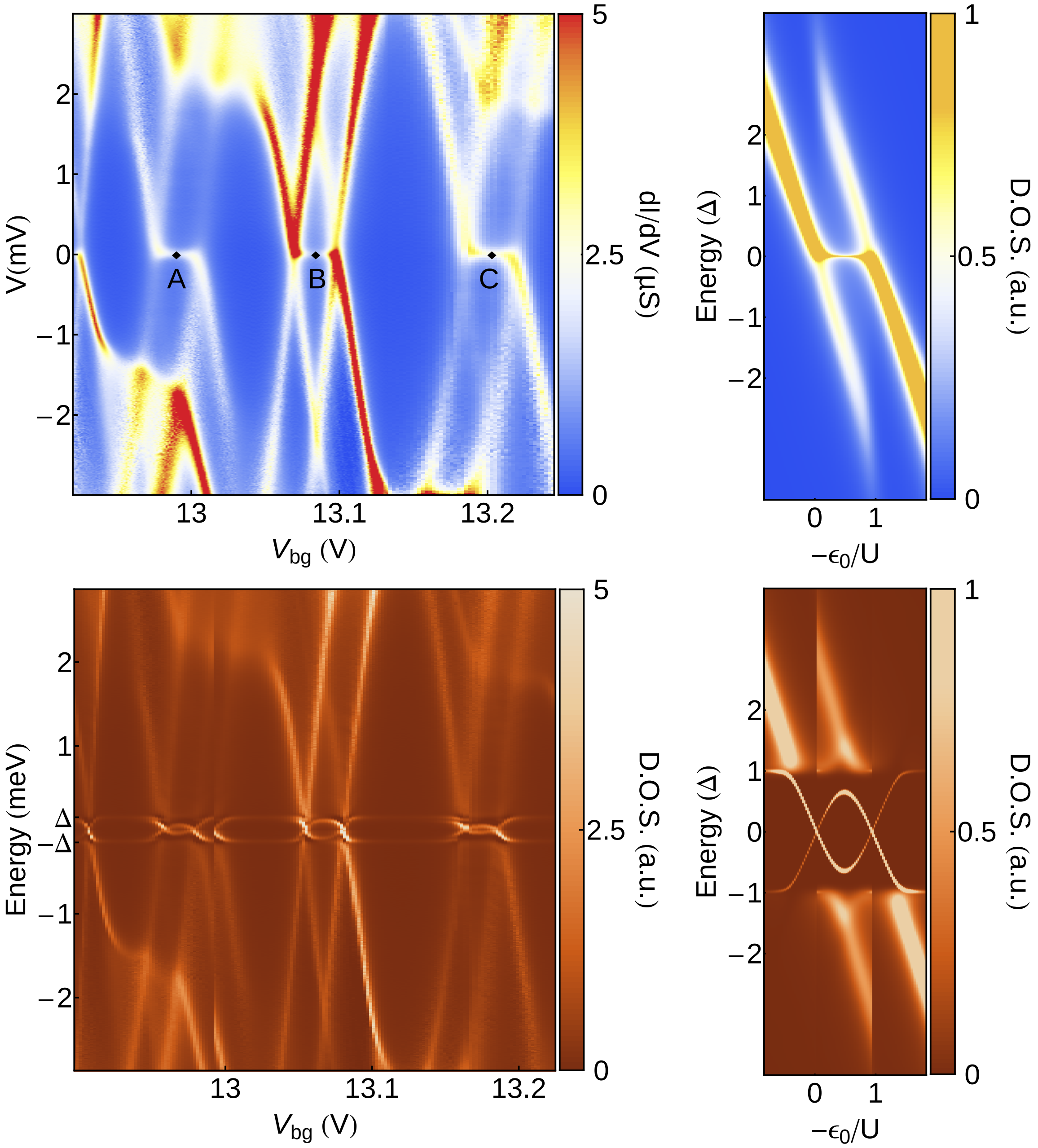

Figure 1.3: On the left: densities of states of the CNT measured as a function of the gate voltage V_{bg} when the leads are driven into their normal state with a magnetic field (upper graph), and when they are in their superconducting state (lower graph). In normal state measurements, Kondo peaks (indicated by black diamond) appear at the Fermi level. In the superconducting state, these peaks disappear because of the opening of a superconducting gap between $-\Delta$ and $+\Delta$. Within this gap, ABSs appear because of proximity effect. They form loop when we tune the gate voltage V_{bg}. All these behaviours are nicely captured by NRG approach, as shown by the matching graphs on the right.

and spin orbit interaction.

Some two-dimensional electron gases (2DEG) in semiconductor heterostructures are also characterized by a strong spin orbit [30, 31]. Hence, they were also proposed as candidate for the observation of Majorana fermions [32]. Moreover, the possibility of patterning the 2DEG and introducing lateral gates offer an even richer degree of control than CNTs or NWs: couplings to the leads as well as charging energies would be tunable parameters, in contrast to our experiment where they are essentially imposed during fabrication of the device. Moreover, as coupling between the tunnel probe and the QD could also be tuned, it would make possible to limit the broadening of ABSs due to the coupling to the probe, thereby increasing the resolution of Andreev Bound States spectra as a spectroscopic tool. We could also, as in Ref. [33], realize this spectroscopy through an extra QD acting as an energy filter and reach an even better resolution.

Part I

Andreev Bound States in Quantum Dots

Superconducting proximity effect and Josephson effect Close to an interface with a superconductor (denoted by S), materials that are not intrinsic superconductors (hereafter called *normal* materials and denoted by X) acquire some characteristic properties of the superconductor. This effect, generically known as “the proximity effect”, is of wide generality although its strength and length-scale depend on the electronic properties of the normal material and on the quality of the interface.

A striking manifestation of this proximity effect can be observed in S-X-S junctions: if X is thin enough and the temperature low enough, such a junction can sustain a supercurrent. Such phenomenon constitutes a generalization of the supercurrent flow through an insulating barrier (S-I-S junction) described by B. Josephson, and, by extension, it is also called Josephson effect.

The physics of the proximity effect was investigated and understood soon after the discovery of the BCS theory. The group led by de Gennes in Orsay notably contributed to this work [27, 34, 35].

With the advent of mesoscopic physics there was a renewed interest on the proximity effect that started in the 90’s. This revival was pushed both by the development of microfabrication techniques that allowed to make elaborate heterostructures at the scales relevant for the proximity effect, but also by the emergence of new ideas in the domain of mesoscopic physics, such as the Landauer-Büttiker scattering formalism [36], Random matrices [37], Nazarov’s circuit theory [38], etc...

This has led to consider proximity and Josephson effects in countless structures, where X could be anything among molecules (graphene, carbon nanotube, fullerene), diffusive normal metals, ferromagnetic materials, semiconductors (two dimensional electron gas or nanowires) and atomic contacts. In the recent years the introduction of new materials has made the field of proximity effect richer with for instance the observation of a striking μm-range proximity effect though ferromagnetic layers presumably due to equal-spin Cooper pairs (a.k.a. “spin-triplet”) [39, 40, 41], or predictions of the presence of composite “Majorana fermions” in exotic proximity structures involving topological insulators or semiconductors with strong spin-orbit coupling [42].

The behaviour of all the above mentioned structures, despite their very different electronic properties, can be qualitatively understood within a remarkably uniform language based on key concepts of the superconducting proximity effect: Andreev reflections and Andreev bound states [26, 28, 43]. These two concepts are easily understood and depicted in the combined framework of the Landauer-Büttiker scattering formalism and the Bogoliubov-de Gennes formulation [44] of the BCS theory [45, 46, 47]. We first introduce them below.

Then we will restrict the topic to proximity effect in Quantum dots (a general introduction to Quantum Dots is provided in appendix A). Many experiments have already reported the measurement of a Josephson supercurrent through QDs [48], but the link between these observations and the underlying phenomena remained rather qualitative. By addressing the DOS of the QD in proximity effect, we reach a deeper understanding of these experiments.

In chapter 2, we will introduce the concepts of Andreev reflection and Andreev Bound States with scattering formalism which provides intuitive pictures of those notions. Afterward, in chapter 3, we will introduce a Green's function description of the superconducting proximity effect in QD. This formal tool affords a handy and straightforward way to calculate observables in a QD. In this part of the thesis, we will first focus on not too strongly coupled QD in which effective non-interacting models are appropriate. Later on, we will address the case of QD displaying Kondo effect [49].

Chapter 2

Scattering description of the proximity effect

In the present chapter, we adopt the scattering approach to describe general properties of the proximity effect. This approach, pioneered by C. Lambert [50] and C. Beenakker [51], allows to obtain the quasiparticle excitation spectrum of a Josephson junction including the Andreev Bound States. From this spectrum can be deduced various observables such as the supercurrent.

Here, we follow closely Beenakker's method and notations to introduce the process of Andreev reflections and the formation of Andreev Bound States in S-X-S junctions. Finally, since the experiments we performed use a carbon nanotubes as a QD, we eventually apply this description to a quantum dot in which interactions are treated in a minimal fashion.

2.1 Andreev reflection

Andreev reflection is the process by which charge carriers from a normal metal (X) can enter a superconductor (S). Addressing this problem amounts to solve the Bogoliubov-de Gennes equations at an X-S interface, and this is a difficult problem since one should in principle determine the superconducting order parameter Δ (see appendix F for definition) self-consistently while solving the equations. Fortunately, in many experimental situations where a weak link is connected to much more massive superconducting electrodes, approximating the order parameter as a step function at the interface yields a simple and yet very good approximation. In this case, the Andreev reflection amplitude can be obtained by simply matching wave functions of the normal metal with those of the bulk superconductor.

Let us consider an electron in the normal metal ($x < 0$) at an energy

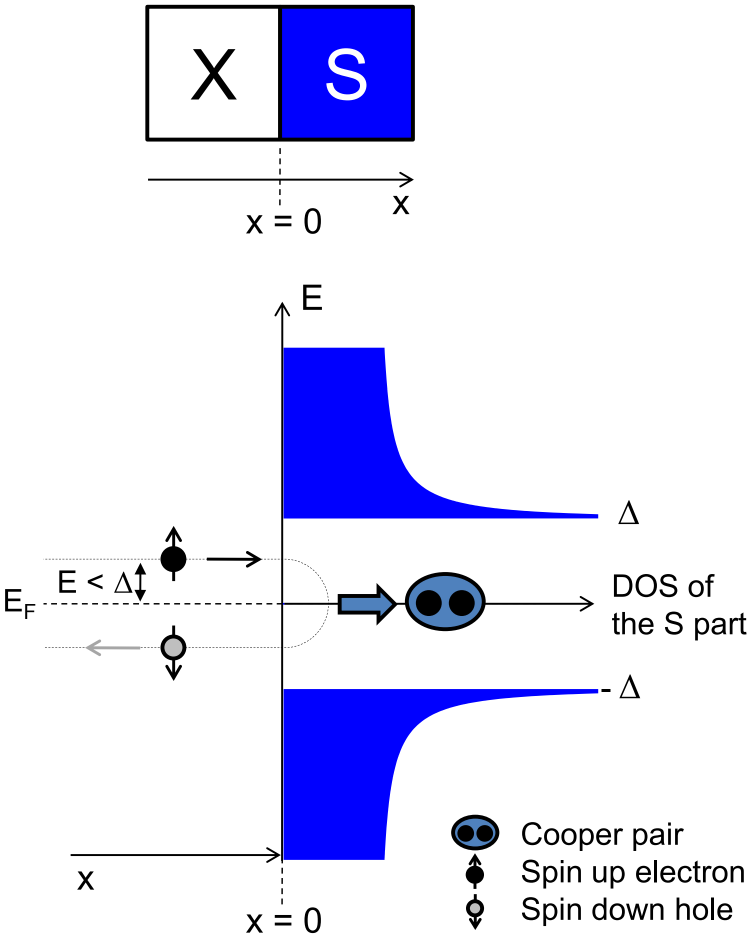

Andreev Reflection of an electron ←● into its time-reversed conjugated hole ○→ at a X-S interface

Figure 2.1: Schematic representation (bottom diagram) of the Andreev reflection of an electron into its time-reversed conjugated hole at a X-S interface. The latter is represented in the top diagram with the X part on the left and the S part on the right. When a right-moving spin up electron in the X part, with an energy E smaller than the superconducting gap Δ, reaches the interface with a S part (represented by its density of states in blue) at $x = 0$, it cannot enter by itself the superconductor. It may be either normally reflected (if the interface is not perfect) or Andreev reflected into its time-reversed conjugated hole (left-moving and spin down). In the latter case, a Cooper pair ●● is transferred to the superconductor S.

(defined with respect to the Fermi level E_F) lower than the superconducting gap $|\epsilon| < \Delta$ propagating toward the superconducting part ($x > 0$). Since the solutions to the BdG equation in the superconductor (equivalent of the Schrödinger's equation in normal materials) are in the Nambu space, we also describe the normal metal states in this space. The incident electron is then a state:

$$\begin{bmatrix} 1 \\ 0 \end{bmatrix} e^{ikx}$$

that we need to match to states in the S region (see Eq. F.7 of section F.2 in appendix F) at the interface ($x = 0$ see Fig. 2.1). For matching the hole part, it is necessary to introduce a reflected hole component on the N side (l.h.s.):

$$\begin{bmatrix} 1 \\ 0 \end{bmatrix} e^{ikx} + \lambda \begin{bmatrix} 0 \\ 1 \end{bmatrix} e^{ikx} \quad = \quad \mu \begin{bmatrix} 1 \\ a\left(\frac{\epsilon}{|\Delta|}\right) e^{-i\phi} \end{bmatrix} e^{ik_+(\epsilon)x}$$

where λ and μ are coefficients to be determined (one rapidly sees that $\mu = 1$) and a is a function of the energy given by the ratio of the coherence factors (see appendix F). Since $|\epsilon| < \Delta$, the wavevectors are imaginary on the S side (r.h.s.) and only the evanescent wave ($\mathrm{Im}\left[k_+(\epsilon)\right] > 0$) is an acceptable physical solution. The hole reflection amplitude is simply:

$$\lambda = a\left(\frac{\epsilon}{|\Delta|}\right) e^{-i\phi}$$

For $|\epsilon| < \Delta$, one has $|a|^2 = 1$ so that, the electron is reflected as a hole with unit probability ($|\lambda|^2 = 1$). Note that the phase of reflected hole relative to that of the incident electron depends both on energy (through $\arg(a)$) and on the phase ϕ of the order parameter of the superconductor (see Fig. F.3). A hole in X incident on S is conversely reflected as an electron. However, a hole propagating to the right has a negative wave vector and has to be matched with a $-k_-(E)$ solution. The reflection coefficient is then $a\left(\frac{\epsilon}{|\Delta|}\right) e^{+i\phi}$, where ϵ is the energy of the reflected electron.

This is the Andreev reflection process that explains how charges pass from N to S: the right-propagating incident electron carries a charge $-e$, and it is reflected as a left-propagating hole of charge $+e$. By conservation, a charge $-2e$ has to enter the superconductor as a Cooper pair, in the so-called "superconducting condensate".

The Andreev process is not restricted to $|\epsilon| < \Delta$; the same reasoning can be made at all energies in exactly the same way, with the same formal result: the a function correctly gives the probability amplitude for the hole reflection process at all energies. Thus the a function is generally called the Andreev reflection amplitude. As shown in appendix F (Fig. F.3), for $|\epsilon| > \Delta$, the Andreev reflection probability is less than unity, falling off rapidly away from the gap edge.

2.1.1 Scattering description of AR

From the point of view of electrons and holes in the normal metal, one can describe the Andreev reflection process using a scattering matrix, that relates the amplitudes of the incoming states on the NS interface and outgoing (reflected) states:

$$\begin{pmatrix} e_{out} \\ h_{out} \end{pmatrix} = a\left(\frac{\epsilon}{|\Delta|}\right)\begin{pmatrix} 0 & e^{-i\phi} \\ e^{i\phi} & 0 \end{pmatrix}\begin{pmatrix} e_{in} \\ h_{in} \end{pmatrix}$$

This scattering matrix is unitary (*i.e.* particle-number conserving) only for energies $|\epsilon| < \Delta$. At larger energies, propagating quasiparticles can enter the superconductor and Andreev reflection is only partial.

2.1.2 Case of non ideal materials and interfaces

The above description of plane wave matching to describe the Andreev reflection is not essential. The process also occurs in diffusive materials, and the Andreev reflection amplitude is exactly the same for diffusive states, as long as the inverse proximity effect can be neglected.

In cases where the inverse proximity effect cannot be neglected, the order parameter has a spatial dependence different from a step function at the interface. Then one cannot simply match the wave functions of the N side with the bulk superconductor wave functions. However the fact that no propagating states exist in S at energies $|\epsilon| < \Delta$ is still true, so that full Andreev reflection remains exactly valid. The only change will be that the detailed energy dependence of the AR amplitude will be quantitatively different from that given above, but not qualitatively. Hence, whatever the interface, whatever the materials, AR remains perfect and can be seen as a spectral property of NS interfaces.

For interfaces with imperfect transparency, a normal (non-Andreev) scattering also occurs at the interface, partly reflecting electrons as electrons and holes as holes, in addition of the AR process. Both these processes can be cast into a single scattering matrix that remains unitary at energies below the gap. The normal scattering process can also be formally separated from the pure AR process. This is what we do in the following.

2.2 ABS in S-X-S systems

The Landauer description of coherent conductors [36] (Fig. 2.2) in the normal state allows to describe transport in terms of independent channels, the Landauer channels. This picture, valid in absence of electron-electron and inelastic interactions inside the device, elegantly deals with interferences in quantum devices and yields a powerful and intuitive description of such systems. This approach can be adapted to describe systems with superconducting reservoirs provided we can neglect the pairing interaction in the central part of the device, that is, when the scattering of electrons and of holes can be considered separately. This assumption is justified if either the central part is not intrinsically superconducting (the pairing interaction is zero inside the central part), or the central part is much shorter than the coherence length of superconductor so that the pairing interaction has a negligible weight in that part compared to the reservoirs. Moreover, as in Ref. [51], we assume that the only scattering in the superconductors consists of Andreev reflection at the SN interfaces, *i.e.* normal scattering happens only within the central part of the device.

We first write the scattering matrix for electrons and holes in this system in the normal state.

2.2.1 Normal state scattering matrices

For electrons in the central part, the vectors of incident (a) and reflected (b) electronic modes in the left (n1 modes) and right (n2 modes) leads are related by the scattering matrix according to:

$$\begin{pmatrix} b^e_{n1} \\ b^e_{n2} \end{pmatrix} = S^e . \begin{pmatrix} a^e_{n1} \\ a^e_{n2} \end{pmatrix}$$

where S^e, the scattering matrix, a priori depends on energy and has the block structure:

$$S^e = S^e(\epsilon) = \begin{pmatrix} r(\epsilon) & t(\epsilon) \\ t'(\epsilon) & r'(\epsilon) \end{pmatrix}$$

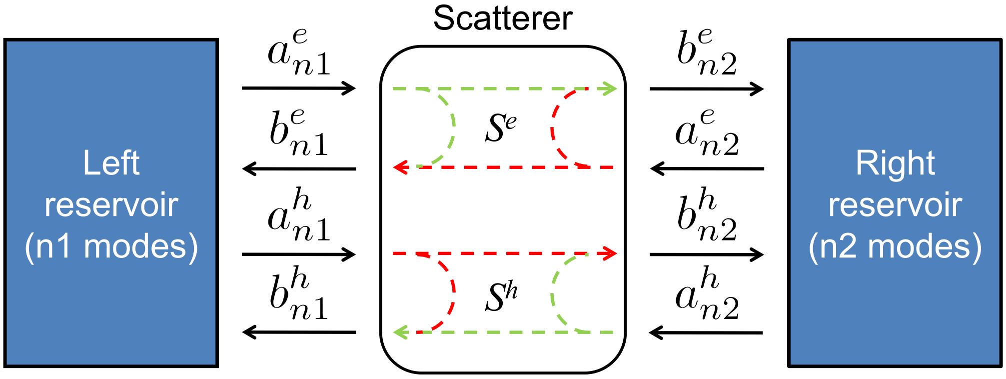

Figure 2.2: In the Landauer description, a coherent conductor is described by a matrix $S_N = \begin{pmatrix} S^e & \mathbf{0} \\ \mathbf{0} & S^h \end{pmatrix}$ containing the probability amplitudes for a mode of a reservoir to be either reflected or transmitted.

(in systems obeying time-reversal symmetry[1] $t' = t$). Similarly, the hole scattering is given by:

$$\begin{pmatrix} b^h_{n1} \\ b^h_{n2} \end{pmatrix} = S^h . \begin{pmatrix} a^h_{n1} \\ a^h_{n2} \end{pmatrix}$$

For a given electron at energy ϵ (relative to E_F), its conjugated hole in Nambu space has opposite energy. In systems where electron and hole components of the Nambu space inside X have the same symmetries as BCS superconductors (that is, all states are spin-degenerate and holes are exact time-reversed symmetric particles of electrons), the scattering of holes can be obtained simply by "projecting the electron movie in reverse motion". In that case the S^e and S^h matrices for holes and electrons are linked by:

$$S^h(\epsilon) = (S^e(-\epsilon))^*$$

Combined scattering of electrons and holes on X can thus be expressed

---

[1] In mesoscopic physics, a time-reversal symmetry is considered to be broken when particles with opposite spins going in opposite directions have different amplitude probability to be transmitted, for example in presence of a magnetic field. However time-reversal symmetry, in the sense of particle physics, is of course not broken: if we really reverse time, we also reverse magnetic field and a particle will go over the same trajectory, simply reversed.

as:

$$\begin{pmatrix} b^e_{n1} \\ b^e_{n2} \\ b^h_{n1} \\ b^h_{n2} \end{pmatrix} = S_N . \begin{pmatrix} a^e_{n1} \\ a^e_{n2} \\ a^h_{n1} \\ a^h_{n2} \end{pmatrix}$$

where S_N can be cast as a block matrix:

$$S_N = \begin{pmatrix} S^e & \mathbf{0} \\ \mathbf{0} & S^h \end{pmatrix}$$

with $\mathbf{0}$ a matrix with all its entries equal to 0.

2.2.2 Andreev scattering

As shown above in section 2.1.1, the Andreev reflection can be described as a scattering process for which the b states become incident and the a are emergent:

$$\begin{pmatrix} a^e_{n1} \\ a^e_{n2} \\ a^h_{n1} \\ a^h_{n2} \end{pmatrix} = S_A . \begin{pmatrix} b^e_{n1} \\ b^e_{n2} \\ b^h_{n1} \\ b^h_{n2} \end{pmatrix}$$

where S_A can also be cast as a block matrix:

$$S_A = a\left(\frac{\epsilon}{|\Delta|}\right) \begin{pmatrix} \mathbf{0} & \begin{matrix} I_{n1}e^{-i\phi_1} & \mathbf{0} \\ \mathbf{0} & I_{n2}e^{-i\phi_2} \end{matrix} \\ \begin{matrix} I_{n1}e^{i\phi 1} & \mathbf{0} \\ \mathbf{0} & I_{n2}e^{i\phi_2} \end{matrix} & \mathbf{0} \end{pmatrix}$$

where I_n is a $n \times n$ identity matrix and ϕ_1 and ϕ_2 are the superconducting phases of the two reservoirs.

2.2.3 Resonant bound states : Andreev Bound States

Cascading the above S_N and S_A matrices, an incident state $a_{in} = \left(a^e_{n1} a^e_{n2} a^h_{n1} a^h_{n2}\right)$ is stationary and bound inside X (with only evanescent tails into the superconductors) whenever $a_{in} = S_A . S_N a_{in}$. This condition implies that the energies which give the roots of the equation[2]:

$$\mathrm{Det}\left[I - S_A . S_N\right] = 0 \tag{2.1}$$

---

[2] I is a $(n1 + n2) \times (n1 + n2)$ identity matrix.

are the energies of these bound states. These states mediated by the Andreev reflection are the so-called ABSs. Therefore, if X is described by an appropriate scattering matrix S_N, the ABSs energies can always be found with relation 2.1. The existence of Andreev Bound States is thus a universal feature of hybrid S-X-S junction[3].

Beenakker and van Houten pointed out [52] that this situation was analogous to a Fabry-Perot optical resonator with phase-conjugating mirrors. The role of the optical cavity is played by the coherent conductor, a CNT in our experiment, and its interfaces with superconducting leads play the role of the mirrors. Andreev reflection is analogous to optical phase conjugation: an electron in the nanostructure with energy below the superconducting gap is reflected as its time-reverse conjugated hole. This hole can be subsequently reflected as an electron, and if the phase acquired during this cycle fulfils a resonant condition, ABSs form. ABSs thus correspond to optical resonant standing waves, being however electronic excitations constituted by a superposition of time-reversed states with opposite spins. Within the superconducting gap, ABS form a discrete spectrum which depends on the superconducting phase difference $\delta = \phi_1 - \phi_2$ between the left and right superconducting electrodes, as we can see by rewriting Eq. 2.1 in the form:

$$\mathrm{Det}\left[I - a\left(\frac{\epsilon}{|\Delta|}\right)^2 \begin{pmatrix} e^{-i\frac{\delta}{2}} & 0 \\ 0 & e^{i\frac{\delta}{2}} \end{pmatrix} S^e(\epsilon) \begin{pmatrix} e^{i\frac{\delta}{2}} & 0 \\ 0 & e^{-i\frac{\delta}{2}} \end{pmatrix} S^h(\epsilon)\right] = 0$$

This phase dependence is the manifestation of the fact that in each AR the electron (resp. hole) acquires a phase[4] ϕ_1 or ϕ_2 (resp. $-\phi_1$ or $-\phi_2$), such that after a cycle the phase acquired depends on δ. The phase difference is thus analogous to the length of the optical Fabry-Perot. This phase dependence is a characteristic signature of the ABSs in S-X-S structures and the proof that they carry supercurrent (see 3.1.5, appendix C and Ref. [51, 53, 54]).

In appendix F, we discuss the well-known case of an infinitely short single channel with perfect and finite transmission.

2.2.4 Supercurrent in S-X-S junctions: contribution of ABSs

The scattering formalism is not restricted to the extraction of the ABSs' spectrum. Beenakker has indeed shown in Ref. [54] the link between the

---

[3] It is also true for S-X structures where bound states can form at interfaces. In this case the ABSs's energies don't depend on the phase.

[4] Not only, as it also acquires an energy-dependent phase $arg\left(a\left(\frac{E}{|\Delta|}\right)\right)$ in each AR, and also a phase due to propagation and scattering in the coherent conductor.

spectrum of a S-X-S junction and the supercurrent flowing through it. He decomposes the latter in two parts:

- the contribution of the ABSs which is related to the derivative of their energies with respect to δ,
- and the contribution of the continuum (for $|E| > \Delta$).

He shows in particular that for the case of a quantum point contact, the second contribution is negligible and all the supercurrent is carried by the ABSs.

In appendix C, we give an alternative demonstration, for the case of a Quantum Dot, of these physical properties using Green's function techniques.

2.3 ABS in S-QD-S system from the scattering description

We now consider the case where the central scatterer is a quantum dot (QD). In a QD, scattering occurs via resonant tunneling through discrete states.

2.3.1 Non-interacting dot

If we consider, as a first approach, that electrons do not to interact in the QD, the lead-QD-lead structure can be modelled as a double barrier system. The energy levels are then discrete spin-degenerate states given by the ladder of waves-in-a-box solutions to the Schrödinger equation.

Let ϵ_r be the energy of one of these resonant levels, relative to the Fermi energy E_F in the reservoirs, and let $\Gamma_L/\hbar$ and $\Gamma_R/\hbar$ be the tunnel rates through the left and right barriers. We denote $\Gamma = \Gamma_L+\Gamma_R$. If $\Gamma \ll \Delta E$ (with ΔE the level spacing in the quantum dot) and $T \ll \Gamma/k_\mathrm{B}$, we can assume that transport through the QD occurs exclusively via resonant tunneling through the spin degenerate level of energy ϵ_r. The conductance G of the QD has thus the form[55, 56, 57]:

$$G = \frac{2e^2}{h}\frac{4\Gamma_L\Gamma_R}{\epsilon_\mathrm{r}^2+\Gamma^2} = \frac{2e^2}{h}T_\mathrm{BW} \tag{2.2}$$

where T_BW is the Breit-Wigner transmission probability at the Fermi level. Assuming the resonance couples to a single mode in the reservoirs (generalization to many modes is straightforward, see Ref. [58]), the normal-state

Breit-Wigner scattering matrix $s_{\epsilon_r}(\epsilon)$ which yields this conductance has the form [56]:

$$s_{\epsilon_r}(\epsilon) = \begin{pmatrix} \left(1 - \frac{\mathrm{i}2\Gamma_L}{\epsilon-\epsilon_r+\mathrm{i}\Gamma}\right) e^{i2\delta_L} & -\frac{\mathrm{i}\sqrt{4\Gamma_L\Gamma_R}}{\epsilon-\epsilon_r+\mathrm{i}\Gamma} \mathrm{e}^{\mathrm{i}(\delta_L+\delta_R)} \\ -\frac{\mathrm{i}\sqrt{4\Gamma_L\Gamma_R}}{\epsilon-\epsilon_r+\mathrm{i}\Gamma} \mathrm{e}^{\mathrm{i}(\delta_L+\delta_R)} & \left(1 - \frac{\mathrm{i}2\Gamma_R}{\epsilon-\epsilon_r+\mathrm{i}\Gamma}\right) e^{i2\delta_R} \end{pmatrix} \tag{2.3}$$

Note that since the reflection phases δ_L and δ_R later vanish in the determination of the energies of the ABS, we do not need to specify them. Büttiker has shown how the conductance, given by Eq. 2.2, follows, via the Landauer formula (see Ref. [36]), from the Breit-Wigner scattering matrix 2.3.

As we are able to describe a non-interacting QD by scattering matrix, we can perfectly describe the superconducting proximity effect in QDs in term of ABSs and find their energies with relation 2.1. Beenakker and van Houten [59] have considered the ABSs occurring through such *spin-degenerate* resonance, that is when both spin components of the ABS are parts of the same resonant level. They found results for the supercurrent in agreement with the perturbative approach of Glazman and Matveev [22], validating their scattering approaches for description of the superconducting proximity effect in QDs with small charging energies.

2.3.2 Weakly-coupled interacting dot: simple effective model

However, in real QDs, in addition to the confinement energy mentioned above, Coulomb repulsion has to be taken into account. In simplest situations one can nevertheless recover a simple effective non-interacting picture, in which each time an electron is added to the QD one merely pays a charging energy and possibly the configuration energy necessary to access the next free orbital (see the appendix A for a more detailed discussion of QDs).

When the coupling to the leads is weak, one needs to invoke states of opposite spin to build an ABS. In a dot where time-reversal symmetry is not broken, the most favorable states for making an ABS correspond to a pair of state arising from a single orbital of the dot, that is a singly-occupied orbital (odd electron number in the dot) followed by the doubly occupied orbital (even electron number). Such a pair of states are the closest in energy, only separated by the effective charging energy of the dot, and the two electrons involved in these states have opposite spin by virtue of the Pauli exclusion principle. Moreover these states are coupled in an identical manner to the reservoirs since this coupling arises from properties of the orbital. Nevertheless taking into account this interaction together with the coupling to the

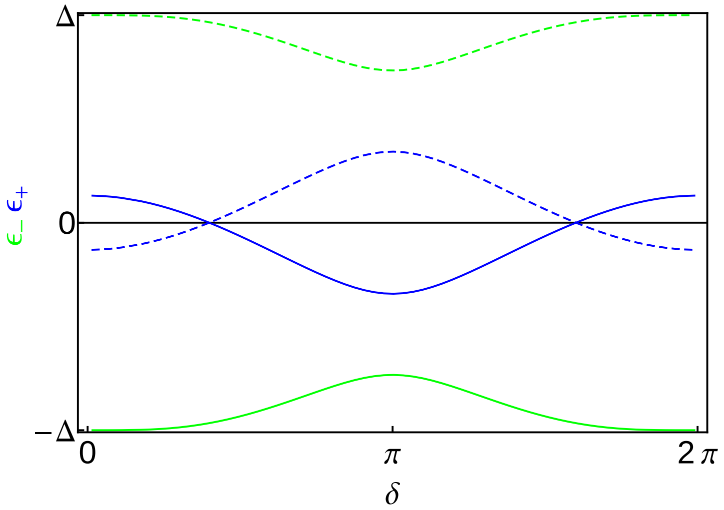

ABSs energies ϵ_- and ϵ_+ from scattering description

Figure 2.3: In solid lines, we have represented ϵ_- and ϵ_+ as a function of δ obtained from Eq. 2.4 with $\epsilon_\uparrow = -2.5\Delta$, $\epsilon_\downarrow = 2.5\Delta$, $\Gamma_L = 2\Delta$, $\Gamma_R = \Delta$. In dashed lines, we have represented the ABSs for the same parameters except that we have inverted spin up and spin down.

electrodes terribly complicates the problem and no fully analytic results exists (See appendix A). Yet, within some range of parameters, most of the effect of Coulomb interaction of the electrons in the dot can be mimicked by introducing a phenomenological breaking of the spin degeneracy of these states (see Appendix A, and Refs [16]). Such a "caricature" of the problem yields a tractable non-interacting effective model that still contains a good deal of the interesting physics of this system. Discussing or justifying this approximation is beyond the scope of this experimental thesis, but in chapter 3 we will show how the results of this phenomenological model compare with exact numerical results.

We thus consider a pair of levels:

$$\begin{aligned}\epsilon_\uparrow &= \epsilon_0 + U/2\\ \epsilon_\downarrow &= \epsilon_0 - U/2\end{aligned}$$

where ϵ_0 is the mean position of the levels (we will see in part II, that this parameter can be controlled experimentally by a gate voltage), and $U = |\epsilon_\uparrow - \epsilon_\downarrow|$ is the effective charging energy (which of the spin up or down state is highest in energy will turn out to be unimportant, we will discuss it later).

The scattering matrix S_N then takes the form:

$$S_N = \begin{pmatrix} s_{\epsilon_\uparrow}(\epsilon) & 0 \\ 0 & s_{\epsilon_\downarrow}(-\epsilon)^* \end{pmatrix}$$

With this scattering matrix, Eq. 2.1 giving the positions of the ABS yields the equation in ϵ:

$$\mathrm{Det}\left[I_2 - a\left(\frac{\epsilon}{|\Delta|}\right)^2 \begin{pmatrix} e^{-i\delta} & 0 \\ 0 & e^{i\delta} \end{pmatrix} s_{\epsilon_\uparrow}(\epsilon) \begin{pmatrix} e^{i\delta} & 0 \\ 0 & e^{-i\delta} \end{pmatrix} s_{\epsilon_\downarrow}(-\epsilon)^*\right] = 0 \quad (2.4)$$

where $\delta = \phi_1 - \phi_2$ is the superconducting phase difference between the two reservoirs.

Expending the determinant, this equation takes the algebraic form[5]:

$$D(\epsilon) \frac{4(\Delta^2 - \epsilon^2)}{\Delta^2 (\epsilon - \epsilon_\uparrow + \mathrm{i}\Gamma)(-\epsilon - \epsilon_r - \mathrm{i}\Gamma)} a\left(\frac{\epsilon}{|\Delta|}\right)^2 = 0$$

with:

$$D(\epsilon) = \left[\epsilon + \frac{U}{2} - \Gamma g(\epsilon)\right]^2 - \epsilon_0^2 - \Gamma^2 \left[1 + \left(1 - \frac{\delta\Gamma^2}{\Gamma^2}\right)\sin^2\left(\frac{\delta}{2}\right)\right] f(\epsilon)^2 \quad (2.5)$$

where $\delta\Gamma = \Gamma_L - \Gamma_R$, $g(\epsilon) = \frac{-\epsilon}{\sqrt{\Delta^2 - \epsilon^2}}$ and $f(\epsilon) = \frac{\Delta}{\sqrt{\Delta^2 - \epsilon^2}}$. Roots of Eq. 2.5 give the energy of the ABSs. As shown in Fig. 2.3, within the gap of the superconductors, there are 2 solutions ϵ_+, ϵ_- to the equation $D(\epsilon) = 0$, such that $-\Delta < \epsilon_-, \epsilon_+ < \Delta$.

2.3.3 Meaning of the sign of the eigenenergies; arbitrariness of the description

In the previous section, we arbitrarily assumed that the spin up electron state has an energy lower by U than the spin down electron state. This choice led to get two eigenenergies ϵ_+ and ϵ_- that are not symmetric with respect to the Fermi level. Making the opposite choice (or equivalently chosen $U < 0$), the sign of the eigen-energies would have been reversed (dashed lines in Fig.

---

[5] To reach this expression we use the fact that $s_{\epsilon_\downarrow}(-\epsilon)^*$ is unitary (*i.e.* $s_{\epsilon_\downarrow}(-\epsilon)^\dagger s_{\epsilon_\downarrow}(-\epsilon) = I_2$) to transform Eq. 2.4 into: $\frac{a\left(\frac{\epsilon}{|\Delta|}\right)^2}{Det\left[s_{\epsilon_\downarrow}(-\epsilon)\right]} \times Det\left[a\left(\frac{\epsilon}{|\Delta|}\right)^* s_{\epsilon_\downarrow}(-\epsilon)\begin{pmatrix} e^{-i\delta} & 0 \\ 0 & e^{i\delta} \end{pmatrix} - a\left(\frac{\epsilon}{|\Delta|}\right)\begin{pmatrix} e^{-i\delta} & 0 \\ 0 & e^{i\delta} \end{pmatrix} s_{\epsilon_\uparrow}(\epsilon)\right] = 0$ and we use the relation $s_{\epsilon_\downarrow}(-\epsilon) = \left(s_{\epsilon_\uparrow}(\epsilon) - 1\right) \times \frac{\epsilon - \epsilon_\uparrow + \mathrm{i}\Gamma}{-\epsilon - \epsilon_\downarrow + \mathrm{i}\Gamma} + 1$.

2.3). However, physical observables, such as the Josephson current or the tunnel density of states will end to be the same whether we choose, in our model, U to be positive (spin up lower in energy) or negative (spin up higher in energy).

This is related to the fact that signs of the energies, that are roots of Eq. 2.5, have no real physical meaning and are just conventional features related to the Nambu space. This is discussed in section F.1.

Chapter 3

Proximity effects in QD in terms of Greens functions

The scattering formalism described above offers a clear physical picture to understand how ABSs form in general, and in a QD, in particular. However a Green's functions (GF) description of the proximity effect in QD is a more straightforward technique to calculate physical observables of the system, such as the Josephson current carried by the QD or its DOS. We stress that the two formalisms are rigorously equivalent (see for example [60, 61, 62] or Appendix A of Ref. [49]), and thus observables could also be computed in the scattering approach. In this chapter divided in three sections, we tackle the problem of a S-QD-S junction using GF techniques.

To calculate the GFs that will allow us to obtain these observables, we need to write down the Hamiltonian of the S-QD-S system. The latter can be correctly described by a single-level Anderson model (introduced in detail in appendix A) but where normal leads are replaced by BCS superconductors. There are, however, no exact analytical solution for this model. Therefore, following Ref. [16], we first use an approximation (see also section A.4.1) which gives rise to an effective non-interacting model that we can solve. Then, we will use Numerical Renormalization Group (NRG) technique, which allows an exact numerical treatment of the QD with superconducting leads, in order to validate the phenomenological model and to find out its region of applicability.

In the first section 3.1, we use the effective model of Ref. [16] in which Coulomb repulsion in the QD is addressed phenomenologically in the same non-interacting picture than in section 2.3. In order to calculate the TDOS and the supercurrent through the QD, we express the Green's functions which will be introduced in subsection 3.1.1. General properties of GFs like self-energy and poles will be included in this subsection in order to gain a physical insight on this formalism. Next in subsection 3.1.2, we explain how to extract from QD's GF a first observable: the QD's density of states. Then we analyze the GF's expression for an asymmetric QD in section 3.1.3, and we extend our model to a double QD in which two QDs are connected in series between two superconducting electrodes in section 3.1.4. In section 3.1.5, we explain how to calculate, from QD's GFs a second observable: the supercurrent flowing through the QD. We also discuss how the phenomenological model describes the singlet-doublet transition of the device and the resulting reversal of supercurrent (the so-called $0 - \pi$ transition) [3, 48].

In section 3.2, we briefly introduced the NRG technique. We will discuss how one can used NRG calculations to obtain exact numerical results on the proximity effect in QD.

Finally in section 3.3, we analyze the influence of the physical ingredients of the model on the QD's DOS and particularly on the ABSs. In parallel to this analysis, we carry out a comparison between NRG and the simplified non-interacting treatment in order to understand the limits of the phenomenological approach.

3.1 Effective description of the S-QD-S junction

3.1.1 Green's function of a QD connected to superconducting leads

We use here exactly the same effective non-interacting picture of a QD coupled to superconducting leads (see section A.4.1 appendix A) as in the scattering description of section 2.3. However, in contrast with the scattering approach where we used known results without making explicit the Hamiltonian of the system, here we write down this Hamiltonian, as we will need it to express the GF.

3.1.1.1 Effective Hamiltonian of a S-QD-S junction

As in section 2.3, we restrict to a single orbital of the QD, as most of the relevant physics is captured in this simple case. There are at most two electrons in the dot, which then are necessarily of opposite spin, due to the Pauli principle. We also adopt the same approximate treatment of the Coulomb interaction by introducing a phenomenological breaking of the spin degeneracy of this single level[1] (See Appendix A). The QD is thus described by a spin up level of energy $\epsilon_\uparrow = \epsilon_0 + U/2$ and a spin down level of energy $\epsilon_\downarrow = \epsilon_0 - U/2$, with U the effective charging energy. Hence the QD itself is simply described by:

$$H_{QD} = \sum_{\sigma=\uparrow,\downarrow} \epsilon_\sigma d^\dagger_\sigma d_\sigma$$

where d_σ is the annihilation operator of an electron in the QD of energy ϵ_σ with a spin σ.

The left and right superconducting electrodes are described by the BCS Hamiltonian:

$$\begin{aligned} H_L &= \textstyle\sum_{l,\sigma} \epsilon_l c^\dagger_{l\sigma} c_{l\sigma} + \sum_l \left(\Delta e^{i\phi_L} c^\dagger_{l\uparrow} c^\dagger_{-l\downarrow} + \Delta e^{-i\phi_L} c_{-l\downarrow} c_{l\uparrow}\right) \\ H_R &= \textstyle\sum_{r,\sigma} \epsilon_r c^\dagger_{r\sigma} c_{r\sigma} + \sum_r \left(\Delta e^{i\phi_R} c^\dagger_{r\uparrow} c^\dagger_{-r\downarrow} + \Delta e^{-i\phi_R} c_{-r\downarrow} c_{r\uparrow}\right) \end{aligned}$$

Here $c_{l(r)\sigma}$ is the annihilation operator of an electron of the left (resp. right) electrode in state $l\,(r)$ with an energy $\epsilon_l\,(\epsilon_r)$, and spin σ. In this notation, l and r represent a synthetic index for all the quantum numbers of the electrons in electrodes, except their spin, and such that $c_{-l-\sigma}$ is the time reversed-state of $c_{l\sigma}$. $\Delta e^{i\phi_{L(R)}}$ is the complex order parameter in electrode $L(R)$ with modulus Δ (also known as the gap energy) and phase $\phi_{L(R)}$.

Finally, the coupling of the dot to the leads is described by a hopping term:

$$\begin{aligned} H_{T_L} &= \textstyle\sum_{l,\sigma} \left(t_L d^\dagger_\sigma c_{l\sigma} + t^*_L c^\dagger_{l\sigma} d_\sigma\right) \\ H_{T_R} &= \textstyle\sum_{r,\sigma} \left(t_R d^\dagger_\sigma c_{r\sigma} + t^*_R c^\dagger_{r\sigma} d_\sigma\right) \end{aligned}$$

where $t_{L(R)}$ is the energy associated to the transfer of an electron between left (right) electrode and the dot. We assume these couplings to be energy-independent as in Refs. [63, 64]. The whole system is schematized in Fig. 3.1.

Electron-hole spinor field operator in Nambu space As superconductivity induces correlations between electrons and holes of opposite spins, we will need to express GF with electron-hole spinor field operators in Nambu space, $\psi_{l(r)} = \begin{pmatrix} c_{l(r)\uparrow} \\ c^\dagger_{-l(-r)\downarrow} \end{pmatrix}$ and $\psi_d = \begin{pmatrix} d_\uparrow \\ d^\dagger_\downarrow \end{pmatrix}$.

---

[1] This lift of degeneracy used to model phenomenologically the Coulomb interaction is not a real Zeeman splitting: there are no magnetic field and the axis of spin quantization is not even specified.

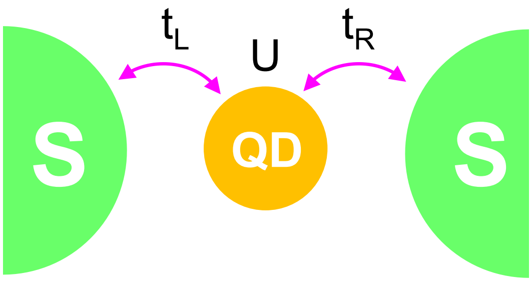

QD connected to superconducting leads

Figure 3.1: In our model, the QD is characterized by three parameters: the coupling to the left (resp. right) lead t_L (resp. t_R) and the effective charging energy U.

In this spinor basis, the Hamiltonian can be written as a matrix expression[2]:

$$H = \sum_{i=l,r} \psi_i^\dagger \mathcal{E}_i \psi_i + \psi_d^\dagger \mathcal{E}_{QD} \psi_d + \sum_l \left[\psi_d^\dagger \mathcal{E}_{T_L} \psi_l + h.c. \right] + \sum_r \left[\psi_d^\dagger \mathcal{E}_{T_R} \psi_r + h.c. \right]$$

where:

$$\mathcal{E}_{QD} = \begin{pmatrix} \epsilon_\uparrow & 0 \\ 0 & -\epsilon_\downarrow \end{pmatrix}, \; \mathcal{E}_{l(r)} = \begin{pmatrix} \epsilon_{l(r)} & \Delta e^{i\phi_{L(R)}} \\ \Delta e^{-i\phi_{L(R)}} & -\epsilon_{l(r)} \end{pmatrix}, \text{ and } \mathcal{E}_{T_{L(R)}} = \begin{pmatrix} t_{L(R)} & 0 \\ 0 & -t^*_{L(R)} \end{pmatrix}$$

that will be useful to write GF in a simple and compact matrix form.

3.1.1.2 Green's function of the Quantum Dot

As discussed in introduction of this chapter, properties of the QD are encoded in the QD's GF. In this section, we define the QD's GF in Nambu space and give its expression (the detailed derivations are given in appendix B).

Definition of the QD Green's function In Nambu notation and in time domain, the QD GF takes the form[3]:

$$\begin{aligned} \hat{\mathcal{G}}_{dd}(t) &= -i \langle T_t \psi_d(t) \psi_d^\dagger(0) \rangle \\ &= -i \begin{pmatrix} \langle T_t d_\uparrow(t) d_\uparrow^\dagger(0) \rangle & \langle T_t d_\uparrow(t) d_\downarrow(0) \rangle \\ \langle T_t d_\downarrow^\dagger(t) d_\uparrow^\dagger(0) \rangle & \langle T_t d_\downarrow^\dagger(t) d_\downarrow(0) \rangle \end{pmatrix} \end{aligned} \tag{3.1}$$

---

[2] In this writing we have dropped an unimportant constant equal to $\sum_l \epsilon_l + \sum_r \epsilon_r + \epsilon_\downarrow$ that does not change the physics.

[3] The symbol $\hat{\ }$ is here to distinguish the 2×2 matrix in Nambu space from its coefficients.

where T_t is the time-ordering operator:

$$T_t \psi_d(t)\, \psi_d^\dagger(0) = \theta(t)\, \psi_d(t)\, \psi_d^\dagger(0) - \theta(-t)\, \psi_d^\dagger(0)\, \psi_d(t)$$

which preserves GF causality, and $\langle A \rangle$ represents the expectation value of operator A (defined by Eq. B.1).

Diagonal elements of $\hat{\mathcal{G}}_{dd}(t)$ give the temporal evolution of a bare electron or hole injected in the QD[4], in this respect they are also called propagators. We will see that this is directly linked to the QD's density of states. Non-diagonal parts of $\hat{\mathcal{G}}_{dd}(t)$, also called "anomalous" GFs, indicate pair correlations amplitude in the QD and are equal to zero in absence of superconductivity.

Expression for the QD GF In section B.3, we carry out the full derivation of the GF from its equation of motion (EOM) in the Matsubara formalism. Below we simply present and use the result of this derivation.

A convenient way to express the GF is to introduce the analytic continuation $\hat{\mathcal{G}}_{dd}(z)$ of the Fourier transform of $\hat{\mathcal{G}}_{dd}(t)$, where z has the dimension of an energy and can take values in the entire complex plane. The resolution of the EOM yields[5]:

$$\hat{\mathcal{G}}_{dd}(z) = \left[z - \mathcal{E}_{\mathcal{QD}} - \hat{\Sigma}(z)\right]^{-1} \tag{3.2}$$

in which the QD's self-energy:

$$\begin{aligned}
\hat{\Sigma}(z) &= \hat{\Sigma}_L(z) + \hat{\Sigma}_R(z) \\
\hat{\Sigma}_L(z) &= \sum_l \mathcal{E}_{T_L} \left[z - \mathcal{E}_l\right]^{-1} \mathcal{E}_{T_L}^\dagger \\
\hat{\Sigma}_R(z) &= \sum_r \mathcal{E}_{T_R} \left[z - \mathcal{E}_r\right]^{-1} \mathcal{E}_{T_R}^\dagger
\end{aligned}$$

is due to the connection to superconducting leads. After summation over indexes l and r, $\hat{\Sigma}(z)$ becomes:

$$\hat{\Sigma}(z) = \sum_{i=L,R} \Gamma_i \begin{pmatrix} g(z) & -f(z)\, e^{i\phi_i} \\ -f(z)\, e^{-i\phi_i} & g(z) \end{pmatrix}$$

---

[4] This point is discussed in section B.3.5.

[5] Here and in the following, we don't write explicitly matrices proportional to the 2×2 unit matrix I_2, but replace them for convenience by a scalar factor. For example, $\begin{pmatrix} z & 0 \\ 0 & z \end{pmatrix} = z \times I_2$ is noted z.

where we have introduced functions $g(z) = \frac{-z}{\sqrt{\Delta^2 - z^2}}$ and $f(z) = \frac{\Delta}{\sqrt{\Delta^2 - z^2}}$, but also exchange rates between the QD and the leads $\Gamma_i = \pi \rho_F |t_i|^2$ with ρ_F the density of states at the Fermi level of the electrodes in their normal state. These rates are the same that those of matrix 2.3.

Properties of the GF The QD's GF contains the local properties of the QD. In particular, eigenstates appear as isolated poles of the diagonal elements of $\hat{\mathcal{G}}_{dd}(z)$ on the real axis, or as a branch cut in the real axis for a continuum of states. If the GF has complex poles, they correspond to quasiparticle states of finite lifetime. From $\hat{\mathcal{G}}_{dd}(z)$, we define the retarded and advanced GF that are the value of $\hat{\mathcal{G}}_{dd}(z)$ approaching the real axis from the upper and lower half of the complex plane [65], respectively (here ω and η are real and $\eta \to 0^+$):

$$\hat{\mathcal{G}}^R_{dd}(\omega) = \hat{\mathcal{G}}_{dd}(\omega + i\eta)$$
$$\hat{\mathcal{G}}^A_{dd}(\omega) = \hat{\mathcal{G}}_{dd}(\omega - i\eta)$$

and from which we will obtain the density of states of the QD.

ABS as real poles and decaying states as complex poles To illustrate the two types of poles that we have mentioned above, let us look at three peculiar cases: an isolated QD, a QD connected to normal leads and a QD connected to superconducting leads.

- The GF describing the isolated QD is given by $[z - \mathcal{E}_{\mathcal{QD}}]^{-1}$. As expected, diagonal elements of the GF have only real poles $\epsilon_\uparrow$ and $\epsilon_\downarrow$ that correspond to energies of the QD's eigenstates which have infinite lifetime. This is characteristic of an eigenstates.
- For a QD connected to normal leads ($\Delta = 0$), the retarded GF is changed in:

  $$\left[\omega + i\eta - \mathcal{E}_{\mathcal{QD}} + i\begin{pmatrix} \Gamma_L + \Gamma_R & 0 \\ 0 & \Gamma_L + \Gamma_R \end{pmatrix}\right]^{-1}$$

  In that case, the poles take complex values $\epsilon_\uparrow - i(\Gamma_L + \Gamma_R)$ and $\epsilon_\uparrow - i(\Gamma_L + \Gamma_R)$. As a consequence, when $t > 0$, the propagator is an exponentially decaying function of the time:

  $$\hat{\mathcal{G}}_{dd}(t > 0) = -i\theta(t)\, e^{-i\mathcal{E}_{QD}t} e^{-(\Gamma_L + \Gamma_R)t}$$

  which means that an electron or a hole injected in the QD has a characteristic lifetime $\hbar/(\Gamma_L + \Gamma_R)$, given by the imaginary part of the poles for escaping to the leads.

- As discussed in section B.3.4, when the leads are superconducting, the poles of the GF are the roots of equation $D(z) = \mathrm{Det}\left(z - \mathcal{E}_{QD} - \hat{\Sigma}(z)\right) = 0$ (or equivalently $\mathrm{Det}\left(\hat{\mathcal{G}}^R_{dd}(z)^{-1}\right) = 0$). On the real axis and when $|\omega| < \Delta$, $D(\omega)$ has two poles ϵ_+ and ϵ_- defined by the equality:

$$\left[\epsilon_\pm + \frac{U}{2} - \Gamma g(\epsilon_\pm)\right]^2 - \epsilon_0^2 - \Gamma^2\left[1 + \left(1 - \frac{\delta\Gamma^2}{\Gamma^2}\right)\sin^2\left(\frac{\delta}{2}\right)\right] f(\epsilon_\pm)^2 = 0 \tag{3.3}$$

where $\Gamma = \Gamma_L + \Gamma_R$, $\delta\Gamma = \Gamma_L - \Gamma_R$ and $\delta = \phi_L - \phi_R$. Eq. 3.3 is exactly the same as 2.5. Hence, these poles coincide with the ABSs calculated in the scattering approach of section 2.3 illustrating the equivalence of the two approaches.

3.1.2 Tunneling spectroscopy of a QD in terms of GF

To observe the ABS, we have chosen to explore our system by tunneling spectroscopy. This technique consists to inject or extract, with a well characterized tunnel probe under a given voltage bias, electrons in the QD and at well defined energies. By measuring the differential conductance between the probe and the QD we have rather direct access to the spectral function of the QD. In this section we give the link between the spectral function of the QD and its GF and we will discuss what would be this link for other types of spectroscopy. We also discuss how the ABSs appear in a tunneling spectroscopy, in particular the fact that each of them appear twice in the spectrum.

3.1.2.1 Definition of the QD's DOS

The spectral function of the QD is defined by the equality (see for example the textbook [65]):

$$\mathcal{A}_{dd}(\omega) = -\frac{1}{\pi}\mathrm{Im}\left[\mathrm{T}r_N\left(\hat{\mathcal{G}}^R_{dd}(\omega)\right)\right]$$

where $\mathrm{T}r_N$ is the trace in Nambu space:

$$\mathrm{T}r_N\left(\hat{\mathcal{G}}^R_{dd}(\omega)\right) = \hat{\mathcal{G}}^{R11}_{dd}(\omega) + \hat{\mathcal{G}}^{R22}_{dd}(-\omega)$$

We can show, that, when a voltage V is applied to the tunnel probe, the tunnel current through the QD is given by (a demonstration is given in appendix D):

$$\langle I(V)\rangle = \frac{2e}{\hbar}|t_{probe}|^2 \times \int_{-\infty}^{+\infty} \mathcal{A}_{probe}(\omega + eV)\,\mathcal{A}_{dd}(\omega)\left[f_{FD}(\omega) - f_{FD}(\omega + eV)\right] d\omega$$

where $f_{FD}(\omega)$ is the Fermi-Dirac distribution, t_{probe} the coupling to the probe and $\mathcal{A}_{probe}(\omega)$ the spectral function of the probe. The differential conductance, which is the quantity that we measure experimentally, is thus given by:

$$G(V) = \frac{2e}{\hbar} \left|t_{probe}\right|^2 \times \int_{-\infty}^{+\infty} \mathcal{A}_{dd}(\omega) \frac{\partial}{\partial V} \left[\mathcal{A}_{probe}(\omega + eV)\left(f_{FD}(\omega) - f_{FD}(\omega + eV)\right)\right] d\omega$$

In our experiments $\mathcal{A}_{probe}(\omega)$ is given by the well known BCS DOS (see Fig. 2.1 and Ref. [47]). The differential conductance gives thus a direct access to the spectral density of the quantum dot.

We can show that the QD's spectral density take the form[6] (see textbook [65]):

$$\mathcal{A}_{dd}(\omega) = \sum_{\alpha,\sigma} \left\{ \left|\left\langle \alpha \left| d_\sigma^\dagger \right| \psi_0 \right\rangle\right|^2 \delta(\omega - E_\alpha) + \left|\left\langle \alpha \left| d_\sigma \right| \psi_0 \right\rangle\right|^2 \delta(\omega + E_\alpha) \right\} \tag{3.4}$$

where $|\psi_0\rangle$ is the system ground state, $|\alpha\rangle$ are all the possible states of the system (QD plus superconducting leads) and E_α their energies with respect to the ground state energy. In this writing, the left term in the sum can be interpreted as the probability to inject an electron in the QD creating an excitation of energy E_α, and the right one as the probability to extract an electron from the QD creating an excitation of energy E_α.

The spectral density we obtained is *local* as we inject electrons in the system only into the QD, and is usually called the tunnel DOS or TDOS.

3.1.2.2 Comparison with other type of QD spectroscopy

The TDOS spectroscopy allows to explore the excitations of a system by creation or annihilation of an electron. This technique, like in the case of ARPES measurements [66], does not conserve the number of quasiparticles of the system under test.

However in ARPES, the system is excited by a photon of several tens of eV which expels an electron collected by a detector. As a result, since a photon cannot expel a hole from the system, the DOS obtained is limited to $\omega < 0$ and we only have access to the second part of the sum in 3.4.

There are other types of spectroscopies to probe the QD density of states that conserve the number of electrons in the system. For example by sending optical photons on the system and measuring the absorption spectra, we

---

[6] There is a more general temperature-dependent form of the TDOS. But in the effective approach, the TDOS does not depend on temperature.

would have access to another type of quantity such as:

$$\sum_{i,f} \left| \left\langle \alpha_N \left| d_{2\sigma}^{\dagger} d_{1\sigma} \right| \psi_{0N} \right\rangle \right|^2 \delta \left(\omega - E_{\alpha N} + E_{0N} \right)$$

where $|\psi_{0N}\rangle$ is the system ground state (energy E_{0N}) with N electrons and $|\alpha_N\rangle$ are the excited states of the system with the same number of electrons (energy $E_{\alpha N}$). Operator $d_{2\sigma}^{\dagger} d_{1\sigma}$ is an "exciton" operator which creates an electron-hole pair in the QD by exciting an electron with a spin σ from an orbital labelled 1 to an orbital labelled[7] 2. This process conserves the number of electron in the system and is always associated to a positive ω because $E_{\alpha N} > E_{0N}$ by definition of the ground state. We then have $\omega = \hbar\nu$ with ν the frequency of absorption.

In the rest of the manuscript, the denomination "DOS" will only concern TDOS as we are only dealing with tunnel spectroscopy.

3.1.2.3 Tunneling into ABSs

Width of ABSs: phenomenological inelastic loss η_{inel} The above theoretical treatment of ABSs predicts they are infinitely thin peaks in the spectral density. Even if this description was correct, in an actual tunneling spectroscopy experiment however, the energy resolution would be limited for example by temperature, voltage noise or coupling to the probe. In order to mimic this effect we include a depairing Dynes parameter [67] in $g(\omega)$ and $f(\omega)$, replacing ω by $\omega + i\eta_{inel}$. This gives a width to ABSs, allowing us to reproduce qualitatively the observed linewidth (see article in part II).

The origin of the measured linewidth is discussed in section D.2 appendix D, where we show that the main contribution is probably due to the coupling to the probe.

Double observation of the ABSs In tunneling spectroscopy measurements, ABSs appear twice in the DOS as is illustrated in Fig. 3.2. These states (like all Bogoliubons as explained in appendix F) have a hole part and an electron part and there is, as a consequence, a finite probability to inject an electron or a hole into an ABS. The injection of an electron (resp. hole) occurs when we apply a negative (resp. positive) voltage V on the tunnel probe. When performing the tunneling spectroscopy of ABSs, they will thus appear both at positive voltage and negative voltage. Therefore, we

---

[7] We precise here, to avoid confusion, that $|\psi_{0N}\rangle$ and $|\alpha_N\rangle$ are many-body states of the system whereas $d_{2\sigma}^{\dagger}$ and $d_{1\sigma}$ are creation and annihilation operators of single particle states.

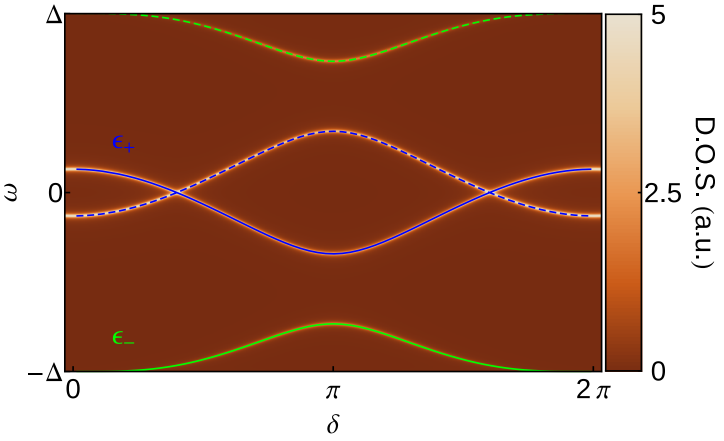

Double observation of the ABSs in the TDOS

Figure 3.2: TDOS of a QD as a function of the energy ω, within $[-\Delta, +\Delta]$, and the superconducting phase difference δ, obtained using GF technique with parameters of Fig. 2.3, superimposed with solid color traces representing the energy of the ABS. The DOS is equal to zero almost everywhere (brown areas), except for four phase-dependent peaks which are the ABSs (in white, they should be infinitely thin, but we give them an artificial width taking $\eta_{inel} = 0.01\Delta$). The ABSs energies ϵ_+ and ϵ_- (respectively in blue and green) are obtained within the scattering formalism (ϵ_+ and ϵ_- are roots of equation 2.5). As the two approaches are equivalent, the blue and green curves perfectly match with the white peaks of DOS.

will observe them twice symmetrically with $V = 0$. This explains why the arbitrariness in the sign of the ABSs's energies, mentioned in section 2.3.3, due to the sign of U and the choice of Nambu space has no incidence on the TDOS measured experimentally.

ABS weight As a consequence, two ABSs (labelled + and -), formed from a single orbital of the QD, appear twice in the TDOS to form four peaks at energies $\omega = \pm\epsilon_\pm$ with $|\epsilon_\pm| < \Delta$ and $D\left(\epsilon_\pm\right) = \text{Det}\left[\hat{\mathcal{G}}_{dd}\left(\epsilon_\pm\right)^{-1}\right] = 0$. Each peak has a different spectral weight at positive and negative energy which can be determined from the QD GF residues:

$$W_1^+ = \lim_{\omega\to\epsilon_+} \frac{\omega + \epsilon_\downarrow + \Gamma g\left(\omega\right)}{D'\left(\omega\right)}$$

$$W_1^- = \lim_{\omega\to\epsilon_-} \frac{\omega + \epsilon_\downarrow + \Gamma g\left(\omega\right)}{D'\left(\omega\right)}$$

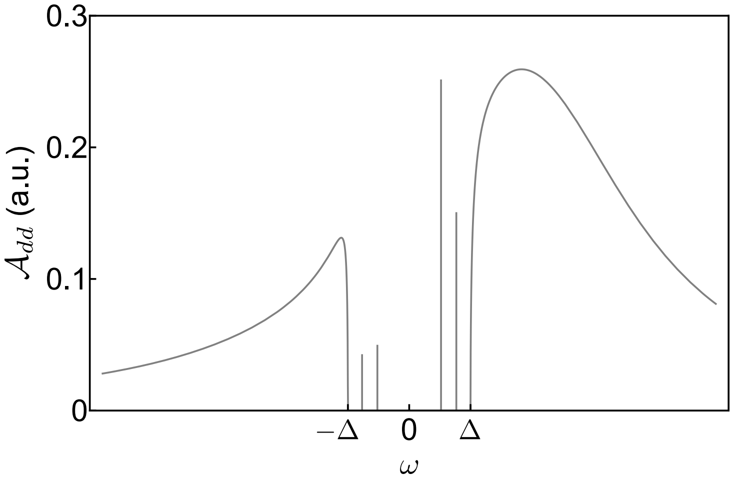

ABSs HAVE DIFFERENT WEIGHTS

Figure 3.3: TDOS of a QD connected to superconducting leads as a function of the energy ω. In $[-\Delta,+\Delta]$, ABSs are infinitely thin and are represented by vertical lines whose heights represent their weights. Parameters of the plot: $\Gamma=2\Delta$, $\epsilon_\uparrow=\Delta$, $\epsilon_\downarrow=2\Delta$, $\delta\Gamma=0$, and $\delta=\frac{\pi}{2}$.

$$W_2^+ = \lim_{\omega\to\epsilon_+} \frac{\omega-\epsilon_\uparrow+\Gamma g(\omega)}{D'(\omega)}$$

$$W_2^- = \lim_{\omega\to\epsilon_-} \frac{\omega-\epsilon_\uparrow+\Gamma g(\omega)}{D'(\omega)}$$

where $W_1^\pm$ and $W_2^\pm$ represent respectively the spin ↑ electron and spin ↓ hole parts of ABS ±.For $|\omega|<\Delta$, the TDOS thus reads:

$$\mathcal{A}_{dd}(\omega) = W_1^+\delta(\omega-\epsilon_+) + W_1^-\delta(\omega-\epsilon_-) + W_2^+\delta(\omega+\epsilon_+) + W_2^-\delta(\omega+\epsilon_-)$$

The latter, plotted on Fig. 3.3 with parameters indicated in the caption, exhibits then two peaks at $\epsilon_\pm$ with weights $W_1^\pm$and two others at $-\epsilon_\pm$ with weights $W_2^\pm$.

ABSs spins As mentioned above, each ABS has a spin ↑ and a spin ↓ part that can be deduced from weights $W_{1(2)}^\pm$. The spin $S^\pm$ of ABS ± can be simply defined as:

$$S^\pm = \frac{1}{2}\left(W_1^\pm - W_2^\pm\right)$$

For the parameters of Fig. 3.3, ABSs have their spin in opposite directions with $S^+\approx-0.104$ and $S^-\approx0.101$. The orientation of these spins is of course relative as the quantization axis is not defined.

3.1.3 Asymmetric QD

In a real sample, the coupling to the left and right leads are generally not equal. When we take into account this asymmetry $\delta\Gamma = \Gamma_L - \Gamma_R$, the general form of the QD GF as a function of $\Gamma = \Gamma_L + \Gamma_R$ and $\delta\Gamma$ is:

$$\hat{\mathcal{G}}_{dd}(z) = \begin{pmatrix} z - \epsilon_\uparrow - g(z)\Gamma & f(z)\, e^{i\frac{\phi_L+\phi_R}{2}} \left(\Gamma\cos\frac{\delta}{2} + i\delta\Gamma\sin\frac{\delta}{2}\right) \\ f(z)\,\Gamma e^{-i\frac{\phi_L+\phi_R}{2}} \left(\Gamma\cos\frac{\delta}{2} - i\delta\Gamma\sin\frac{\delta}{2}\right) & z - \epsilon_\downarrow - g(z)\Gamma \end{pmatrix}^{-1}$$

For a phase difference $\delta = 0$, only the total coupling strength Γ enters the Green functions (we actually take $\phi_R = 0$ and $\phi_L = \delta$ to get rid of phase factors that play no role in the TDOS):

$$\hat{\mathcal{G}}_{dd}(z)_{\delta=0} = \begin{pmatrix} z - \epsilon_\uparrow - g(z)\Gamma & f(z)\Gamma \\ f(z)\Gamma & z - \epsilon_\downarrow - g(z)\Gamma \end{pmatrix}^{-1}$$

The coupling asymmetry $\delta\Gamma = \Gamma_L - \Gamma_R$ plays therefore a role at finite phase difference. For instance, at $\delta = \pi$, the Green's functions read:

$$\hat{\mathcal{G}}_{dd}(z)_{\delta=\pi} = \begin{pmatrix} z - \epsilon_\uparrow - g(z)\Gamma & -f(z)\delta\Gamma \\ -f(z)\delta\Gamma & z - \epsilon_\downarrow - g(z)\Gamma \end{pmatrix}^{-1}$$

showing that the spin up and spin down levels are completely decoupled at $\delta = \pi$ in a perfectly symmetric QD where $\delta\Gamma = 0$.

In the extreme opposite case where $|\delta\Gamma| = \Gamma$, the dot is closed on one side. There still are ABSs, but there is no phase dependence of the Green functions. In other words, an asymmetry reduces the phase dependence of the ABSs and consequently, as we will see later in section 3.1.5, the supercurrent passing through the QD (see in particular Eq. 3.11). This is linked to a loss in transmission of the dot in the normal state as the latter depends strongly on $\delta\Gamma$. The Breit-Wigner formula (see for example [56]) gives us indeed the QD conductance:

$$G(\omega) = \frac{e^2}{h}\sum_\sigma \mathcal{T}_\sigma(\omega) = \frac{e^2}{h}\sum_\sigma \frac{4\Gamma_R\Gamma_L}{(\epsilon_\sigma - \omega)^2 + (\Gamma_R + \Gamma_L)^2} \tag{3.5}$$

From which we can isolate the transmission, for the channel of spin σ, $\mathcal{T}_\sigma(\omega)$ as a function of Γ and $\delta\Gamma$:

$$\mathcal{T}_\sigma(\omega) = \frac{4\Gamma_R\Gamma_L}{(\epsilon_\sigma - \omega)^2 + (\Gamma_R + \Gamma_L)^2} = \frac{\Gamma^2 - \delta\Gamma^2}{(\epsilon_\sigma - \omega)^2 + \Gamma^2}$$

We see that for a maximum asymmetry $\Gamma = \delta\Gamma$ the transmission is equal to zero, this situation corresponding to an open circuit (Γ_L or Γ_R equal to zero). It is interesting to notice that this transmission takes a particularly simple expression when the level ϵ_σ is at resonances with the electrodes Fermi level ($\omega = \epsilon_\sigma = 0$):

$$\mathcal{T}_{\sigma,\omega=\epsilon_\sigma=0} = 1 - \left(\frac{\delta\Gamma}{\Gamma}\right)^2$$

As a consequence, whereas the lifetime of a charge in the QD is limited by the bigger coupling because this charge sees the two contacts in parallel, the transmission in series is rather limited by the smallest coupling. Indeed when a charge is going in the QD through the more open contact, it will go back where it comes from rather than going through the less transmitted contact.

3.1.4 Extension of the effective model to a double QD

In this section we explain how to apply this formalism to the case of a double QD (DQD) in which two QDs are in series between the superconducting leads.

In our experiments, the CNT behaves as a DQD because of the influence of the probe. The latter acts as a scatterer which separates the CNT in two QDs which are strongly coupled together. Further in the manuscript (see part III), measurement which proves this interpretation will be shown and compared to other experiments with similar geometry.

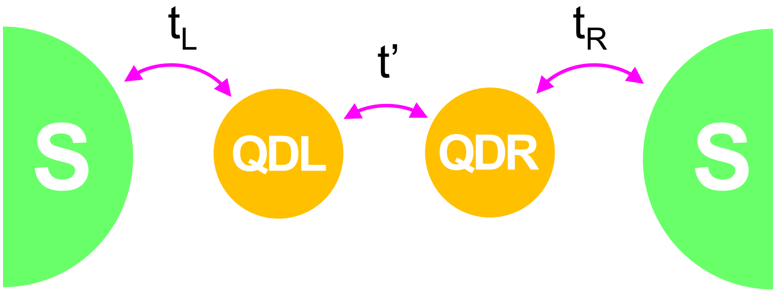

Figure 3.4: Our DQD model consists of two coupled QDs in series, QDL being connected to the left lead and QDR to the right lead.

DQD Hamiltonian To modify our model to a DQD, we need to replace first, in H, H_{QD} by H_{DQD}:

$$H_{DQD} = \sum_{\sigma,\alpha=L,R} \epsilon_{\alpha\sigma} d^{\dagger}_{\alpha\sigma} d_{\alpha\sigma} + \sum_{\sigma} \left(t' d^{\dagger}_{L\sigma} d_{R\sigma} + t'^{*} d^{\dagger}_{R\sigma} d_{L\sigma} \right)$$

with indexes L and R referring to the QDL or QDR (*cf* Fig. 3.4), σ the spin, and t the interdot coupling. The second modification consists in changing H_{T_i}:

$$\begin{aligned} H_{T_L} &= \textstyle\sum_{l,\sigma} \left(t_L d^{\dagger}_{L\sigma} c_{l\sigma} + t^{*}_{L} c^{\dagger}_{l\sigma} d_{L\sigma} \right) \\ H_{T_R} &= \textstyle\sum_{r,\sigma} \left(t_R d^{\dagger}_{R\sigma} c_{r\sigma} + t^{*}_{R} c^{\dagger}_{l\sigma} d_{R\sigma} \right) \end{aligned}$$

This is a crude approach missing a lot of important physics, such as interdot electrostatic interaction ($U_m n_{L\uparrow} n_{R\downarrow}$), exchange ($-JS_L.S_R$)... But it contains the essential ingredients to understand how ABSs form over the all DQD.

DQD spinors, Green functions and spectral density By introducing new spinors ψ_d and ψ_e [8]:

$$\psi_d = \begin{pmatrix} d_{L\uparrow} \\ d^{\dagger}_{L\downarrow} \\ d_{R\uparrow} \\ d^{\dagger}_{R\downarrow} \end{pmatrix} \quad \text{and} \quad \psi_e = \begin{pmatrix} c_{l\uparrow} \\ c^{\dagger}_{-l\downarrow} \\ c_{r\uparrow} \\ c^{\dagger}_{-r\downarrow} \end{pmatrix}$$

we can give to H the form;

$$H = \sum_{e} \psi^{\dagger}_{e} \mathcal{E}_e \psi_e + \psi^{\dagger}_{d} \mathcal{E}_{DQD} \psi_d + \sum_{e} \left[\psi^{\dagger}_{d} \mathcal{E}_T \psi_e + h.c. \right]$$

where $\mathcal{E}_e$, $\mathcal{E}_{DQD}$ and $\mathcal{E}_T$ are 4×4 matrices with block structures:

$$\mathcal{E}_e = \begin{pmatrix} \mathcal{E}_l & 0_2 \\ 0_2 & \mathcal{E}_r \end{pmatrix} \quad \mathcal{E}_{DQD} = \begin{pmatrix} \mathcal{E}_{QDL} & \mathcal{E}_{T_{ID}} \\ \mathcal{E}_{T_{ID}} & \mathcal{E}_{QDR} \end{pmatrix} \quad \mathcal{E}_T = \begin{pmatrix} \mathcal{E}_{T_L} & 0_2 \\ 0_2 & \mathcal{E}_{T_R} \end{pmatrix}$$

with $\mathcal{E}_{QDL} = \begin{pmatrix} \epsilon_{L\uparrow} & 0 \\ 0 & -\epsilon_{L\downarrow} \end{pmatrix}$, $\mathcal{E}_{QDR} = \begin{pmatrix} \epsilon_{R\uparrow} & 0 \\ 0 & -\epsilon_{R\downarrow} \end{pmatrix}$ and $\mathcal{E}_{T_{ID}} = \begin{pmatrix} t' & 0 \\ 0 & -t'^{*} \end{pmatrix}$

Replicating exactly the single QD approach, we can calculate the DQD Green functions and obtain:

$$\hat{\mathcal{G}}_{dd}(z) = \frac{\mathbf{1}}{z - \mathcal{E}_{\mathcal{DQD}} - \hat{\Sigma}_{DQD}(z)}$$

---

[8] The index e designates pairs of index l, r chosen such that they appear in only one pair.

where $\Sigma_{DQD}(z)$ is the self-energy due to the superconducting leads:

$$\begin{aligned}\hat{\Sigma}_{DQD}(z) &= \sum_e \mathcal{E}_T \left[z-\mathcal{E}_e\right]^{-1} \mathcal{E}_T^{\dagger} \\ &= \begin{pmatrix} \hat{\Sigma}_L(z) & 0_2 \\ 0_2 & \hat{\Sigma}_R(z) \end{pmatrix}\end{aligned}$$

The total DQD spectral density is obtain similarly than before:

$$\mathcal{A}_{dd}(\omega) = -\frac{1}{\pi}\mathrm{Im}\left[\mathrm{T}r_{DQD}\left(\hat{\mathcal{G}}_{dd}^{R}(\omega)\right)\right]$$

$\mathrm{T}r_{DQD}$ is the trace in Nambu space over the two QDs[9]:

$$\mathrm{T}r_{DQD}\left(\hat{\mathcal{G}}_{dd}^{R}(\omega)\right) = \hat{\mathcal{G}}_{dd}^{R11}(\omega) + \hat{\mathcal{G}}_{dd}^{R22}(-\omega) + \hat{\mathcal{G}}_{dd}^{R33}(\omega) + \hat{\mathcal{G}}_{dd}^{R44}(-\omega)$$

3.1.5 Supercurrent within the effective model

The supercurrent flowing through the QD can be calculated, as the TDOS, with GFs. We will show in this section that it can be directly related to the QD density of states that we measure[10]. Unfortunately, this supercurrent is not measurable experimentally in our present setup. Nevertheless, the following explains how we can have indirect access to the magnitude of supercurrents in our samples from the measured spectra. Note that this evaluation of the QD supercurrent might be checked in the future, using a more elaborate setup giving direct access to the loop supercurrent, as was done for atomic contacts [68, 69] (see Fig. 3.5).

Using the expression of the supercurrent we obtained from the QD's GF, we discuss how our model describe the so-called $0-\pi$ transition.

3.1.5.1 Calculation of the supercurrent

Supercurrent definition Since number of particles and phase are conjugated quantum variable, the equilibrium supercurrent I_J flowing through a Josephson junction is given by the fundamental relation [43, 53, 54]:

$$I_J = \frac{2e}{\hbar}\left\langle \frac{dH}{d\delta} \right\rangle$$

---

[9] Tunneling rates between the tunnel probe and the two sides of the DQD may be different. For fitting of experimental TDOS, we may thus introduce a factor of relative intensity α: $Tr_N\left(\hat{\mathcal{G}}_{dd}^{R}(\omega)\right) = \alpha \times \left(\hat{\mathcal{G}}_{dd}^{R11}(\omega) + \hat{\mathcal{G}}_{dd}^{R22}(-\omega)\right) + \left(\hat{\mathcal{G}}_{dd}^{R33}(\omega) + \hat{\mathcal{G}}_{dd}^{R44}(-\omega)\right)$

[10] The system being at equilibrium, there is no quasiparticle current through the QD, but just a DC supercurrent.

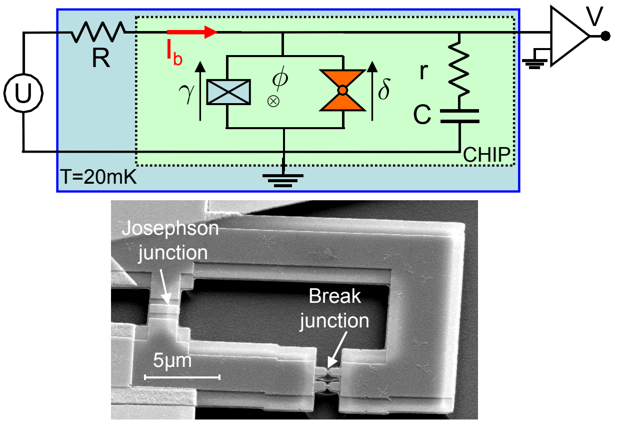

Figure 3.5: Diagram of the experimental setup and a SEM picture of the sample used to measure the current-phase relation of an atomic contact (Fig. from Ref. [69]). The atomic contact is obtained within the break junction by bending of the sample and forms in parallel with a large Josephson junction an atomic SQUID. The current-phase relation is extracted from the switching current of the atomic SQUID.

where H is the Hamiltonian of the junction and δ the superconducting phase difference across the junction[11].

In a QD described by the effective Hamiltonian given in section 3.1.1.1, a convenient form of this relation can be obtained by performing a gauge transformation on the operators of the leads:

$$c_{l(r)\sigma} \rightarrow c_{l(r)\sigma} e^{i\frac{\phi_{L(R)}}{2}}$$

which transfers the phase into the tunnel matrix elements $t_{L(R)} \rightarrow t_{L(R)} e^{i\frac{\phi_{L(R)}}{2}}$. Then it can be shown that the Josephson current carried by the QD from

---

[11] If we want to relate this current with the time-derivative of the charge in the left lead, we can write $I_J = e\frac{d}{dt}\left\langle \hat{N}_L(t)\right\rangle = e\frac{d}{dt}\left\langle e^{i\frac{H}{\hbar}t}\hat{N}_L e^{-i\frac{H}{\hbar}t}\right\rangle = \frac{ie}{\hbar}\left\langle \left[H, \hat{N}_L(t)\right]\right\rangle$. But the commutator of $\hat{N}_L(t)$ with the full Hamiltonian introduces spurious terms of the type $\left\langle c^\dagger_{kL\uparrow} c^\dagger_{-kL\downarrow}\right\rangle$ because of charge fluctuations within the lead. These fluctuations appear because the mean-field BCS Hamiltonian doesn't conserve the charge: $\left[H_{BCS-MF}, \hat{N}_L\right] \neq 0$. This is not the case for the Hamiltonian on which has not been performed a mean-field approximation, so we can consider that these terms are not relevant for current calculation through the system. For a more detailed discussion see Ref. [70].

the left to the right takes the simple expression[12]:

$$I_J = \frac{ie}{\hbar}\left\langle [H_T, N_L] \right\rangle \tag{3.6}$$

where $N_{L(R)}$ is the number operator of the left (right) electrode[13]:

$$N_{L(R)} = \sum_{l(r),\sigma} c^{\dagger}_{l(r)\sigma} c_{l(r)\sigma}$$

From expression 3.6, we can relate the current to correlation functions between the QD and the left lead:

$$I_J = \frac{ie}{\hbar}\sum_{l,\sigma}\left\{ t_L \left\langle d^{\dagger}_{\sigma} c_{l\sigma} \right\rangle - t_L \left\langle c^{\dagger}_{l\sigma} d_{\sigma} \right\rangle \right\} \tag{3.7}$$

that we can calculate with GF techniques.

Lesser and greater GF Correlation functions in expression 3.7 are slightly different from those defined in Eq. 3.1. They are linked to the QD greater Green functions (taking $t \to 0$):

$$\hat{\mathcal{G}}^{>}_{ld}(t) = -i\left\langle \psi_l(t)\, \psi^{\dagger}_d(0) \right\rangle \tag{3.8}$$

At equilibrium, one can show that its Fourier transform is simply related to Fermi-Dirac distribution f_{FD}, the retarded and the advanced GFs which both contain the equilibrium properties of the system:

$$\hat{\mathcal{G}}^{>}_{ld}(\omega) = f_{FD}(-\omega)\left[\hat{\mathcal{G}}^{R}_{ld}(\omega) - \hat{\mathcal{G}}^{A}_{ld}(\omega)\right] \tag{3.9}$$

(a demonstration of this relation is given in section B.4).

Expression of the current as a function of the QD Green's functions By combining Eq. 3.7, 3.8 and 3.9, we get, after some algebra, the following intermediate expression for I_J:

$$I_J = -\frac{2e}{\hbar}\int f_{FD}(-\omega)\sum_l \mathrm{Re}\left\{\mathrm{T}r_N\left[\mathcal{E}_{T_L}\left(\hat{\mathcal{G}}^{R}_{ld}(\omega) - \hat{\mathcal{G}}^{A}_{ld}(\omega)\right)\right]\right\}\frac{d\omega}{2\pi}$$

---

[12] We take here the example $\phi_L = \delta$ and $\phi_R = 0$ without any loss of generality.

[13] Because of charge conservation, I_J could also be written $I_J = -\frac{ie}{\hbar}\left\langle [H_T, N_R] \right\rangle$, see appendix C for demonstration

which is actually a Fourier transform taken at $t = 0$. The GF of the QD does not appear explicitly in this expression. However, since $\hat{\mathcal{G}}_{ld}(z)$ obeys the Schrödinger-like equation[14]:

$$z \times \hat{\mathcal{G}}_{ld}(z) = \mathcal{E}_l \hat{\mathcal{G}}_{ld}(z) + \mathcal{E}_{T_L}^{\dagger} \hat{\mathcal{G}}_{dd}(z)$$

we have:

$$\hat{\mathcal{G}}_{ld}(z) = [z - \mathcal{E}_L]^{-1} \mathcal{E}_{T_L}^{\dagger} \hat{\mathcal{G}}_{dd}(z)$$

with notations of section 3.1.1.1. From this expression, we can write a very compact formula for the current that is only function of the known QD's GF and self energy of the left lead:

$$\begin{aligned} I_J \; = \; & \tfrac{2e}{\hbar} \int f_{FD}(\omega) \,\mathrm{Re}\, \mathrm{Tr}_N \, [\hat{\Sigma}_L(-\omega - i\eta)\, \hat{\mathcal{G}}_{dd}(-\omega - i\eta) \\ & -\hat{\Sigma}_L(-\omega + i\eta)\, \hat{\mathcal{G}}_{dd}(-\omega + i\eta)] \tfrac{d\omega}{2\pi} \end{aligned} \tag{3.10}$$

In appendix C, we show how equation 3.10 is equivalent to Beenakker's formula of Ref. [51, 58] giving the supercurrent carried by the ABSs:

$$I_{ABS} = -\frac{e}{\hbar} \sum_{\pm} \tanh\left(\frac{\beta \epsilon_{\pm}}{2}\right) \frac{\partial \epsilon_{\pm}}{\partial \delta} \tag{3.11}$$

and discuss the contribution of the continuum.

Supercurrent in DQDs

To obtain the supercurrent carried by a DQD between two superconducting leads, one can generalize Eq. 3.10 simply replacing $\hat{\Sigma}_L(z)$ by $\hat{\Sigma}^L_{DQD}(z)$ with:

$$\hat{\Sigma}^L_{DQD}(z) \; = \begin{pmatrix} \hat{\Sigma}_L(z) & 0_2 \\ 0_2 & 0_2 \end{pmatrix}$$

3.1.5.2 Singlet-doublet transition

The singlet-doublet transition is a quantum transition between two ground states of the QD with different spins: a spin-singlet state (S=0) and a magnetic doublet (S=1/2) [24, 71]. In the TDOS, this transition is directly visible through the progressive intercrossing, inside the superconducting gap, of the

---

[14] This is actually an Equation of Motion (EOM), see Eq. B.7 in section B.3.

two inner resonances[15] [16]. In other words, this means that an ABS that is above the Fermi level (or below depending on the chosen point of view, as discussed in section 2.3.3) crosses the latter. Hence this ABS, which was initially empty, suddenly becomes filled. This induces a change of ground states. We will see, in section 3.3.2 (see in particular Fig. 3.14), how this transition is described by the phenomenological model and the Numerical Renormalization group (introduced briefly in section 3.2).

3.1.5.3 Reversal of supercurrent ($0-\pi$ transition) in a S-QD-S junction: description with our phenomenological approach

One of the manifestation of the singlet-doublet transition is the so called $0-\pi$ transition [72, 73, 74]. The $0-\pi$ transition is a sign reversal of the current-phase relation induced by a change of a parameter in the system. This phenomenon has been observed in a wide variety of controllable Josephson junctions [3, 73, 74, 75], including CNT based junctions [8, 20, 76] where the parameter of control is the CNT's chemical potential that is tuned with a back gate voltage. In those experiments, the observation of the $0-\pi$ transition is performed through measurement of the critical current. During the transition, the latter decreases, cancels and then increases again indicating its change of sign. Such junctions are suggested as potential element in the architecture of novel quantum devices [48]. Here, we give a brief illustration, based on our phenomenological model, of the $0-\pi$ transition and discuss the role of the Coulomb repulsion. Despite the rough approximations we have made in this model, the predicted behaviour of the system is consistent with the observation realized in the references mentioned above.

Reversal of the current changing ϵ In a QD, the $0-\pi$ transition appears when the Coulomb repulsion inside the QD is sufficiently high such that a single electron may be localized in the QD, the latter being as a consequence in its magnetic ground state S=1/2. In Ref. [72], Spivak *et al.* showed that the transfer of a Cooper pair through the dot may be then accompanied by an exchange of spin between electrons of the pair which translates into a negative contribution in the supercurrent. When this contribution is higher than the direct transfer of Cooper pairs from one electrode to the other, the supercurrent reverses its sign.

---

[15] ABSs we see in the TDOS are excitations which correspond to transitions between these two states (S=0 and S=1/2). At the quantum transition, these two states are degenerate and ABSs are thus zero energy excitations. That's why a progressive change of ground states coincides with the crossing of an ABS with the Fermi level.

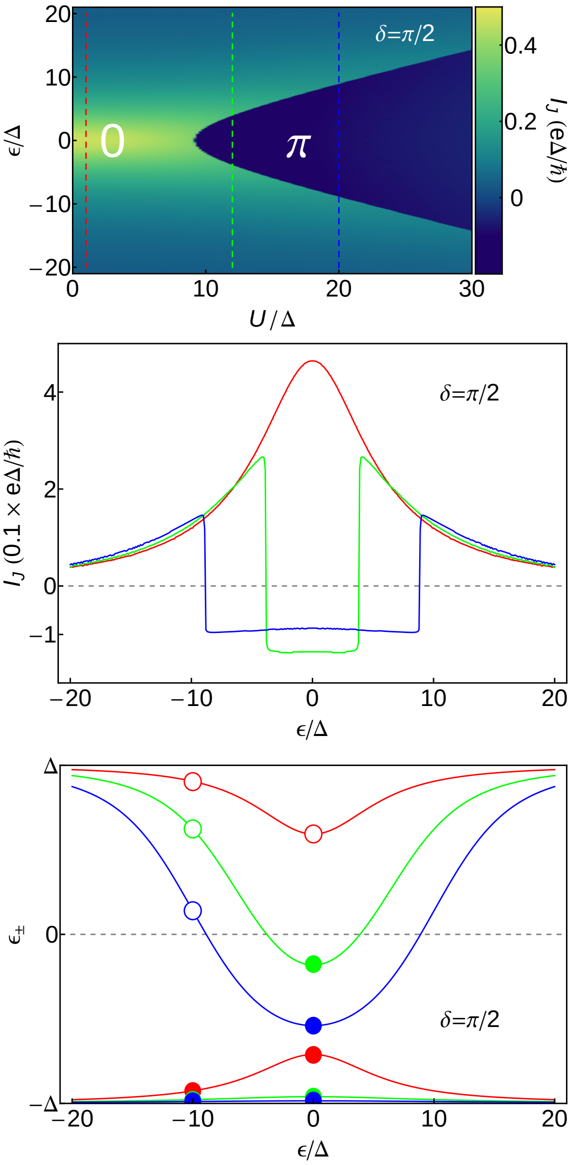

Figure 3.6: Phase diagram of the Josephson current (top) in color scale as a function of the mean position level ϵ of the QD and the phenomenological Coulomb repulsion U at $\delta = \pi/2$. Below, there are two graphs: one in the middle with three cuts (in red, green and blue) of the diagram, indicated by the dashed line on the colorplot, showing the jumps in the supercurrent when ϵ is changed and another one at the bottom with the corresponding ABSs. The jumps in supercurrent correspond to the filling or emptying of an ABS when it crosses the Fermi level. Here when $\epsilon = -10\Delta$, the upper ABS is empty (empty circle), but if ϵ is increased to 0, the ABS may cross the Fermi level and becomes filled (filled circle). Parameters used for calculation are: $U = 1$, 12, 20Δ (resp. for the red, green and blue curve), $\Gamma = 6.25\Delta$, $\delta\Gamma = 1.75\Delta$, $\eta = 0.001\Delta$ and $T = 0$. I_J is obtained from Eq. 3.10 and the energy of the ABSs are obtained from Eq. 3.3 based on the phenomenological model.

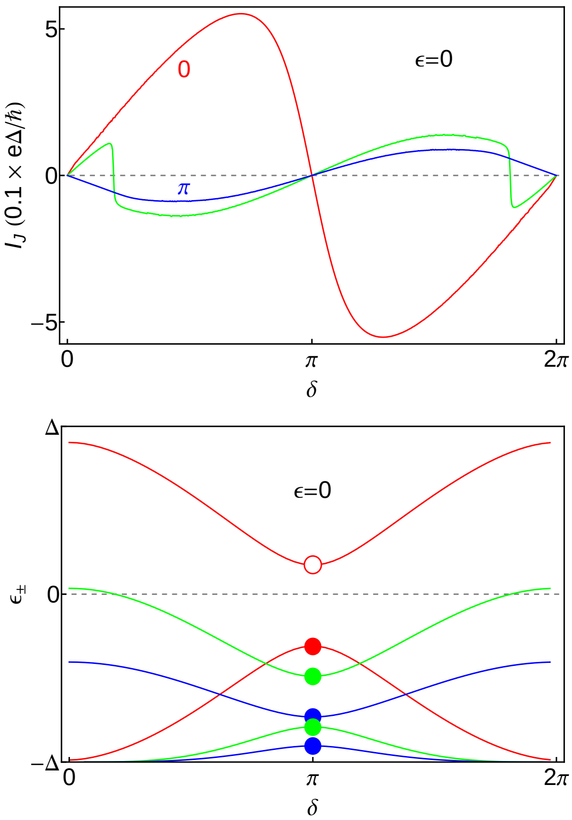

Phase dependence of 0 and π junctions

Figure 3.7: Phase dependence of the Josephson current, at the top, with $\epsilon = 0$ for the same parameters than in Fig. 3.6 and $U = 1$, 12 and 20 respectively for the red, green and blue curves. The supercurrent can either increase (red curve) or decrease (blue curve) with δ depending if the junction is in the 0 (small U) or π (large U) regime. For intermediate values of U, the junction can transit, by tuning the phase, between the two regimes. Below the corresponding phase dependence of the ABSs are traced. In the 0 regime the ABSs are on each side of the Fermi level, whereas in the π regime they are on the same side.

This can be seen in the colorplot of Fig. 3.6 where we have represented calculation of the Josephson current carried by a QD connected between two superconducting leads, at a superconducting phase difference $\delta = \pi/2$, as a function of the mean position level, noted here ϵ, and the Coulomb repulsion inside the QD U normalized with the superconducting gap Δ. I_J is obtained from Eq. 3.10 (or Eq. C.10) based on the phenomenological model.

In this diagram, there are two areas: one of positive Josephson current that appears in green and yellow and one where the current is negative and which is blue (they are respectively labelled 0 and π on the graph). Below, we have chosen to trace three cuts of this diagram: the current is plotted as a function of ϵ (controlled experimentally with gates) and shows, for sufficiently high U, abrupt transitions from positive to negative current. Comparing this graph with the one below, we can see that these sudden jumps correspond exactly to the crossing of an ABS with the Fermi level.

Phase dependence The phase dependence of these ABSs is represented in Fig. 3.7 as well as the supercurrent carried by the QD. For small U, the junction is in its ground state for $\delta = 0$, where its energy reaches its minimum. The S-QD-S junction is then in its 0-state. However if U is large, the junction is in its lower energy state for $\delta = \pi$, the supercurrent flows then in opposite direction than in the previous case. The junction is, this time, in its π-state. For intermediate values of U, variation of δ may cause the crossing of one ABS with the Fermi level inducing jumps in the current-phase relation. When the junction is in this regime, it is conventionally called $0'$ or π' junction depending if the system is more stable at $\delta = 0$ or $\delta = \pi$.

3.2 Exact treatment of the Quantum Dot with superconducting leads: the Numerical Renormalization Group

In this section we briefly discuss how one can used NRG calculations to obtain exact numerical results on the proximity effect in QD. The comparison of this technique with the simplified non-interacting treatment made in the previous sections will be carried out in the next section.

3.2.1 Anderson impurity model in NRG

Like before we consider a single orbital of the quantum dot, but in contrast to the simplified approach, the NRG approach yields the exact solutions of the system, taking into account the Coulomb interaction in the dot. This problem is exactly the Anderson impurity model (AIM) with superconducting leads, described by the Hamiltonian:

$$H = H_{QD} + H_L + H_R + H_{T_L} + H_{T_R}$$

with:

$$H_{QD} = \epsilon_{orb}\left(n_\uparrow + n_\downarrow\right) + E_c n_\uparrow n_\downarrow \text{ with } n_\sigma = d_\sigma^\dagger d_\sigma$$

$$\begin{aligned} H_L &= \sum_{l,\sigma} \epsilon_l c_{l\sigma}^\dagger c_{l\sigma} + \sum_l \left(\Delta e^{i\phi_L} c_{l\uparrow}^\dagger c_{-l\downarrow}^\dagger + \Delta e^{-i\phi_L} c_{-l\downarrow} c_{l\uparrow}\right) \\ H_R &= \sum_{r,\sigma} \epsilon_r c_{r\sigma}^\dagger c_{r\sigma} + \sum_l \left(\Delta e^{i\phi_R} c_{r\uparrow}^\dagger c_{-r\downarrow}^\dagger + \Delta e^{-i\phi_R} c_{-r\downarrow} c_{r\uparrow}\right) \end{aligned}$$

$$\begin{aligned} H_{T_L} &= \sum_{l,\sigma} \left(t_L d_\sigma^\dagger c_{l\sigma} + t_L^* c_{l\sigma}^\dagger d_\sigma\right) \\ H_{T_R} &= \sum_{r,\sigma} \left(t_R d_\sigma^\dagger c_{r\sigma} + t_R^* c_{r\sigma}^\dagger d_\sigma\right) \end{aligned}$$

Here, d_σ is the annihilation operator of an electron with a spin σ in the orbital of energy ϵ_{orb} and E_c is the charging energy due to the repulsion between two electrons occupying the QD. Operator $c_{l(r)\sigma}$ annihilates, in the left (resp. right) electrode, an electron of spin σ in state l (r) with an energy $\epsilon_{l(r)}$. In this notation, l and r represent a synthetic index for all the quantum numbers of the electrons in electrodes, except their spin, and such that $c_{-l-\sigma}$ is the time reversed-state of $c_{l\sigma}$. $\Delta e^{i\phi_{L(R)}}$ is the complex order parameter in electrode $L(R)$ with modulus Δ (also known as the gap energy) and phase $\phi_{L(R)}$. $t_{L(R)}$ is the energy associated to the transfer of an electron between left (right) electrode and the dot.

In the resolution of the problem, the method takes into account all four states of the uncoupled orbital, with their spin degeneracy:

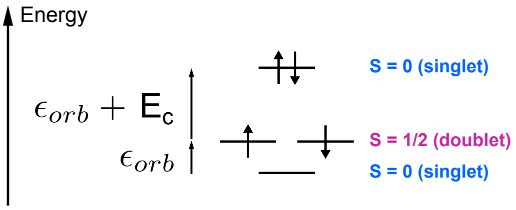

For the numerical calculations we have used the “NRG Ljubjana” open-source code written by Rok Žitko[16]. We gratefully acknowledge extended help from the author.

For any given set of parameters of the Hamiltonian, the NRG calculation yields the quasi-exact[17] complete low energy spectrum of a discretized system. In particular it determines the ground state, and the subgap excitations (the ABSs) giving their total spin and degeneracies. NRG can also provide arbitrary spectral functions of operators, and in particular, the tunneling density of states into the dot. Since NRG calculation is performed for a discretized Hamiltonian, the spectral function is represented in form of a weighted set of delta peaks. For the sub-gap part this is, in fact, an exact representation of the ABSs. For the continuum, however, in order to obtain a smooth plot, one has to do spectral averaging (over several NRG calculations with different discretizations) together with some broadening.

3.2.2 Zero vs finite superconducting phase difference across the QD

In principle, the AIM with an arbitrary number of identical leads (normal or superconducting) remains a “single-channel” problem, since one can perform a suitable Gram-Schmidt orthogonalization to a single effective channel, while all other states fully decouple.

In practice however, in the case of two superconducting channels with different SC amplitude and/or phase the results of such a transformation is difficult to use in NRG. In that case, in order to circumvent this difficulty, one has rather recourse to a “two channels” NRG calculations (one channel for each lead), which is unfortunately much more demanding in terms of computational power. Indeed, compared to the zero phase difference case, an NRG calculation of a QD at finite phase difference is slower by about three orders of magnitude. This explains why in the following we give only results of NRG calculations at zero phase difference.

---

[16] See http://nrgljubljana.ijs.si/ for an introduction to quantum impurity problems, an explanation of the NRG method, downloadable number-crunching NRG code, documentation and examples.

[17] It is not formally exact because the resolution is performed with discrete states instead of a continuum, but we can control the precision of the results.

3.3 Predictions for the DOS of a QD connected to superconductors

In this section we look how the DOS of the QD, and in particular the ABSs, depends on the parameters of the effective model we have used to obtain the Green's functions. To better grasp the limitations of this effective model, we compare its results with those of the exact NRG solution of the Anderson impurity model. We introduce the following correspondence between the notations of the NRG (see section 3.2.1) and those of the effective model (see section 3.1.1.1):

$$\begin{array}{ccc} \epsilon_{orb} & \leftrightarrow & \epsilon_0 - U/2 \\ E_c & \leftrightarrow & U \end{array}$$

in order to compare their respective results. In the following, we will call ϵ_0 the "mean position level" and U the "charging energy" for both approaches. Concerning the coupling to the leads Γ_L and Γ_R, they are defined in the same way in both approaches.

Among the parameters of the models we discuss here, we will distinguish those that are tunable parameters (that we can tune during the experiment[18]): the mean position level ϵ_0 and phase dependence δ, and others that will be considered as fixed sample-dependent, or setup-dependent parameters: the couplings to the leads $\Gamma = \Gamma_L + \Gamma_R$, its asymmetry $\delta\Gamma = \Gamma_L - \Gamma_R$ and the charging energy U.

3.3.1 Modification of the spectral density of a QD upon coupling to superconducting contacts

Superconducting proximity effect in QD modifies its TDOS in a characteristic way. In order to identify signatures that are peculiar to this effect, we first look how the connection to normal leads modifies the QD's spectral density and then we turn them superconducting. Experimentally the latter transition can be achieved by lowering a magnetic field or the temperature.

Spectral density of a QD connected to normal leads An isolated QD has a very simple spectral density composed of two Dirac peaks spaced of the charging energy at $\omega = \epsilon_0 - U/2$ and $\epsilon_0 + U/2$. They correspond to eigenstates of the isolated QD and have, as a consequence, infinite lifetime.

---

[18] We need to mention that there are other parameters that we can control experimentally and are not in the model as the temperature, the magnetic field or the current flowing through the sample.

That's why they are infinitely thin. As we can see in Fig. 3.8, NRG and the effective approach give the same TDOS (plotted in dashed gray in the first line of graphs) for this elementary case.

When we couple the QD to two normal leads, the levels of the dots are not anymore eigenstates: an electron placed into the QD can escape to the leads in a finite time. Hence, the levels are broaden in a Lorentzian shape. In the effective approach, their half-width at half-maximum are given by $\Gamma_L + \Gamma_R$ (see Fig. 3.8, first graph from the top of the central column), whereas NRG shows levels that are sensitively wider for the chosen set of parameters. The most striking difference, between NRG and the effective approach, is the formation of a Kondo peak[19] at the Fermi level that is not captured at all by the effective approach but only by NRG (a brief discussion about this particularity of the effective non-interacting model can be found in section A.4.2 appendix A). Because the Kondo peak gets wider with increasing Γ, the comparison between the two approaches become completely inaccurate for large coupling to the leads.

Since this effect essentially disappears of the TDOS when the leads are turned superconducting, we will ignore Kondo effect in this chapter, but this phenomenon will be tackled in details in part III.

Spectral density of a QD connected to superconducting leads: formation of ABSs When the leads connected to the QD are turned superconducting (Fig. 3.8 second line of graphs from the top), a superconducting gap is induced in the dot around the Fermi level and ABSs appear in it. As they are eigenstates, they have infinite lifetime and appear as infinitely thin peaks.

Taking $\eta_{inel} \neq 0$, we increase their linewidth such that they become visible in the DOS. We can then compare results of the effective model with exact NRG calculations (in which the ABSs' linewidth is added artificially). In the third line of graphs of Fig. 3.8, we can see that the TDOS obtained from the two different approaches are qualitatively similar. ABSs are located approximately at the same energies and continuums outside of the gap are comparable. This similarity between approaches hold only for large charging energy and small or moderate coupling to the leads compared to the superconducting gap. For large Γ, the effective model breaks down and gives TDOS which shows large discrepancy with exact NRG calculations.

---

[19] See appendix A.

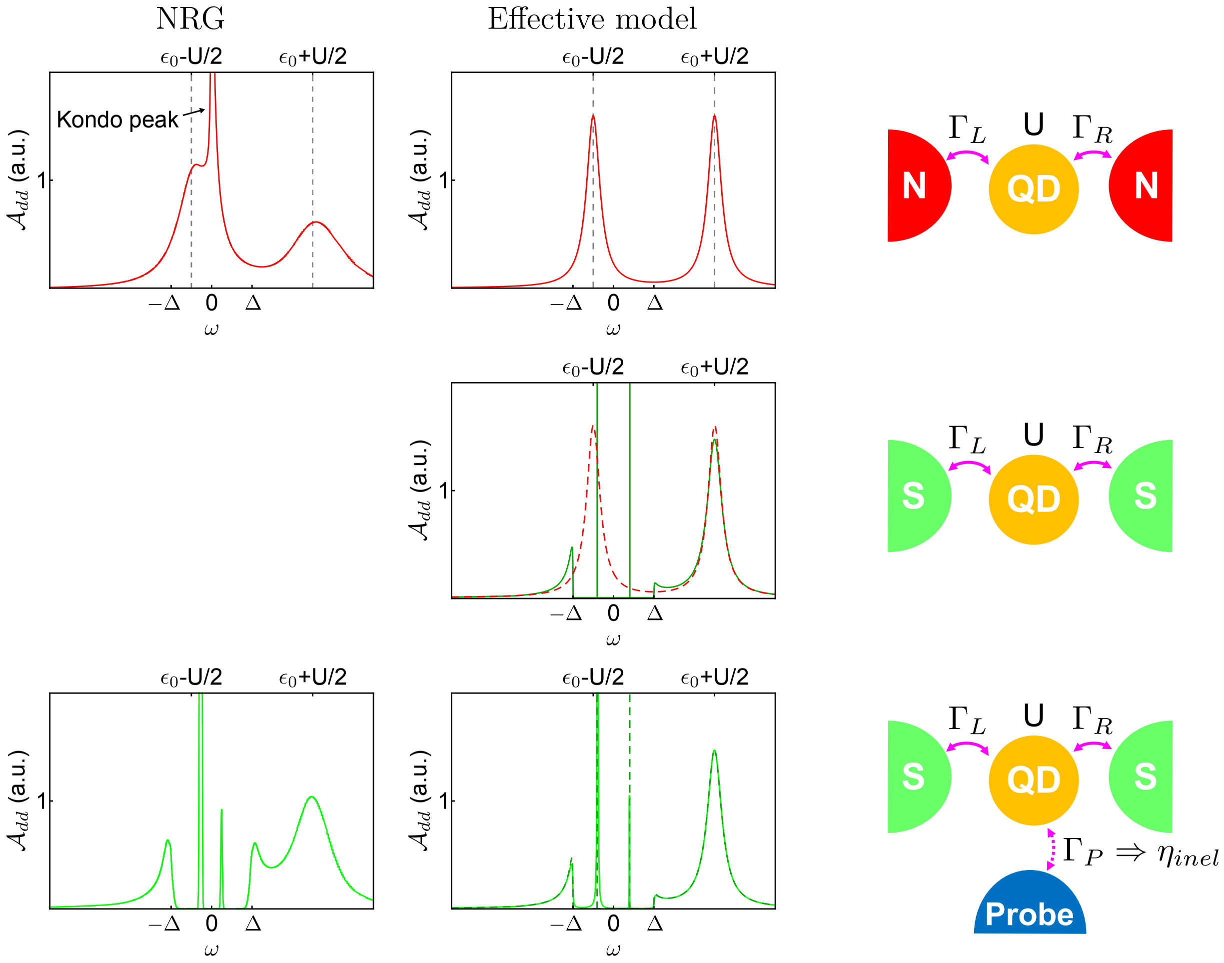

TDOS OF A QD WHEN CONNECTED TO ELECTRODES

Figure 3.8: The left and central columns represents TDOS of a QD as a function of the energy ω, respectively obtained with NRG and the effective model, in different situations. From top to bottom: spectral density in arbitrary unit of a QD connected to normal leads (in dashed gray, we have traced the TDOS of the isolated QD), a QD connected to superconducting leads (just for the effective model) and the same thing but with a linewidth added to the ABSs. In the third line of graphs, we gave the linewidth to the ABSs taking $\eta_{inel} = 0.03\Delta$ in the effective model and added artificially in NRG. The finite linewidth can model the reduction of the ABSs lifetime due to the connection to an external tunnel probe. Parameters for the figures are:$\epsilon_0 = 1$, $\Gamma = 0.2\Delta$, $U = 3\Delta$ and $\delta = 0$.

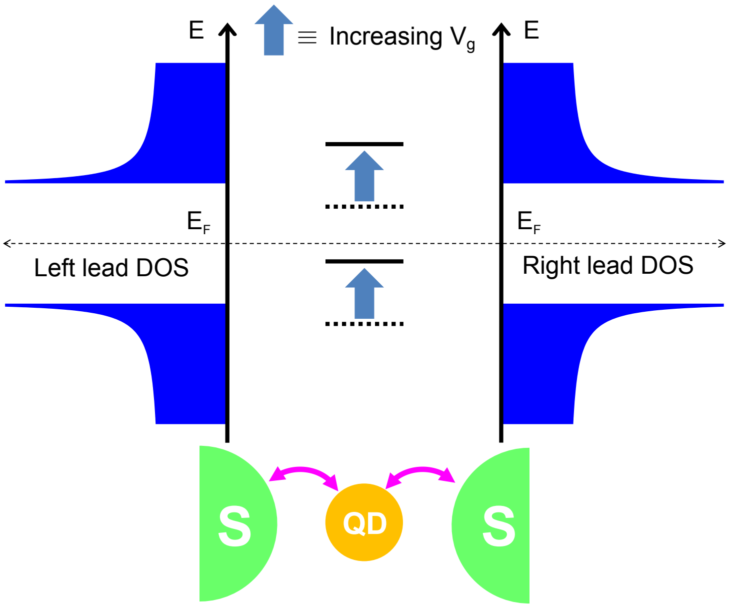

Figure 3.9: Energies of the QD levels can be tuned with a back gate voltage coupled capacitively to the sample.

3.3.2 Influence of the parameters on ABSs

3.3.2.1 Tunable parameters

In our experiment, we control the superconducting phase difference δ between the superconducting electrodes connected to the QD with a magnetic field. With a gate voltage, we can tune the energy level of the QD's orbital which is equivalent, in the model, to control ϵ_0 (see Fig. 3.9). Experimental details on how we control these parameters are given in part II.

3.3.2.2 Phase dependence: signature of the ABSs

As mentioned above (section 3.2.2), calculations of the TDOS at $\delta \neq 0$ is a too much time-demanding process in NRG. In this respect, the effective model provides the interesting possibility to access the phase-dependence of the TDOS. In Fig. 3.10, we have represented, for three different values of δ (in green, blue and red), the TDOS of a QD connected to two superconducting leads. Below, is plotted the phase dependence of the ABSs (degenerate for the chosen parameters) which are 2π-periodic. This phase dependence is a signature of the ABSs and an indirect evidence that they carry supercurrent (see section 3.1.5 above).

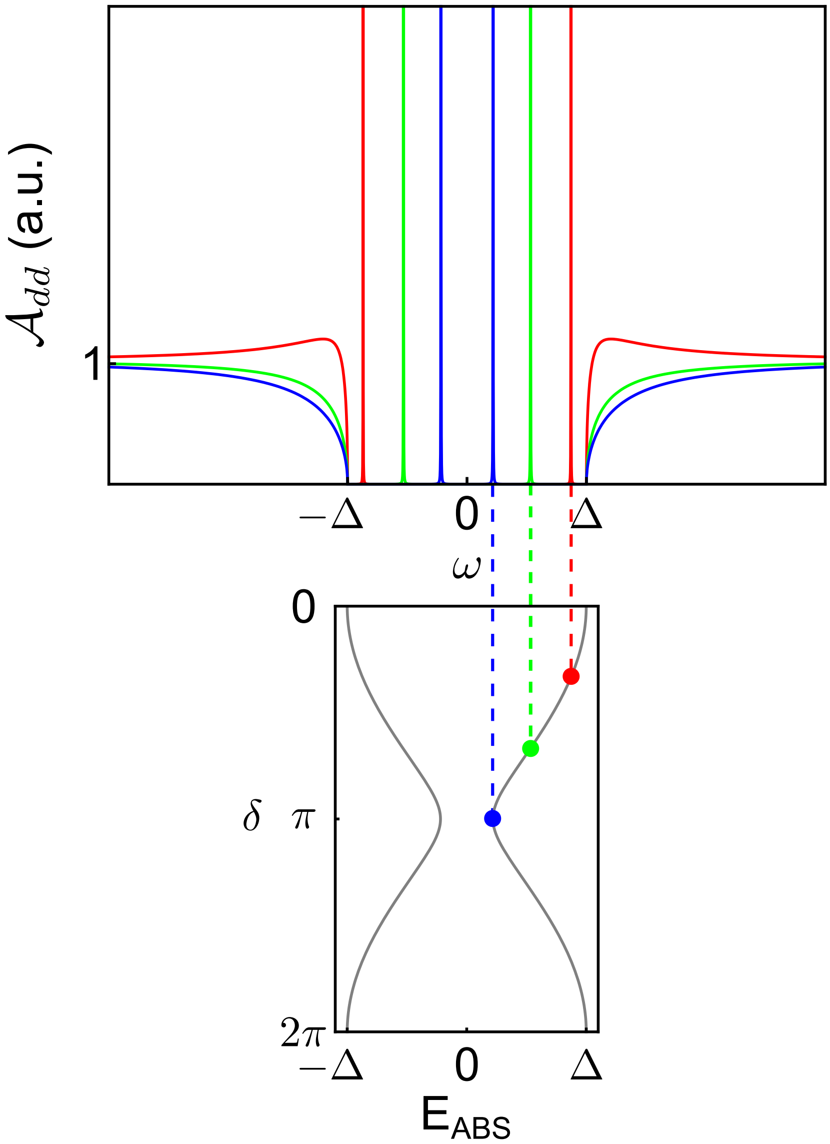

Figure 3.10: Plot of the spectral density of a QD connected to superconducting leads (top) as a function of the energy ω obtained with the effective model for three different phases and energies of the ABSs (bottom) as a function of δ. The ABS are 2π-periodic with δ (not shown). Parameters taken for these plots: $U = 0$, $\epsilon_0 = 0$, $\Gamma_L = 10\Delta$, $\Gamma_R = 8\Delta$, $\eta = 0.00001\Delta$, and $\delta = \pi/3$ (red) , $2\pi/3$ (green) and π (blue) .

3.3.2.3 Influence of Γ_L, Γ_R and U on ABSs "gate dependence"

The other parameters of the model Γ_L, Γ_R and U are not tunable[20] and corresponds to intrinsic aspects of the sample that depend on microscopic details determined during fabrication of the sample. To understand their influence on the QD spectral density, it is helpful to look at the TDOS dependence with the mean position level (ϵ_0 tuned with V_g) for different parameters Γ_L, Γ_R and U. First we analyze, as in previous section, the case of a QD connected to normal leads which is contained in the models, simply setting $\Delta = 0$, and then look at the case of a QD connected to superconducting leads ($\Delta = 1$), to see how ABSs are affected by those parameters.

- Dependence with the mean level position ϵ_0 in the normal state:

In Fig. 3.11, we have arranged side by side three calculations of TDOS of a QD connected to normal leads. In addition to NRG (right) and the effective approach (left), we have chosen to represent results obtained within a self-consistent mean field approach (central graphs) that we will not described here but which is explained in appendix B.

Effective model In the effective model, as we have seen before (see first line of Fig. 3.8), for a given ϵ_0 when $U \neq 0$, we obtain two broad levels with Lorentzian shapes in the TDOS (in the particular case $U = 0$, the degeneracy between those levels is not broken and there is only one Lorentzian). The half-width at half maximum of these levels is equal to $\Gamma = \Gamma_L + \Gamma_R$. When ϵ_0 is changed, these Lorentzians are simply linearly translated. The Fermi level of the leads E_F play no particular role, this invariance will be broken when $\Delta \neq 0$.

Self-consistent approach The self-consistent approach gets a step further in modeling the interaction, as occupancy of the QDs starts to play its role and introduces selection rules in the spectrum of excitations. Thereby, for ϵ_0 well above 0 (resp. well under 0), the TDOS shows a single peak at $\epsilon_0 - U/2$ (resp. at $\epsilon_0 + U/2$) corresponding to the only excitation available when doing tunneling spectroscopy: addition (resp. extraction) of an electron when the QD is empty (resp. filled). When ϵ_0 is between $-U/2$ and $U/2$, the QD is singly occupied and two excitations are available: injection of an electron at $\epsilon_0 + U/2$ (orbital plus charging energy) or extraction of the electron which

---

[20] Later, in this thesis, we will see however that these parameters may vary with the gate voltages. But as these variations are small in the voltage ranges that we consider here, we ignore these dependences in this part.

has an energy of $\epsilon_0 - U/2$. These selection rules generate the diamond shape features that is commonly observed in QD's density of states (see appendix A).

Numerical Renormalization Group The NRG, which is the more complete approach as it is "exact", gives a similar spectrum than the self-consistent approach except for low energies where a Kondo peak forms for single occupancy ($-U/2 < \epsilon_0 < U/2$). This is the only approach within those three that captures the physics of Kondo effect. Moreover looking at the cuts in Fig. 3.11, we see that quasiparticles peaks at $\pm U/2$ are much wider in the NRG approach than in the effective model and the self-consistent approach.

- Dependence with the mean position level ϵ_0 in the superconducting state:

If now the leads are driven superconducting, this spectral density is modified. We have already seen that a superconducting gap $[-\Delta, +\Delta]$ is induced around the Fermi level and that this gap contains Dirac peaks at the energies of the ABSs (note that the continuum is also affected). As shown in Fig. 3.12 and 3.13, locations of these ABSs evolves with ϵ_0 and this evolution depends on the parameters of the system.

Characteristic pattern: pairs of bell-shaped resonances ABSs appear in the gap only when $\epsilon_0 - U/2$ and $\epsilon_0 + U/2$ are in a range of $\sim \Gamma$ of the gap. Otherwise, the ABSs are weak and very close to the gap edge such that they don't show up as a separate features in the DOS. When the mean position of the levels is tuned (see Fig. 3.12), ABSs move to draw facing pairs of bell-shaped resonances centred at $\epsilon_0 = 0$ with their bases resting against opposite edges of the superconducting gap. By changing the total coupling to the leads $\Gamma = \Gamma_L + \Gamma_R$, we change the profile of these bells. In Fig. 3.12, whereas the effective model and NRG are in perfect agreement for $U = 0$, it shows a striking difference for small U: ABSs are degenerate in NRG and not in the effective model. This latter aspect underlines one of the limits of the phenomenological approach for taking properly into account interactions in the QD. ABSs having spin, their degeneracy is indeed broken in the presence of a Zeeman field, like the one we have inserted in the effective model to describe the Coulomb repulsion. Yet interactions have no reason to break the spin degeneracy since they are not directly sensitive to the spins of electrons. A more systematic investigation of the influence of U on the ABSs is shown in Fig. 3.13.

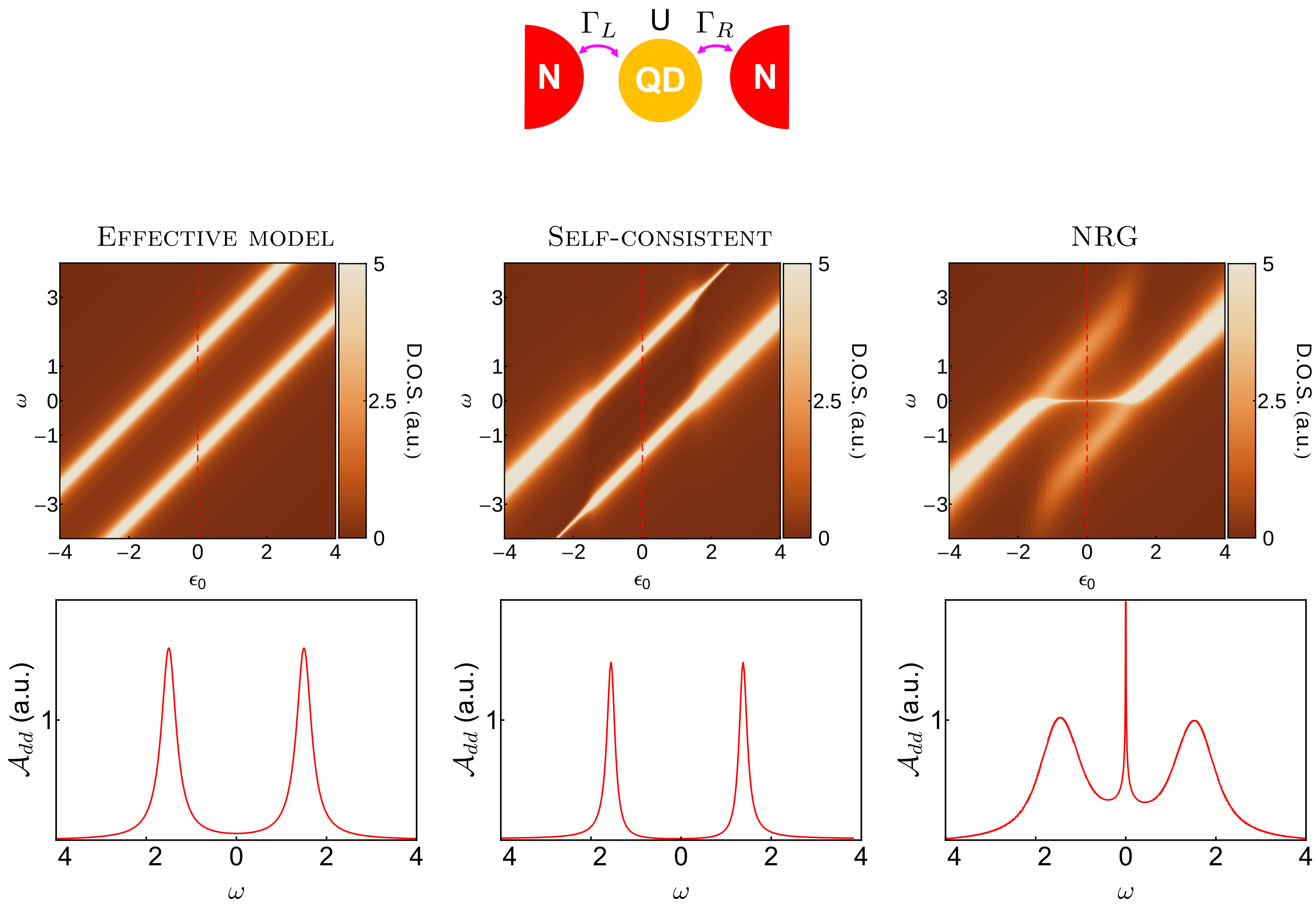

Figure 3.11: Colorplots (left) and cuts (right) of calculated spectral density for a QD connected to normal leads as a function of the energy ω and the levels mean position ϵ_0 within three different approaches: effective model, self-consistent mean field approximation and NRG. QD levels are broaden in a Lorentzian shape due to the couplings to the leads $\Gamma = \Gamma_L + \Gamma_R$ and splitted because of the charging energy U. Self-consistent approach and NRG include selection rules related to the occupancy of the dot (responsible of the diamond-shape pattern), whereas the effective model is not sensitive to this aspect. NRG is the only approach within those three that captures the Kondo effect occurring at low energies. Parameters taken for these calculations are $\Gamma = 0.2$, and $U = 3$ in arbitrary unit.

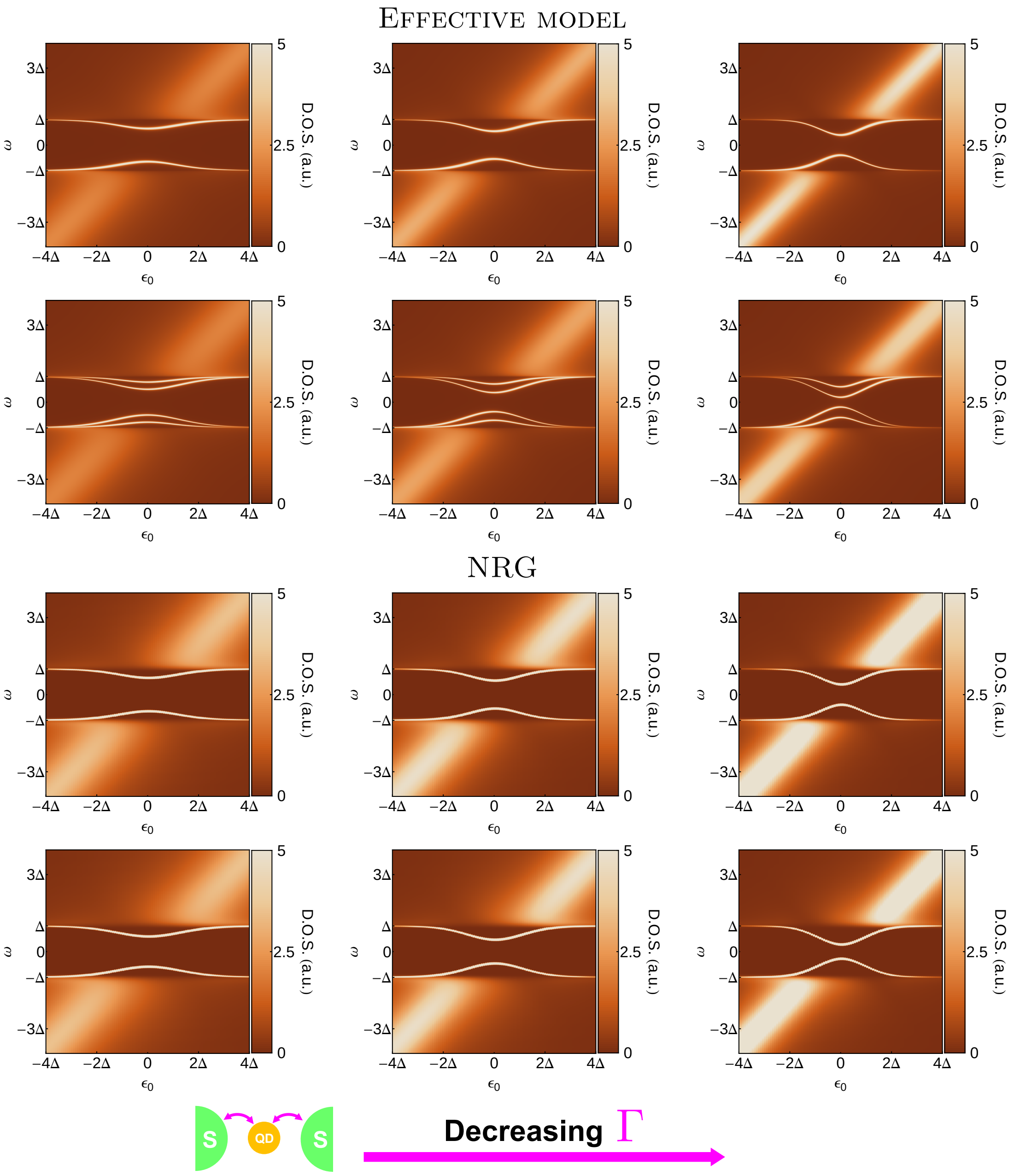

Figure 3.12: DOS as a function of the energy ω and the levels mean position ϵ_0 calculated within the effective model (6 upper graphs) and using NRG (6 lower graphs) for decreasing Γ from the left to the right for $U = 0$ (first and third lines) and $U = 0.6\Delta$ (second and fourth lines). The coupling to the leads influences strongly the ABSs dependence with ϵ_0. Parameters: $\delta = 0$, $\Gamma_L = \Gamma_R = 0.7$, 0.5, and 0.3Δ, and $\eta_{inel} = 0.01\Delta$.

Influence of the strength of U It shows that, as just mentioned, for small U (left graphs) the phenomenological approach fails to describe correctly this influence because ABSs are predicted to be degenerate by the NRG whereas the effective non-interacting model predicts that this degeneracy is broken.

For $U \sim \Delta$ (central graphs), the degeneracy between ABS is broken in both approaches and four resonances corresponding to two ABSs may appear within the gap. However in NRG, this happens only when one of the ABS has crossed the Fermi level, *i.e.* after the singlet-doublet transition mentioned in section 3.1.5.2. It results in a “hanging” ABS for a reduced region of ϵ_0. This feature is missed by the phenomenological approach because it is due to selection rules related to QD's occupancy[77], not taken into account in this approach. Indeed, in the ground state, the QD is either occupied by an odd number of electron or by an even number of electron (superconducting singlet-states): the spin S of the dot is thus either equal to 1/2 or 0. As tunneling spectroscopy explores excitations of the system through injection of electrons, it allows only to see transitions that do not conserve the spin of the dot. In Fig. 3.14, we have plotted the energies of the different states available for the system[21] as a function of ϵ_0. There are four of them: two $S = 0$ states with one that is always higher in energy and two degenerate $S = 1/2$ states. For ϵ_0 far from 0, the ground state is a $S = 0$ state and tunneling spectroscopy allows to explore only the degenerate $S = 1/2$ doublet, resulting in a single resonance between 0 and Δ in the TDOS. After crossing of an ABS with the Fermi level, the ground state is the degenerate doublet $S = 1/2$, and transition toward $S = 0$ states can be seen by tunneling spectroscopy, resulting in two resonances between 0 and Δ in the TDOS. As the effective approach ignores selection rules due to QD occupancy, all the possible transitions are seen in the spectrum and ABSs are never “interrupted” this way. It can be noticed that it is not because states cannot be seen through transition authorized by tunneling spectroscopy that they do not exist. Besides, performing a spectroscopy through microwave irradiation, we would obtained transition between $S = 0$ states, completing the whole spectrum.

For large U, the calculated TDOS are in satisfying agreement between the two approaches (at least concerning the ABSs). The two central bells cross to form a loop, and the external states merge into the continuum beyond $\pm\Delta$ (see Fig. 3.13). At some point only one ABS appears in the spectral density (but twice, at $\omega > 0$ and $\omega < 0$), the other one being stuck to the edge. This is the most common situation in our measurements.

---

[21] Be careful that we distinguish states of the whole system and excitations of the system (which are transitions between states).

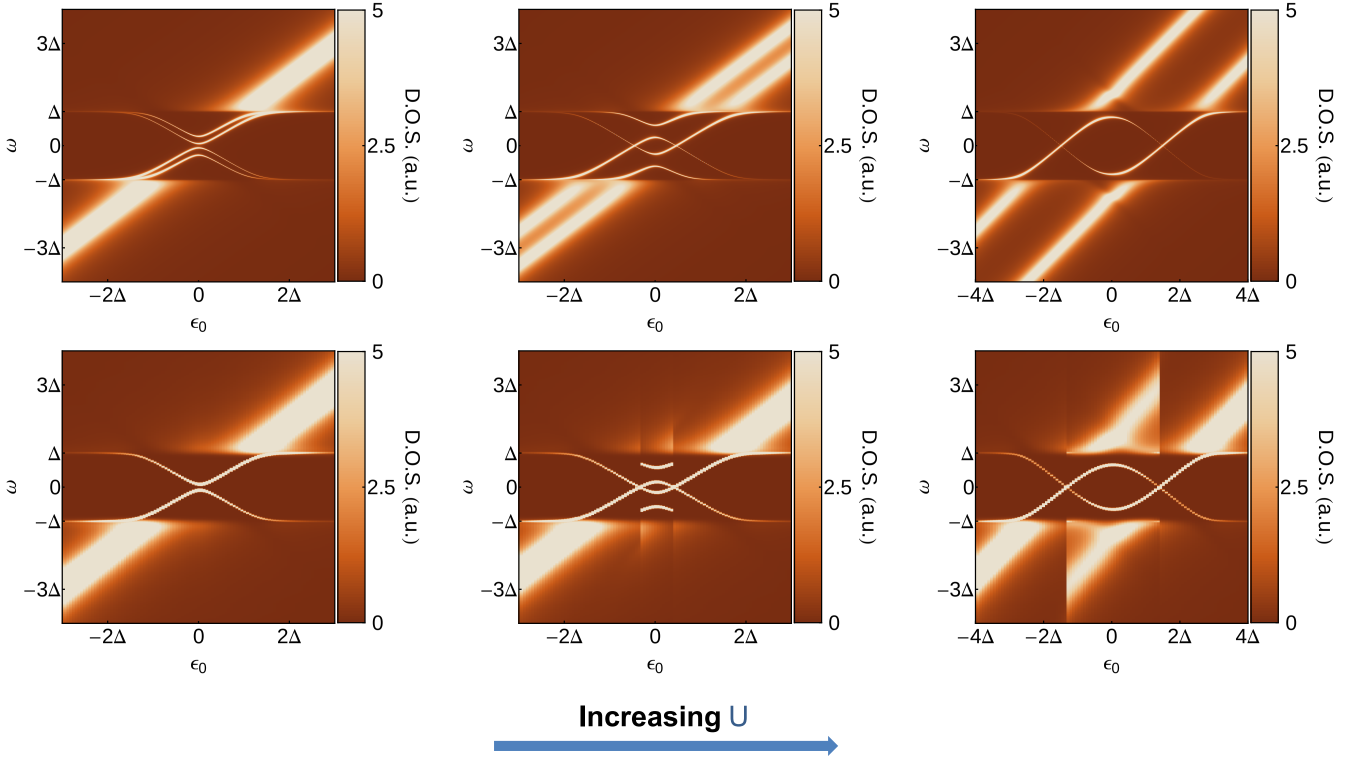

INFLUENCE OF THE CHARGING ENERGY IN THE PHENOMENOLOGICAL MODEL (UPPER GRAPHS) AND IN NRG (LOWER GRAPHS)

Figure 3.13: Color scaled representations of TDOS of a QD connected to superconducting leads as a function of ϵ_0. The three upper graphs are obtained within the effective non-interacting approach and the lower graphs are obtained by NRG calculations. In the effective model, we see that increasing U splits the ABSs until a loop is formed in the spectral density and one of the ABSs merge into the continuum. If we compare with the exact results obtained in NRG, we see that the effective model capture many features of the ABSs that develop in an interacting QD. There are however some differences. For example, when U is small compared to Δ, we see that, in opposition to the effective model, in NRG calculations the degeneracy between ABSs is not broken. For U close to Δ, NRG predicts that there is a “hanging” excitation that appears when ϵ_0 is close to the Fermi level. This is due to selection rule (see Fig. 3.14) that are completely ignored in the effective model. However for large U, the effective model is in good agreement with NRG concerning the ABSs. Parameters used for calculations: $\delta = 0$, $\eta_{inel} = 0.01\Delta$ (only for the effective model), $\Gamma = 0.2\Delta$, $U = 0.25$, 1 and 3Δ.

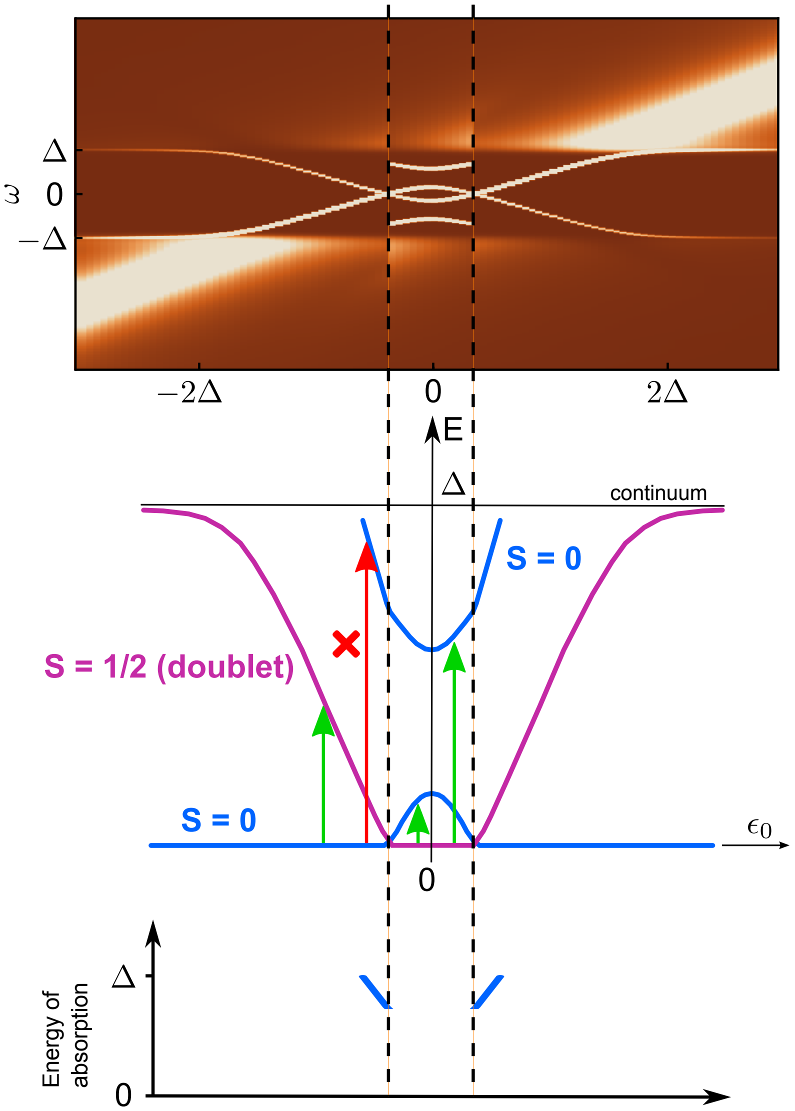

ENERGY OF THE GROUND STATE AND SINGLET-DOUBLET TRANSITION

Figure 3.14: On the top, is represented a spectrum calculated in NRG of Fig. 3.13, where a “hanging” ABS appear around $\epsilon_0 = 0$. Below, we have plotted energies of the four lowest states (in energy) of the system as a function of ϵ_0 (the ground state is always chosen as the origin). The blue lines indicate energies of $S = 0$ states, whereas energies of degenerate $S = 1/2$ states are traced in pink. As measuring the TDOS, we do not conserve the spin of the dot (one electron is added or extracted) we cannot see transitions between $S = 0$ states (red arrow), but only transition between $S = 0$ and $S = 1/2$ states (green arrows). The inversion of ground state, or singlet-doublet transition, occurring at the crossing of an ABS with the Fermi level induces a lift of degeneracy between excitations of the system. As a consequence, an abrupt transition between two and four resonances in the gap happens in the TDOS. The lower graph shows what we should obtain by microwave spectroscopy as a function of the frequency and ϵ_0: we would explore transitions from $S = 0$ ground states to $S = 0$ excited states.

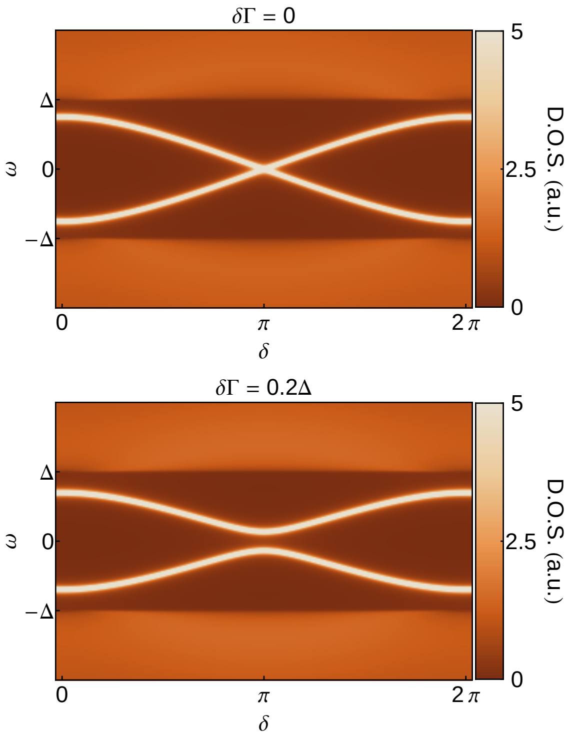

Effect of the contact asymmetry on the ABSs

Figure 3.15: DOS obtained from the phenomenological approach for symmetric (top) and asymmetric (right) contacts connected to the QD. On the left $\delta\Gamma = 0$ and on the right $\delta\Gamma = 0.2\Delta$. The contact asymmetry $\delta\Gamma$ introduces a coupling between the ABSs which form an avoided crossing at $\delta = \pi$ when $\delta\Gamma \neq 0$. For both DOS, we used $\Gamma = 1.8\Delta$, $\epsilon_0 = 0$, $E_{ex} = 0$ and $\eta_{inel} = 0.01\Delta$ in the calculation.

Role of the coupling asymmetry $\delta\Gamma = \Gamma_L - \Gamma_R$ in the phase dependence As we explain previously, in section 3.1.3, the coupling asymmetry to the electrodes $\delta\Gamma = \Gamma_L - \Gamma_R$ only plays a role at finite δ. In figures 3.12 and 3.13, the TDOS is always calculated at a phase difference $\delta = 0$, so that only the total coupling strength Γ enters the Green's functions and $\delta\Gamma$ has no influence.

However, we can then see the influence of the coupling asymmetry $\delta\Gamma$ in the phase dependence of the spectral density. Figure 3.15 represents two colorplots of the spectral density phase dependence for $\delta\Gamma = 0$ and $\delta\Gamma \neq 0$ but with a similar Γ. The asymmetry introduces a coupling between ABSs which anticross at $\delta = \pi$ only when $\delta\Gamma \neq 0$.

Role of the interdot coupling t' Compared to a single QD, the DQD nature of the CNT introduces new physics which is governed by the strength of the interdot coupling t'. In chapter 7 of part III, we will see how it affects the electronic structure of the CNT within a self-consistent approach (NRG for DQD is not done here as it is more complicated and time-demanding than for single QD).

Here, we analyze its influence on the ABSs formation within our crude approach and particularly their phase dependence. When $t' = 0$, the electrical circuit is open between the two superconducting leads: no supercurrent can flow and there is thus no phase dependence of the DOS. Yet ABSs do form in both QDs, they just do not carry supercurrent and are not coupled with each others. In Fig. 3.16, the gate dependence of the DQD density of states exhibit the characteristic "bells" within $[-\Delta, +\Delta]$ which appear independently.

If now $t' \neq 0$, the electrical circuit is closed and can sustain supercurrent. The "bells" are now interacting because of the interdot coupling and form an anticrossing where ABSs cross each other as on Fig. 3.16. At this anticrossing ABSs get their maximum phase dependence and it remains essentially phase independent elsewhere.

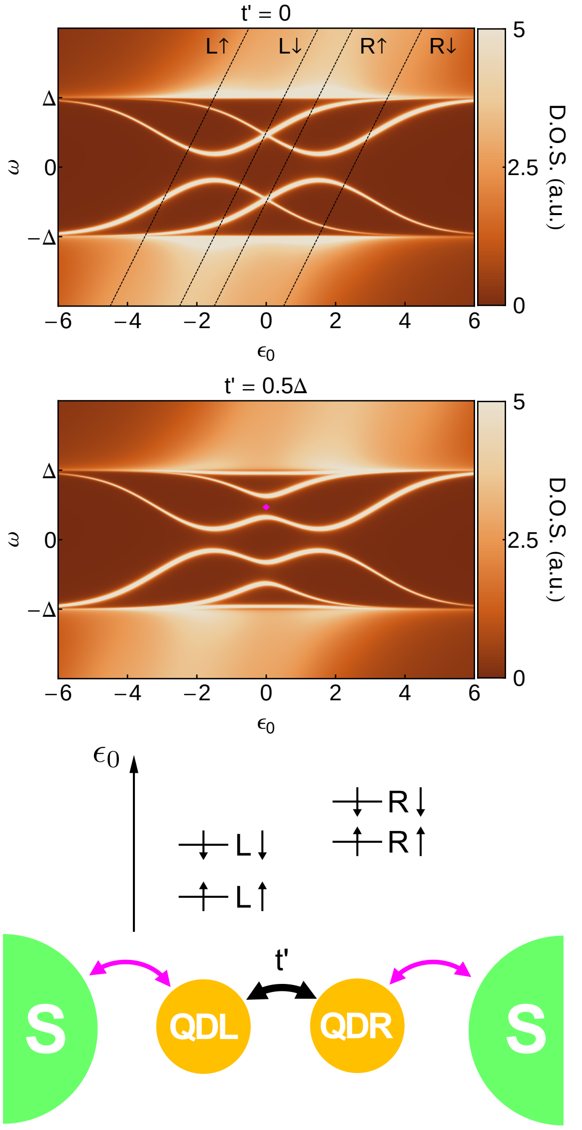

Avoided crossings of the ABSs due to interdot coupling

Figure 3.16: Colorplots of the QD's TDOS as a function of the energy ω and the mean position of the levels ($\epsilon_{L\uparrow}$, $\epsilon_{L\downarrow}$, $\epsilon_{R\uparrow}$ and $\epsilon_{R\downarrow}$) noted ϵ_0. When ABSs of QDL and QDR cross each other they may couple if $t' \neq 0$ and form an avoided crossing, as for example where indicated by the diamond. At these avoided crossing, the flux dependence is maximum. On the left graph, dashed lines labelled $L\uparrow$ and $L\downarrow$ (resp. $R\uparrow$ and $R\downarrow$) are inserted to indicate where are, for each value of ϵ_0, levels of spin up and down of the left (resp. right) QD. Parameters are: $\epsilon_{L\uparrow} = \epsilon_0 + 2,5\Delta$, $\epsilon_{L\downarrow} = \epsilon_0 + 0,5\Delta$, $\epsilon_{R\uparrow} = \epsilon_0 - 0,5\Delta$, $\epsilon_{R\downarrow} = \epsilon_0 - 2,5\Delta$, $\Gamma_L = \Gamma_R = 1,2\Delta$, $\eta_{inel} = 0,01\Delta$ and $\delta = \pi$.

Part II

Experimental observation of the Andreev Bound States

Andreev Bound States concept has led to many successful interpretations for experiments on mesoscopic superconductivity [69, 78, 79, 80, 81], and exotic or high-T_c superconductors [82, 83, 84, 85, 86]. Moreover they are now inspiring possible experimental realizations in mesoscopic circuits for the observation of Majorana Bound States [32, 42, 87, 88], which supposedly behave as non-abelian anyons [89]. Despite the fundamental interest they arouse and though there have been already some strong indications of their existence [69], no direct observation of individually resolved ABSs were performed so far. In this chapter we present the first observation of ABSs realized by tunneling spectroscopy in a supercurrent-carrying CNT.

For the purpose of probing the ABSs, we have fabricated samples with open superconducting loops closed by a CNT in order to form S-CNT-S structures with a tunable superconducting phase difference δ. Additionally, in the middle of these structure, a superconducting tunnel probe is connected to the CNT in order to measure its DOS.

With such devices, we observed individually resolved ABSs and their δ-dependence, which is the ABSs's main signature and is related to their supercurrent-carrying nature. Moreover thanks to external gate voltages and by confronting our experimental results with the phenomenological DQD model described in previous part, we were able to link ABSs with the electronic structure of the CNT and to extract information on parameters of the system such as the coupling to the leads and the charging energy of the QDs.

In this part of the thesis, we first describe the samples and the measurement setup. Then we present the ABSs tunneling spectroscopy that we have realized in a CNT connected to superconducting leads, and discuss the observation of the $0 - \pi$ transition in the TDOS of our device. Finally, we discuss the performance of our device as a magnetic flux sensor using the δ-dependence of the ABSs.

Chapter 4

Description of the samples and measurement setup

In this section, we describe the samples we measured and discuss the role of controllable parameters of the experiment: gate voltages, bias voltage, magnetic field, temperature. We also describe the measurement setup which is connected to these samples in order to measure CNTs' DOS.

4.1 Samples description and role of controllable parameters

Samples geometry Samples we used to perform ABSs spectroscopy are composed of several metallic structures connected to CNTs (see part IV). These structures are constituted by a superconducting "fork" and a superconducting tunnel probe connected to a single CNT, as depicted on Fig. 4.1.

Within this geometry, we create two QDs (QDL and QDR in Fig. 4.1) localized between the two arms of the fork and on each side of the tunnel probe.

Voltage bias V The fork, which is well connected to the CNT, is grounded, whereas the tunnel probe, which is weakly coupled to the CNT, is biased with a voltage V. By tuning this voltage we control the energies at which we probe the TDOS of the CNT (see appendix D). This TDOS is extracted from lock-in measurements of the differential conductance $G(V)$ between the tunnel probe and the fork (see subsection 4.2).

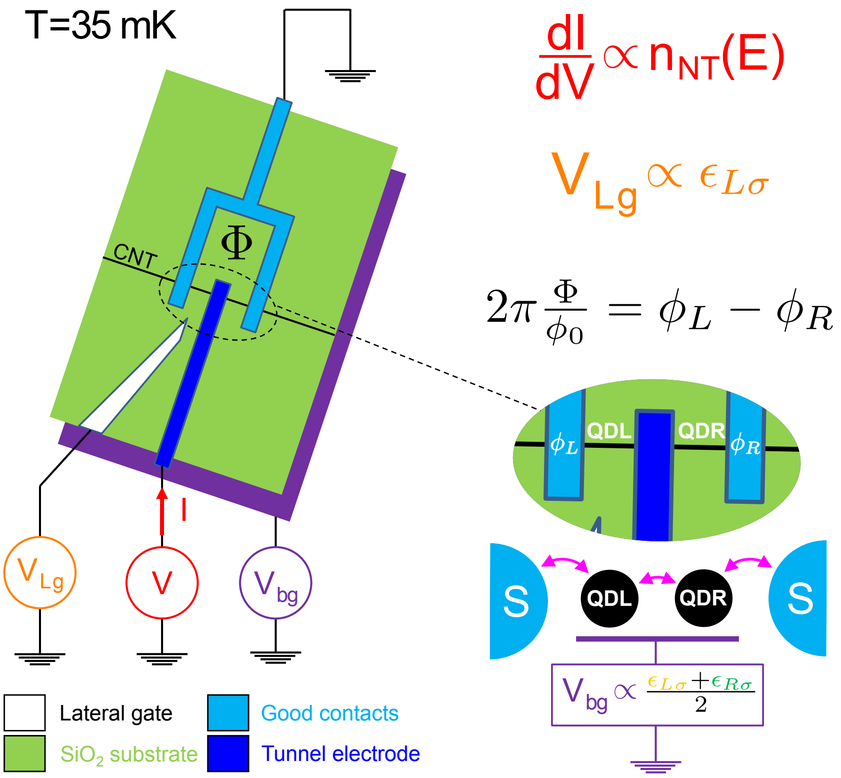

Diagram of the structures and connection to control devices

Figure 4.1: Each structure is connected to two (or three) DC voltage sources: a back gate voltage V_{bg} which controls the CNTs' electro-chemical potential (some structures have an additional lateral gate voltage V_{Lg} which allows to tune locally the electro-chemical potential) and a voltage bias V that we apply on the tunnel probe in order to measure the differential conductance $G\left(V\right)$. From $G\left(V\right)$, we extract the CNT's DOS (see appendix D). Additionally, we can generate, perpendicularly to the sample, a magnetic field that we use either to tune the magnetic flux Φ in order to produce a superconducting phase bias $\delta = \phi_L - \phi_R$ across the CNT (low magnetic field ≤ 50 Gauss), or to drive the electrodes in their normal state (high magnetic field ≥ 500 Gauss.).

Gate voltages Each sample is capacitively coupled to a back gate voltage V_{bg}, and some structures (but not all) have an additional lateral gate coupled to the left part of the CNT[1] biased with a voltage V_{Lg}. When biased, the back gate voltage V_{bg} shift the electro-chemical potential of CNTs homogeneously, thereby accumulating electrons or holes in the CNT, whereas V_{Lg} has just a local influence and allows to change the number of charge carriers only on one side of the CNT (in QDL).

Magnetic flux Φ In our experiment the two superconducting contacts are connected to the CNT on one side and shorted together on the other side, thereby forming a loop with the CNT. In this geometry, with the magnetic flux Φ enclosed by the loop, we control the superconducting phase difference $\delta = \phi_L - \phi_R$ between the two superconducting electrodes connected to the QD.

As the total magnetic flux threading the loop determines the integral of the phase gradient around the complete loop [47], the flux Φ and the superconducting phase difference δ are related through the relation:

$$\Phi = \frac{\Phi_0}{2\pi}\left(\delta + \delta_{Al}\right) - \Phi_{screen}$$

where $\Phi_0 = h/2e$ is the flux quantum, δ_{Al} is the phase difference accumulated along the aluminum part of the loop and Φ_{screen} is a screening flux created by the current I_{loop} that develops in the loop. This two contributions are respectively proportional to the kinetic inductance $\mathcal{L}_K^{Al}$ of the aluminum part of the loop ($\delta_{Al} = \frac{2\pi}{\Phi_0}\mathcal{L}_K^{Al} I_{loop}$) and the geometric inductance $\mathcal{L}_G$ of the loop ($\Phi_{screen} = \mathcal{L}_G I_{loop}$).

However, as $\mathcal{L}_K^{Al}$ and $\mathcal{L}_G$ are negligible compared to the kinetic inductance $\mathcal{L}_K^{CNT}$ of the CNT[2], the magnetic flux threading the loop essentially imposes a phase difference δ across the CNT. The latter is thus simply given by:

$$\delta = 2\pi\frac{\Phi}{\Phi_0}$$

across the CNT (see Ref. [90] for a detail discussion on how to achieve a good phase bias).

The magnetic field is generated with a current circulating in a superconducting coil below the sample. When we want to generate a magnetic field in order to tune the superconducting phase difference, we use magnetic field lower than 50 Gauss. But we can also generate a higher magnetic field (of

---

[1] A right lateral gate was also coupled to the sample but floating.

[2] We have indeed $\mathcal{L}_G < \mathcal{L}_K^{Al} \ll \mathcal{L}_K^{CNT}$, as $\mathcal{L}_G \approx 1$pH, $\mathcal{L}_K^{Al} \approx 10$pH and $\mathcal{L}_K^{CNT} > 10$nH.

the order of 500 Gauss) in order to drive the aluminum electrodes in their normal state.

Temperature Measurements presented in chapter 5 and 7 were performed at fixed temperature, in a dilution fridge with a base temperature of 35 mK.

In chapter 9 of part III, we also performed temperature dependence measurements. This is performed heating up the sample between 35 mK and ~ 1 K increasing the temperature of the dilution fridge.

4.2 Measurement setup

The measurement setup is similar to the one of Ref. [90] where the reader can find all the details. Here we just describe the basic principles of measurements.

The measurement setup is sketched in Fig. 4.2. Voltages are applied on the samples with Yokogawa 7651 DC generators and the differential conductance is measured using standard lock-in techniques with a SR830 Lock In Amplifier (LIA).

A small AC voltage excitation, (sinusoidal with a 0.3 Vrms amplitude and a frequency ranging between 150 and 200 Hz) generated by the LIA, is divided by 100 and combined with a DC signal (delivered by a voltage source) in a low noise summing amplifier. This signal is then divided by 1000 and applied on the tunnel probe. The resulting current I is converted to a voltage by a home-made current to voltage converter (CVC), described in Ref. [91], with a gain of 10^7 (determined by a feedback resistance R of 10 MΩ) and then measured by the LIA. This measurement gives us access to the differential conductance $G\left(V\right) = \frac{dI}{dV}$.

To reduce as much as possible the amount of noise, all the amplifiers are battery powered in order to decouple the experiment from the rest of the electronics, and contained in an Electro-Magnetic Interference (EMI) shielding in order to isolate the measurement setup from ambient electromagnetic noise. Furthermore, the voltage is applied on the sample through the CVC (mounted right at the output connector of the refrigerator in order to avoid for extra noise) in order to obtain a differential sensing of the voltage applied on the sample with respect to a well-referenced cold ground. And finally there is an additional home made amplifier with unit gain at the output, decoupling the experiment from the LIA in order to avoid ground loops.

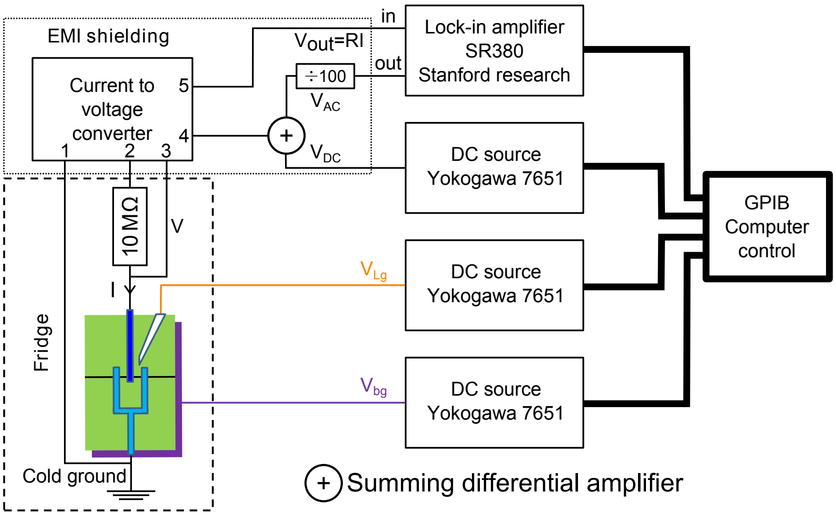

Measurement setup

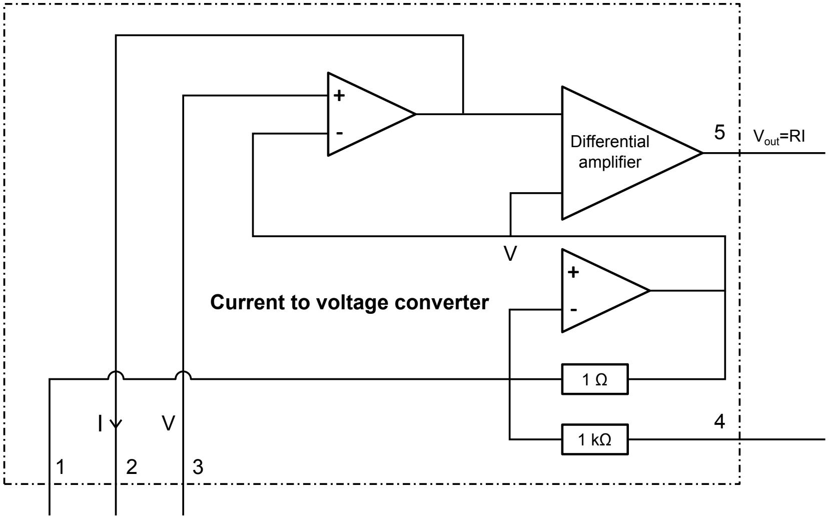

Simplified diagram of the current to voltage converter

Figure 4.2: Diagram (top) of the measurement setup and simplified schematic (bottom) of the current to voltage converter (CVC). Measured structures are cooled down on top of a Sionludi dilution fridge at a base temperature of 35 mK. Their back gate and lateral gate are connected to DC generators through filters (not represented). A voltage V, including a DC part and an AC excitation, is applied on the tunnel probe. The resulting current is amplified and converted into a voltage by the CVC, it is then measured with the Lock-In Amplifier (AC coupled). From this measurement, we deduce the differential conductance $G = \frac{dI}{dV}$. All low levels signals amplifiers are battery-powered and contained in an Electro-Magnetic Interference (EMI) shielding in order to isolate the measurement setup from ambient electromagnetic noise. The signal V_{OUT} (see bottom diagram) is measured through a home made amplifier with unit gain (not represented) that decouples the experiment ground from the rest of the electronics in order to avoid the so-called ground loops.

Chapter 5

Tunneling spectroscopy of the Andreev Bound States

In this chapter which is the heart of the thesis, we first reproduce our article published in Ref. [92] and its supplementary information on the observation of the ABSs by tunneling spectroscopy of a CNT connected to superconducting leads. Then we discuss the singlet-doublet transition that we do observe in Ref. [92] but that we didn't mention.

5.1 Paper "Andreev bound states in supercurrent-carrying carbon nanotubes revealed"

Revealing the electronic structure of a carbon nanotube carrying a supercurrent

J.-D. Pillet[a], C. H. L. Quay[a], P. Morfin[b], C. Bena[c,d], A. Levy Yeyati[e] and P. Joyez[a]

[a]*Quantronics Group,*
Service de Physique de l'Etat Condensé,
CNRS URA 2426, IRAMIS, CEA
F-91191 Gif-sur-Yvette, France
[b]*Laboratoire Pierre Aigrain (LPA), CNRS UMR 8551,*
Université Pierre et Marie Curie (Paris VI) - Université Denis
Diderot (Paris VII) - Ecole Normale Supérieure de Paris (ENS Paris)
[c]*Laboratoire de Physique des Solides, CNRS UMR 8502,*
Université Paris-Sud, Bât. 510, F-91405 Orsay, France
[d]*Institut de Physique Théorique, CEA/Saclay,*
CNRS URA 2306, Orme des Merisiers,
F-91191 Gif-sur-Yvette, France and
[e]*Departamento de Física Téorica de la Materia Condensada C-V,*
Universidad Autónoma de Madrid, E-28049 Madrid, Spain.

Carbon nanotubes (CNTs) are not intrinsically superconducting but they can carry a supercurrent when connected to superconducting electrodes [1–4]. This supercurrent is mainly transmitted by discrete entangled electron-hole states confined to the nanotube, called Andreev Bound States (ABS). These states are a key concept in mesoscopic superconductivity as they provide a universal description of Josephson-like effects in quantum-coherent nanostructures (e.g. molecules, nanowires, magnetic or normal metallic layers) connected to superconducting leads [5]. We report here the first tunneling spectroscopy of individually resolved ABS, in a nanotube-superconductor device. Analyzing the evolution of the ABS spectrum with a gate voltage, we show that the ABS arise from the discrete electronic levels of the molecule and that they reveal detailed information about the energies of these levels, their relative spin orientation and the coupling to the leads. Such measurements hence constitute a powerful new spectroscopic technique capable of elucidating the electronic structure of CNT-based devices, including those with well-coupled leads. This is relevant for conventional applications (e.g. superconducting or normal transistors, SQUIDs [3]) and quantum information processing (e.g. entangled electron pairs generation [6, 7], ABS-based qubits [8]). Finally, our device is a new type of dc-measurable SQUID.

First envisioned four decades ago [9], ABS are electronic analogues of the resonant states in a Fabry-Pérot resonator. The cavity is here a nanostructure and its interfaces with superconducting leads play the role of the mirrors. Furthermore, these “mirrors” behave similarly to optical phase-conjugate mirrors: because of the superconducting pairing, electrons in the nanostructure with energies below the superconducting gap are reflected as their time-reversed particle – a process known as Andreev Reflection (AR). As a result, the resonant standing waves – the ABS – are entangled pair of time-reversed electronic states which have opposite spins (Fig. 1a); they form a set of discrete levels within the superconducting gap (Fig. 1b) and have fermionic character. Changing the superconducting phase difference φ between the leads is analoguous to moving the mirrors and changes the energies $E_n(\varphi)$ of the ABS. In response, a populated ABS carries a supercurrent $\frac{2e}{h}\frac{\partial E_n(\varphi)}{\partial \varphi}$ through the device, while states in the continuous spectrum (outside the superconducting gap) have negligible or minor contributions in most common cases [5]. Therefore, the finite set of ABS generically determines Josephson-like effects in such systems. As such, ABS play a central role in mesoscopic superconductivity and can be seen as the superconducting counterpart of the Landauer channels for the normal state: in both cases, only a handful of them suffices to account for all the transport properties of complex many-electron systems such as atomic contacts or CNTs. In effect, the ABS concept quantitatively explains the Josephson effect in atomic contacts [10]; it also explains tunneling spectroscopy of vortex cores and surface states in some superconductors [11]. However, there has been to date no detailed direct spectroscopic observation of individual ABS. Interest in such spectroscopy has increased with recent proposals for using ABS as quantum bits [8], and AR as a source of entangled spin states [6].

Nanotubes are particularly good candidates for the observation of ABS. First, CNT-superconductor hybrid systems are expected to show a small number of ABS, and the typical meV energy scales involved in nanotube devices are comparable with conventional superconducting gaps. These are favourable conditions for a well-resolved spectroscopy experiment. Second, given the length of CNTs, it is possible to introduce an additional tunnel probe which enables straightforward tunneling spectroscopy [12]. Furthermore, CNTs are of fundamental interest as nearly ideal, tunable one-dimensional systems in which a wealth of phenomena (e.g. Luttinger-liquid behavior [13], Kondo effects [3, 14] and spin-orbit coupling [15]) has been observed, whose rich interplay with superconducting coupling has attracted a lot of interest [16–22].

Our sample is described in Figure 1. A CNT is well connected to two superconducting metallic contacts 0.7 µm apart, leaving enough space to place a weakly-coupled tunnel electrode in between. The electrodes are made of aluminum with a few nm of titanium as a sticking layer (see SI for details); they become superconducting below $\sim 1\,\mathrm{K}$. The two outer contacts are reconnected, forming a loop. A magnetic flux Φ threaded through the loop produces a superconducting phase difference $\varphi = \frac{2e}{h}\Phi$ across the tube. By measuring the differential conductance of the tunnel contact at low temperature ($T \sim 40\,\mathrm{mK}$) we observe (see Fig. 2a, 3a) well-defined resonances inside the superconducting gap. The energies of these resonances strongly depend on the voltage applied on the back-gate of the device, and vary periodically with the phase difference accross the CNT, a signature of ABS. From the raw measurement of the differential conductance between the tunnel probe and the loop we can extract the density of states (DOS) in the tube (see e.g. fig. 2b) through a

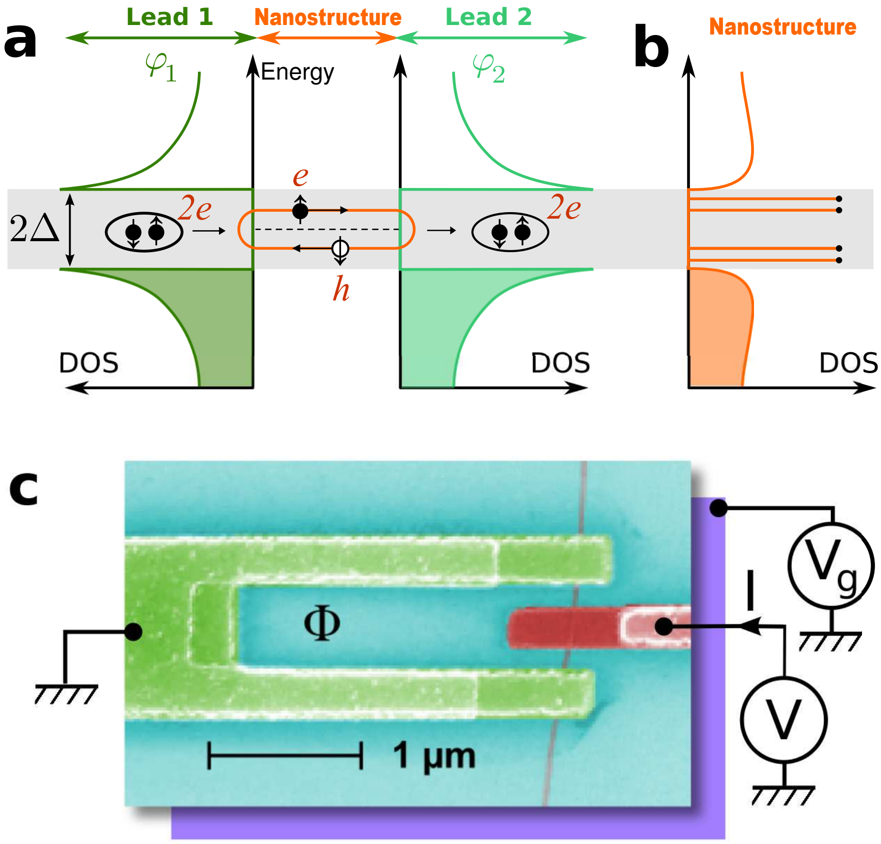

Figure 1: **a** : Generic schematic for an Andreev Bound State (ABS) in a nanostructure between two superconducting leads, which have Densities of States (DOS) with a gap Δ, and with respective superconducting phases $\varphi_{1,2}$. At energies within the superconducting gap (grey band) the Andreev reflection process (which reflects an electron (e) as a hole (h) – its time-reversed particle – and vice versa) leads to the formation of discrete resonant states of entangled $e-h$ pairs confined between the superconductors. These states –the ABS– are electronic analogues to the resonances in an optical Fabry-Pérot cavity. **b** : The local DOS in the nanostructure is thus expected to display a set of resonances in the gap at the energies of the ABS. The energies of the ABS should depend periodically on the superconducting phase difference $\varphi = \varphi_1 - \varphi_2$ which is analogous to the optical cavity length. **c** : Color-enhanced scanning electron micrograph of a device fabricated for the spectroscopy of ABS in a CNT which appears here as the thin vertical grey line. The substrate consists of highly doped silicon serving as a back gate (figured here in violet), with a 1µm-thick surface oxide layer. A grounded superconducting fork (green) is well connected to the tube, forming a loop. The measurement of the differential conductance $\partial I/\partial V$ of a superconducting tunnel probe (red) weakly connected to the tube gives acces to the density of states in the CNT, where ABS are confined. The energies of the ABS can be tuned by varying the gate voltage V_g and the magnetic flux Φ threading the loop.

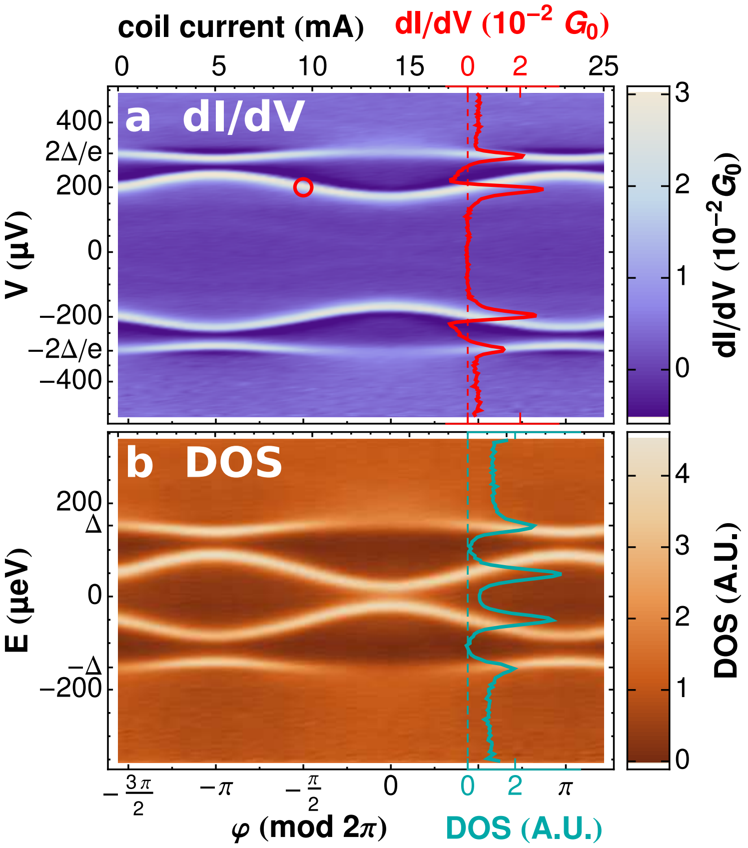

Figure 2: **a**: Differential conductance of the tunnel probe at a fixed gate voltage$V_g = -0.5\,\mathrm{V}$ as a function of the bias voltage V of the probe junction (vertical axis) and of the current in a coil (top axis) which controls the flux Φ through the loop. The sharp resonances are the signature of the ABS, and the periodicity of the pattern demonstrates that ABS coherently connect the two end contacts and are sensitive to their superconducting phase difference φ (bottom axis). The solid color traces correspond to cross sections of the data at the flux indicated by the dashed line. $G_0 = 2e^2/h$ denotes the conductance quantum. **b** DOS in the CNT as deconvolved from the data in panel a, assuming BCS DOS in the tunnel probe. The device can be operated as a dc-current SQUID magnetometer by biasing it at a point which maximize $\partial I/\partial\Phi$, as indicated by a red circle. The fact that the phase is not zero at zero current in the coil is due to a residual magnetic field in our setup.

straightforward deconvolution procedure (see SI). Figure 2 shows the dependence of the ABS spectrum on the flux in the loop at a fixed gate voltage. By dc-biasing this device at a point which maximizes $\partial I/\partial\Phi$ (see Fig. 2a), it can be used as a SQUID magnetometer which combines the advantages of Refs [23] and [3]. Being nanotube-based, our SQUID should be

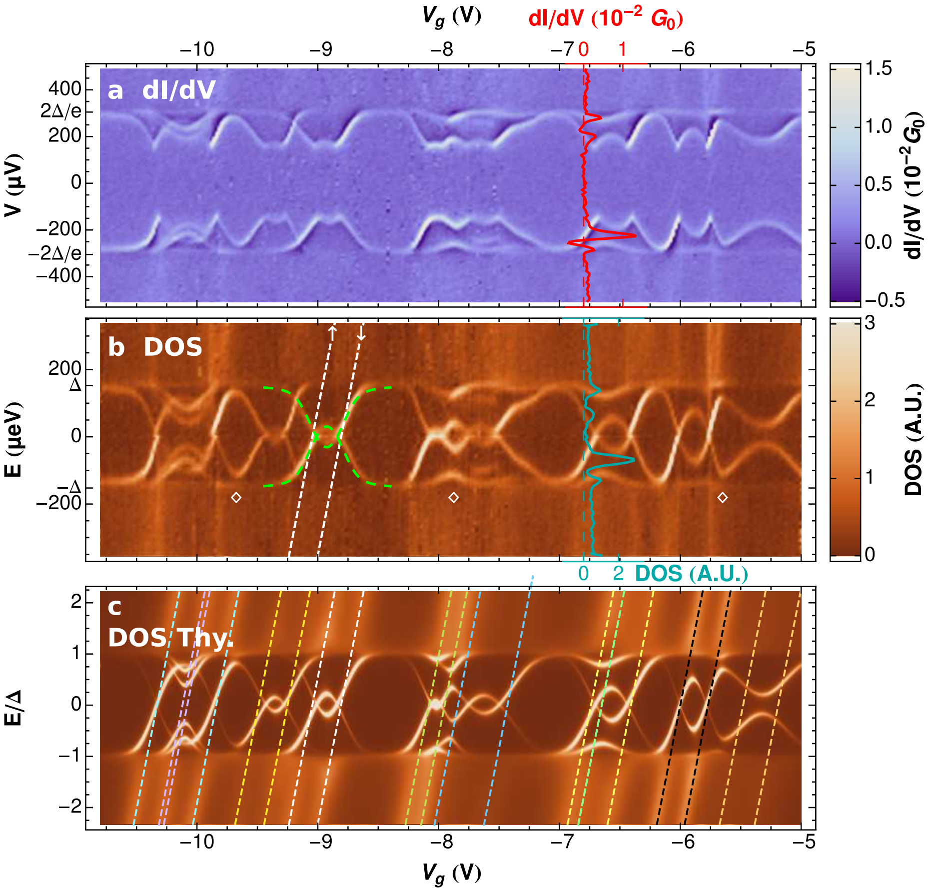

Figure 3: **Note: These color plots display well on computer screens. However, the printed appearance might be too dark depending on the printer used.**

a Gate dependence of the differential conductance of the tunnel probe. **b** DOS in the CNT as deconvolved from the data in panel a, after correcting for the gating effect of the probe junction which appears as a slight horizontal shear in panel a. The ABS form an intricate pattern of intertwined lines. Predicted from a basic quantum-dot model for the CNT, the green dotted bell-shaped lines are the positions of ABS arising from a single Spin-Split Pair of Levels (SSPL - white dashed lines) crossing the gap as the gate voltage is increased. The spin labelling indicates only the relative orientations of the spins in these levels. Most of the resonances observed in this panel have similar shapes and can be attributed to different SSPL. However, some resonances corresponding to two different SSPL are connected together where indicated by the diamonds. **c** Calculated DOS involving several coupled SSPL in a double quantum dot model. Here a SSPL is represented by a pair of dashed lines of the same color. The positions of the levels and their coupling to the electrodes were adjusted to provide best overall agreement with 2b. This simple model captures many of the observed features and shows how ABS spectroscopy allows the identification of the dot levels, and in particular of their relative spin, without applying any magnetic field.

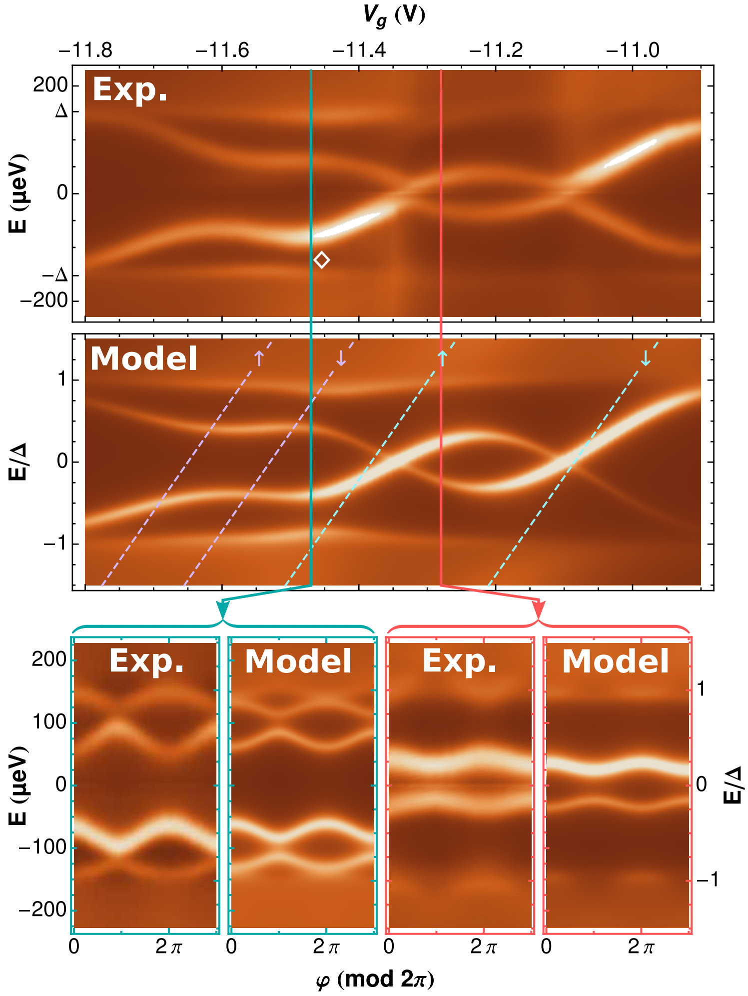

Figure 4: top panels: experimental deconvolved DOS as a function of V_g and predictions of our double quantum dot model, at phase $\varphi = 0$. Bottom pannels: experimental phase dependence taken at gate voltages indicated by the plain coloured lines in the top panels, and corresponding predictions of the model. All theoretical panels use the same set of parameters; the corresponding level positions are indicated by the dashed lines in the second pannel. The spin labelling indicates only the relative orientations of the spins in these coupled levels.

able to detect the reversal of magnetic moments of only a few Bohr magnetons[3]. At the same time, the present device can be read out with a dc current measurement (similar to [23]) and requires a single gate voltage, making it easier to operate than Ref. [3]. The gate voltage dependence of the DOS shows a pattern of resonance lines (Fig. 3b) which is more or less intricate depending on the strength of the coupling to the leads (see SI).

We now show that the ABS observed in this device arise from the discrete molecular levels in the CNT. For this we describe phenomenologically our nanotube as a Quantum Dot (QD) coupled to superconducting leads (See the SI for a detailed discussion of the model). The essential physics of ABS in this system is already captured when one considers a single orbital of the QD filled with either one or two electrons. Due to the Pauli exclusion principle, these two electrons have opposite spins and can thus be coupled by Andreev Reflection. Also, the doubly occupied state is higher in energy by an effective charging energy $\tilde{U}$ which can be determined from the experimental data. Hence, the minimal effective model consists of a Spin-Split Pair of Levels (SSPL) whose parameters are the splitting $\tilde{U}$, the mean position $\overline{E}$ of the SSPL relative to the Fermi level (which is controlled by the gate voltage V_g), and the coupling to the leads (see Fig. S1a in SI). Previous theoretical work [24, 25] has shown that there can be up to four ABS, symmetric (in position, but not in intensity) about the Fermi Level. For sufficiently large $\tilde{U}$ (respectively, $\overline{E}$), however, the two outer (respectively, all) ABS merge with the continuum and are no longer visible in the spectrum [24–26].

We now discuss the dependence of the ABS energies on the gate voltage V_g. The ABS appear as facing pairs of bell-shaped resonances centred at $\overline{E}(V_g) = 0$ and with their bases resting against opposite edges of the superconducting gap (see green dashed curves in Fig. 3b.). For large enough $\tilde{U}$ the inner resonances cross at the Fermi energy, forming a loop (Fig. 3b.). Such loops are a distinct signature of SSPL in this model (spin-degenerate levels ($\tilde{U} = 0$) cannot give loops). Most of the features observed in Fig. 3b can be identified as such pairs of bell-shaped resonances corresponding thus to different SSPL in the nanotube.

Closer inspection reveals however that adjacent resonances are sometimes coupled, forming avoided crossings (as indicated by $\diamondsuit$ symbols in Fig. 3b, 4), so that we need to consider the case where two SSPL contribute simultaneously to the spectral properties within the superconducting gap. For this, we extend the model to two serially-connected QD each containing a SSPL, with a significant hopping term in between. This model is fairly natural, given that the centre tunnel probe electrode is likely to act as an efficient scatterer. The full description of the model, the derivation of the retarded Green function from which we obtain the spectral properties, and the parameters used to produce the theoretical panels in Figures 3&4 are detailed in the SI. Assuming for simplicity that all states in the two dots are identically capacitively coupled to the gate and that the couplings to the leads are independent of V_g, we can locally reproduce most features of the gate-voltage dependence of the DOS, and simultaneously the flux dependence at fixed V_g (see fig. 4). By summing contributions of independent SSPLs and pairs of coupled SSPLs, (i.e. isolated orbitals and coupled pairs of QD orbitals) we can also reproduce the observed dependence on an extended V_g range (See Fig. 3 b & c, and discussion in the SI).

Note that a single superconducting terminal is sufficient to induce ABS in a QD (in which case, of course, there can be no supercurrent) (see Refs. [27, 28]). Given this, and in light of our analysis, we think that some features observed in Refs [29, 30] which were tentatively explained as out-of-equilibrium second order AR can now be reinterpreted as equilibrium ABS spectroscopy on a QD well connected to one superconducting lead, as in Refs. [27, 28], with the second lead acting as a superconducting tunnel probe.

The agreement between experiment and theory in Figs. 3 and 4 shows that ABS spectra constitute an entirely new spectroscopic tool for QDs and CNTs. This spectroscopy provides extremely detailed information, in particular about the relative spin state of the nanotube levels without requiring high magnetic fields. Note that, in contrast to the usual Coulomb blockade spectroscopy of QDs, the energy resolution is here essentially independent of the temperature (as long as $k_B T \ll \Delta$) and of the strength of the coupling to the leads. It should therefore allow the exploration of the transition between the Fabry-Pérot (where the Luttinger-Liquid physics is expected to play a role [18, 19]) and the Coulomb blockade regimes in CNT. We also expect this new technique to be able to provide key insights in cases where simple charge transport measurements are not sufficient to fully probe the physics at work. In particular, it should allow detailed investigation of the competition between superconductivity and the Kondo effect [16] which arise for stronger couplings to the leads. Also, used in combination with an in-plane magnetic field, it could also probe spin-orbit interactions [20–22]. Finally it should be emphasized that even while our phenomenological model successfully describes the observed experimental data further theoretical work is needed in order to establish a truly microscopic theory which should predict the level splittings from the bare many-body Hamiltonian.

The information extracted from such spectroscopy may also help to optimize Field Effect Transistors, SQUIDs or even Nano Electromechanical devices based on nanotubes, by better understanding how current is carried through the device. It could also be used for evaluating recently proposed devices for quantum information processing such as entangled electron pair generation by crossed Andreev reflection [6] or ABS-based quantum bits [8]. Regarding the latter, our observation of tunable ABS is heartening even though the measured spectroscopic linewidth ($30 - 40\,\mu\mathrm{eV}$ FWHM) seems to question the feasability of such qubits (if it were intrinsic to the sample, it would correspond to sub-ns coherence time). The present linewidth is however likely to be caused simply by spurious noise in the experimental setup. More investigations are needed in order to assess the potential of nanotube ABS as qubits.

To summarize, we have performed the first tunneling spectroscopy of individually resolved ABS which provide a universal description for the Josephson effect in weak links. The analysis of the ABS spectrum constitutes a powerful and promising spectroscopic technique capable of elucidating the electronic structure of CNT-based devices, including those with well-coupled leads.

Acknowledgments

This work was partially supported by ANR project SEMAFAET, C'Nano projet SPLONA, Spanish MICINN under contracts NAN2007-29366 and FIS2008-04209.

The authors gratefully acknowledge discussions with the Quantronics group, Ophir Auslander, Juan Carlos Cuevas, Reinhold Egger, Milena Grifoni, Takis Kontos, Hélène le Sueur, Alvaro Martín-Rodero, Pascal Simon and Christoph Strunk.

References

---

[1] Kasumov, A. Y. *et al.* Supercurrents through Single-Walled carbon nanotubes. *Science* **284**, 1508–1511 (1999).

[2] Jarillo-Herrero, P., van Dam, J. A. & Kouwenhoven, L. P. Quantum supercurrent transistors in carbon nanotubes. *Nature* **439**, 953–956 (2006).

[3] Cleuziou, J. P., Wernsdorfer, W., Bouchiat, V., Ondarcuhu, T. & Monthioux, M. Carbon nanotube superconducting quantum interference device. *Nature Nanotechnology* **1**, 53–59 (2006).

[4] Pallecchi, E., Gaass, M., Ryndyk, D. A. & Strunk, C. Carbon nanotube Josephson junctions with Nb contacts. *Applied Physics Letters* **93**, 072501–3 (2008).

[5] Beenakker, C. W. J. Three "universal" mesoscopic Josephson effects. *cond-mat/0406127* (2004). Transport Phenomena in Mesoscopic Systems, edited by H. Fukuyama and T. Ando (Springer, Berlin, 1992).

[6] Recher, P., Sukhorukov, E. V. & Loss, D. Andreev tunneling, Coulomb blockade, and resonant transport of nonlocal spin-entangled electrons. *Physical Review B* **63**, 165314 (2001).

[7] Herrmann, L. G. *et al.* Carbon nanotubes as Cooper-Pair beam splitters. *Physical Review Letters* **104**, 026801 (2010).

[8] Zazunov, A., Shumeiko, V., Bratus', E., Lantz, J. & Wendin, G. Andreev level qubit. *Physical Review Letters* **90** (2003).

[9] Kulik, I. Macroscopic quantization and proximity effect in S-N-S junctions. *Soviet Physics JETP-USSR* **30**, 944–& (1970).

[10] Della Rocca, M. L. *et al.* Measurement of the Current-Phase relation of superconducting atomic contacts. *Physical Review Letters* **99**, 127005 (2007).

[11] Fischer, Ø., Kugler, M., Maggio-Aprile, I., Berthod, C. & Renner, C. Scanning tunneling spectroscopy of high-temperature superconductors. *Reviews of Modern Physics* **79**, 353 (2007).

[12] Chen, Y., Dirks, T., Al-Zoubi, G., Birge, N. O. & Mason, N. Nonequilibrium tunneling spectroscopy in carbon nanotubes. *Physical Review Letters* **102**, 036804 (2009).

[13] Bockrath, M. *et al.* Luttinger-liquid behaviour in carbon nanotubes. *Nature* **397**, 598–601 (1999).

[14] Buitelaar, M. R., Nussbaumer, T. & Schönenberger, C. Quantum dot in the Kondo regime coupled to superconductors. *Physical Review Letters* **89**, 256801 (2002).

[15] Kuemmeth, F., Ilani, S., Ralph, D. C. & McEuen, P. L. Coupling of spin and orbital motion of electrons in carbon nanotubes. *Nature* **452**, 448–452 (2008).

[16] Glazman, L. I. & Matveev, K. A. Resonant Josephson current through Kondo impurities in a tunnel barrier. *JETP Letters* **49**, 659–662 (1989).

[17] Spivak, B. I. & Kivelson, S. A. Negative local superfluid densities: The difference between dirty superconductors and dirty Bose liquids. *Physical Review B* **43**, 3740 (1991).

[18] Fazio, R., Hekking, F. W. J. & Odintsov, A. A. Josephson current through a Luttinger liquid. *Physical Review Letters* **74**, 1843 (1995).

[19] Caux, J., Saleur, H. & Siano, F. Josephson current in Luttinger Liquid-Superconductor junctions. *Physical Review Letters* **88**, 106402 (2002).

[20] Dell'Anna, L., Zazunov, A., Egger, R. & Martin, T. Josephson current through a quantum dot with spin-orbit coupling. *Physical Review B* **75**, 085305 (2007).

[21] Dolcini, F. & Dell'Anna, L. Multiple Andreev reflections in a quantum dot coupled to superconducting leads: Effect of spin-orbit coupling. *Physical Review B* **78**, 024518 (2008).

[22] Zazunov, A., Egger, R., Jonckheere, T. & Martin, T. Anomalous Josephson current through a Spin-Orbit coupled quantum dot. *Physical Review Letters* **103**, 147004 (2009).

[23] Giazotto, F., Peltonen, J. T., Meschke, M. & Pekola, J. P. Superconducting quantum interference proximity transistor. *Nature Physics* **6**, 254–259 (2010).

[24] Yoshioka, T. & Ohashi, Y. Numerical renormalization group studies on single impurity Anderson model in superconductivity: A unified treatment of magnetic, nonmagnetic impurities, and resonance scattering. *Journal of the Physical Society of Japan* **69**, 1812–1823 (2000).

[25] Vecino, E., Martín-Rodero, A. & Levy Yeyati, A. Josephson current through a correlated quantum level: Andreev states and pi junction behavior. *Physical Review B* **68**, 035105 (2003).

[26] Meng, T., Florens, S. & Simon, P. Self-consistent description of Andreev bound states in Josephson quantum dot devices. *Physical Review B (Condensed Matter and Materials Physics)* **79**, 224521–10 (2009).

[27] Deacon, R. S. *et al.* Tunneling spectroscopy of Andreev energy levels in a quantum dot coupled to a superconductor. *Physical Review Letters* **104**, 076805 (2010).

[28] Dirks, T. *et al.* Andreev bound state spectroscopy in a graphene quantum dot. *arXiv:1005.2749* (2010). URL `http://arxiv.org/abs/1005.2749`.

[29] Eichler, A. *et al.* Even-Odd effect in Andreev transport through a carbon nanotube quantum dot. *Physical Review Letters* **99**, 126602–4 (2007).

[30] Grove-Rasmussen, K. *et al.* Superconductivity-enhanced bias spectroscopy in carbon nanotube quantum dots. *Physical Review B (Condensed Matter and Materials Physics)* **79**, 134518–5 (2009).

nature physics

SUPPLEMENTARY INFORMATION

DOI: 10.1038/NPHYS1811

SUPPLEMENTARY INFORMATION FOR:

ANDREEV BOUND STATES IN SUPERCURRENT-CARRYING CARBON NANOTUBES REVEALED

J-D. Pillet, C. H. L. Quay, P. Morfin, C. Bena, A. Levy Yeyati and P. Joyez

Sample fabrication

Carbon nanotubes were grown by chemical vapor deposition from catalyst grains deposited on a 1 µm SiO_2 insulating layer atop a highly doped Si substrate used as a back gate. As measured with an atomic force microscope, the tubes have diameters of 1-3 nm and are thus expected to be single-walled carbon nanotubes (SWNT). The SWNTs are then located with respect to gold alignment marks using Scanning Electron Microscopy (SEM) and electron-beam lithography of a MAA-PMMA bilayer is used to form a suspended mask through which we deposit the electrodes. The electrodes consist of 3 nm Ti/100 nm Al for the loop and 1 nm Ti/40 nm Al for the tunnel probe; they are deposited through the suspended mask at different angles in a single pump-down. The loop, which is well-connected to the CNT was deposited first after 2 hours of heating at 110°C in a vacuum of $\sim 10^{-7}$mb followed by rapid quenching down to -80°C. Evaporation is started when the temperature is around 0°C. The tunnel contact is then evaporated at another angle. This process yields quite frequently contact resistances measured at room temperature of $15 - 25\,\mathrm{k}\Omega$ and $\sim 100\,\mathrm{k}\Omega$ respectively which depend weakly on back gate voltage. Room temperature conductance measurements between two well-connected electrodes on either side of such tunnel probes indicate that the latter does not cut the tube. After lift-off, the sample was wire-bonded and cooled down in a dilution refrigerator equiped with carefully filtered lines.

Measurements

The differential conductance of the tunnel probe was measured using standard lock-in techniques at frequencies $\sim 200\,\mathrm{Hz}$ and an ac excitation of 2 µV. All electrical lines are shielded and filtered and we use a room temperature amplifier with a low back action on the tunnel contact to ensure a low electronic temperature. In previous experiments a very similar setup was shown to have a tunneling spectroscopy resolution of $\sim 15\,\mu$eV [1].

Extracting the Density of States (DOS) from the differential conductance

Assuming thermal equilibrium and energy-independent transmission between the probe and the tube, the tunnel current is expressed as

$$I(V) \propto \int \left(n_{TP}(\epsilon - \mathrm{eV}) - n_{NT}(\epsilon)\right) \rho_{NT}(\epsilon)\rho_{TP}(\epsilon - \mathrm{eV}) d\epsilon$$

where n_i are Fermi functions and ρ_i are DOSs, with NT (TP) standing for Nanotube (Tunnel probe). In the present experiment, the tunnel probe is superconducting. We assume that its DOS is nearly BCS, with a phenomenological Dynes "depairing" imaginary part $i\gamma\Delta$ added to the energy, to smooth out the BCS singularity (here γ is a dimensionless parameter) [2]:

$$\rho_{TP}(\epsilon) = \mathrm{Re} \frac{|\epsilon|}{\sqrt{(\epsilon + i\gamma\Delta)^2 - \Delta^2}}$$

The differential conductance can be expressed as a convolution product ($\otimes$)

$$\frac{\partial I}{\partial V}(V) \propto \left(g \otimes \rho_{NT}\right)(eV) = \int g(eV - \epsilon, V)\rho_{NT}(\epsilon) d\epsilon$$

of the unknown tube DOS ρ_{NT} with the fixed function

$$g(E, V) = \left(n_{NT}(E - eV) - n_{TP}(E)\right) \rho'_{TP}(E) - n'_{TP}(E)\rho_{TP}(E),$$

with respect to E.

Since convolution is a linear operation, its implementation on a discretized set of data $\left[\frac{\partial I}{\partial V}\right]$ can be expressed as a matrix operation :

$$\left[\frac{\partial I}{\partial V}\right] \propto M_g . \left[\rho_{NT}\right]$$

where M_g is a matrix appropriately sampling g over its two variables. We obtain the least-square error estimate of the DOS in the nanotube by left-multiplying the latter equation by the Moore-Penrose pseudo-inverse [3] of M_g. The differential conductance can thus be deconvolved to get ρ_{NT} simply by multiplying it by a fixed matrix. We have checked that edge effects due to the finite measurement range are negligible. The adjustable parameters in this deconvolution process are the probe gap Δ, the depairing amplitude γ, and the temperature. However, variations of the temperature within a reasonable range have a negligible effect; thus, the Fermi functions can effectively be replaced by step functions. The values of γ providing adequate deconvolution (i.e. artefact-free, positive DOS) depend on the data sampling; they were determined empirically and found to fall in the 0.5%-2% range. The value of $\Delta = 152 \pm 5\,\mu\mathrm{eV}$ was determined to provide best overall consistency and is compatible with the estimated gap of our Ti/Al bilayer.

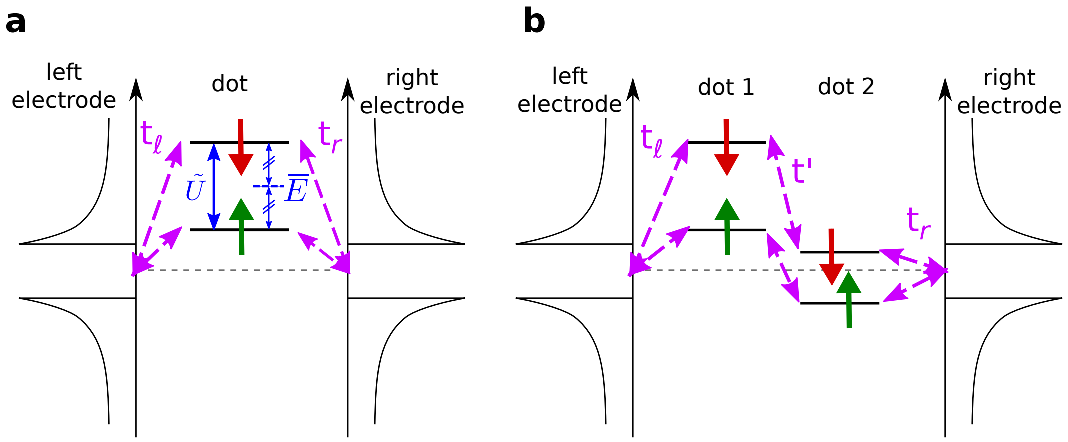

Figure S1: Schematic representation of the models used for describing the experimental data using a single (left panel) our a double (right panel) Quantum Dot model. See text for a more detailed explanation.

Spectral density for a double-quantum dot model connected to superconducting leads

Like in many experiments on nanotubes, our model is directly based on the standard quantum dot picture: The dot is seen as a series of electronic orbitals with different configuration energy that can each accommodate two electrons, and the Coulomb interaction between electrons is taken into account by a charging energy for each added electron. Even when this system is a many-body problem which cannot be solved exactly when the coupling to the leads is finite, it is possible to have a fairly good representation of its spectral properties using an effective non-interacting model. We shall first discuss how this effective model arises from a more general interacting Hamiltonian and then derive the DOS within this simple framework.

We start with a model of the nanotube as a double Quantum Dot (QD) connected to superconducting leads, restricting to a single orbital per dot, but with interactions and arbitrary couplings. Note that this model with a single dot (Fig. S1a, corresponding to the Anderson impurity model) would be sufficient to have ABS, but we have found necessary to consider a double dot structure to capture all the features observed in the data. The model is schematically depicted in Fig. S1b and the corresponding Hamiltonian can be written as $\hat{H} = \hat{H}_d + \hat{H}_T + \hat{H}_L + \hat{H}_R$, where

$$\hat{H}_d = \sum_{\alpha,\sigma} \epsilon_\alpha d^\dagger_{\alpha\sigma} d_{\alpha\sigma} + \sum_\alpha U_\alpha n_{\alpha\uparrow} n_{\alpha\downarrow} + \sum_\sigma t' d^\dagger_{1\sigma} d_{2\sigma} + \text{h.c.},$$

describe the electronic states and their Coulomb interactions in the central region. Here $d^\dagger_{\alpha\sigma}$ creates an electron in dot $\alpha = 1, 2$ with spin $\sigma =\uparrow, \downarrow$ and $n_{\alpha\sigma} = d^\dagger_{\alpha\sigma} d_{\alpha\sigma}$. The interactions are reduced to the local charging energies U_α on each dot. For the sake of simplicity we neglect the interdot Coulomb interaction which was found to be negligible in experiments on double QD systems based on CNTs [4]. The term in t' corresponds to the interdot tunneling.

On the other hand the leads are described as ideal conductors accomodating one spin-degenerate channel with BCS pairing:

$$H_j = \sum_{\boldsymbol{k}\sigma} \xi_{\boldsymbol{k}} c^\dagger_{j\boldsymbol{k}\sigma} c_{j\boldsymbol{k}\sigma} + \sum_{\boldsymbol{k}} \left(\Delta e^{i\varphi_j} c^\dagger_{j\boldsymbol{k}\uparrow} c^\dagger_{j,-\boldsymbol{k},\downarrow} + \text{h.c.} \right),$$

where $c^\dagger_{j\boldsymbol{k},\sigma}$ creates an electron with wavevector$\boldsymbol{k}$ in lead $j = L/R$, $\xi_{\boldsymbol{k}}$ and Δ are the single-particle energy and the gap parameter respectively (assumed to be equal for $j = L/R$) while in the main text $\varphi = \varphi_L - \varphi_R$ denotes the superconducting phase difference between the leads. The leads are also characterized by a normal density of states ρ_n. Finally, the spin-conserving tunneling Hamiltonian can be written as $H_T = \sum_{j\boldsymbol{k}\sigma} t_j c^\dagger_{j\boldsymbol{k}\sigma} d_{\alpha_j\sigma} + \text{h.c.}$, where $\alpha_j = 1(2)$ for $j = L(R)$ and t_j denote the hopping elements $t_{\ell,r}$ illustrated in the right panel of Fig. S1. For simplicity we take t_j and t' to be real quantities.

Finding the spectral properties of this model in the general case, including the effects of electron correlations, is a formidable task. For the case of the Anderson impurity model with superconducting leads several techniques have been applied, including Hartree-Fock approximation (HFA) [5], perturbation theory in U [6], Quantum Monte Carlo [7] and Numerical Renormalization Group (NRG) [8, 9]. In brief these works demonstrate that the system exhibits a magnetic S=1/2 ground state for $\Delta > k_B T_K$, where T_K is the Kondo temperature. In this regime the Andreev states spectrum predicted by the more sophisticated numerical techniques (NRG) [9] can be mimicked by a those of a simple non-interacting HFA [5] in which the level splitting between the two spin orientations is simply the charging energy times the difference in their population. We expect that other effects such as spin-orbit or exchange interactions (that the Anderson model cannot handle) could also modify the level splitting.

To describe in a simple way the behavior of the Andreev states spectrum in the different regimes, in the present work we thus adopt a phenomenological non-interacting approach similar to HFA but with effective parameters. For this, we replace H_d by $H_d^{eff} = \sum_{\alpha,\sigma} \tilde{\epsilon}_{\alpha\sigma} d^\dagger_{\alpha\sigma} d_{\alpha\sigma} + \sum_\sigma t' d^\dagger_{1\sigma} d_{2\sigma} + \text{h.c.}$, where $\tilde{\epsilon}_{\alpha\downarrow} = \tilde{\epsilon}_{\alpha\uparrow} + \tilde{U}_\alpha$. In this way the model describes both the case of nearly degenerate spin states (for $\tilde{U}_\alpha \ll \Delta$) and well resolved spin states (for $\tilde{U}_\alpha \gg \Delta$). The effective charging energy $\tilde{U}_\alpha$ is then a parameter which has to be determined by fitting the experiment. Notice that the ordering of the spin states implied by $\tilde{\epsilon}_{\alpha\downarrow} = \tilde{\epsilon}_{\alpha\uparrow} + \tilde{U}_\alpha$ is conventional. We cannot tell which spin direction is populated first in a given dot but once a spin orientation is selected for the first electron, the second electron should have the opposite. It should be emphasized that spin symmetry is not broken on average.

We can then obtain the spectral properties of this model from the retarded Green function in the orbital-Nambu space defined as $\hat{G}_\sigma(t,t') = -i\theta(t,t') < \left[\psi_\sigma(t), \psi^\dagger_\sigma(t')\right]_+ >$, where $\psi_\sigma = (d_{1,\sigma}, d_{2,\sigma}, d^\dagger_{1,-\sigma}, d^\dagger_{2,-\sigma})$. In the frequency representation this quantity adopts the form $\hat{G}_\sigma(\omega) = \left[\omega - \hat{h}_\sigma - \hat{\Sigma}(\omega)\right]^{-1}$, where

$$\hat{h}_\sigma = \begin{pmatrix} \tilde{\epsilon}_{1,\sigma} & t' & 0 & 0 \\ t' & \tilde{\epsilon}_{2,\sigma} & 0 & 0 \\ 0 & 0 & -\tilde{\epsilon}_{1,-\sigma} & -t' \\ 0 & 0 & -t' & -\tilde{\epsilon}_{2,-\sigma} \end{pmatrix}$$

and

$$\hat{\Sigma}(\omega) = \begin{pmatrix} \Sigma_1^{ee} & 0 & \Sigma_1^{eh} & 0 \\ 0 & \Sigma_2^{ee} & 0 & \Sigma_2^{eh} \\ \Sigma_1^{he} & 0 & \Sigma_1^{hh} & 0 \\ 0 & \Sigma_2^{he} & 0 & \Sigma_2^{hh} \end{pmatrix},$$

with $\Sigma^{ee}_{\alpha_j} = \Sigma^{hh}_{\alpha_j} = \Gamma_j g(\omega)$ and $\Sigma^{eh,he}_{\alpha_j} = -\Gamma_j e^{\pm i\varphi_j} f(\omega)$. In these expressions $f(\omega) = \Delta/\sqrt{\Delta^2 - (\omega + i\eta)^2}$ and $g(\omega) = -(\omega + i\eta) f(\omega)/\Delta$ are the dimensionless BCS green functions of the uncoupled leads (where we have included a finite inelastic relaxation rate η as a phenomenological parameter) and $\Gamma_j = \pi\rho_n t_j^2$ are the so-called normal tunneling rates to the leads. Obtaining $\hat{G}_\sigma(\omega)$ thus corresponds to the inversion of a 4×4 matrix which we perform numerically. From this quantity one can directly express the spectral densities as

$$\rho_{\alpha\sigma}(\omega) = -\frac{1}{\pi}\text{Im}\left[\hat{G}_\sigma(\omega)\right]_{\alpha,\alpha}.$$

Note that in the fits of the differential conductance we allow for different tunneling rates, Γ^p_α between the probe electrode and the two sides of the double-QD. This is justified by the broken symmetry which is expected between the two quantum dots. Figures 3c and 4 thus show the quantity $\sum_{\alpha,\sigma} \Gamma^p_\alpha \rho_{\alpha\sigma}(\omega)$. We do not fit the total intensity but rather fix the relative visibility Γ^p_1/Γ^p_2 (the complete list of parameters for the fits of Figs. 3c and 4 is given below).

Parameters used for the theoretical figures

The parameters used in figure 3c of the article are:

group	1		2				3		4				5		6		7			
V^0_n(V)	-10.12	-10.08	-10.33	-9.84	-9.49	-9.25	-9.045	-8.807	-8.08	-7.95	-7.84	-7.43	-6.739	-6.408	-6.65	-6.65	-6.00	-5.77	-5.48	-5.19
spin	↑	↓	↑	↓	↑	↓	↑	↓	↑	↓	↑	↓	↑	↓	↑	↓	↑	↓	↑	↓
$\Gamma_{\ell,r}/\Delta$	0.90		0.81		1.21		1.0		0.81		1.96		1.21		2.10		0.75		2.40	
t'/Δ	-		1.25				-		0.8				-		-		1.1			
visibility	0.5		1		0.5		1		1		0.5		1		0.5		1		0.5	

and those in figure 4 of the article are:

group	1			
V^0_n(V)	-11.65	-11.53	-11.382	-11.085
spin	↑	↓	↑	↓
$\Gamma_{\ell,r}/\Delta$	2.10		1.11	
t'/Δ	1.0			
visibility	0.5		1	

In these tables, V^0_n is the gate voltage at which the given level crosses the Fermi level. The spin orientation shown here only indicate the relative spin orientation within a given group. We have assumed that all levels have identical capacitances to the gate. Their respective energies as a function of the gate voltage are thus given by $\epsilon_n(V_g) = \lambda\Delta \times (V_g - V^0_n)$, with a value of $\lambda = +12\,V^{-1}$ determined in data where the Coulomb diamonds are most visible. For groups of levels involving two SSPL, one of them is coupled to the left lead with Γ_ℓ, the other one to the right lead with Γ_r, and they are coupled together with a hopping term t', as show on the right panel of Figure S1. For single SSPLs $\Gamma_{\ell,r}$ denotes either the left or right coupling. The visibility gives the relative weight of a pair of levels in the measurement of

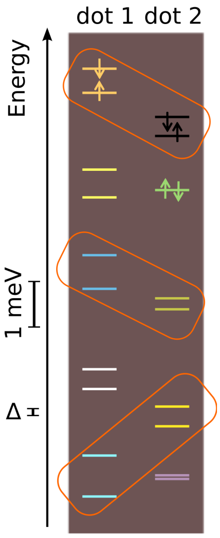

Figure S2: Possible arrangement of the levels of Fig. 3c in the two dots. In this picture, each color corresponds to a pair of levels extracted from the ABS spectroscopy and given in the table (we use the same colors as the lines in Fig. 3c). The various orbitals were assigned to either dot to yield the most uniform level spacing in each dot, which is of course an "aesthetic" and arbitrary assumption we cast on the system. The boxes represent the pairs of levels for which we needed to take into account inter-dot coupling, to reproduce avoided crossing. In each pair the electrons are of opposite spin, but there is no preferred overall orientation. Hence, the arrows shown here only indicate the relative spin orientation of the levels, as obtained from ABS spectroscopy.

the DOS by the tunnel probe (see previous section).

From these parameters we can give a tentative picture of the ladder of levels in the two dots, as shown in Fig S2. Such a level representation is easier to apprehend than the set of apparently random lines shown in Fig 3c.

Quantum dot vs. Fabry-Pérot description

We also measured a device, shown in Fig. S3, which was better coupled to the leads than the sample analyzed in the main text (for which we had coupling Γ in the range $0.8-2.4\times\Delta$). The DOS at energies $|E|\geq\Delta$ (the continuum) shows weak modulations with the gate voltage rather than sharp features. These modulations can arise in two different regimes.

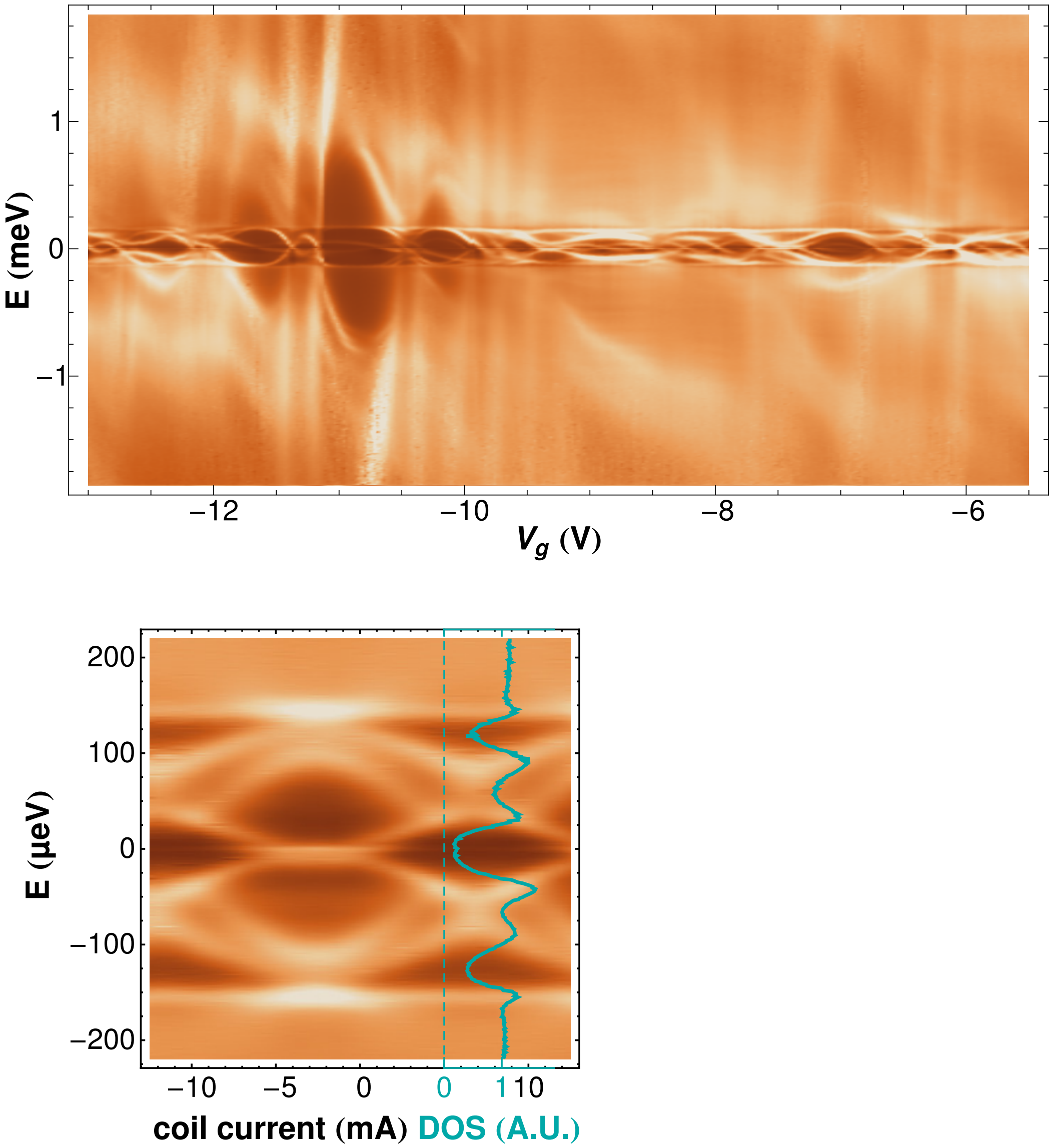

Figure S3: Top panel : Deconvolved DOS data from a different device than the one shown in the main text. We see almost everywhere more ABS in the gap, each extending on larger V_g range and overlapping with others. This indicates that the nanotube in this device was better coupled to the leads than the one in the main article. Bottom panel: flux dependence at $V_g = -6.02V$.

In the first regime, the nanotube is characterized by a continuum of states (this would be true for nanotube devices in which finite-size effects are negligible). In this situation the weak modulations of the DOS at energies above the gap are generated by Fabry-Perot interference due to weak backscattering at the two contacts. Moreover, for energies below the gap, this model predicts continuous bands of ABSs.

The second situation that can give rise to weak modulations of the DOS above the gap is that of a nanotube exhibiting discrete levels that are well separated in energy (i.e. a short nanotube behaving as a quantum dot), but also well coupled to the leads. This is the model discussed in the previous two sections. Above the gap, this model shows that the good coupling with the leads gives rise to weak modulations of the DOS: the stronger the coupling, the smoother the fluctuations in the DOS. However, inside the gap, one should see discrete Andreev levels that are not broadened by the coupling with the leads. Nevertheless, the good coupling makes the variation of the ABS energies with the gate voltage slower than in the weak coupling situation, thus the observed ABS remain within the gap for larger intervals of gate voltages and, consequently, a larger number of ABS resonances are observed at a given gate voltage.

Thus we see that, while two possible models for the nanotube can give rise to the same type of features in the spectroscopic features above the gap, inside the gap the two models give rise to very distinct features, as long as one can resolve discrete ABS. In particular, since our experimental data shows distinct ABS inside the gap, it suggests that the studied nanotube behaves as a discrete quantum dot rather than as a plain continuum of states. On the other hand, a continuum model properly including all the effects of backscattering should also be able to account for the observed features.

Our results indicate that for nanotube devices with good coupling to the leads, quantum dot models may be more broadly applicable than previously thought. This also underlines that in efforts to reveal Luttinger Liquid physics in nanotube devices, it is important to take finite-size effects and in particular discrete energy spectra into account.

Width of the resonances - Lifetime of the ABS

The analysis of the ABS linewidth in the deconvolved DOS gives a FWHM of 30-40 µeV, independent of gate voltage and flux. If this linewidth is intrinsic, it would correspond to a sub-ns coherence time of the ABS. Possible extrinsic sources for this linewidth are

- Charge or flux noise. These cannot be the dominant contribution to the linewidth since the latter is essentially independant of the flux and of the gate voltage.

- The tunneling current from the probe. The electron tunneling rate from the probe limits the lifetime of the ABS. This rate can be exactly evaluated by integrating the differential current measurements. This mechanism would give a linewidth of less than 1 μeV for all peaks shown.
- Non thermal-equilibrium voltage noise on the tunnel probe. This would smear out the measured peaks and it would also dephase the ABS by the capacitive action of the probe. The level of noise necessary to explain the observations would be somewhat higher than what was measured ($\sim 15\,\mu$eV) previously in a very closely related setup [1]. This cannot be ruled out at present, however.
- Finally, a finite residual density of states in the superconducting gap could also yield this linewidth. This can easily be included in the theory by the introduction of a Dynes depairing parameter [2], and it is exactly what we have done to produce the theoretical predictions of the DOS from the Green functions. This turns out to produce ABS linewidth independent of gate voltage and flux. The observed linewidth is qualitatively reproduced for a Dynes depairing parameter of $\sim 10-15\%$ of Δ. Unfortunately we could not check directly in this setup the density of states of the superconducting electrodes, and moreover, it is difficult to distinguish such a depairing effect from that of voltage noise [10]. Repeating such an experiment with different superconducting materials could shed some light on this issue.

For the time being, the simplest candidate explanation for the measured linewidth is the presence of uncontrolled noise in the measurement. Further investigation is clearly needed to precisely establish the origin of the measured linewidth and assess the potential of ABS as qubits.

---

[1] le Sueur, H., Joyez, P., Pothier, H., Urbina, C. & Esteve, D. Phase controlled superconducting proximity effect probed by tunneling spectroscopy. *Physical Review Letters* **100**, 197002 (2008).

[2] Dynes, R. C., Narayanamurti, V. & Garno, J. P. Direct measurement of Quasiparticle-Lifetime broadening in a Strong-Coupled superconductor. *Physical Review Letters* **41**, 1509 (1978).

[3] Wikipedia. Moore–Penrose pseudoinverse. http://en.wikipedia.org/wiki/Moore-Penrose_pseudoinverse (2010).

[4] Gräber, M. R. *et al.* Molecular states in carbon nanotube double quantum dots. *Physical Review B* **74**, 075427 (2006).

[5] Rozhkov, A. V. & Arovas, D. P. Josephson coupling through a magnetic impurity. *Physical Review Letters* **82**, 2788 (1999).

[6] Vecino, E., Martín-Rodero, A. & Levy Yeyati, A. Josephson current through a correlated quantum level: Andreev states and pi junction behavior. *Physical Review B* **68**, 035105 (2003).

[7] Siano, F. & Egger, R. Josephson current through a nanoscale magnetic quantum dot. *Physical Review Letters* **93**, 047002 (2004).

[8] Tanaka, Y., Oguri, A. & Hewson, A. C. Kondo effect in asymmetric Josephson couplings through a quantum dot. *New Journal of Physics* **9**, 115–115 (2007).

[9] Lim, J. S. & Choi, M. Andreev bound states in the Kondo quantum dots coupled to superconducting leads. *Journal of Physics: Condensed Matter* **20**, 415225 (2008).

[10] Pekola, J. P. *et al.* Environment-assisted tunneling as an origin of the dynes density of states. *Phys. Rev. Lett.* **105**, 026803 (2010).

5.2 Singlet-doublet transition observed in the TDOS

In the experimental data presented in Fig. 4 of Ref. [92], we observe the crossing of an ABS with the Fermi level around $V_{bg} = -11.35$ V. At this point, the system undergoes a singlet-doublet transition. This means that the ground state of the system changes, for increasing gate voltage, from a spin-singlet ground state (S=0) to a degenerate magnetic ground state (S=1/2) (see section 3.1.5.2). When the ground state is a singlet, the energy of the system is minimized for a superconducting phase difference between the leads δ equal to 0, whereas in the magnetic ground state the energy is minimized for $\delta = \pi$ [16, 71]. This induces a π phase shift in the phase dependence of the ABSs' energies and, as a consequence, a reversal of the supercurrent.

Reversal of supercurrent ($0-\pi$ transition) In Fig. 5.1, we have represented, on the top, the TDOS of the device measured as a function of the gate voltage for $\delta = \pi$. Below, we show two graphs of the TDOS and the supercurrent calculated, using the phenomenological model (see section 3.1 of chapter 3), with parameters[1] used in Fig. 4 of Ref. [92], for the same gate voltage range but for $\delta = \pi/2$ (the supercurrent is equal to 0 at $\delta = 0$). These calculations confirm that the crossing of an ABS with the Fermi level coincides with a brutal transition of the supercurrent from positive to negative values. This behaviour is called $0-\pi$ transition and has inspired some potential applications, such as a transistor in which the direction of a supercurrent can be reversed by adding just one electron to a quantum dot [48].

The order of magnitude obtained for the supercurrent, from our phenomenological approach, is smaller from what would be expected from the Ambegaokar and Baratoff formula[2] [93] which rather predicts 10 nA for a junction such as ours. It is however in good agreement with experimental results of Ref. [7, 8, 9, 20] where the critical currents measured are of the order of the nA.

---

[1] There is a mistake in Fig. 4 of Ref. [92]: in the top panel the experimental and predicted DOS as a function of V_g are respectively measured and calculated at $\varphi = \pi$ and not $\varphi = 0$. Moreover the φ axis in the bottom panel is shifted of π.

[2] This formula gives the critical current I_c as a function of the normal state resistance R_N of a tunnel junction and the superconducting gap $I_c = \frac{\Delta\pi}{2R_N}$.

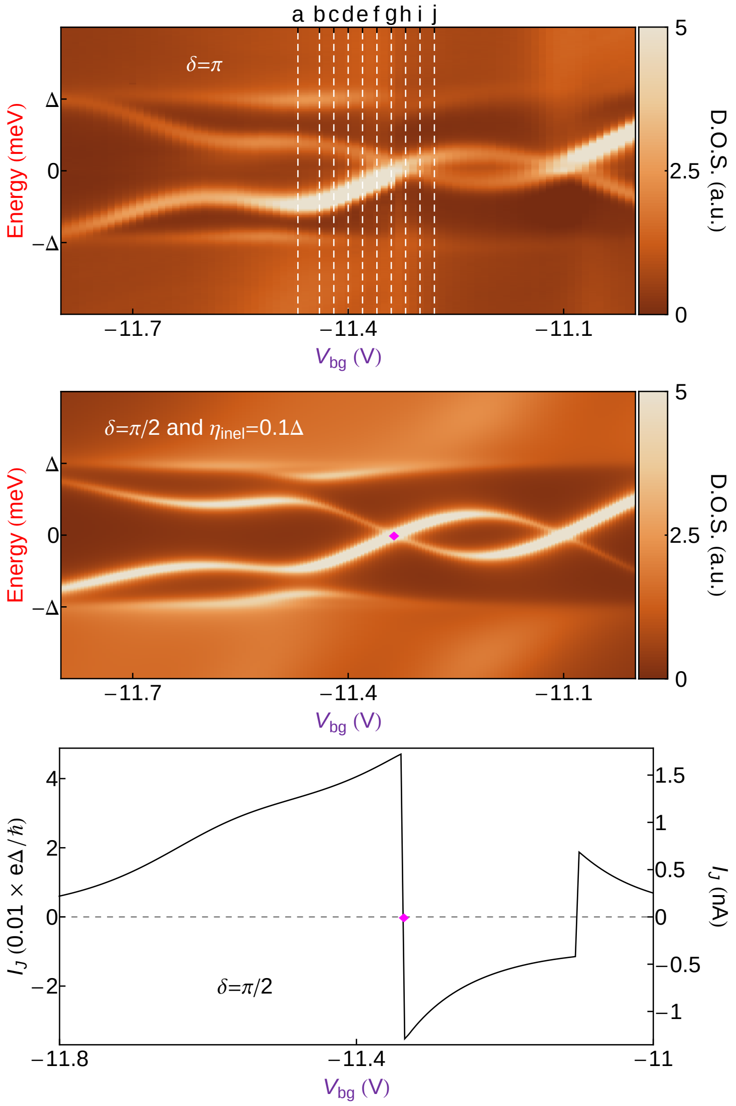

$0-\pi$ TRANSITION OF A DQD WITH PARAMETERS OF REF. [92]

Figure 5.1: The top graph represent the TDOS of the CNT plotted as a function of the gate voltage and the energy for a superconducting phase difference across the junction $\delta = \pi$. Below, we show the TDOS of a DQD connected to superconducting leads as a function of the back gate voltage obtained from the phenomenological approach of Ref. [16] with parameters used in Fig. 4 of Ref. [92]. At the bottom, we have traced the Josephson current calculated with the same parameters. Parameters are: $\delta = \pi/2$, $\Gamma_L = 2.10\Delta$, $\Gamma_R = 1.11\Delta$, $t' = \Delta$ and $\epsilon_{\uparrow(\downarrow)L(R)} = \lambda\Delta\left(V_{bg} - V_{bg\uparrow(\downarrow)L(R)}\right)$ with $V_{bg\uparrow L} = 11.65$ V, $V_{bg\downarrow L} = 11.53$ V, $V_{bg\uparrow R} = 11.382$ V, $V_{bg\downarrow R} = 11.085$ V and $\lambda = 12$ V^{-1}. We see that the crossing of the inner ABS with the Fermi level coincides with a brutal transition of the supercurrent from positive to negative values (magenta diamond). This transition is smoothed if we add a phenomenological broadening η_{inel} to the ABSs, the supercurrent magnitude remaining of the same order of magnitude though slightly reduced (this reduction has also been predicted in Ref. [94] for the case of a ballistic S-N-S junction coupled to a normal side probe).

π phase shift in the δ-dependence of the ABSs In Ref. [92], we did not performed supercurrent measurements and were thus not able to observe reversals of the supercurrent. These measurements were not possible in our setup[3]. However, we did see, in the TDOS of the CNT, the π phase shift in the δ-dependence of the ABS's energies.

This is what we show in Fig. 5.2. We have represented measurements of the TDOS as a function of the energy and the superconducting phase difference δ across the CNT. They are taken at different gate voltages indicated by the white dashed lines in Fig. 5.1. We observe up to four resonances inside the gap corresponding to two ABSs of different energy (two orbitals, each one belonging to a different QD, are involved in their formation). The outer ABS has a smaller phase dependence and merge into the continuum during the transition. The inner one has a larger δ-dependence meaning that it is carrying more supercurrent. Its energy increases when we tune δ from 0 to π and hence we have a 0-junction which means that the ground state is a spin-singlet.

Across the singlet-doublet transition, we observe the progressive intercrossing of the two inner resonances inside the gap. Eventually, when this intercrossing is complete the whole δ-dependence of the TDOS has acquired a π phase shift. We have thus a π junction. The ground state is hence a degenerate magnetic doublet. For the states in the intermediate region, conventionally designed as 0' or π' [16], the ground state depends on the superconducting phase difference δ we impose across the junction.

---

[3] As mentioned in section 3.1.5, evaluation of the QD supercurrent might be checked in the future, using a more elaborate setup giving direct access to the loop supercurrent, as was done for atomic contacts [68, 69]).

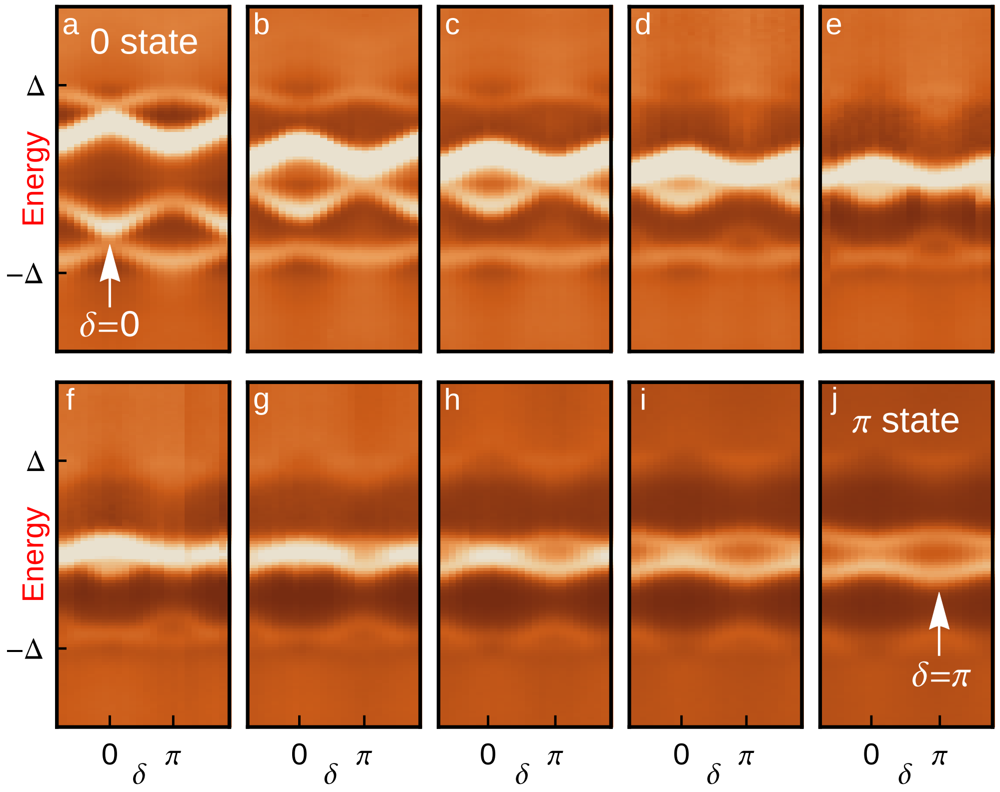

Phase dependence across the singlet-doublet transition

Figure 5.2: TDOS of the CNT plotted as a function of the energy and the superconducting phase difference δ imposed across the S-CNT-S junction. They are taken, across the singlet-doublet transition, at different gate voltages (indicated by the white dashed line of Fig. 5.1). We observe that the system, initially in a 0 state, ends into a π state after the progressive crossing of an ABS with the Fermi level. From these spectra, we can see that, when the system is in a singlet ground state (a), it is more stable when $\delta = 0$ because the inner ABS is lower in energy (as indicated by the white arrow in (a)). In contrast, when the system is in a magnetic ground state (j), the system is more stable for $\delta = \pi$ (see white arrow in (j)).

Chapter 6

Measurement of the flux sensitivity of our devices

In this chapter of the thesis, we study the magnetic flux sensitivity of our devices. The latter have indeed current-voltage characteristics that depend on the flux enclosed inside their loops, these behaviours relying on the phase-dependence of the ABSs' energies.

Our devices work thus as flux-tunnel current transducers showing flux noise down to $5.10^{-5}\phi_0/\sqrt{\mathrm{Hz}}$. As in Ref. [8], thanks to CNTs' aspect ratios, such device should be able to detect the reversal of the magnetic moment of single nanometer-sized particles or single molecules. They are moreover easier to operate than devices of Ref. [8] since they can be read through a simple DC measurements of the current, as in Ref. [95].

Here, we discuss the principle of detection of a small signal generated by variation of the magnetic field. Then we present our measurement technique to evaluate the devices' flux noise. Finally we explain how we optimize, with gates, the operation point of our devices and discuss their performances as well as the limiting sources of noise of our CNT-based magnetometer.

6.1 Principle of detection

The detection principle of our CNT device is based on the flux dependence of ABSs' energy. As previously explained (see section 4.1), the flux Φ enclosed by the superconducting loop imposes a superconducting phase difference across the CNT. Since the phase difference determines the energy position of ABS, a flux variation will modify the CNT TDOS. In this sense our device constitutes a flux-tunnel current transducer.

In Fig. 6.1, we show two current-voltage characteristics measured at

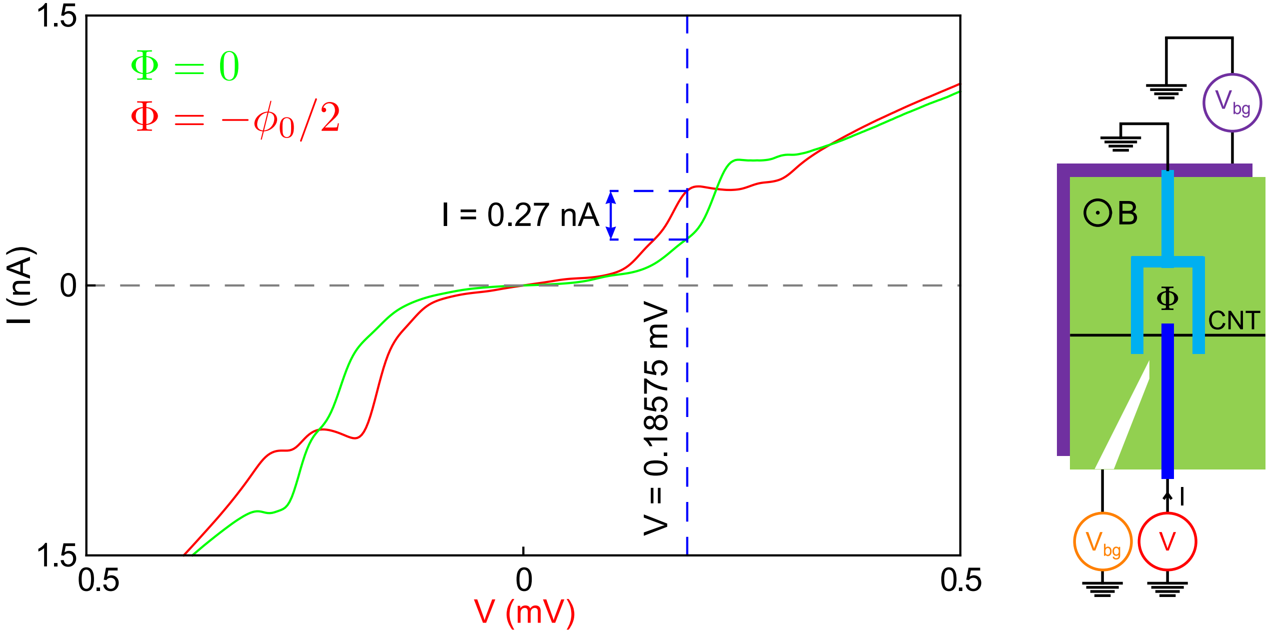

I-V CHARACTERISTICS FOR DIFFERENT FLUX

Figure 6.1: In red and green are shown I-V characteristics of our device respectively for a flux inside the loop Φ equal to $-\phi_0/2$ and 0. At voltage bias $V = 0.1875$ mV, the variation of tunnel current reaches 0.27 nA. On the right, a schematic of the CNT-based device is represented with the DC sources connected the tunnel probe and the gates. Orientation of the magnetic field B is indicated.

35 mK for different values of the applied flux. At given voltage bias V, a current variation ΔI is induced when Φ is changed of half a flux quantum. The detection of a variation of the magnetic field relies on this property of the device.

6.2 Definition of the flux sensitivity

We define the flux sensitivity of our device as the smallest signal (generated by a magnetic flux variation) we can detect within a bandwidth δf. This limit is given by the flux noise $S_\Phi \delta f$, expressed in ϕ_0^2, where S_X is the power spectrum of the noise on X. It constitutes thereby the relevant figure of merit to characterize performances of our device as a flux sensor.

If I_N is the intrinsic current-noise of the device in the bandwidth δf, the equivalent flux noise is given by:

$$S_\Phi \delta f = \phi_0^2 S_{I_N} \times \left(\frac{dI}{d\Phi} \right)^{-2}$$

The flux sensitivity is therefore optimum when the flux-tunnel current transfer function $\frac{dI}{d\Phi}$ is maximum and the current noise is minimum.

In the following, we describe the setup we use for measurements of the transfer function $\frac{dI}{d\Phi}$. Then we explain how we maximize the latter. And finally we evaluate the flux noise of our device S_Φ and discuss its performance as a magnetic flux sensor.

6.3 Setup

In order to measure the differential flux-tunnel current transfer function, we use Lock-In measurement techniques described in section 4.2. The setup, represented in Fig. 6.2, combined $\frac{dI}{d\Phi}$ and $G = \frac{dI}{dV}$ measurements.

For G and $\frac{dI}{d\Phi}$ measurements, two Lock-In Amplifiers (LIA), operating at different frequencies, generate two AC excitations (respectively V_{AC} and $V_{AC}^{'}$), each one being subsequently combined with a DC voltage (respectively V_{DC} and $V_{DC}^{'}$) generated with a programmable DC source 7651 from Yokogawa. One of the composite signal is applied on the tunnel probe for G measurement, whereas the other is applied, through a 200 Ω resistor, on a superconducting coil, inside the fridge and underneath the sample, for $\frac{dI}{d\Phi}$ measurements.

The resulting current flowing through the sample is amplified by the current to voltage converter (see Fig. 4.2) and the output signal is then fed to

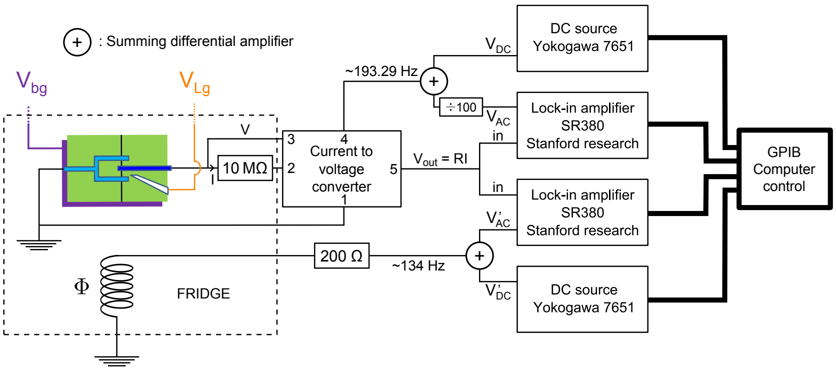

Figure 6.2: Schematic of the measurement setup

the inputs of the two LIAs for independent narrow band measurements of $\frac{dI}{d\Phi}$ and G, respectively at 134 Hz and 193.29 Hz.

6.4 Maximization of the flux-tunnel current transfer function $\frac{dI}{d\Phi}$

As mentioned in section 6.2, the flux sensitivity of our device is optimized when the flux-tunnel current transfer function $\frac{dI}{d\Phi}$ is maximized. Similarly to the differential conductance G, it depends on the bias voltage V applied across the device, the flux Φ enclosed inside its loop, and the gate voltages V_{bg} and V_{Lg}. In order to find the optimum operating point, one has thus to measure $\frac{dI}{d\Phi}$ as a function of these four parameters at the same time, a procedure which is highly time-demanding.

We can however find a quicker method. In our sample, at a fixed V_g, the flux variation of an ABS is maximum around $\phi_0/3$. At this magnetic flux, the position in energy of an ABS is generally around $\Delta/2$. So, to roughly map regions with high flux sensitivity in the (V_{bg}, V_{Lg}) plane, we DC biased the device at $\Phi \approx \phi_0/3$ and $V \approx \frac{3}{2}e\Delta$ (voltage corresponding to $\Delta/2$ of the deconvoluted DOS) and sweep V_{bg} and V_{Lg}. Thereafter, we fixed V_{bg} and V_{Lg} at the highest $\frac{dI}{d\Phi}$ and we measured the flux-tunnel current transfer function as a function of V and Φ in order to find the the best operating point.

In Fig. 6.3, we show measurements of the differential conductance G and the flux-tunnel current transfer function $\frac{dI}{d\Phi}$ (respectively the upper and lower graphics). They are taken in the superconducting state, at low magnetic field and at 35 mK, as functions of V_{bg} and V_{Lg} at $V = 0.2$ mV and $\Phi \approx \phi_0/3$.

In differential conductance measurements, areas of low conductance appear in violet, areas of negative conductance in dark violet and areas of high conductance in white. These measurements resemble those obtained in the normal state (see chapter 7) except that ABSs appear much thinner than normal resonant levels of the CNT. In the inset with the thick orange frame, we have zoomed on the area indicated by the dashed orange frame where ABSs of the left and right QD meet each other to form avoided crossings. Such pattern is a manifestation of the coupling between the left and right QD which happens when they are both in resonance. This situation is favorable for the flow of supercurrent between the left and right electrodes of the fork, and therefore for a large Φ-dependence. However, we do observe also large flux dependence, though smaller, in situations where one of the dot in not necessarily at resonance.

Below, flux-tunnel current transfer function measurements show that, in this situation, the tunnel current variation induced by the flux excitation is maximum. This is the expression of a large flux-dependence of the ABSs, or equivalently a large supercurrent circulating in the loop formed by the fork and the CNT. In the thick yellow frame, we have represented a zoom on the same area than before but for the $\frac{dI}{d\Phi}$ measurements. The large yellow point indicates where we have chosen to optimize $\frac{dI}{d\Phi}$ adjusting V and Φ: at the avoided crossings formed by the ABSs ($V_{bg} = 10.96$ V and $V_{Lg} = -2$ V).

In Fig. 6.4, we have represented the dependence with V and Φ of the differential conductance and flux-tunnel current transfer function measurements at this operating point. As expected, we see that $\frac{dI}{d\Phi}$ is close to zero where the ABSs have no flux dependence and is maximum where the ABSs energies are strongly phase dependent. A maximum value of $\frac{dI}{d\Phi}$ is obtained at $\Phi = 0.32\phi_0$ and $V = -0.1875$ mV and reaches 1.6 nA/ϕ_0.

In the following, we evaluate the flux sensitivity of our device at this optimal point by measurement of the flux noise with a spectrum analyzer.

6.5 Flux noise measurements

In Fig. 6.5, we show the noise spectrum from 10 to 1610 Hz of the output signal of the current to voltage converter (CVC, see Fig. 6.2), measured at the operating point indicated by the brown dot in Fig. 6.4 ($V_{bg} = 10.96$ V, $V_{Lg} = -2$ V, $\Phi \approx 0.32\phi_0$ and $V = -0.1875$ mV). The AC flux excitation, controlled with V'_{AC}, is taken with an amplitude equal to $0.01 \times \phi_0$ with a frequency equal to 134 Hz. Yet, we don't send any AC excitation directly on the tunnel probe (*i.e.* $V_{AC} = 0$).

On the tunnel current noise spectrum, we observe a peak at 134 Hz corresponding to the AC flux excitation we send to the coil, and a noise floor between $\sim 10^{-12}$ and $\sim 10^{-11}$ V^2/Hz. This noise floor is partly due to intrin-

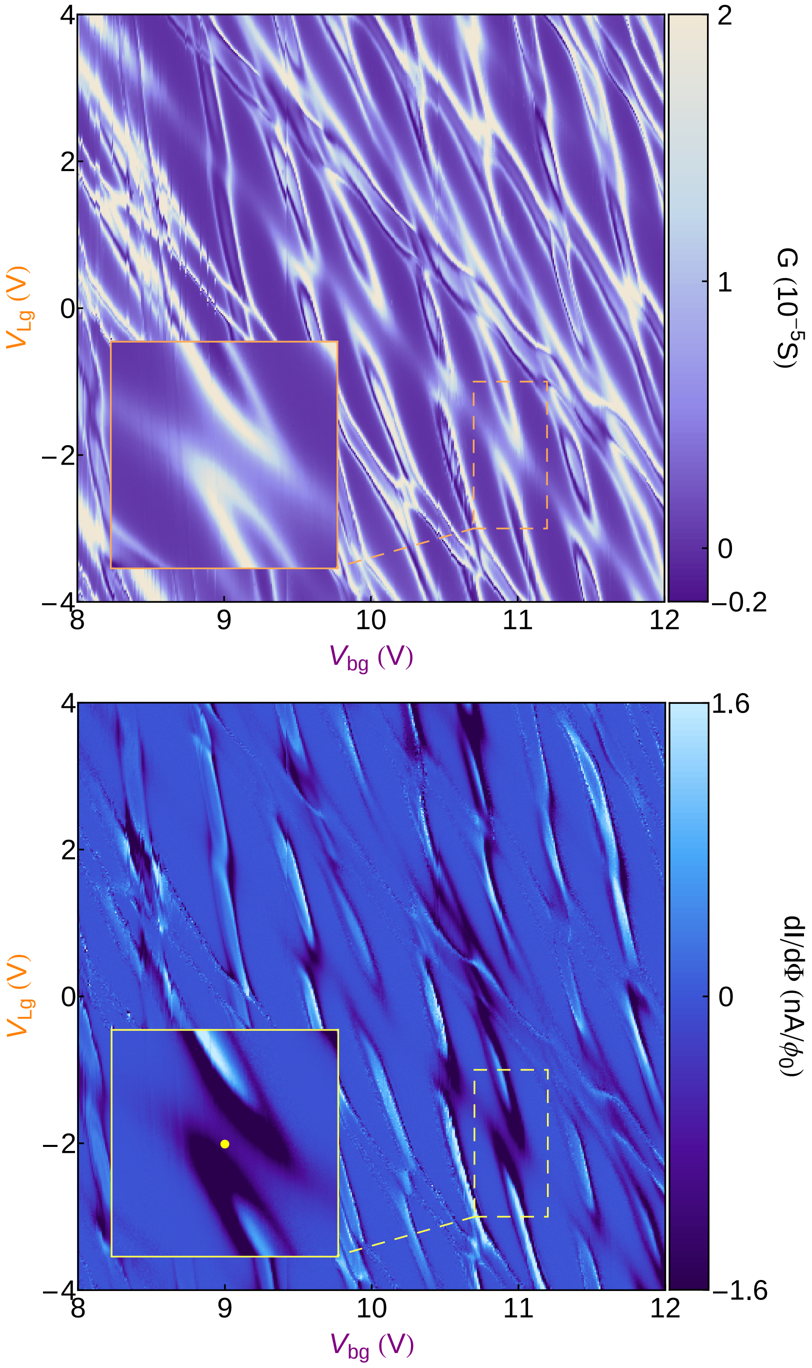

Figure 6.3: Colorplots of the differential conductance (upper graphic) and flux-tunnel current transfer function (lower graphic) measured as functions of V_{bg} and V_{Lg}, with $V = 0.2$ mV and $\Phi \approx \frac{1}{3}\phi_0$. In orange and yellow frames, we have zoomed on a region where ABSs of the left and right QDs of the device meet and form an avoided crossing. This yields a high flux dependence of the tunnel current and is favorable for detection of small magnetic flux variation inside the loop of the device. The yellow point indicates the operating point where measurements of Fig. 6.4 were taken.

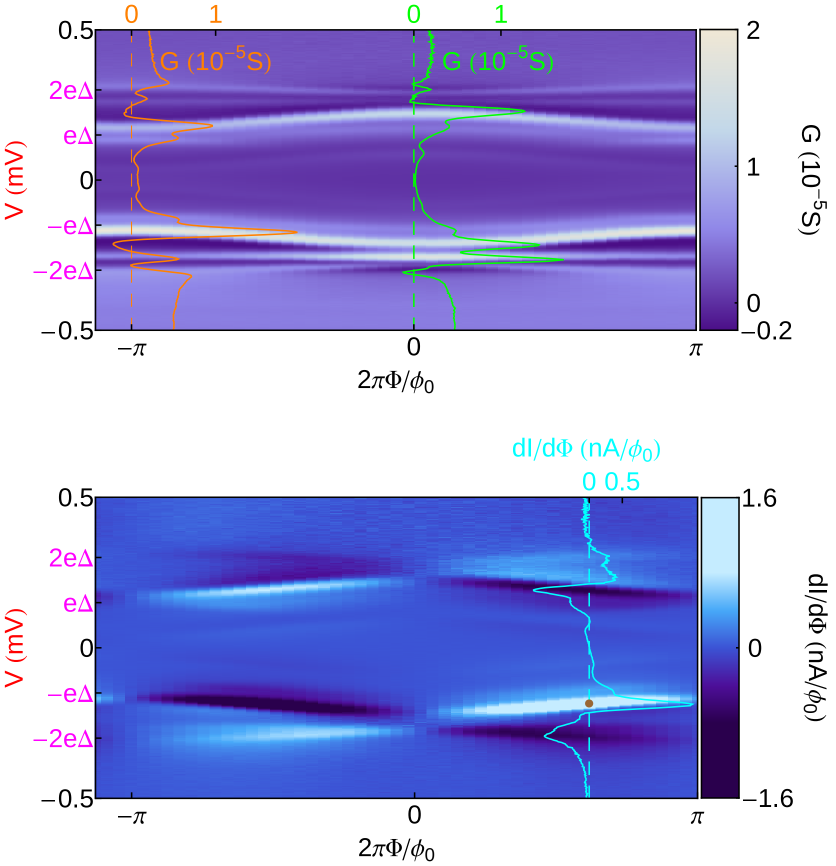

Figure 6.4: Colorplots of the differential conductance (upper graphic) and flux-tunnel current transfer function (lower graphic) measured as functions of the voltage bias across the device V and the flux inside the loop Φ. In differential conductance measurements, two cuts are represented at $\Phi = 0$ and $\Phi = -\phi_0/2$ where the ABSs' energies reach their extreme positions. In flux-tunnel current transfer function measurement, a cut is represented at $\Phi \approx 0.32 \times \phi_0$ where we obtain our largest $\frac{dI}{d\Phi}$. The brown point indicates where the spectrum of Fig. 6.5 was taken.

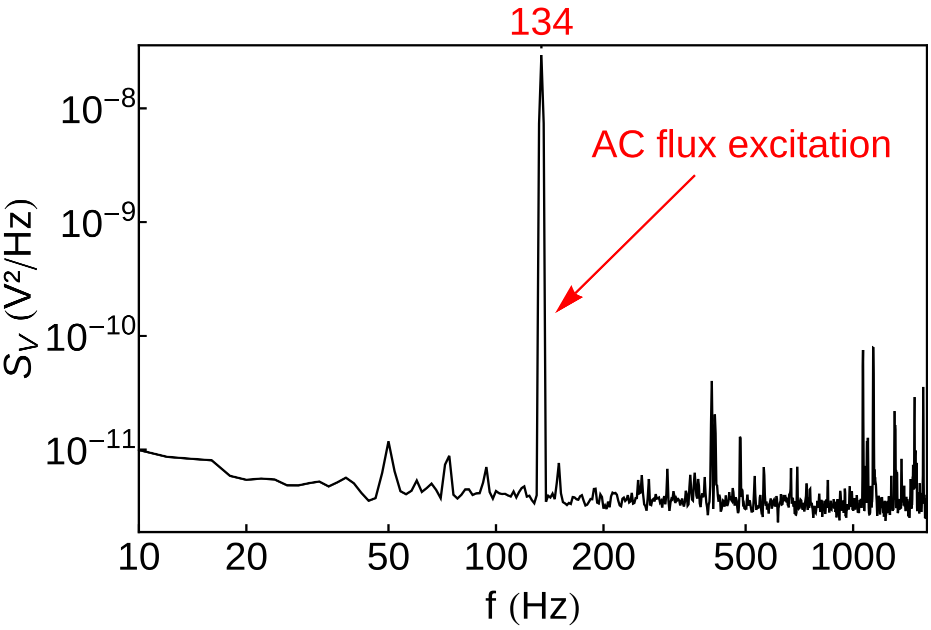

Spectrum analyzer measurement of the output signal

Figure 6.5: Graph representing the density of noise of the output signal of the CVC, when an AC excitation at 134 Hz with an amplitude corresponding to $0.01 \times \phi_0$ is send to the coil below the sample and generating the magnetic field. A peak is clearly visible at 134 Hz and there is a noise floor between 10^{-11} and 10^{-12} V^2/Hz. This noise floor gives the limit of flux sensitivity S_Φ of our device.

sic charge noise of the device which depends experimentally on gate voltages, but the principal source of noise in our device is the shot noise [36]. Indeed, when biased, the device carries a current of quasiparticle which induces noise (because of the discrete charge of the carriers) proportional to the current amplitude. Therefore, as can be seen in Fig. 6.6, this noise increases with the bias voltage applied across the device.

In Fig. 6.5, at the bottom of the AC flux excitation peak, this noise floor reaches $S_V = 3.10^{-12}$ V^2/Hz. As we know that the peak is induced by an excitation with a RMS amplitude corresponding to $0.01 \times \phi_0$, it gives us a benchmark to convert this voltage noise in its equivalent flux noise. The integral below the peak being equal to 10^{-7} V^2, the flux noise at 134 Hz of our device $S_\Phi^{1/2}$ is equal to:

$$S_\Phi^{1/2} = \sqrt{\frac{(0.01 \times \phi_0)^2}{\langle V_{ex} \rangle^2} S_V} = 5.10^{-5} \phi_0 / \sqrt{\mathrm{Hz}}$$

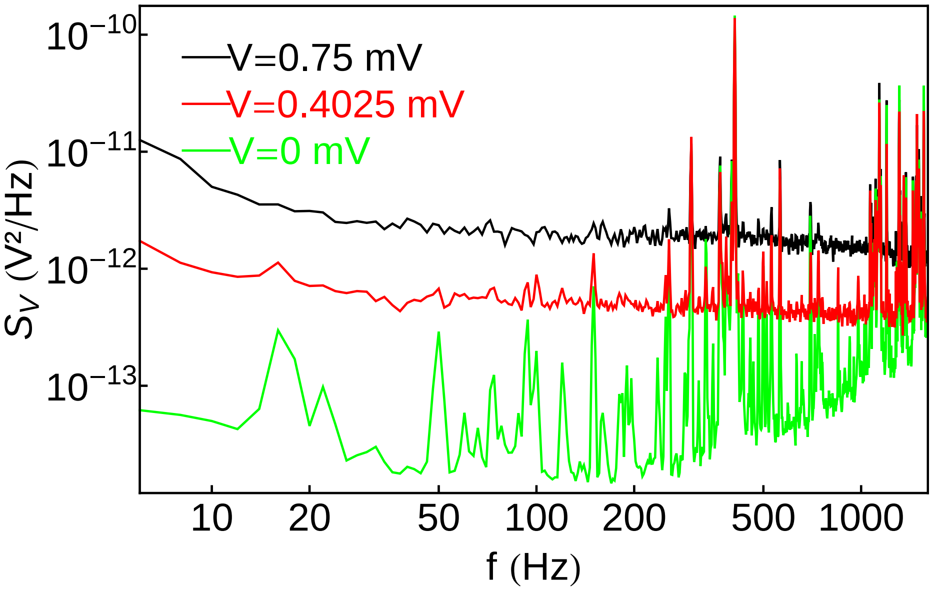

Voltage dependence of the noise floor

Figure 6.6: Noise floor of the device measured with a spectrum analyzer for different voltage bias applied between the tunnel probe and the grounded superconducting loop. The fact that the noise increases with the quasiparticle current carried by the device is an indication that the noise floor may be partly due to shot noise.

Our flux sensitivity is therefore low enough to detect in less than 1 s a flux variation of $10^{-4}\phi_0$.

Part III

Second experiment: exploring Kondo and Andreev Bound States in a Double Quantum Dot

In confined quantum conductors, Coulomb repulsion between electrons may lead to the localization of one or several electrons and consequently to a many-body effect called the Kondo effect (see appendix A). It occurs when these localized electrons, forming an artificial magnetic impurity, are coupled to electrodes with continuous density of states. Through cotunneling spin-flip processes, conduction electrons of the leads screen the spin of the localized electrons resulting in a many-body singlet state. When the impurity has a 1/2 spin, the Kondo effect manifests by a peak at the Fermi level in the density of states (DOS) of the QD. The most spectacular experimental consequence of this effect is the opening (for symmetrically contacted QD) of a perfectly transmitted conduction channel at the Fermi level (with a conductance of $2e^2/h$) for temperature well below the so-called Kondo temperature T_K.

Carbon nanotube-based electronic devices generally exhibit Kondo effect when cooled down at temperatures reached in a cryogenic fridge [96, 97]. Like semiconductor heterostructures, nanowires or molecular devices, these coherent quantum conductors have thereby offered the opportunity to explore, in a controlled way, various type of Kondo effects[1] with electronic transport experiments. As spins of electrons play an important role in these phenomena, they are strongly affected by an eventual spin ordering inherent to the electrodes or the quantum conductor. The various nature of the electrodes that can be contacted to carbon nanotubes (CNT) or nanowires has thereby motivated many experimental realizations aiming to explore the interplay between Kondo effect and ferromagnetism [98, 99] or BCS superconductivity [5, 9, 10, 14, 18, 19, 20, 21, 100]. Otherwise, in certain situations, a local spin ordering takes place directly in the QD by formations, for example, of singlet or triplet states between electrons belonging to different orbitals [101, 102], or different part of the conductor when the latter behaves as a double quantum dot (DQD). This second situation can be achieved either by defining several coupled quantum dots during fabrication [103, 104, 105, 106, 107, 108] or in presence of a parasitic magnetic impurity [11, 109]. Whether the spin ordering forms in the leads or the QD, the Kondo effect is modified compared to the spin-1/2 Kondo state and, sometimes, even suppressed.

In this part of the thesis, we present tunneling spectroscopy measurements, in the normal and superconducting states, performed on a CNT-based device with several gates coupled to the sample. This experiment was following the one presented in part II and realized for two different purposes. First, we were able to verify the DQD behaviour of our device using external gates which were lacking in the previous experiment. Secondly, as parameters extracted from measurements of part II suggested that our sample should have

---

[1] See for example references indicated in section A.5.2.

Kondo temperature (between 0.5 and 2K) higher than the base temperature of our fridge (35 mK), we took measurements in the normal state in order to observe how Kondo effect develops in our samples. The results we obtained shed light on the interplay between Kondo effect and two phenomena that lead to different type of spin orderings: exchange between two QDs and BCS superconductivity induced in the CNT by proximity effect.

In chapter 7, we show experimental results proving the DQD behaviour of our sample and comment the role of microscopic parameters. Then in chapter 8, we analyze the interplay between Kondo effect and superconductivity within a single effective QD. Finally in chapter 9, we focus on effects that are inherent to the DQD behaviour of our device and discuss in particular splittings of the Kondo resonance that we observe in our sample.

Chapter 7

Proof of Double Quantum Dot behaviour

In the previous part, interpretation of our measurements was based on the supposition that our CNT-based device behaves as a double quantum dot (DQD). We supposed that the tunnel probe splits the CNT into two coupled QDs. Other experiments realized on three terminals devices based on a single CNT [105, 108] have already shown the DQD behaviour of such structures and motivated a theoretical proposal of a scheme for a spin quantum bit based on a DQD contacted with ferromagnetic leads [110].

In this chapter, we present TDOS measurements, taken in the normal state and at 35 mK, of a CNT-based device with multiple gates (see Fig. 7.1). A single and a double QD show qualitatively distinct behaviour. In a DQD, if the gates are coupled differently to the two dots, the stability diagram shows two families of parallel lines, each one reflecting the addition of electrons in one of the QD. Therefore, measuring the TDOS as a function of the gate voltages, we can demonstrate the DQD behaviour of our device.

In section 7.1, we first show the charge stability diagram of the device and explain why the different features we observe are consistent with a system of two coupled QDs. We will discuss the role of each parameter characterizing our device (see Fig. 7.1). Then in section 7.2, we show that we obtain a satisfactory agreement between our measurements and TDOS of a DQD obtained within a self-consistent mean-field approximation on the intradot Coulomb repulsion. It yields, in particular, a correct description of the role of the interdot coupling in contrast to the phenomenological approach presented in chapter 2.

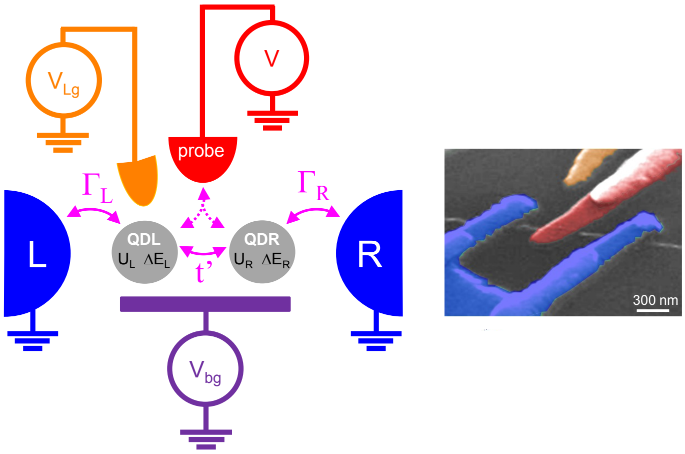

Figure 7.1: Schematic representation of the system with its parameters (left) and SEM picture with false colors of a typical sample (right). The behaviour of the device can be characterized by exchange rates with the left (resp. right) leads $\Gamma_{L(R)}$, charging energies $U_{L(R)}$, energy difference between orbitals $\Delta E_{L(R)}$ and the coupling t' between the left and right dots (QDL and QDR). These parameters are orbital dependent and vary with the gate voltages. We measure the TDOS of the CNT with a tunnel probe (in red) that is weakly coupled to the device.

7.1 Charge stability diagram of a DQD

In Fig. 7.2, we have represented the charge stability diagram of the device. It maps the CNT's TDOS measured at the Fermi level of the electrodes (*i.e.* $V = 0$ on the probe) as a function of V_{Lg} and V_{bg}. Here, we discuss in detail the pattern we observe.

Electronic levels of the left and right dot In the upper graph that shows the raw data, we see that the TDOS resembles a diamond pattern with pairs of bright lines running mainly in two directions and forming avoided crossings. Below, in the lower graph, we have superimposed the same data with two sets of orange and green parallel lines. The latter correspond schematically to a typical TDOS we expect in absence of coupling between the dots (coupling by exchange of electrons, or capacitive coupling), whether they are in sequential [111, 112] or coherent [107, 108] regime. When an electronic level of one of the dots is at resonance with the Fermi level of the electrodes, a current can flow between the probe and the fork giving rise to a peak of conductance. As the right dot is more weakly influenced by V_{Lg} than V_{bg} and the left QD is more evenly affected by V_{Lg} and V_{bg}, slopes of the lines allow to identify that green lines correspond to electronic levels of the right dot, whereas orange lines to those of the left dot.

Even-odd alternation These lines are separated by Coulomb blockaded areas, or valleys, in blue. In this regions, none of the dots are at resonance but rather at a stable charge state. As distances between these lines are related to addition energies of the dots (see section A.3), we can identify the parity of these valleys. For an odd occupancy, addition of an electron costs a charging energy $U_{L(R)}$ due to repulsion between electrons. For an even occupancy, as the last occupied orbital is already filled, the addition energy is given by the charging energy plus the energy difference between orbitals $U_{L(R)} + \Delta E_{L(R)}$. In Fig. 7.2, two levels with opposite spins belonging to same orbital appear therefore as a neighboring pair. The large blue pockets between pairs of lines define regions where dots are in an even-even configuration, whereas a pair of lines delimits regions where occupancy of the corresponding dot is odd (as indicated in the lower graph of Fig. 7.2).

Levels width When the temperature k_BT is negligible compared to the coupling to the leads $\Gamma_{L(R)}$ (as in our experiment, see next chapter), the sharpness of the resonances emphasized, for each orbitals, the strength of the coupling to the electrodes [56, 113]. Thin sharp lines correspond to

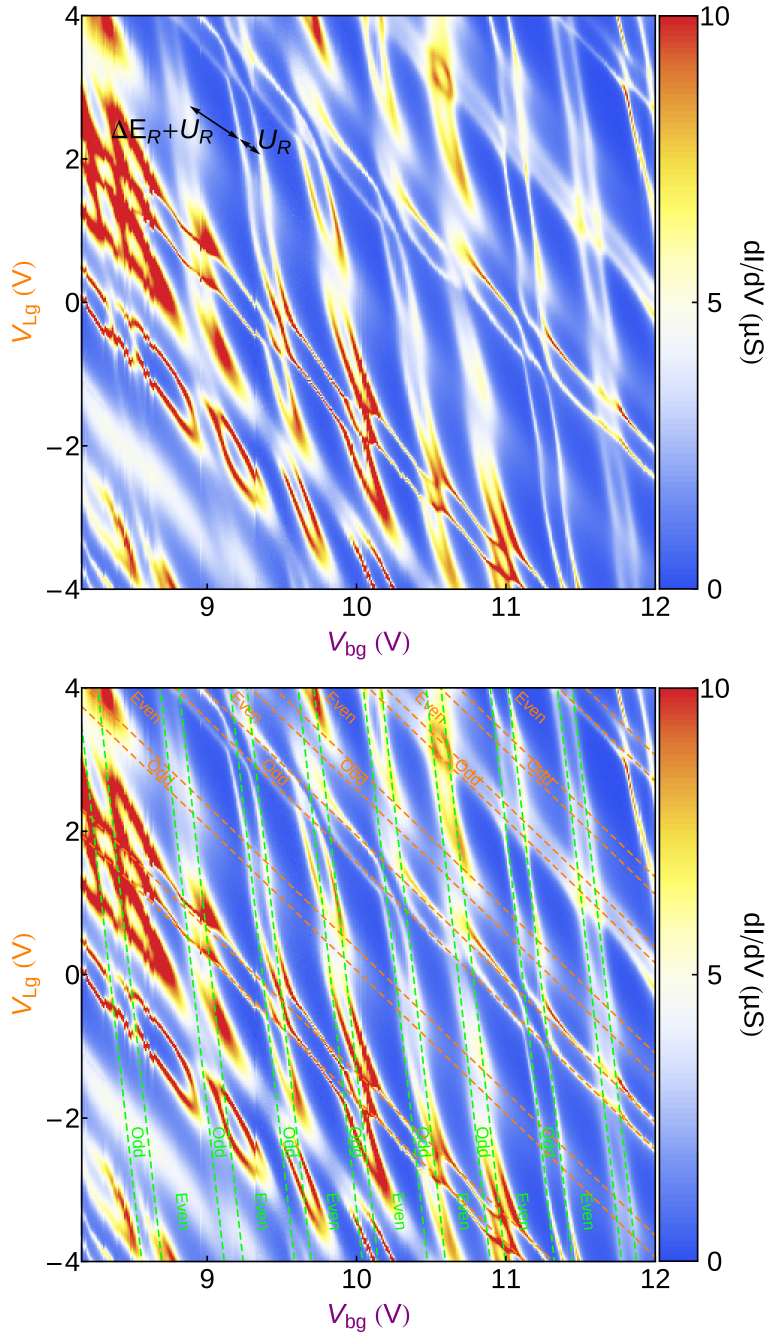

Figure 7.2: Colorplot of the CNT TDOS (represented twice) measured, in the normal state, at $V = 0$ as a function of V_{Lg} and V_{bg} and showing the DQD behaviour of the device. The upper graph shows the raw data. On the lower graph, we have added guides to the eyes showing electronic levels of the isolated QDs (in absence of coupling, *i.e.* $t' = 0$). Orange (resp. green) lines highlight to resonances of the left (resp. right) QD. Distances between lines are proportional to the addition energy $U_{L(R)}$ for odd valleys and $U_{L(R)} + \Delta E_{L(R)}$ for even valleys. The avoided crossings reveal the interdot coupling by electron exchange.

weaker coupling and large fuzzy lines to strong coupling. We also observe that two levels of a pair sometimes connect forming a wide single band. This may be due to a Kondo resonance. We will not discuss Kondo effect, here, but it will be addressed in the next chapter.

Avoided crossings When electronic levels of two different orbitals meet, in the (V_{bg}, V_{Lg}) plane, they generally (but not always) form an avoided crossing. This behaviour underlines the coupling between the dots. The usual electrostatic approach[1] [111, 112] or the phenomenological model presented in chapter 2 fail to describe all the features of the avoided crossings we observe. In the next section, we propose another approach based on a self-consistent mean-field approximation on the intradot Coulomb repulsion.

7.2 Description of the avoided crossings in the stability diagram

7.2.1 Mean-field approximation on the Coulomb repulsion

The phenomenological approach of section 3.1.4 does not capture the appearance of avoided crossings because the Coulomb repulsion was taken into account with a phenomenological splitting that forbids spin fluctuations of electrons in QDs. Levels of opposite spin, belonging to different QDs, remains thus uncoupled when electrodes are in their normal state (they are however coupled by superconductivity). As a consequence, they simply cross each other in the stability diagram whatever the value of t'.

Following Bruus and Flensberg [65], we can take into account correlations, due to Coulomb repulsion inside the DQD performing a self-consistent calculation of the DQD occupancy within a mean-field approximation. We do not describe in detail this approximation here but send the reader to appendix E.

This approach renders correctly the pattern observed (see Fig. E.2 of annex E). Like in the electrostatic classical approach, regions corresponding

---

[1] Actually, the electrostatic approach does predict avoided crossing for capacitive coupling between dots (the honeycomb lattice). However, the latter is *a priori* small compared to the other parameters in our device [105]. Moreover, it is predicted to give rise to angular avoided crossings whereas they are rather smooth in our data. Furthermore, the hopping between dots is necessary in the model to interpret the phase dependence of the ABSs shown in previous chapter; if $t' = 0$ the loop is open and there is no phase dependence.

to different charge states are separated by frontiers corresponding to conductance peaks. However this coherent approach allows to understand the width of these frontiers and the fact that the latter are rounded rather than angular as in an electrostatic approach [111, 112] (see Fig. E.1 and E.2 of annex E).

7.2.2 Interdot couplings

This approach confirms that the avoided crossings we observe are indeed induced by the interdot coupling. They occur near points where the levels would cross in absence of interdot coupling t', that is to say where the orange and green dashed lines cross in the lower graph of Fig. 7.2. Because of interdot coupling t', the levels hybridize to form bonding and antibonding energy levels.

In Fig. 7.3, we have shown a zoom of Fig. 7.2 on a particular avoided crossings. These data can be reproduced using the theoretical approach developed in annex E. As shown in Fig. 7.3, results obtained theoretically are in reasonable agreement with experiment for an interdot coupling approximately equal to $t' \approx 0.5$ meV. To extract this value, we have actually anticipated on next chapter where we explain how to convert gate voltages in energy thanks to measurements of the Coulomb diamonds (see Fig 8.4 below).

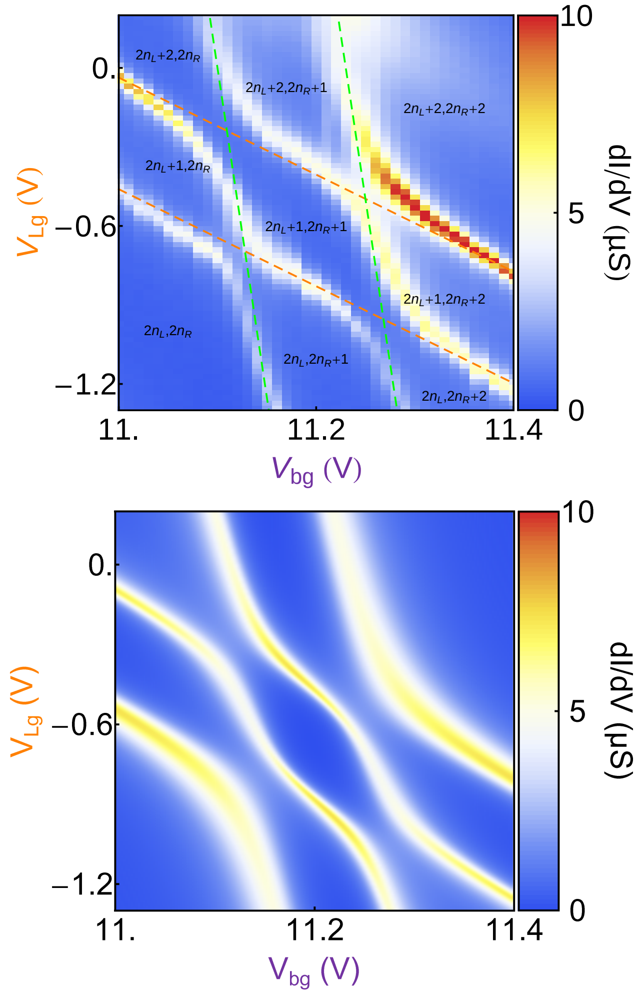

Comparison between experiments and self-consistent theory

Figure 7.3: The upper graph represents a zoom on the stability diagram of Fig. 7.2. The dashed green and orange lines show the supposed trajectories of the electronic levels for $t' = 0$. We have also indicated the charge state of the valleys. The lower graph represents the TDOS of the DQD calculated within the theoretical approach described in annex E. We can see that this approach describes the avoided crossings observed experimentally. Parameters are: $\Gamma_L = 0.15$ meV, $\Gamma_R = 0.25$ meV, $t' = 0.5$ meV, $U_L = 1.35$ meV, $U_R = 1.1$ meV, $\epsilon_L = 64.5$ meV and $\epsilon_R = 99.9$ meV.

Chapter 8

Kondo vs superconductivity in single QD

Kondo effect and superconductivity are often argued to develop a delicate interplay (and sometimes a competition) in QDs [22, 23, 24, 25, 114, 115]. This is because the conduction electrons of the leads are condensed into spin-singlet Cooper pairs (S=0) which cannot participate to spin-flip processes responsible of the Kondo effect (see section A.5), and also because the superconducting gap induced by the leads in the QD suppresses the Kondo peak. This interplay was explored in several experiments performed on S-QD-S junctions, with visible Kondo effect when the leads are driven into their normal state. They consisted either in electronic transport (for example with nanotubes, nanowires, etc...)[5, 9, 10, 14, 18, 19, 116], or in tunneling spectroscopy experiments (molecules adsorbed on superconducting surface)[21]. Interpretations of these experiments are not direct: the former are realized far from equilibrium and the latter suffer from a lack of controllable parameters (the chemical potential, for example, cannot be controlled).

In this chapter, we analyze the interplay between superconductivity and Kondo effect through the tunneling spectroscopy of the Andreev Bound States (ABSs) in a CNT. We measured the TDOS of our DQD-device maintaining one of the QD in an even charge state. This way, we obtain the TDOS of an (effective) single QD isolated from the other one. Comparing measurements taken in the normal (N) and superconducting (S) state, we get a direct observation of the interplay between superconductivity and Kondo effect. This observation leads however to the conclusion that Kondo effect doesn't change qualitatively the formation of the ABSs in our range of parameters neither determine whether the system's ground state is a spin-singlet or a magnetic state (see section 3.1.5.2).

8.1 TDOS of an effective single QD

In this section, we focused on the particular regions of the (V_{bg}, V_{Lg}) space, or stability diagram, depicted in Fig. 8.1. We present measurements taken along the black dashed lines of the stability diagrams, parallel to the levels of QDR, as a function of the gate voltages and the voltage applied on the probe V. Along this lines, one of the dots is maintained in an even charge state (*i.e.* "out of resonance"). Therefore, these measurements yield the spectroscopy of the other dot that is quasi-isolated from the other dot. We will compare measurements taken in the normal and the superconducting state in order to figure out whether or not we see a signature of Kondo effect in the ABSs.

8.1.1 Comparison between measurements in the Normal and Superconducting state

8.1.1.1 N state measurements

Upper graphs of Fig. 8.2 and 8.3 show tunneling spectroscopy measurements taken along the black dashed lines of Fig. 8.1 as function of the voltage applied on the probe and the gate voltages. Along these trajectories, the left and right QDs are effectively isolated from each other.

In those measurements, we observe diamond-shaped valleys of blockade in blue where the dot is in a well-defined charge state (QDL in Fig. 8.2 and QDR in Fig. 8.3). Alternation between small and large diamonds emphasizes the succession between even and odd occupancies of the dot. Indeed, as discussed in previous chapter and in appendix A (section A.3.2), widths and heights of the diamonds correspond to the addition energy (allowing to convert gate voltages into energy, see Fig. 8.4). For odd occupancy, the latter is given by the Coulomb repulsion between electrons $U_{L(R)}$, whereas for even occupancy the energy difference between orbitals $\Delta E_{L(R)}$ adds as the last occupied orbital is full. From diamonds of Fig. 8.2 and 8.3, we evaluate charging energies of $U_R \approx 1$ meV and $U_L \approx 2$ meV, and energy differences between orbitals of $\Delta E_R \approx 2$ meV and $\Delta E_L \approx 3$ meV. The overall pattern, called the Coulomb diamonds, is well known and routinely observed in experiments on single QDs (see references of appendix A).

In even valleys, the TDOS is suppressed around $V = 0$. In contrast, in odd valleys, we observe the formation of resonances, the so-called Kondo ridges. The widths of these resonances give the Kondo temperatures (see appendix A). Extraction of the latter are discussed in section 8.1.2.

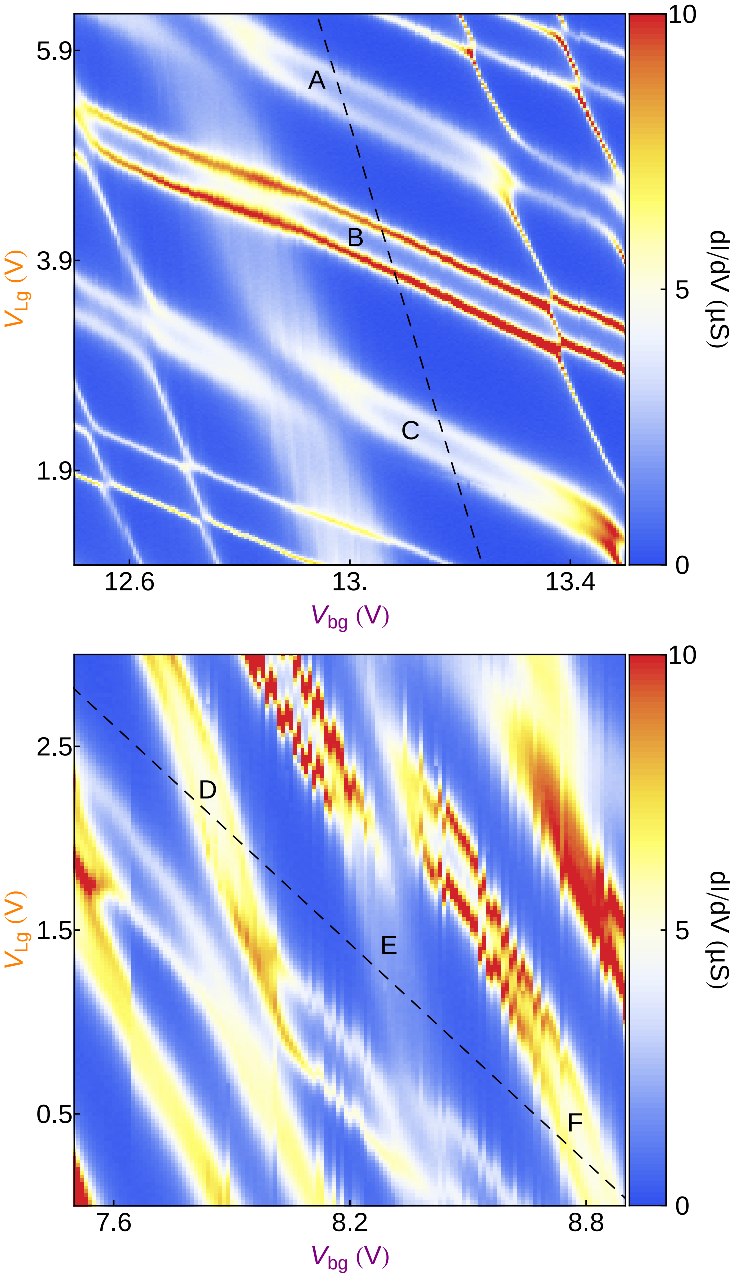

Stability diagrams

Figure 8.1: Color scaled measurements of the TDOS in the N state in two different regions of the (V_{bg}, V_{Lg}) plane. The black dashed lines indicate the trajectories followed in Fig. 8.2 and 8.3. Along them the right and left dot are maintained in an even charge state in order to perform the spectroscopy of effective single QDs. A, B, C, D, E and F are Kondo ridges we will analyze in the following.

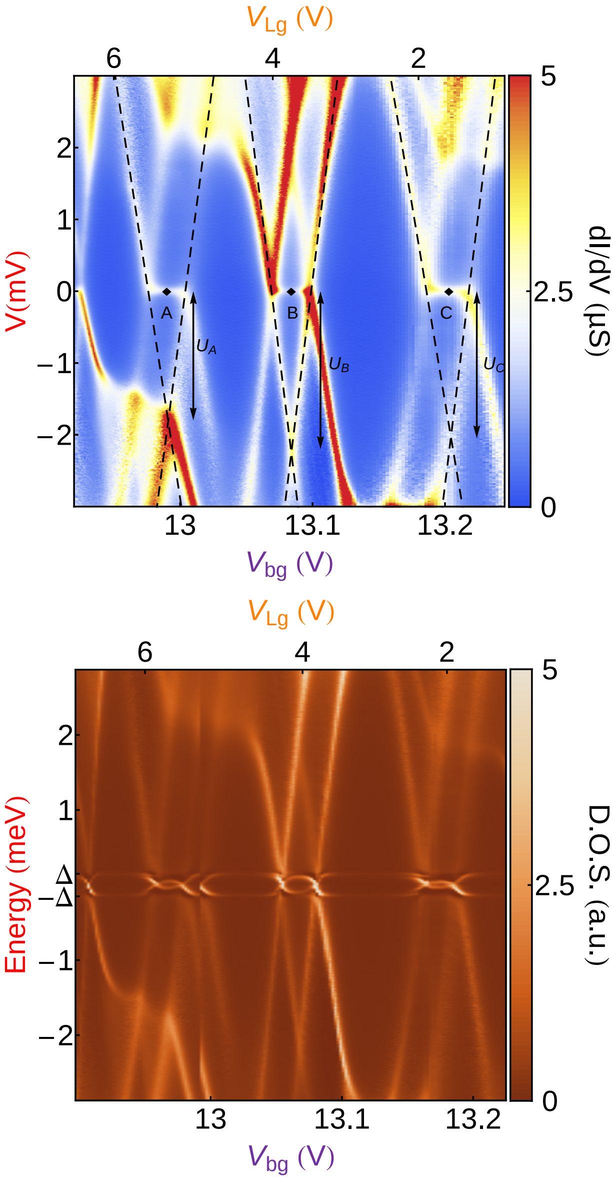

Coulomb diamonds of QDL in the N and S states

Figure 8.2: The upper graph shows differential conductance measurements taken in the normal (N) state as a function of V and the gate voltages of our CNT-based device. These measurements are performed on an effective single dot (the left one) while the other dot is maintained out of resonance with an even occupancy. The measurements show the development of Kondo ridges in diamonds where the dot has an odd occupancy. Double arrows indicate the charging energy of each diamond in odd valleys which is given by their half height (here $U_A = 1.8 \pm 0.2$ meV, $U_B = 2.2 \pm 0.1$ meV and $U_C = 2.05 \pm 0.1$ meV). Dashed lines show two edges of each diamond: their slopes give the factor of proportionality to convert gate voltages in energy. Below, we show the same measurements but taken in the superconducting (S) state. We see that ABSs have formed in odd valleys suggesting that they come from the hybridization, through Andreev reflections, of two levels of opposite spin belonging to the same orbital. The discontinuity at $V_{bg} = 13$ V is a jump of offset charge.

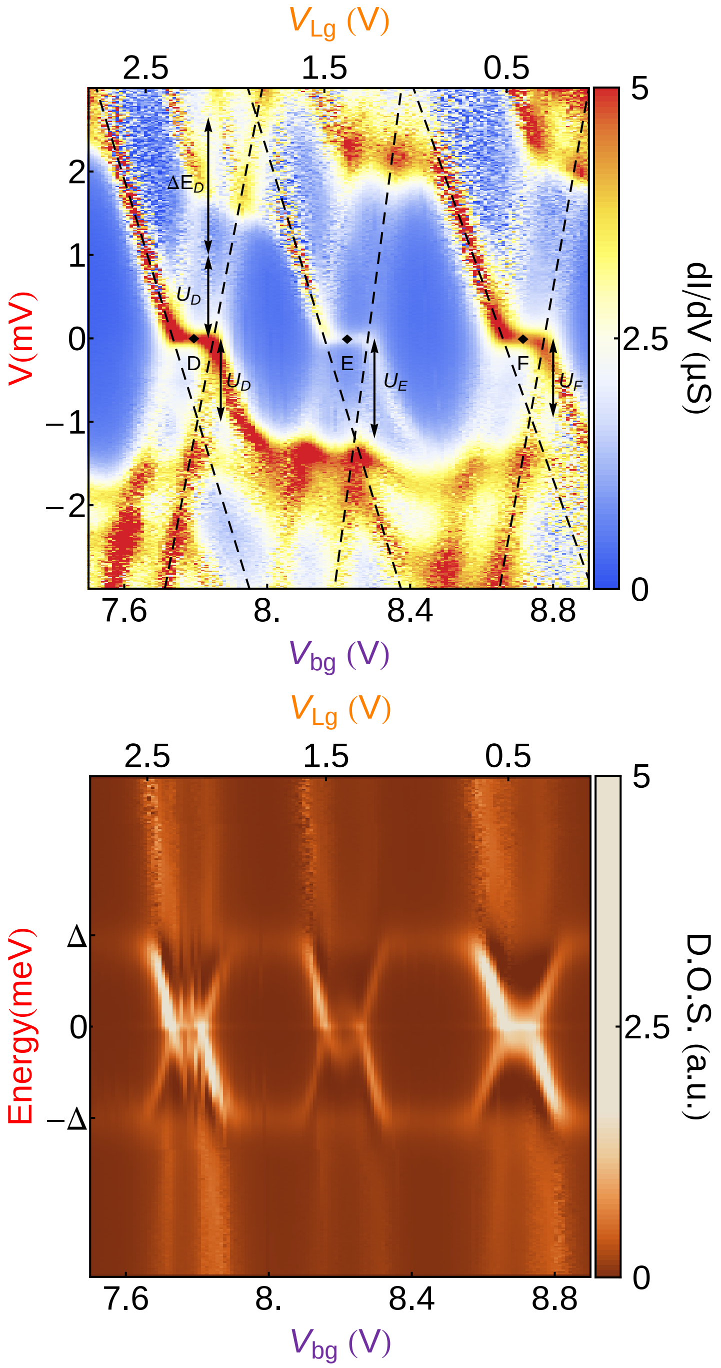

Coulomb diamonds of QDR in the N and S states

Figure 8.3: Similar measurements than in Fig. 8.2 but for the right dot. The energy difference between orbitals is extracted from the size of the large diamond between D and E. From sizes of diamonds D, E and F, we get $U_D = 1 \pm 0.15$ meV, $U_E = 1.2 \pm 0.15$ meV and $U_F = 0.95 \pm 0.15$ meV.

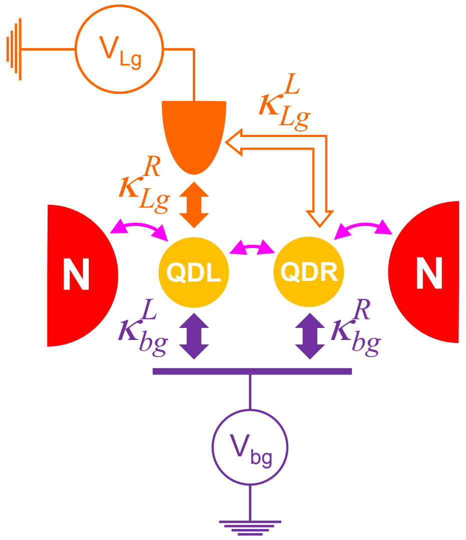

INFLUENCE OF THE GATES ON THE QDS

Figure 8.4: The QDs' electro-chemical potentials are controlled linearly by the back and lateral gates through conversion factors $\kappa_{bg}^{L(R)}$ and $\kappa_{Lg}^{L(R)}$. A variation of gate voltage $\Delta V_g = (\Delta V_{bg}, \Delta V_{Lg})$ induces an electro-chemical potential variation $\Delta\mu = (\Delta\mu_L, \Delta\mu_R)$ through the linear relation (this relation is not always linear but this assumption is justified experimentally in our case, see [117]) $\Delta V_g = \kappa\Delta\mu$ where $\kappa = \begin{pmatrix} \kappa_L^{bg} & \kappa_R^{bg} \\ \kappa_L^{Lg} & \kappa_R^{Lg} \end{pmatrix}$. From the aspect ratio of the diamonds and the slopes observed in Fig. 7.2, we can extract: $\kappa_{Lg}^{R} \approx -0.5 \pm 0.1$ meV.V^{-1}, $\kappa_{bg}^{R} \approx -9 \pm 1$ meV.V^{-1}, $\kappa_{Lg}^{L} \approx -3 \pm 0.3$ meV.V^{-1} and $\kappa_{bg}^{L} \approx -6 \pm 0.6$ meV.V^{-1}.

8.1.1.2 S state measurements

The lower graphs of Fig. 8.2 and 8.3 show TDOS measurements, of the same diamonds but with the leads in their S state (obtained after deconvolution of the differential conductance, see section D.3).

Between + and $-\Delta$, we observe the opening of a superconducting gap induced by proximity effect. Within this gap, ABSs appear as bright and thin lines which form loops of different size. In diamond B, the loop is as large as the gap, whereas in diamond F, the loop is almost closed. ABSs appear in odd valleys (just like the Kondo ridges) showing that they form by hybridization, through Andreev reflections, of two levels with opposite spin and belonging to the same orbital. This is expected as we know from NRG (see Fig. 3.14 of section 3.3 in chapter 3) that the formation of a loop occurs only for odd occupancy as it is related to a change of ground state from a spin-singlet $S = 0$ (even number of electrons) to a $S = 1/2$ doublet (odd number of electrons). In even valleys, ABSs have merged with the continuum and stay at the edge of the superconducting gap that can then be estimated.

Yet, the behaviour of the ABS does not seem to be impacted whether or not there is Kondo effect. Indeed, we know that we are able to predict (at least qualitatively) the formation of loops from the phenomenological model (see part I), even if the latter completely ignores Kondo effect (see section A.4.2). We will see in section 8.2 that NRG predicts the formation of a loop when T_K becomes smaller than Δ but only in the regime $U \gg \Gamma \gg \Delta$. However, in our experiment we rather have $U > \Gamma \sim \Delta$ (see below) and the role of Kondo effect remains rather limited.

8.1.2 Kondo temperatures

The Kondo temperature T_K can be estimated from the shape of the Kondo ridges. For this, we fit the latter with Lorentzian curves whose half widths at half maximum (HWHM) give the order of magnitude of T_K, provided that $T \ll T_K$, through the relation $e \times \text{HWHM}/k_B \sim T_K$ (see appendix A and Ref. [101, 118, 119]). This is what we have done, for example, in Fig. 8.5 for the ridge A.

The obtained Kondo temperatures, for our sample, is generally around ~ 0.5 K which means that they are all smaller than the superconducting gap ($\Delta = 0.15$ meV or 1.74 K). These values are in agreement with Kondo temperatures obtained by fitting the temperature dependences of the heights of the ridges [120]. We did not measure systematically these dependences for practical reasons, but some of them are presented and commented in next chapter.

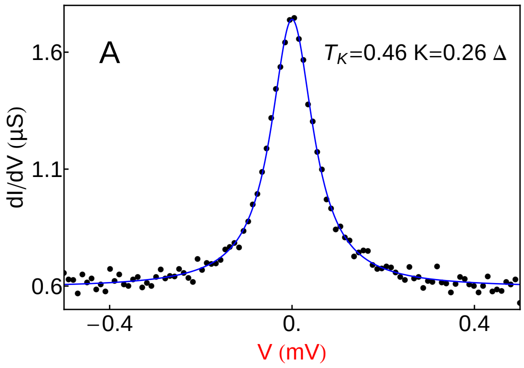

Figure 8.5: Kondo resonance measured in the middle of diamond A represented in Fig. 8.2. The resonance is fitted by a Lorentzian function (full line) whose HWHM give the order of magnitude of the Kondo temperature $T_K \sim e \times \mathrm{HWHM}/k_B$. In our sample, T_K generally lies around 0.5 K. The corresponding Γ_L and Γ_R extracted using Eq. 8.1 are approximately equal to 1 or 2Δ (with $\Delta = 0.15$ meV).

From the known form of the Kondo temperature in the middle of the ridge[1] [49, 115, 119, 121]:

$$T_K = \sqrt{\frac{\Gamma U}{2}} \exp\left(-\frac{\pi U}{8\Gamma}\right) \tag{8.1}$$

we can then estimate the couplings to the leads $\Gamma_L \approx \Gamma_R \approx 0.3$ meV. We can notice that we have Γ_L and $\Gamma_R \gg k_B T$ ($k_B T \approx 3$ μeV). As mentioned in section 7.1, the widths of the electronic levels in the normal state are thus indeed given by $\Gamma_{L,R}$ rather than $k_B T$.

8.2 Comparison of the data with NRG calculations

In Fig. 8.6 and 8.7, we present superconducting states TDOS measurements of diamonds A from F (on the left) and TDOS calculated with NRG (on the right). In our NRG calculations, the parameters are:

- the charging energies U, obtained from the size of the diamonds (see Fig. 8.2 and 8.3),

---

[1] We need to mention that, in this definition of the Kondo temperature, Γ is the HWHM of the electronic levels of the QD. This is the convention we use everywhere in this thesis.

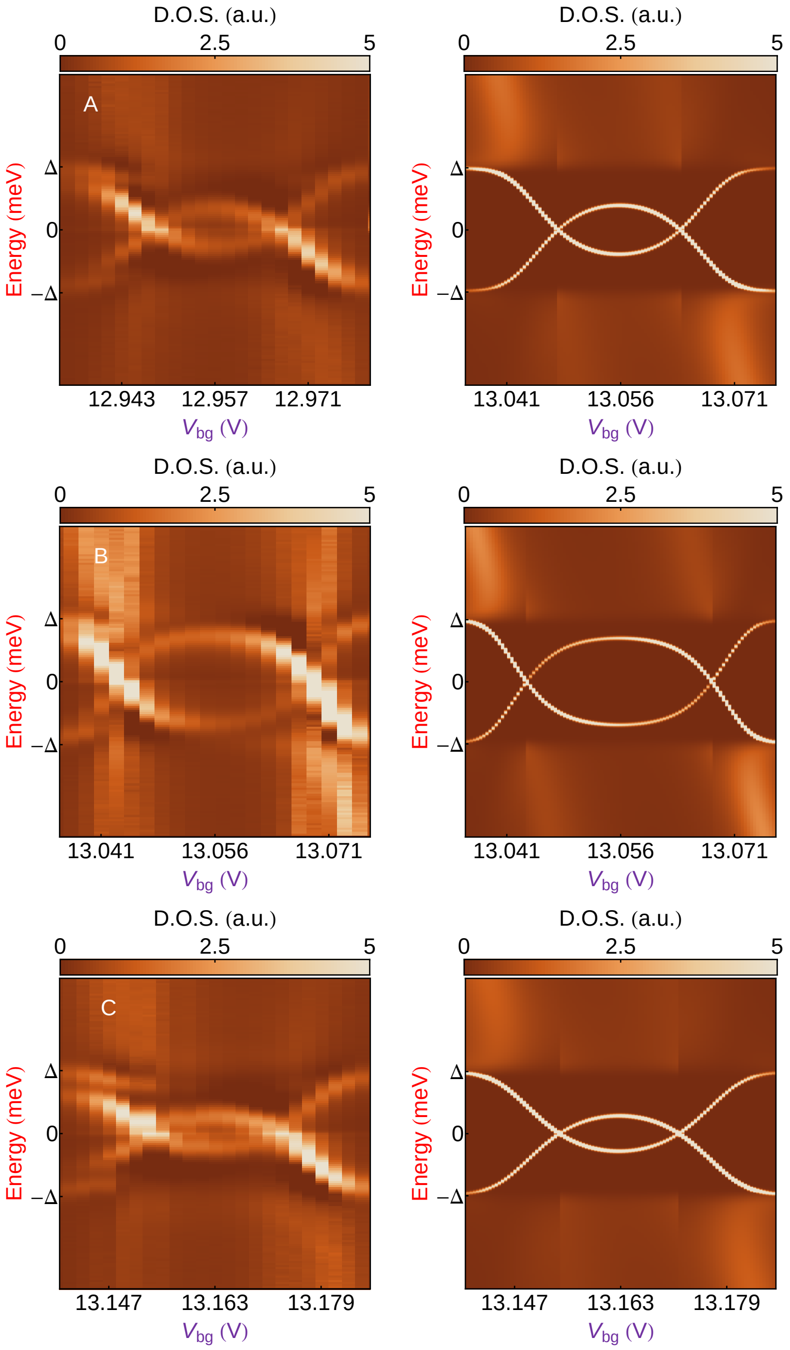

Figure 8.6: TDOS measured (on the left) in diamonds A, B and C in the superconducting case. We observe ABSs forming loops when we tune the gate voltage. On the right, we present results obtained by NRG. For the calculations, we used charging energies extracted in Fig. 8.2 and the coupling are obtained by fitting the loops formed by the ABSs (from A to C): $\Gamma = 1.367\Delta$, 1.0085Δ, 1.739Δ ($\Delta = 0.15$ meV). We have added an artificial width to the ABSs in our calculations because otherwise they would be infinitely thin and we could not see them.

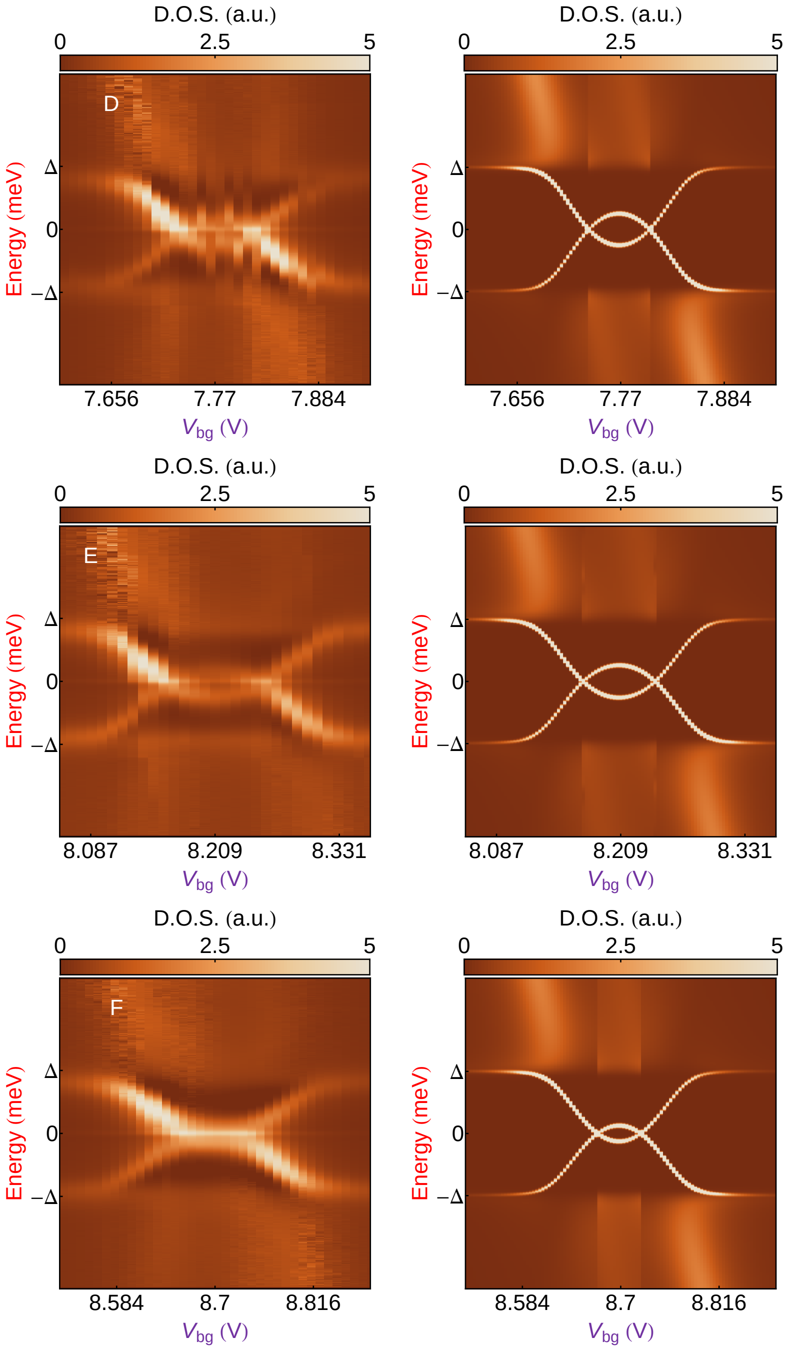

Figure 8.7: Graphs similar to those of Fig. 8.6 but for diamonds D, E and F. Couplings obtained with NRG are (from D to F): $\Gamma = 1.01\Delta$, 1.163Δ, 1.152Δ.

- the superconducting gap Δ that can directly be read in TDOS measurements,
- the conversion factor from gate voltages to energy which is given by the aspect ratio of the diamonds,
- and the couplings to the lead Γ (only one lead is relevant in these measurements: the left for A, B and C, and the right for D, E and F) that are fit parameters obtained from the size of the loop.

With the single fit parameter Γ, we obtain a very satisfying agreement between NRG and the experimental results.

A new spectroscopic tool As explained in Ref. [92], this good agreement shows that ABSs spectra constitute an entirely new spectroscopic tool for quantum dots and CNTs. Fits shown in Fig. 8.6 and 8.7 give a direct measurements of the coupling to the leads Γ. The energy resolution, in contrast to the usual Coulomb spectroscopy, is essentially independent of the temperature (as long as $k_B T \ll \Delta$). In our experiment, the resolution is rather limited by the coupling between the CNT and the tunnel probe (see appendix D). This parameter could, in principle, be improved, by reducing it, in a subsequent experiment. The sharpness of the ABSs (which are much thinner than the electronic levels of the QD in the normal state) should yield a better precision than the Coulomb spectroscopy in regime of strong coupling to the leads $\Gamma \sim U$. Sensitivity of this procedure is illustrated in Fig. 8.8. Provided that U is measured with enough precision (*i.e.* more than Γ), the size of the loop yields a value of Γ with less than 10% of uncertainty.

Influence of the Kondo effect Results of Fig. 8.6 and 8.7 also shows that in our range of parameters ($U > \Gamma \sim \Delta$), Kondo effect seems to play no particular role concerning the formation of ABSs in our experiment. This explains why the phenomenological model, described in section 3.1, qualitatively captures how ABSs form in QDs even though it completely ignores Kondo effect (see section A.4.2).

In Ref. [24], NRG calculations of Bauer *et al.* predict that the crossing of ABSs with the Fermi level, *i.e.* the singlet-doublet transition in single QD, follows a universal behaviour with T_K/Δ but only in the regime $U \gg \Gamma \gg \Delta$. This could be realized fabricating samples where the leads are more strongly coupled and define smaller QDs. However, to really state that Kondo effect arises in S-QD-S device, a more straightforward proof could be, for example, the direct detection of a Kondo cloud. The latter is a cloud of electrons which

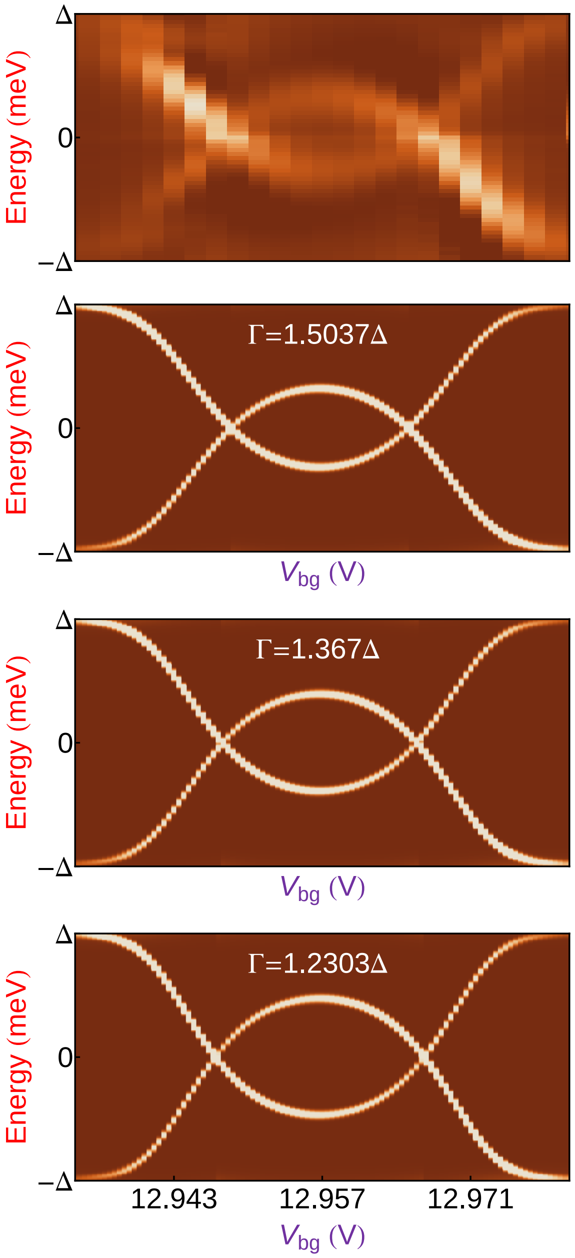

Sensitivity of the measurement of Γ

Figure 8.8: The upper graph is a zoom between ±Δ of the TDOS measured in diamond A, in the superconducting state. Below, three graphs show NRG calculations of TDOS obtained using the nominal value of U_A measured in Fig. 8.2 and three different values of Γ (from top to bottom): $\Gamma = 1.367\Delta \times 1.1$, $\Gamma = 1.367\Delta$ and $\Gamma = 1.367\Delta \times 0.9$. The difference, between the three calculated TDOS, is sufficient to determine Γ with a precision of 10%.

is predicted to form over a mesoscopic distance from the QD when there is Kondo effect. Several experimental realizations were already proposed for detection of this cloud in the normal state: for example by tunneling spectroscopy measurements on adatoms adsorbed on a metallic surface [122], or by measurements of persistent currents in quantum wires [123].

Chapter 9

Specific Double Quantum Dot features

In chapter 7, we proved, with measurements of the stability diagram, the DQD behaviour of our device. Afterward, we analyzed the interplay between Kondo effect and superconductivity along lines of the (V_{bg}, V_{Lg}) plane where the device behaves as an effective single QD (the other dot being maintained out of resonance in an even charge state). Here, we will focus on specific effects that we observe in TDOS measurements of the device which cannot be interpreted by a single dot behaviour.

In a first section, we present measurements of the TDOS of an effective single QD (taken as in previous chapter with the other dot in an even charge state) where we observe, beside conventional Kondo (CK) effect, split Kondo (SK) resonances. These split resonances are not predicted to occur in single QD [49]. In section 9.2, we will analyze in details a transition between CK and SK occurring in a region of the stability diagram where the coupling between the two dots t' is so large ($t' \gg \Gamma, U$) that they can be regarded as a single one. Finally, in section 9.3, we discuss the hybridization of Kondo resonances in two weakly coupled QDs ($t' < \Gamma, U$).

9.1 Conventional and split Kondo (CK and SK) in a single effective QD

Charge stability diagram In Fig. 9.1, we show a stability diagram of our device measured at $V = 0$ as a function of the gate voltages. It is very similar to the one presented in chapter 7, but with a richer variety of interdot couplings. Widths of the avoided crossings emphasize interdot couplings from very weak ($t' \ll \Gamma, U$ as in rectangle α of Fig. 9.1) to very strong ($t' \gg \Gamma, U$

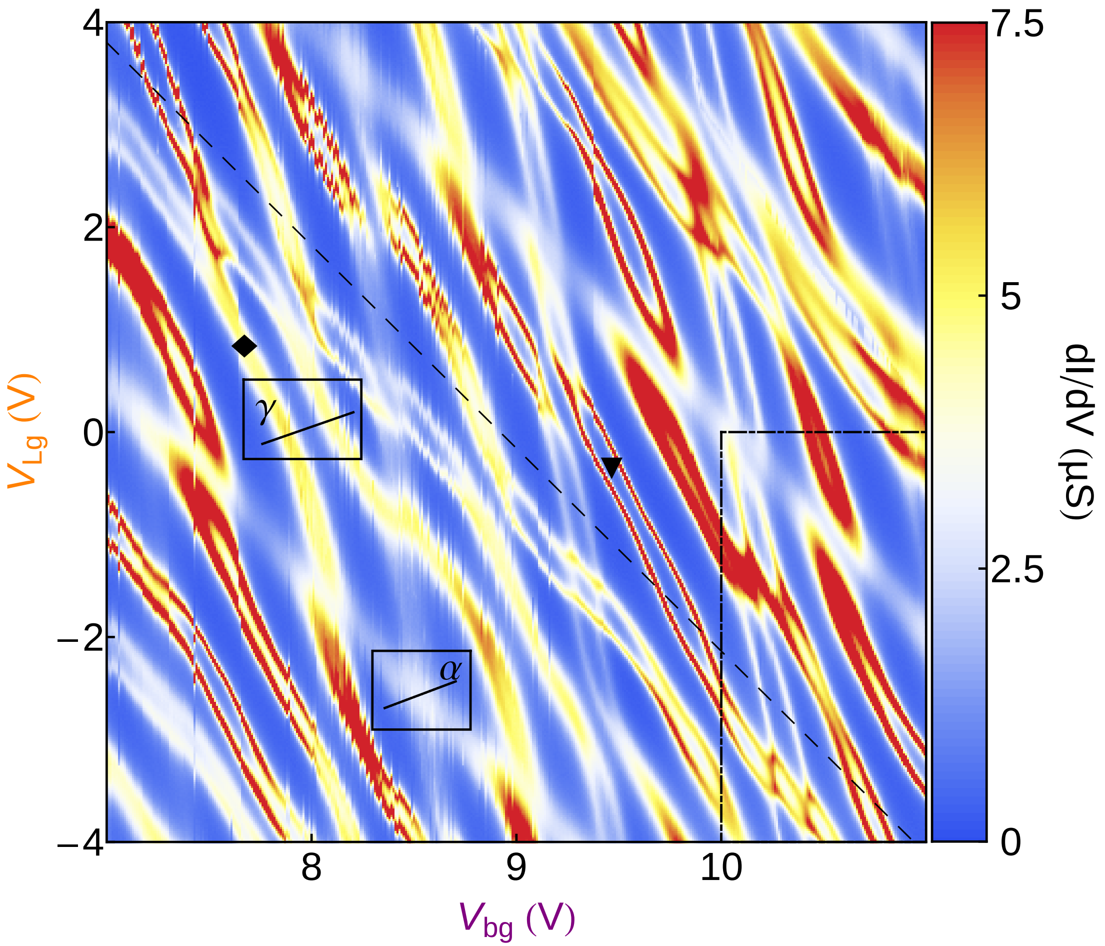

DQD behaviour of the CNT

Figure 9.1: Color scaled graph of the differential conductance of our device, similar to the one of Fig. 7.2. It is measured at $V = 0$ as a function of the back gate voltage V_{bg} and the left side gate voltage V_{Lg}. The data are taken at 35 mK between the tunnel probe and the aluminum fork driven in their normal state with a magnetic field. The black diamond indicates a point where a Kondo ridge connects two electronic level of the same orbital, whereas the black triangle shows an orbital with no ridge of conductance between its levels.

as in rectangle γ of Fig. 9.1).

As discussed in chapter 7, when two levels of the same orbital appear as a single wide stripe (as indicated by the small black diamond in Fig. 9.1) rather than two peaks, it is a manifestation of CK effect (a Kondo resonance connects these two levels). In contrast, when two levels of the same orbital appear as two distinct peaks (see the point indicated by the black triangle), it shows the absence of Kondo resonance.

Coulomb diamonds in normal (N) state In the upper graph of Fig. 9.2, we show the Coulomb diamonds of the right QD, taken in the N state, following the black dashed line of Fig. 9.1 where the left dot is maintained in an even charge state. We observe 15 Coulomb diamonds. Even diamonds (*i.e.* corresponding to an even charge state of the DQD) are featureless around $V = 0$, whereas odd diamonds present characteristic features of the Kondo effect around $V = 0$. Some of them are CK resonances but others are SK resonances.

TDOS in the superconducting (S) state of the ABSs In the lower graph of Fig. 9.2, the TDOS are taken in the S state. It shows that the behaviour of the ABSs is qualitatively the same whether the Kondo ridge is split or not. The loops formed by ABSs are slightly larger in diamonds with SK ridges. This is presumably due to larger charging energies in diamonds where SK ridge have formed. It corresponds then to diamonds where T_K should be smaller implying a weaker Kondo effect.

Origin of the SK effect The origin of this SK effect is at present not known with certainty, but could be due to exchange with the other QD[1]. SK effect has already been seen in other experiments performed on CNTs [10, 11, 98, 109], semi-conductor QDs [103, 106] or gold nanoparticles in the Kondo regime [125]. In Ref. [103, 106], SK was only observed (in contrast to us) for even occupancy (each QD in odd occupancy) and was interpreted as spin entanglement between the excess electrons on each dot. In Ref. [10, 11], it was explained by the probable coupling via exchange interaction to a localized electron trapped in the gate oxide close to the nanotube. It was suggested, in Ref. [109], that the interaction with magnetic particles of

---

[1] Recent theoretical works based on NRG calculations [124] shows that a splitting of Kondo ridges could happen for odd occupancy of the DQD provided that there is a non-negligible interdot coupling together with an interdot Coulomb repulsion comparable to the intradot Coulomb repulsion. Interdot Coulomb repulsion is however generally smaller than Coulomb repulsion in DQD CNTs [105].

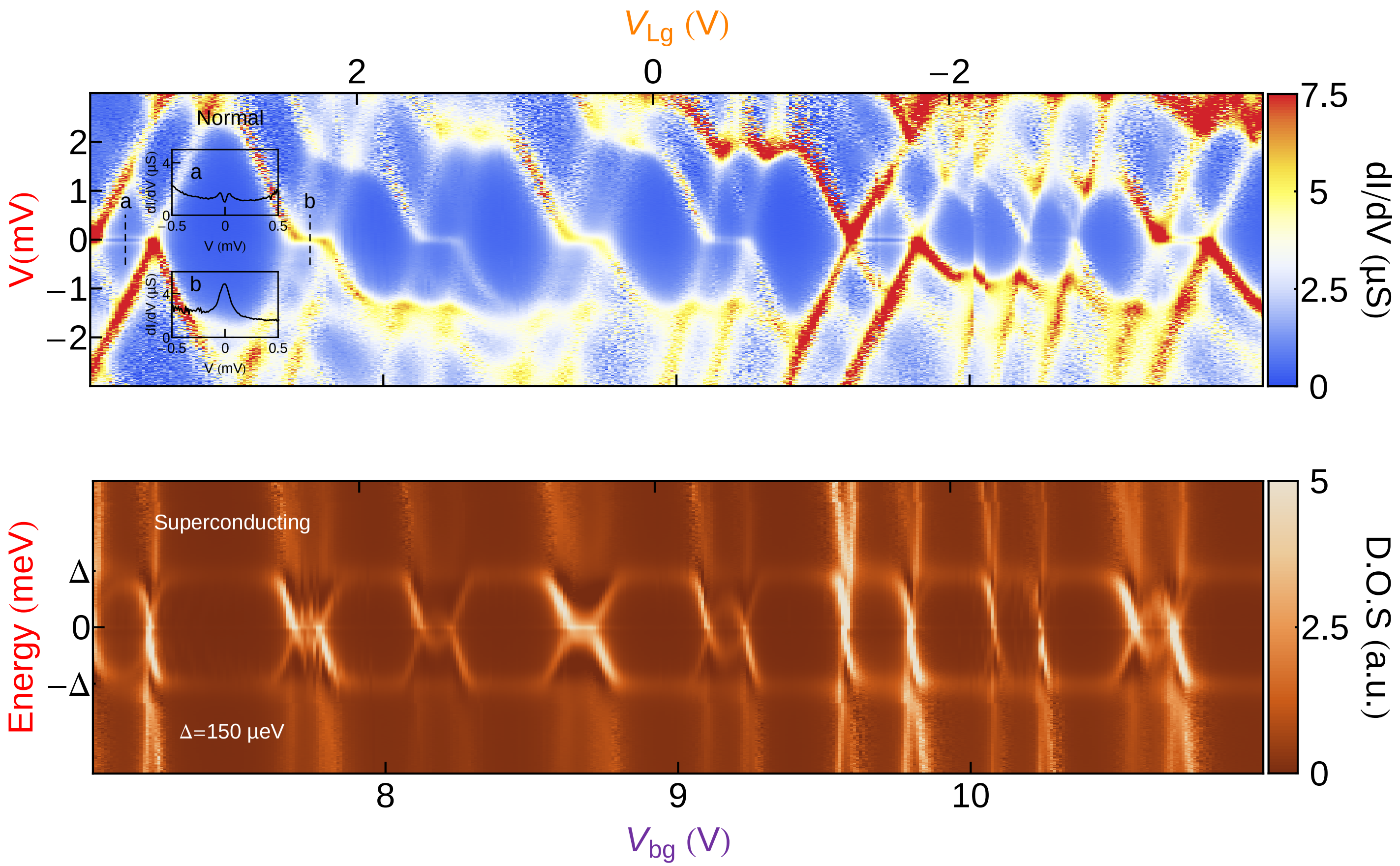

Figure 9.2: Color scaled graph of the TDOS measured along the black dashed line of Fig. 9.1 in the normal (in blue, yellow and red) and superconducting state (in white and brown). In the normal state, we observe a clear even-odd alternation with Kondo resonances around $V = 0$ for odd occupancy. In black, we have plotted cut of the conductance for voltages applied on the probe between -0.5 and 0.5 mV for the first and third diamond on the left (a and b). We can see two types of Kondo resonances: conventional and split. Whether the Kondo resonances is split or not in the normal state, ABSs spectra, measured in the superconducting case, do not show any qualitative difference in their behaviour: they form loops of different size when we tune the gate voltages. The discontinuity which appears around $V_{bg} = 10$ V in the normal state is a jump of offset charge

the catalyst pads used for CNTs' growth (see part IV) could be responsible of this split Kondo. However, this should not be the case in our sample as these particles should remain far from the QDs. In Ref. [125], the authors showed that the split Kondo they observed was caused by the RKKY interaction between a single electron localized in a gold QD and magnetic impurities deposited deliberately on the electrodes. This splitting could also be caused by a magnetic field [11, 98, 126]. This is however excluded in our experiment as we apply magnetic fields which should induce Zeeman splitting of only 3 μeV, below our experimental resolution.

More investigation is needed to understand the origin of these SK ridges.

9.2 Strongly coupled QDs: transition from CK to SK

Here, we focus on the transition between CK and SK resonance, in a region of the stability diagram where the coupling between the two dots t' is so large that they can be regarded as a single one. In section 9.2.1, we will show that we can drive the system across this transition with gate voltages. Afterward, in section 9.2.2, we will see that we can extract two characteristic Kondo energy scales from the temperature dependence of the CK and SK resonances.

9.2.1 Gate-controlled transition

Gate driven transition In Fig. 9.3, we show a color scaled measurement of the differential conductance taken at $V = 0$ as a function of the gate voltages. We observe two pairs of two lines moving in parallel with a slope that is intermediate between those of the independent QDs (given by the orange and green dashed line for the left and right QD). The coupling between the two dots t' is actually so large that they can be regarded as a single composite QD. The coupled QDs form bonding and antibonding orbitals that we can fill sequentially from $2n$ (empty orbitals) to $2n + 4$ (filled orbitals) electrons tuning the gate voltages. We recognize even and odd valleys of the large effective dot, with more or less developed Kondo effect in the odd valleys.

Measurements of Fig. 9.4 show differential conductance measurements as a function of V following the red dashed arrow along the center of the $2n+1$ valley of the composite dot in the N (upper graph) and S (lower graph) state.

On this trajectory, N state measurements (upper graph) clearly show a transition from a CK peak to a SK peak. This transition is continuous:

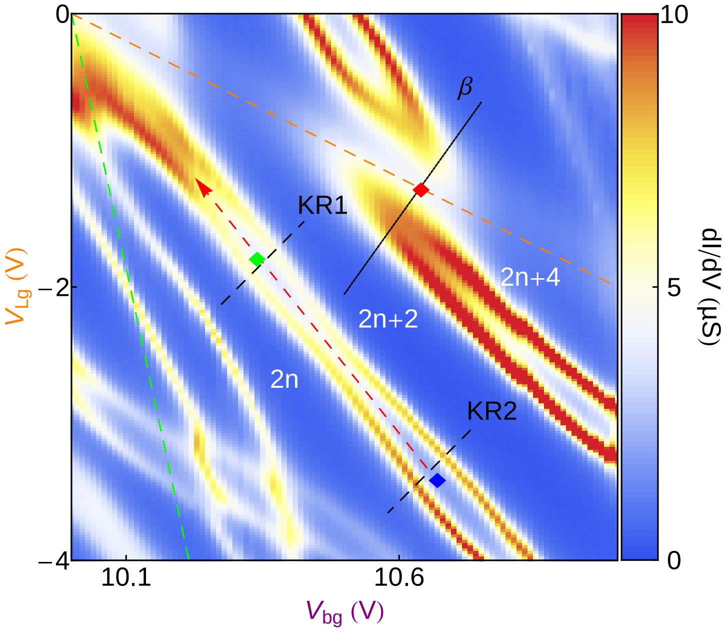

Figure 9.3: Color scaled graph of differential conductance measurements taken at $V = 0$ as a function of the gate voltages in the dashed-dotted rectangle of Fig. 9.1. Along the red arrow, the coupling between the two dots is so strong that they almost merge into a single one. The green and orange dashed lines show the respective slopes of the right and left QD when they are isolated from each other. Some valleys of even occupancies are indicated ($2n$, $2n+2$ and $2n+4$). A fuzzy Kondo resonance follow the orange dashed line and hybridize with an orbital of the right dot at the point indicated by a red diamond.

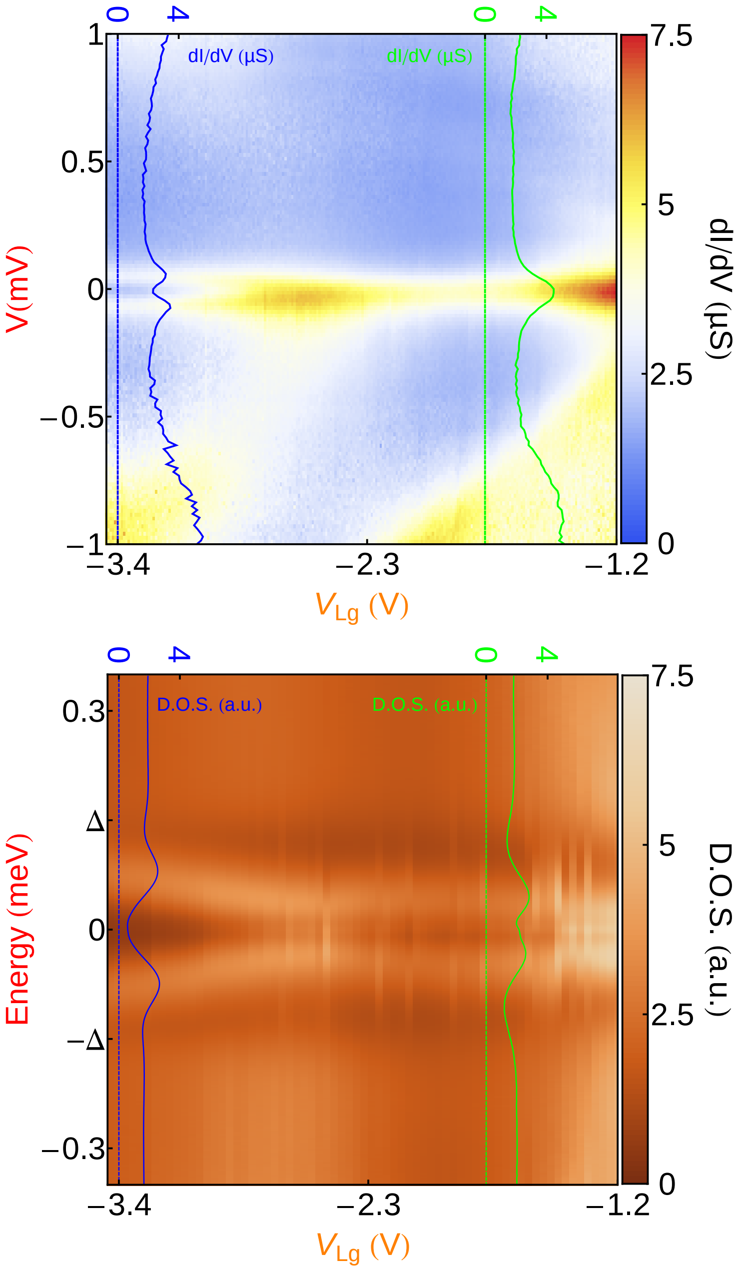

Figure 9.4: Two graphs of TDOS measured along the red dashed arrow in the stability diagram of Fig. 9.3. The upper diagram is measured in the N state and the lower one in the S state. In the upper graph, we observe a CK peak for gate voltages above $V_{Lg} \approx -2.9$ V. It evolves into a SK resonance below −2.9 V. In dark blue and green, we have plotted cuts at points indicated by blue and green diamonds in the stability diagram of Fig. 9.3. In the S case, the Kondo peaks have disappeared because of the opening of a superconducting gap. They are replaced by an ABS whose energy changes with the gate voltage. They get closer to the edge of the gap where there is a SK resonance in the N state.

the splitting of the resonance decreases, for increasing gate voltage, until it completely closes. Interpretation of the transition observed in Fig. 9.3 and 9.4 is not straightforward, as, by changing the electrostatic environment of the CNT with the gates, several internal parameters of the system may be modified. For example, the left (resp. right) charging energies U_L (resp. U_R) can change as the effective size of the QD depends on gate voltages. The tunneling rates $\Gamma_{L(R)}$ may also depend strongly on the gate voltages as the latter will distort the internal electrostatic barriers that control the transit of electrons. Finally, the interdot coupling t' or the interdot Coulomb repulsion U_{ID} (we ignore this parameter in the model developed in section 3.1.4) may also be modified by the gates and change the properties of the composite QD. All of these parameters influence the formation of a Kondo state: it is not possible to identify which one changes and is responsible of this splitting.

In the S state, CK and SK resonances disappear with the opening of the induced S gap. They are replaced by an ABS whose energy is changing with the gate voltage. In Fig. 9.2, the loops formed by these ABSs seem bigger for orbitals where SK ridge appears in the normal state suggesting a smaller coupling to the leads.

ABSs in diamonds with CK or SK ridge In Fig. 9.5, we have represented TDOS measured, in the N and S state, along two cuts (KR1 and KR2) of the Kondo ridge of the $2n + 1$ valley (see Fig. 9.3).

In N state measurements, we observe Coulomb diamonds with different type of Kondo effect: a CK resonance for KR1 and a SK resonance for KR2. When the leads are driven in their S state, the TDOS measured along KR1 and KR2 becomes very similar. Kondo ridges are replaced by ABSs which, as usual, form loops when we tune the gate.

We observe however a more important difference between KR1 and KR2 if we measure the S state TDOS as a function of the superconducting phase difference δ between the leads. In Fig. 9.5, we show such δ-dependences taken in the middle of the Kondo ridges (two lower graphs). While ABS of KR1 is almost insensitive to the phase, ABS of KR2 shows a large δ-dependence with an amplitude that is roughly half the gap. The supercurrent flowing in the loop formed by our device is thus higher when the working point is the middle of KR2 (where there is a SK ridge in the N state), than the middle of KR1 (where the ridge is conventional in the N state). In both cases, the phase dependence shows that the device is in a π state. This is expected as this δ-dependences are measured in the middle of the loops where the system's ground state is a magnetic doublet (see section 3.1.5.2).

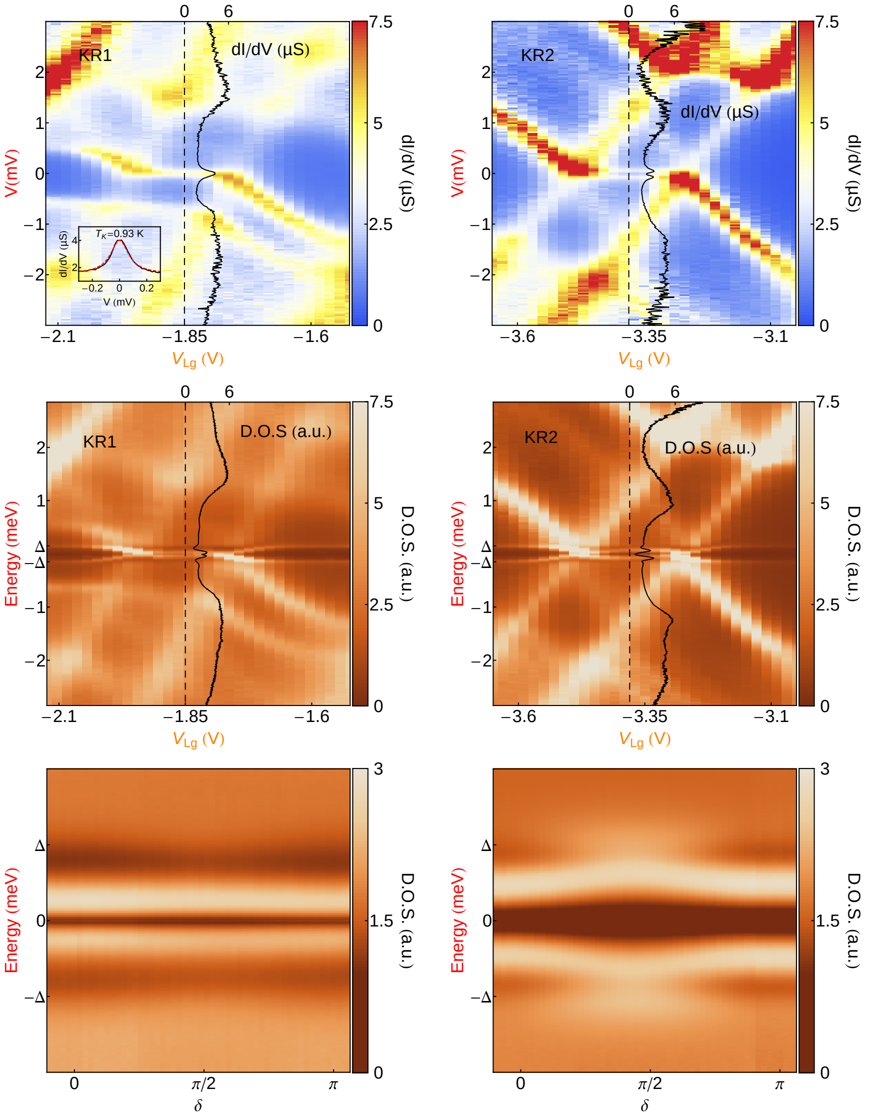

Figure 9.5: The four upper graphs show color scaled differential conductance measurements of the device taken along black dashed lines of Fig. 9.3 (KR1 and KR2) as a function of V, in the N (graph in blue, yellow and red) and S state (graph in white and brown). In the N case, we observe Coulomb diamonds with Kondo resonances: CK ridge for KR1 and SK ridge for KR2. Cuts taken in the middle of the diamonds are plotted in black. For KR1, a fit with a Lorentzian function of the CK resonance is plotted in the inset and allows to extract a Kondo temperature $T_K = 0.93$ K. In the S case, the TDOS measured as a function of V_{bg} are very similar: we observe ABSs forming loop. In the middle of the diamonds, we measured dependence with the difference of superconducting phase δ between the leads. We observe a much larger dependence of the ABS's energy for KR2 suggesting a higher supercurrent circulating in the loop.

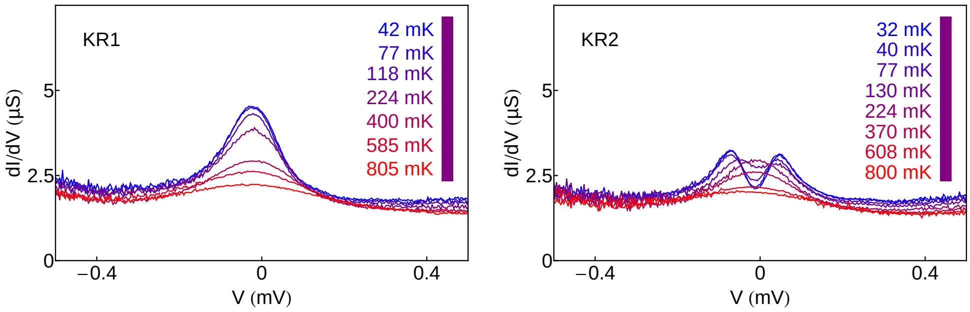

Figure 9.6: Temperature evolution of the CK ridge KR1 and the SK ridge KR2. For increasing temperature, KR1 follows the usual logarithmic decrease of spin 1/2 Kondo resonances. The SK resonance KR2 first merges into a single resonance which then decreases until it vanishes.

9.2.2 Temperature dependences

In Fig. 9.6, we show the temperature dependence of the differential conductance measured in the middle of Kondo ridges KR1 and KR2. We observe that the amplitude of the CK ridge KR1 decreases with increasing temperature. This is the expected behaviour for CK effect. For KR2, the differential conductance shows two peaks around $V = 0$ distant of 120 μV. When we increase the temperature, these two peaks merge into a single one above a threshold temperature T^*. Beyond T^*, this single peak subsequently decreases in amplitude.

As shown in Fig. 9.7, the conductance at $V = 0$ of the CK resonance (where the Kondo peak is maximum) has the usual logarithmic decrease of spin-1/2 Kondo resonances [119, 120]. We can extract T_K from this temperature dependence using the empirical formula for the conductance $G(T)$ of Ref. [120]:

$$G(T) = \frac{G_{T=0}}{\left(1 + (2^{1/0.22} - 1)\left(\frac{T}{T_K}\right)^2\right)^{0.22}}$$

which is widely used to fit experimental data in experiments on the Kondo effect (see for example Ref. [5, 10, 14]). We obtain reasonable fits for values of the Kondo temperatures $T_K = 800 \pm 50$ mK. These values are comparable to those obtained in other experiments performed on CNTs [9, 96, 97].

As was done in section 8.1.2, we can also evaluate the Kondo temperature from the shape of the KR1 Kondo ridge measured as a function of V. In order to do so, we fit the ridge with a Lorentzian function with a half width at half

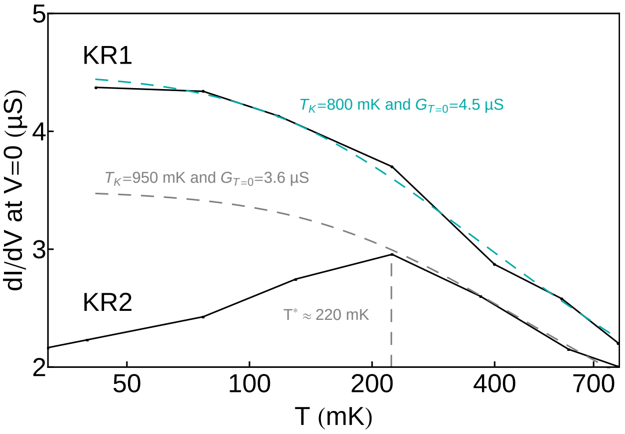

Figure 9.7: Temperature dependences in logarithmic scale of the Kondo resonances amplitude at $V = 0$. We see that the conventional Kondo resonance KR1 follows the usual logarithmic decrease, whereas the split Kondo resonance KR2 has a non-monotonic temperature dependence with a maximum around $T = 220$ mK. A fit is plotted in cyan for KR1 with the empirical formula of Ref. [120]. They give Kondo temperatures around 0.8 K in agreement with those obtain from fits of the Kondo ridge (see Fig. 9.5). In dashed gray, we have plotted a fit, using the same formula, for the SK ridge KR2 that matches with point above T^*. It yields a Kondo temperature of 950 mK.

maximum HWHM given by:

$$\mathrm{HWHM} \sim \frac{k_B T_K}{e}$$

where e is the charge of the electron, k_B the Boltzmann constant and T_K the Kondo temperature. As shown in the inset of Fig. 9.5 (N state of KR1), this fit gives a Kondo temperature slightly different than those obtained from the temperature dependence. This procedure can therefore gives a good order of magnitude for T_K but the only reliable method to measure precisely T_K is the temperature dependence.

In contrast to KR1, for KR2 the temperature dependence of the conductance measured at $V = 0$, is non monotonic. As shown in Fig. 9.7, the conductance increases until T^*, around 220 mK, and then decreases until the peak has completely vanished.

Such non-monotonic temperature dependence has also been observed in Ref. [125] and was interpreted as the manifestation of the competition between the Kondo effect and RKKY interaction. In our sample, the origin of the suppression of CK effect for $T < T^*$ is not clearly identified. It may be due to the interaction with another QD [127] or with a parasitic spin that could be localized in a neighboring impurity (for example another CNT or a charge trapped in the gate oxide). They would form a non-degenerate ground state, and, therefore, suppress the Kondo effect which happens only for degenerate ground states of the QD (spin up and spin down). The Kondo resonance would be replaced in the Coulomb diamond by finite bias cotunneling features at voltages corresponding to transition between the ground state and an excited state (as appear in Ref. [101, 102, 128]). This would look like two symmetric peaks centered around $V = 0$. Note that in the case of an antiferromagnetic coupling due to superexchange [129], these peaks would be distant of $2J \approx 8t_p^2/U$ with t_p the coupling to the impurity [130]. Unfortunately, it is not possible for us to identify experimentally the real reason of this splitting.

More investigation on DQD physics is needed to understand these results.

9.3 Weakly coupled QDs: hybridization of two Kondo resonances

In this section we discuss, the influence of a weak interdot coupling ($t' < U, \Gamma$) when two Kondo resonances meet in the (V_{bg}, V_{Lg}) plane, that is to say when the two last occupied orbital of the two QDs are degenerate and both half occupied.

This situation occurs in the stability diagram of Fig. 9.3. Indeed, following the orange dashed line, a fuzzy Kondo resonances of the left dot meets an orbital of the right dot. At the point of meeting (red diamonds of Fig. 9.3), the two orbitals form an avoided crossing. Its width is smaller than the width of the Kondo resonance underlining a small interdot coupling (*i.e.* $t' < U, \Gamma$). Far from the point of meeting, the two levels of the right dot orbital are connected by a ridge of conductance but remains distinguishable. However, they completely reconnect when they start to hybridize with the Kondo resonance of the left dot.

This weak avoided crossing is an intermediate situation between weak coupling ($t' \ll U, \Gamma$) and strong coupling $t' \gg U, \Gamma$. In Fig. 9.8, we illustrate these three situations showing cuts of avoided crossings (labelled α, β and γ) in the stability diagram. These cuts are measured along the dotted lines of Fig. 9.1 and Fig. 9.3. In these three situations, the interdot coupling t' plays a predominant role. Let's discuss them separately.

Very weak interdot coupling When the QDs are almost uncoupled (as we suppose along α), each QD is independently in the Kondo regime when singly occupied. They develop their own single dot Kondo resonance at the Fermi level (see diagram (a) of Fig. 9.9). We thus observe, in the (V_{bg}, V_{Lg}) plane, two conventional Kondo resonances that simply add their DOS, and apparently cross each other. Therefore, if we measure the TDOS of the DQD maintaining the two orbitals of the two QDs in a degenerate situation (the two orbitals are maintained at equal energy following the dotted black line in rectangle α of Fig. 9.1), we observe, as shown in Fig. 9.8, a single peak that is just the sum of the two Kondo resonances of the two independent QDs.

Very strong interdot coupling In the extreme opposite case, that is to say if t' is the biggest energy scale of the system (and is in particular bigger than T_K), orbitals of the left and right QDs hybridize to form bonding and antibonding orbitals delocalized over the DQD. The two QDs actually merge to form an effective single QD. As explained in section 9.2, the slope of this new single dot is roughly the average one of the left and right dot. In the rectangle γ of Fig. 9.1, we thus see two wide parallel stripes which simply show the area where the bonding and antibonding orbitals are successively singly occupied and develop Kondo effect (see Fig. 9.10). As shown in Fig. 9.8, following the black dotted line in rectangle γ of Fig. 9.1 we thus observe two successive conventional Kondo resonances as we would expect with two orbitals of a single QD.

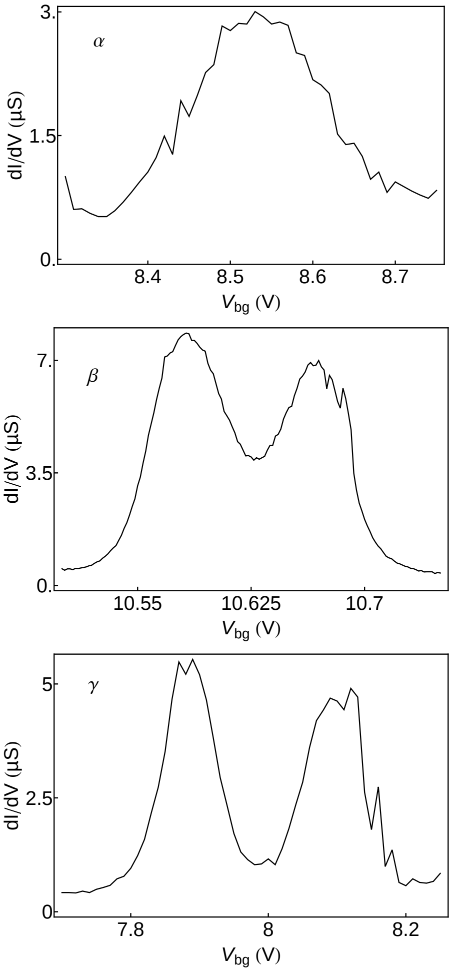

Figure 9.8: Differential conductance of the device measured at $V = 0$ along the dotted line α, β and γ of Fig. 9.1 and 9.3. Along these lines, two orbitals of the two dots, showing Kondo effect, are degenerate and cross the Fermi level. In those three graphs, we are confronted to different situations that we interpret as being of different interdot coupling t'. When t' is small (situation α, $t' \ll U, \Gamma$), we observe one peak in the TDOS which is the superposition of the two Kondo resonances of the uncoupled dot. For large t' (situation γ, $t' \gg U, \Gamma$), the two QDs can be regarded as a single one and the two orbitals of the two dots form bonding and antibonding orbitals. If t' is intermediate and moderate (situation β, $t' < U, \Gamma$), the two Kondo resonances are hybridized and form a split resonance.

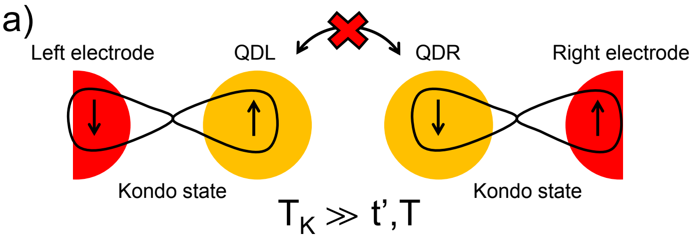

Formation of two independent Kondo singlet states

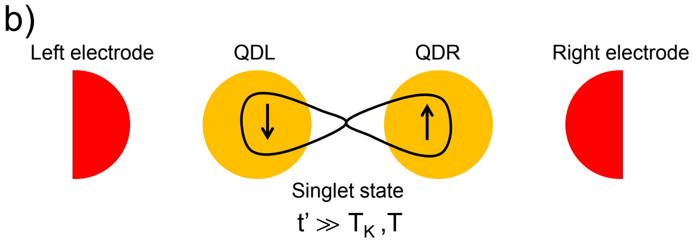

Formation of a local singlet state preventing Kondo effect

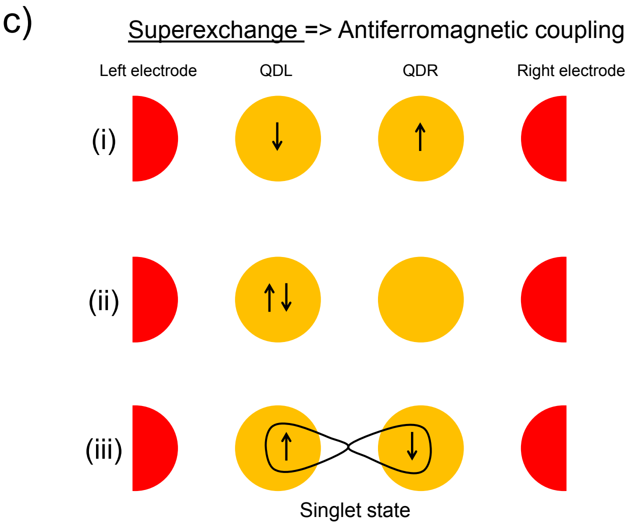

Antiferromagnetic coupling through superexchange

Figure 9.9: The upper diagram (a) shows what happens for strong coupling to the leads and vanishing interdot coupling ($T_K \gg t'$): two independent Kondo states form between dots and leads. In the Kondo state, electrons are delocalized between leads and dots (see the simplified wave function of Ref. [131]). In the second diagram (b), the coupling between the dots favors the formation of a local singlet state which prevents Kondo effect ($T_K \ll t'$). In this singlet state, electrons are localized and could be described by the simple vector $\frac{|\uparrow\downarrow\rangle - |\downarrow\uparrow\rangle}{\sqrt{2}}$. The formation of this singlet state is due to an effective ferromagnetic interaction between the dots illustrated by the sequence (c). When the last orbital of each dot is singly occupied (i), an effective antiferromagnetic coupling may arise by superexchange through an intermediate virtual state of double occupancy (ii). This leads to the formation of a spin-singlet state delocalized over the two dots (iii).

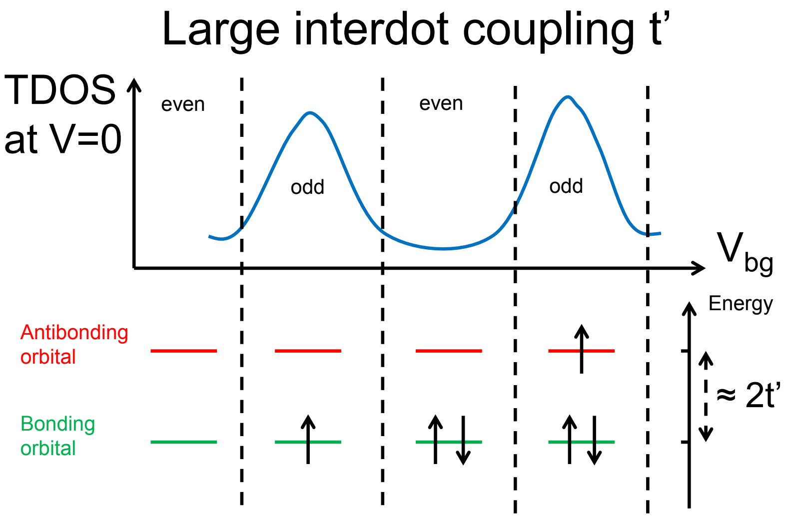

Figure 9.10: Schematic representation explaining TDOS measurements γ of Fig. 9.8. When the dots are very strongly coupled, they merge into a single effective dot and form bonding and antibonding orbitals distant of an energy $\approx 2t'$. By tuning the gates, these orbitals fill sequentially and Kondo effect happens for odd occupancies of the effective single dot.

Intermediate interdot coupling If the coupling between the QDs is intermediate between the two previous situation (as we suppose along β), single dot Kondo effect develops independently in the two QDs if their last occupied orbitals are not degenerate. However, when the two Kondo ridges meet each other in the (V_{bg}, V_{Lg}) plane (*i.e.* when orbitals of the QDs are degenerate), we can see "an avoided Kondo ridge crossing" forming with a non-zero conductance minimum in-between. If we measure the TDOS as a function of the gate voltages following the black dotted line β (along which the orbitals are roughly maintained degenerate), we thus observe two peaks symmetrical with the point of meeting (see Fig. 9.8). The transition between the previous case (γ) and this one is actually continuous for decreasing t' with the conductance at $V = 0$ falling to zero when the two ridges move away from each other. This case is of particular interest because, in contrast with the two others, it leads to specific physics of the DQD as we will explain in the following.

In Fig. 9.11, we have represents the TDOS of the DQD measured along the dotted line β and as a function of V. We recognize, on the left and the right, two blue areas of blockade where the occupancy of the DQD is even with no feature around $V = 0$. In between these two regions, we observe a large region of conductance, that resembles an odd diamond of a single QD with a Kondo ridge (see N state measurements of KR1 in Fig. 9.5, or for example Ref. [96]). However, in contrast to single QD, the Kondo ridge of Fig. 9.11 is interrupted between V_{Lg} =-1.2 and -1.45 V. This part is replaced by an asymmetric split Kondo resonance, as can be seen in the inset.

This "avoided Kondo ridge crossing" can be interpreted in terms of competition between formation of a singlet state in the DQD and independent Kondo effect between the two dots (see the two upper diagrams of Fig. 9.9). When the coupling between QDs, characterized by t', is absent, we are in the α case and QDs develop Kondo effect independently. If t' gets a bit larger, an effective antiferromagnetic exchange between the dots is generated by superexchange [129, 132] (see lower diagram of Fig. 9.9), characterized by the energy scale $J \sim 4t'^2/U$. If J gets of the order of magnitude of T_K, this antiferromagnetic exchange favors the formation of a non-degenerate singlet state within the DQD. This state prevents the development of singlet Kondo state as the latter is based on the degeneracy of two spin states. The Kondo peak is then split into two peaks distant of an energy $2J$ [130] that are interpreted in some theoretical works as molecular levels between Kondo resonant states [133, 134].

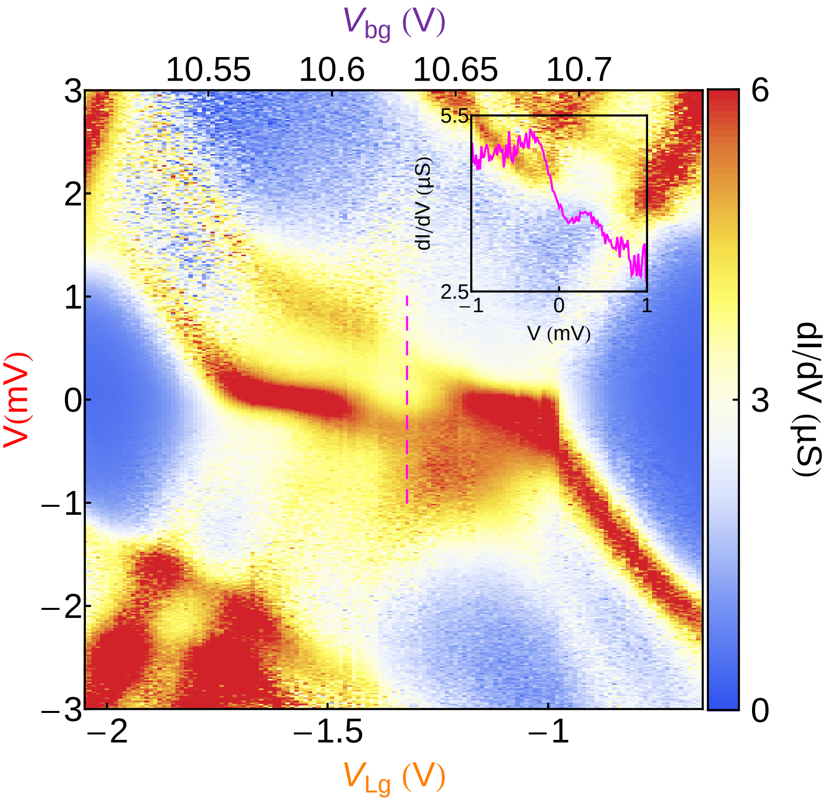

Figure 9.11: TDOS of the device measured in the N state along the black dotted line in the stability diagram of Fig. 9.3. We see two regions of blockade on the left and on the right where the occupancy of the DQD is even. In the middle, we see a Coulomb diamond with a Kondo ridge that is interrupted between V_{Lg} =-1.2 and -1.45 V. This part of the Kondo ridge is replaced by an asymmetric split Kondo resonance, as can be seen in the cut of differential conductance represented in the inset and measured along the magenta dashed line.

Part IV

Samples fabrication

Chapter 10

Fabrication of a sample

In order to perform the spectroscopy of ABSs in carbon nanotubes (CNTs), it is necessary to well connect an individual CNT with two superconducting electrodes less than a μm apart and place a weakly coupled tunnel electrode in between. The fabrication of this superconducting CNT-based circuit concerns three steps:

- on chip CNTs growth,
- localization of CNTs,
- nanofabrication of superconducting CNT-based circuit.

All these steps rely on the use of standard e-beam lithography technique that we describe in detail in the following section. In section 10.2, we explain how we synthesized on chip high quality CNTs, sufficiently long and isolated to be contacted individually. Then in section 10.3 and 10.4, we present the techniques used to localize and fabricate on such CNTs the circuits designed to observe the ABS by tunneling spectroscopy. The last section is devoted to room temperature characterization of samples in their final form.

10.1 Lithography techniques

Along our fabrication scheme, we use electron lithography three times in order to fabricate resist masks, as depicted on Fig. 10.1 and 10.2, with patterns smaller than 100 nm.

10.1.1 Coating the substrate with resist

Mask fabrication starts by coating the substrate with an electro-sensitive resist single layer of polymethyl-meta-acrylate (PMMA) for the case depicted

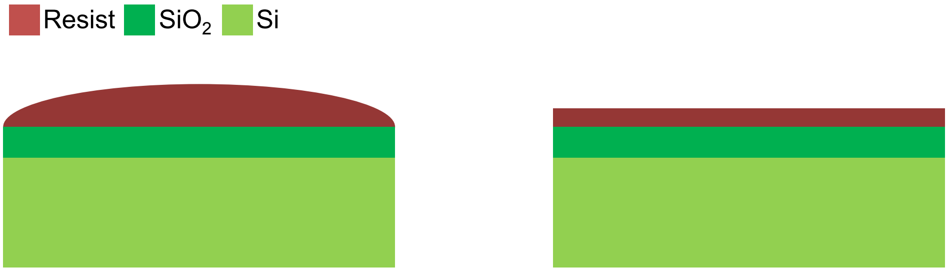

(a) Resist deposition (b) Spinning and baking

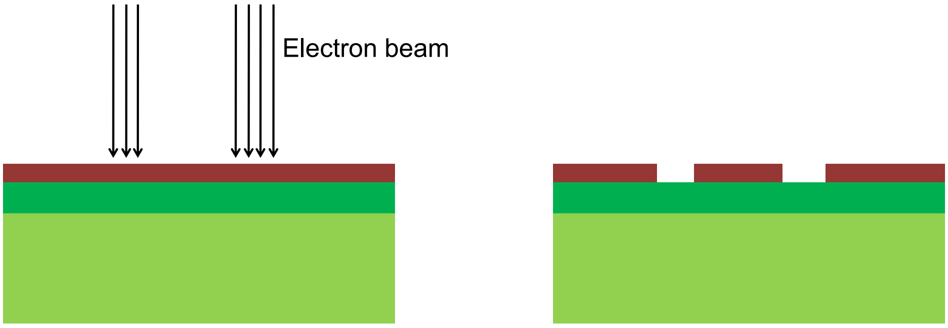

(c) Exposure (d) After development

Figure 10.1: Typical procedure of electronic lithography

in Fig. 10.1 or a bilayer of polymethyl-meta-acrylate/meta-acrylate acid (PMMA/MAA) for the case depicted in Fig. 10.2. Parameters used are detailed in subsection 11.1.

10.1.2 Exposure

Once substrate is coated, we expose the resist with the electron beam of a SEM Philips XL30 fitted with Elphy Quantum lithography system from Raith. The Elphy Quantum software (EQ) controls the exposure of patterns defined in a GDSII file (for example see Fig. 10.9).

These patterns are divided by the software when needed into rectangles and triangles that are scanned step by step in meander. The electron beam stays at each step during a time called dwell time until the programmed charge dose is reached. With a positive resist, polymer chains are locally broken in these exposed areas which will be removed during the development.

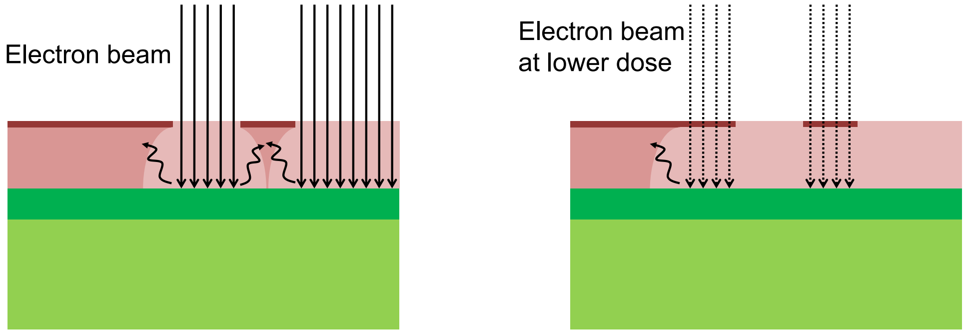

(a) Exposure of a PMMA/MAA bilayer (b) Exposure of undercut boxes

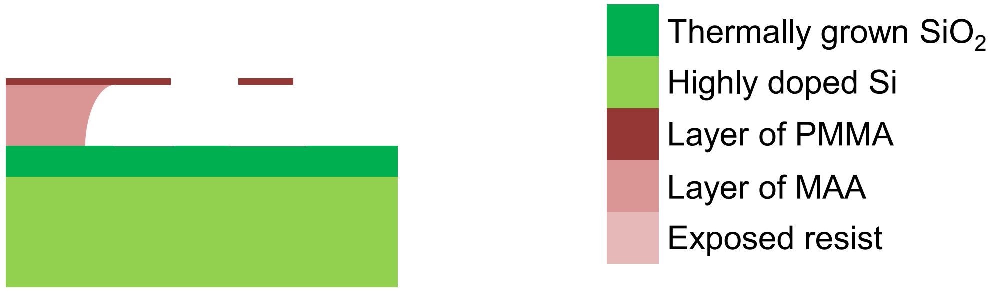

(c) Development

Figure 10.2: Similar procedure than figure 10.1 but for a PMMA/MAA bilayer

We choose the appropriate exposure dose depending on the resist deposited on the chip (see subsection 11.2.1 in chapter 11) and the pattern we want to obtain. If the coating is a bilayer, we expose generally undercut boxes at low doses (see Fig. 10.2 (b)) in order to have a larger undercut, required to perform a subsequent angle evaporation. Doses for undercut boxes are high enough to get rid of MAA during development but not of PMMA, getting part of the mask suspended.

10.1.3 Development

After exposition, we develop the resist in methyl-isobutyl ketone (MIBK) diluted 1:3 in volume with isopropanol (IPA) for 45 s. We subsequently rinse the chip in IPA to stop development and dry it under N_2 flow. MIBK dissolve the exposed resist yielding the designed patterns (see in section 11.2.2).

10.2 Nanotubes growth on Si substrate

In this section we describe the method to obtain CNTs on an insulating layer of thermally grown silica (SiO_2) atop highly doped silicium (Si) substrate. As we want in the end to perform transport experiments, we need CNTs with coherence lengths greater than 1 μm. This is provided by a chemical vapor deposition technique which yields CNTs with a low defect concentration [135] in comparison for example to arc discharge technique [136, 137].

10.2.1 Substrate characteristics

We use commercial 4-inch wafers constituted by a 1 μm thick insulating layer of SiO_2 atop a Si substrate. The SiO_2 layer is obtained by oxidation of a Si crystal. Si is heavily doped (typically 5 mΩ/cm) remaining conducting even at very low temperature. We use it as a back gate capacitively coupled to the sample.

Such commercial wafers provide us a sufficiently flat surface to fabricate electrical circuits with elements of the order of the nanometer like CNT. We cut up these wafers with a diamond tip in chips of 1×1 cm^2 and we process them individually (see Fig. 10.3).

10.2.2 CNT grown by Chemical Vapor Deposition (CVD)

To obtain CNTs we choose the CVD technique. It provides individual CNTs with low defect density, single wall, with diameters of 1-3 nm and lengths of

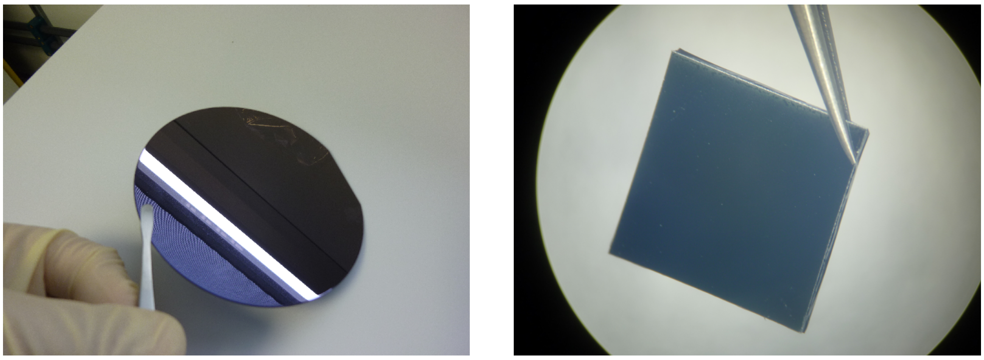

(a) Si Wafer (b) 1×1 cm^2 chip

FIGURE 10.3 – Samples are fabricated on a chip cut out from a highly doped Si wafer with a 1μm thick oxide layer.

up to tens of micrometres.

Catalyst deposition In this method CNTs grow from catalyst pads deposited on the substrate as depicted in Fig. 10.4. In order to isolate a single CNT and have zones free of catalyst for circuit fabrication, we prepare catalyst pads of 1×1 or 2×2 μm^2 sufficiently far from each other to get a low CNT density (see Fig. 10.4).

We obtain catalyst pads by dispensing, through a resist mask made from a single layer of PMMA (see table 11.1), a few drops of a suspension of the catalyst in methanol (see recipe in subsection 11.3.1 and [135]). After evaporation of the methanol and lift off of the resist (see for details subsection 11.3.2), only catalyst pads networks patterned on the mask remain on the chip (see Fig. 10.4 (d)).

The chip is then divided into four parts that will give four different samples. Each one has a network of 30 catalyst pads distant of 40 μm

Nanotubes growth by chemical vapor deposition (CVD) After catalyst deposition, the chip is placed in a quartz tube. This quartz tube lies in a furnace[1] (see Fig. 10.5) which can heat up to 900°C. It is linked by pipes on one end to gas cylinders of Ar, H_2 and CH_4, and on the other end to an exhaust pipe.

The growth starts by heating up the quartz tube to 900°C with a flow of Ar (1500 ml/min) passing through the tube. Then, during 8 minutes a H_2 flow (200 ml/min) cleans the chip. The growth is then performed by

---

[1] We used the furnace of LPA Mesoscopic Physics group at ENS Paris.

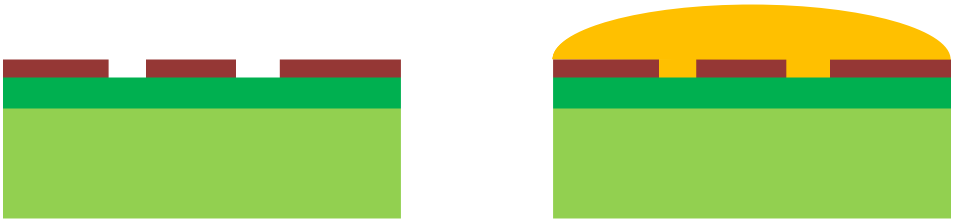

(a) Single layer of PMMA mask (b) Deposition of catalyst suspension

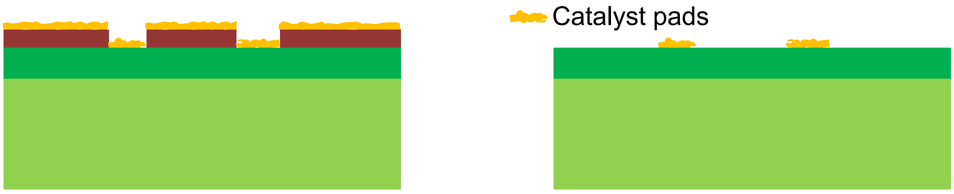

(c) After methanol evaporation (d) Pads of catalyst after lift off

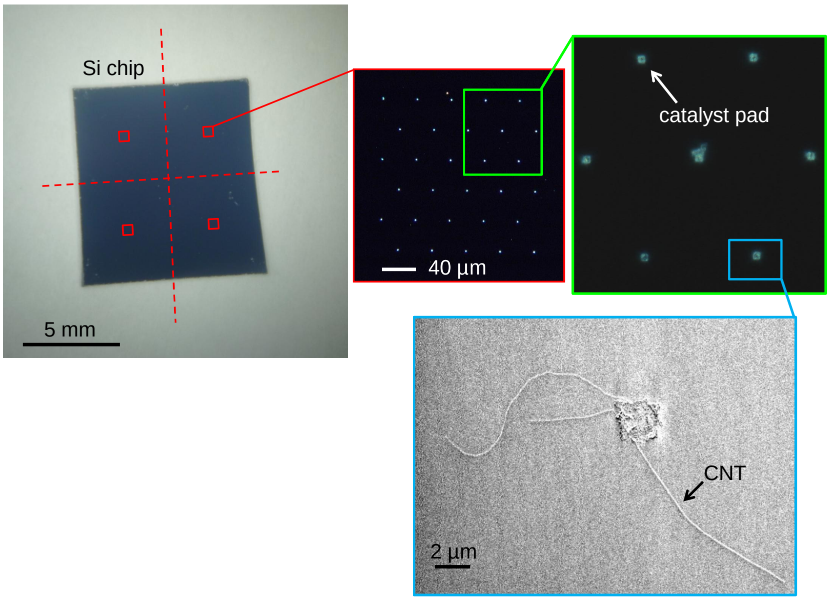

Catalyst deposition and CNTs growth

Figure 10.4: Procedure of catalyst deposition (diagrams a, b, c and d). Optical microscope pictures (red and green frames) in dark field showing the resulting catalyst pads and SEM picture (blue frame) showing a single catalyst pad after CNT growth.

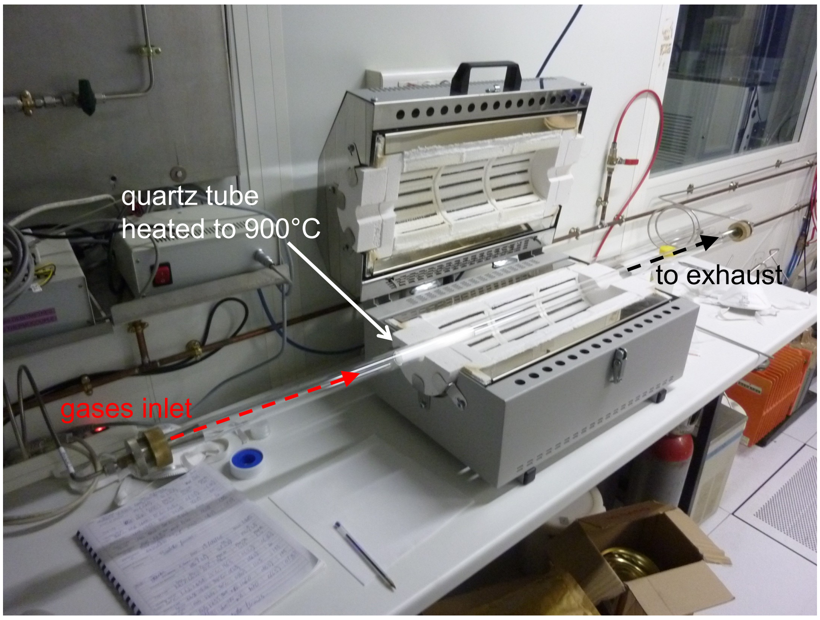

Figure 10.5: Picture of the ENS CVD furnace.

injecting an additional flow of CH_4 during 10 minutes (1000 ml/min) after that the furnace slowly cools down to room temperature in an Ar flow.

10.3 Localizing nanotubes

To locate nanotubes, we first add gold alignment marks on the chip by performing standard e-beam lithography on a MAA-PMMA bilayer (see table 11.1). These gold alignment marks include 7 large crosses of 200 μm (distant of 1392.5 μm) on the edge of the chip and a grid of 12×12 small labelled crosses inside a 150 μm^2 box in the center of the chip (see Fig. 10.6), where CNTs were grown.

We locate CNTs on the chip using our SEM Philips XL30 working in Ultra High Resolution mode with accelerating voltages that ranges over 0.5 and 1.5 kV. In order to minimize carbon contamination and possible damage of CNTs, we imaged them quickly. We take pictures of approximately 25×35 μm in 1 minute.

In the SEM we find the central region where we grew CNT, using large crosses. CNTs are located with respect to the labelled crosses (see Fig. 10.7a) by taking pictures.

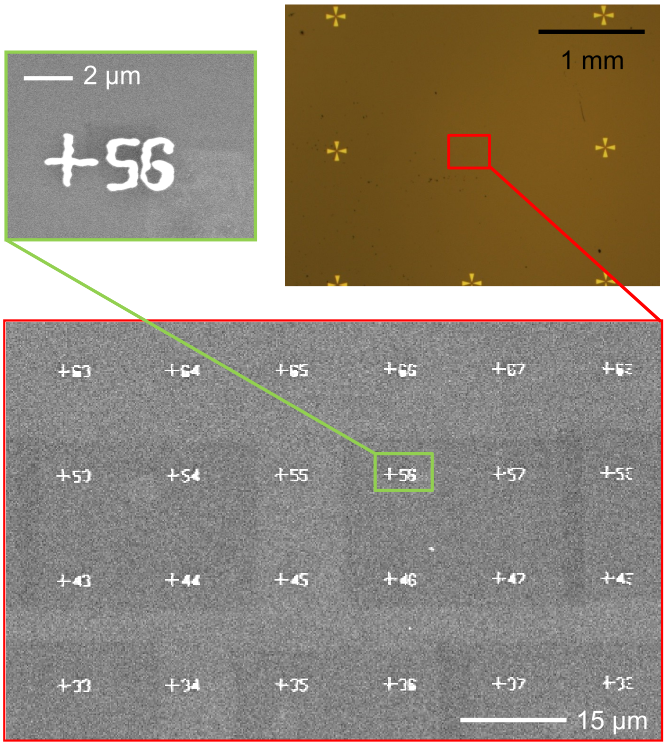

Gold alignment marks for CNTs localization and for fabrication

Figure 10.6: The central area where CNTs are grown is located thanks to large crosses (optical microscope picture on the top right). Small crosses are used to define a coordinate system for lithography alignment of the contacts on the CNTs (SEM pictures with red and green frames).

10.4 Contacting nanotubes with metallic leads

The sample we want to obtain includes a superconducting fork well connected to a CNT and at the same time a superconducting tunnel probe weakly coupled to its central part in order to measure the density of states (see section “experimental measurement of the TDOS” and Fig. 10.8). In this section we explain how we obtain these two types of contact in a single lithography step.

10.4.1 Mask fabrication to contact CNTs

Drawing the circuits for e-beam lithography Once CNTs are located, we draw (see Figs. 10.7a and 10.9) a circuit to connect them (our drawings are encoded in standard GDSII database file format). The drawing is done in layer in which SEM pictures of labelled crosses and CNTs are inserted. On Fig. 10.7a, we have represented, in dark red and on top of such a picture, several structures constituted by a fork and a tunnel probe. These structures are linked to pads of 300 μm^2 (see Fig. 10.9), that will subsequently serve to bond the sample with aluminum wires of $25\mu\text{m}$ and connect it to the measurement circuit (see Fig. 10.10).

Alignment procedure Prior to the exposure step, we perform a three steps alignment. On the first step we focus on the surface of the sample at three different places on three scratches at corners of the chip. EQ software will use these data to interpolate the correct focus at the position where the exposure is performed in case the sample is not laid down flat on the sample holder. On the second step, we define the chip coordinate system thanks to large crosses. And on the last step, we used small crosses to fine-tune the geometry of the exposed field.

We performed this exposure on a bilayer of PMMA-MAA (see section 11.1). This gives a suspended mask that will allow us to perform metal angle evaporation (see below).

10.4.2 Metal deposition

In order to obtain the two required types of superconducting contact on the CNT in a single step (well connected electrodes and tunnel contacts), we evaporate the metal (as described in subsection 11.4.1) at two different angles (see Fig. 10.11). We evaporate all the contacts in a single pump down instead of fabricating the good contacts and the tunnel contacts in

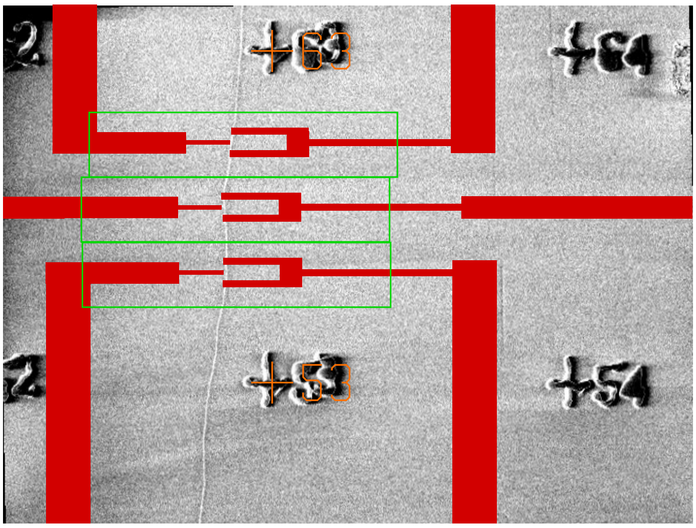

(a) Drawing in GDSII format of the circuits in Elphy Quantum on top of a SEM picture showing the CNT used to make the sample of Ref. [92] and gold alignment marks labelled 53 and 63. In green are represented undercut boxes and in orange replica of the labelled crosses we use to align the drawing.

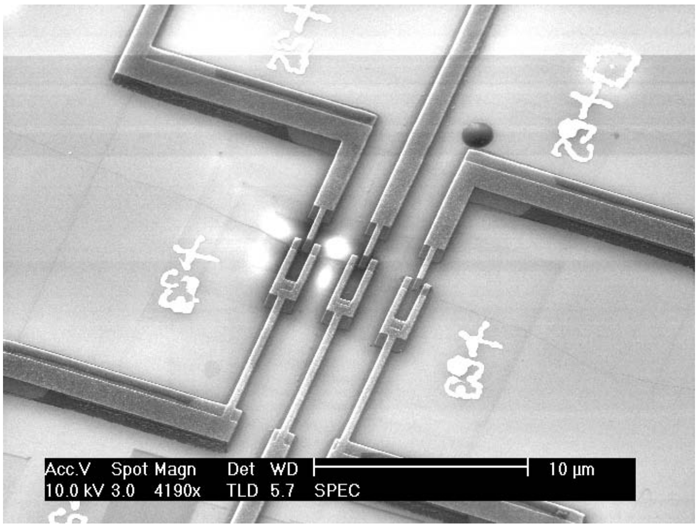

(b) SEM picture of the sample T9 (left) fabricated on this CNT

Figure 10.7: Pictures of the sample of Ref. [92]. Differential conductance measurement of the structure on the left are presented in the supplementary information of Ref. [92].

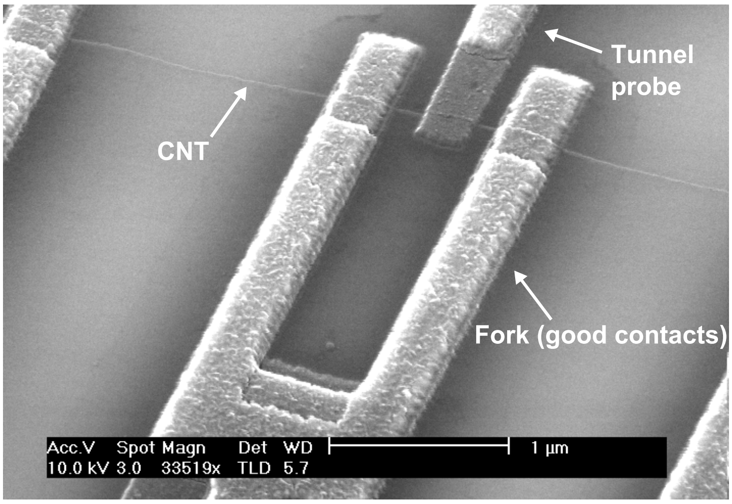

Figure 10.8: SEM picture of the sample of Ref. [92]

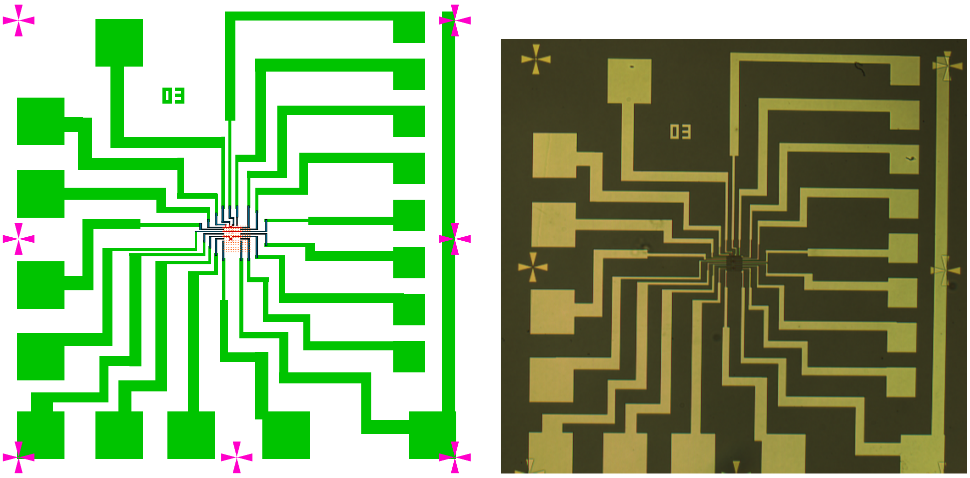

Figure 10.9: Drawing in a GDSII file and picture taken after angle evaporation with an optical microscope of the sample of Ref. [92]

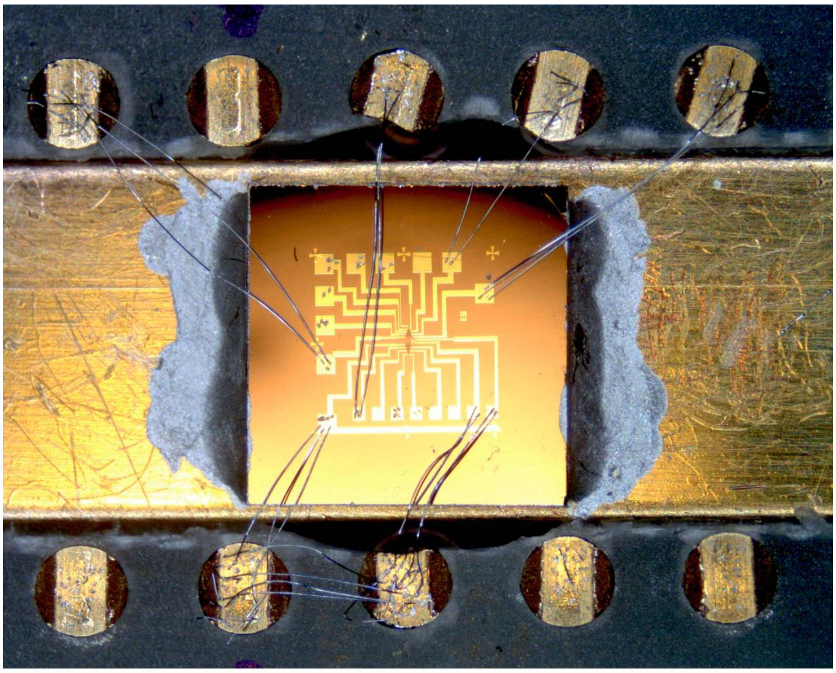

(a) Sample D03 on a 5 mm chip glued by silver paint on the metallic part of a sample holder. On this metallic part can be applied a back gate voltage to tune the chemical potential of the CNT. The sample is bonded to contacts for transport measurements.

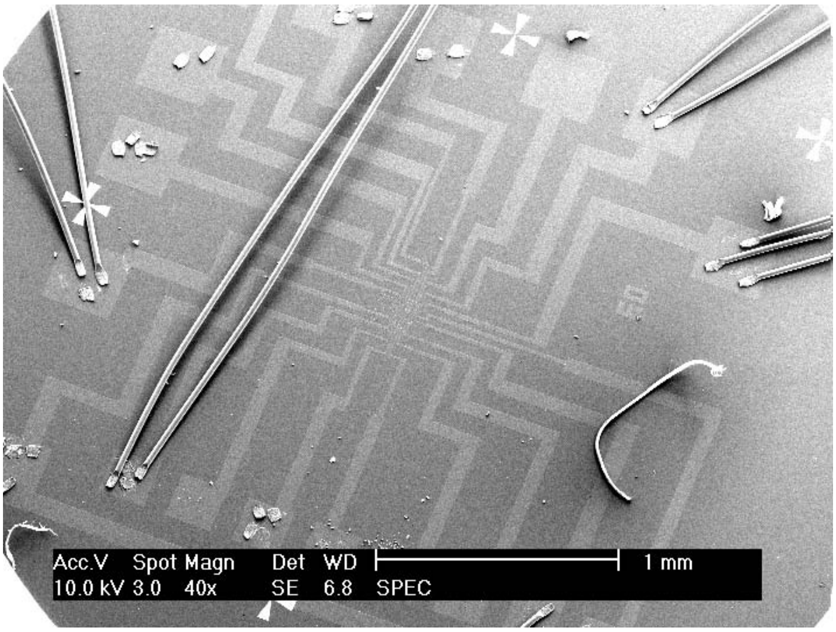

(b) SEM picture of sample D03 with aluminum bonding wires

Figure 10.10: Picture of the sample of Ref. [92] after measurements

two consecutive processes because reprocessing killed the contacts previously made each time we tried.

Electrodes composition We choose Aluminum (Al) to fabricate these superconducting contacts because of its well-known superconducting BCS behaviour below 1.2 K. However Al directly evaporated on CNT doesn't provide measurable contacts [138]. In order to obtain good electrical contacts, we thus need to add, between CNTs and Al, a sticking layer of Palladium (Pd) or Titanium (Ti) thin enough for Al to induce superconductivity in CNTs.

Contacting a single wall CNT is generally achieved with Pd electrodes because it affords statistically the best contacts [139]. Also efficient though less reliable than Pd, other materials such as Ti or Platinum (Pt) provides as well transparent contacts. We chose a sticking layer of Ti as we did not have Pd in our evaporator[2].

A thin layer of Ti (3 nm thick) proves to be enough to obtain well connected contacts. To obtain tunnel contacts, we evaporate only 1 nm of Ti. It gives us contacts which are on average ten times more resistive than contacts with 3 nm of Ti (see section 10.5). We evaporate on top of these Ti layer 100 nm of Al for the fork and 40 nm of Al for the tunnel probe.

We need to mention that Ti is actually superconducting below 400 mK and one can imagine that we could have simply evaporate only Ti instead of a Ti/Al bilayer. However the temperature of the fridge (35 mK) is not negligible compare to the Ti superconducting gap and temperature could excite quasiparticles which would limit our spectroscopic resolution. With a Ti/Al bilayer we get superconducting electrodes with a superconducting gap which can be three times higher. The resulting gap decreases exponentially with the Ti thickness [140], we choose then a thickness of Ti negligible compare to the Al thickness (1 or 3 nm compared to 40 or 100 nm).

Evaporation Before evaporation the sample is heated up to 110°C for two hours. It is subsequently cool down to -80°C, evaporation being started at 0°C (see Fig. 10.12). We choose to perform this temperature cycling for two reasons:

1. we expect to get rid of the residual water on the chip surface during heating up,

---

[2] Actually we had at our disposal two evaporators. One of them could evaporate Pd but it was not possible to cool down the sample holder at liquid N_2 temperature. Furthermore its loadlock pressure was higher of one order of magnitude.

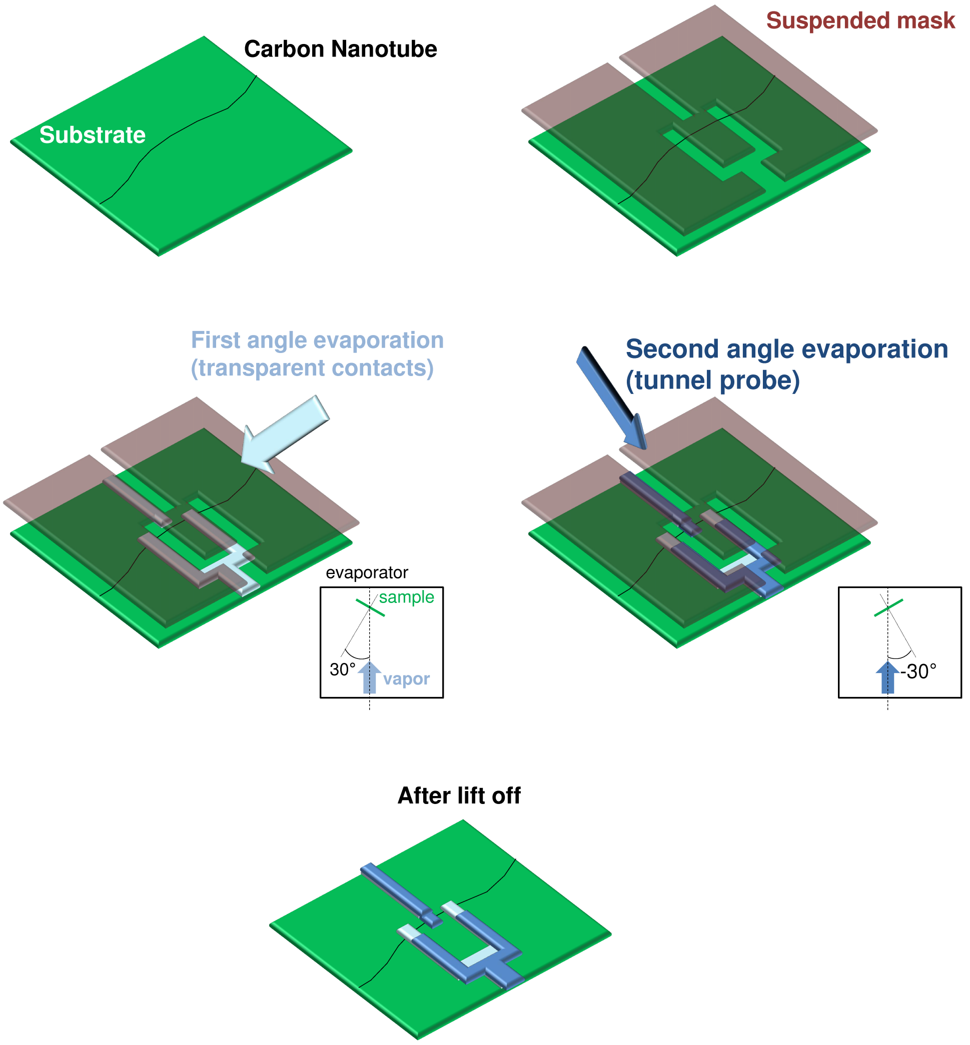

Figure 10.11: Well connected and tunnel contacts are evaporated in a single pump down at different angles.

2. we want to benefit from the fact that pressure in the loadlock is lower at low temperature and this way to minimize pollution of the contacts during evaporation.

Our detailed procedure of evaporation is the following:

- we pump the sample during 12 hours in the evaporator to reach a pressure of 5.10^{-8} mbar in the loadlock,
- we heat the sample at 110°C during 2 hours to get rid of the residual water on the surface of the chip,
- we start circulation of liquid nitrogen in the sample holder to rapidly cool down the sample[3] (see the temperature evolution during evaporation on Fig. 10.12). Temperature reaches 0°C in 1 minute and continues to decrease.
- At 0°C, we start the deposition of a 3 nm layer of Ti the normal axis of the sample being tilted of 30° with respect to the direction of evaporation (like on Fig. 10.11). Afterward we evaporate 1 nm of Ti the sample being tilted of -30°. At this point the temperature is around -40°C and the pressure gets down to 3.10^{-8} mbar.
- Next we evaporate 100 nm of Al at -30° and 40 nm of Al at +30°. At the end temperature has reached -80°C.
- Finally the sample is heated up at room temperature.

10.5 Room temperature characterization

When fabrication is finished, we test our samples in a probe station at room temperature. Sample contact resistances are measured between pairs of big aluminum pads.

Transparency of the good contacts The transparency of the good contacts are evaluated by two-points measurements between two nearby forks.

---

[3] Pipelines have to be cooled down before. It avoids that the liquid nitrogen evaporates before reaching the sample holder and allows a more rapid cooling.

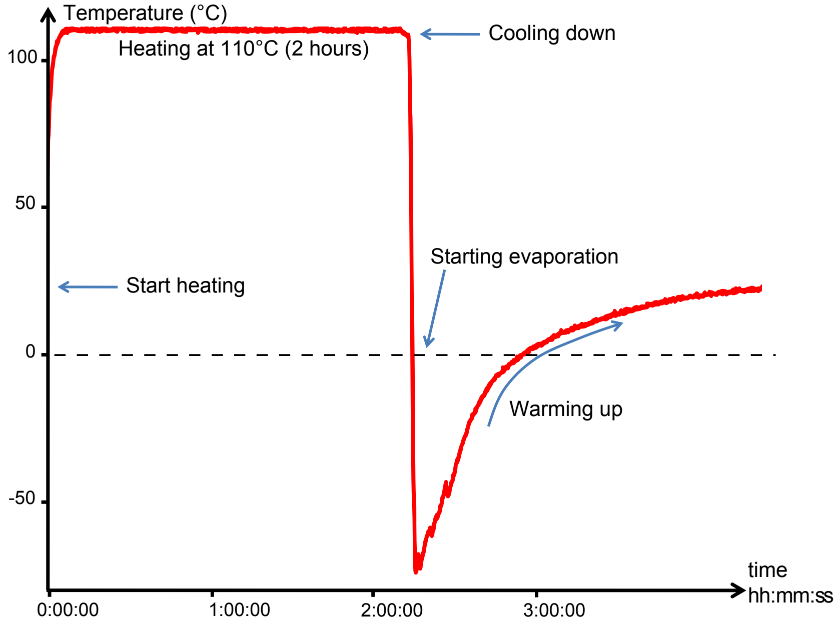

Figure 10.12: Evolution of temperature in the loadlock during our evaporation procedure

This measurement gives, for roughly one third of the samples, contact resistances between 11 and 50 kΩ[4]. This result has to be compared to the maximum resistance expected for a ballistic CNT which corresponds to about 6.5 kΩ [141]. Transmissions of devices are then included between 0.5 and 0.1[5].

If this first test is conclusive, we test resistances between tunnel probes and their corresponding forks.

Tunnel contacts characterization To be in the tunneling regime, the resistance between a tunnel probe and its corresponding fork has to be 10 times higher than quantum of resistance $R_K = h/e^2$. At room temperature, this two-points measurement gives generally on a given sample very heterogeneous results between 80 kΩ and 10 MΩ or even more. They could thus not all be selected to perform the spectroscopy of ABS.

We found out experimentally that, once cooled down, a sample is indeed

---

[4] The rest of the samples were either not showing measurable contacts or contacts up to several MΩ.

[5] The criterion to know if contacts are good enough for us is not simple. But we knew from theoretical estimation that if the transmission was lower than 0.1, we expected the ABS to have an energy dependence with the phase smaller than 5% of $|\Delta|$. This has to be compared with the ABS full width at half maximum (FWHM) which gives approximately our limit of resolution. The ABS we have observed have a FWHM of roughly 10% of $|\Delta|$.

in the tunnel regime if its room temperature tunnel contact is above 150 kΩ. At 35 mK such resistances increase to reach values above 200 kΩ.

Our procedure of fabrication gives us about 10% of samples with well connected electrodes and tunnel electrodes with appropriate contact resistances at the same time. It yields well connected electrode 30% of the time. But when we obtain good contacts, tunnel contacts are in the required range only 20-30% of the time. The efficiency of this fabrication process is only 10% in the end.

Influence of the probe We have checked if the tunnel probe did not cut electrically the CNT by measuring the two-points resistance at room temperature between pairs of good contacts that are separated by a tunnel probe (see Fig. 10.13). This indicates that tunnel probes don't cut electrically CNT. However this test has not been done systematically on our sample as it requires a specific geometry which was not needed for the experiment we wanted to perform.

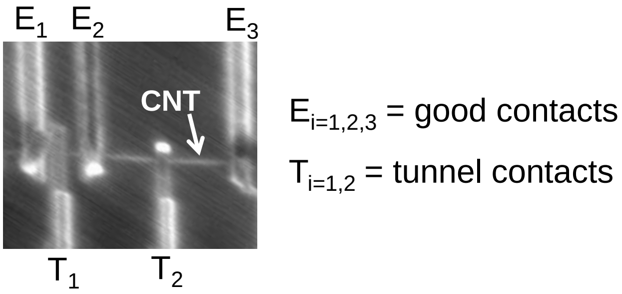

Pairs of electrode	Resistance value between them
E_1-E_2	14 kΩ
E_2-E_3	34 kΩ
T_1-E_1	750 kΩ
T_1-E_2	720 kΩ
T_2-E_2	500 kΩ
T_2-E_3	480 kΩ

INFLUENCE OF THE TUNNEL PROBE ON THE CONDUCTANCE BETWEEN GOOD CONTACTS

Figure 10.13: SEM picture and two-points resistance values of a test sample used to prove that tunnel probes don't cut electrically CNT between two good contacts.

Chapter 11

Parameters and techniques for fabrication

11.1 Preparation of the resist layers or bilayers

To coat the substrates, we deposit on it drops of resist diluted in solvent. We then spin it at 4000 revolutions per minute (rpm) to form an homogeneous layer. Next we bake it on a hot plate at 170°C. This procedure can be repeated to form a thicker layer of resist or a bilayer of distinct resists. The baking at 170°C evaporates the solvent and avoids the mixing of the different layers on the chip.

We use two different kinds of masks that are obtained by different recipes given in table 11.1. They differ by the type of resist layer coated on the substrate. This is either a single layer of polymethyl-meta-acrylate (PMMA) or a bilayer of polymethyl-meta-acrylate/meta-acrylate acid (PMMA/MAA). MAA being more electro-sensitive than PMMA, a bilayer of PMMA/MAA gives suspended masks after development.

11.2 Exposure: parameters and resulting masks after development

11.2.1 Parameters of exposure

In this table are detailed parameters used during exposure in the SEM for each type of mask.

Mask for the catalyst pads (thick PMMA single layer):

1. Spin 950K A6 PMMA[a] at 4000 rpm for 1 minute,
2. bake at 170°C for 1 minute,
3. spin another identical layer,
4. bake at 170°C for 10 minutes.

This first recipe gives a thick single layer of PMMA which is sufficient for catalyst deposition.

Mask for the alignment marks (PMMA/MAA bilayer):

1. Spin MAA 8.5 EL10[b] at 4000 rpm for 1 minute,
2. bake at 170°C for 10 minutes,
3. spin 950K PMMA A3[c] at 4000 rpm for 1 minute,
4. bake at 170°C for 15 minutes.

This second recipe gives a bilayer of PMMA/MAA which makes the lift off easier after metal deposition.

Mask for the contacts to the nanotube (PMMA/thick MAA bilayer):

1. Spin MAA 8.5 EL10 at 4000 rpm for 1 minute,
2. bake at 170°C for 1 minute,
3. Spin MAA 8.5 EL10 at 4000 rpm for 1 minute,
4. bake at 170°C for 10 minutes,
5. spin 950K PMMA A3 at 4000 rpm for 1 minute,
6. bake at 170°C for 15 minutes.

This third recipe gives a bilayer of PMMA/MAA with a thick layer of MAA. For a given shift between metal evaporations (see Fig. 10.11), this thickness will allow us to perform angle evaporations with smaller angle than with a thinner layer of MAA.

---

[a] PMMA of molecular weight 950000 diluted at 6% in anisole from MicroChem

[b] MAA of molecular weight 8500 diluted at 10% in ethyl-lactate from MicroChem

[c] PMMA of molecular weight 950000 diluted at 3% in anisole from MicroChem

Table 11.1: Recipes to obtain an homogeneous layer of PMMA or bilayers of PMMA/MAA.

pattern exposed	Dose and parameters
catalyst pads	$350\mu C/cm^2$ at 25 kV spot 1[1]
alignment marks	$4000\mu C/cm$ at 10 kV spot 5
contacts to the nanotubes	$250\mu C/cm^2$ ($\times 1.4$ for small structures) at 25 kV spot 1
undercut boxes	$25\mu C/cm^2$ at 25 kV spot 1

When we want to expose an area, we have to choose a dose defined in $\mu C/cm^2$. But for patterns defined by lines, the dose is defined in $\mu C/cm$ and the width of the obtained patterned line depends on the magnitude of the dose.

The chosen step of exposure is 2 nm for the small structures to obtain a high enough resolution. We choose several μm for large structure.

Once we have chosen the current of exposure and the step, EQ calculate automatically the dwell time given by:

$$t_{dwell\,time} = \frac{Dose \times step^2}{current}$$

11.2.2 Resulting masks after development

- Development for a PMMA single layer:

Development of a 950K A6 PMMA single layer gives an non suspended mask. If we wanted to evaporate metal, a suspended mask would be preferable (see below). But when we want to deposit catalyst, a single thick layer is sufficient to obtain well defined patterns that will give compact and dense catalyst pads yielding an efficient and controlled growth of CNT (see Fig. 11.1).

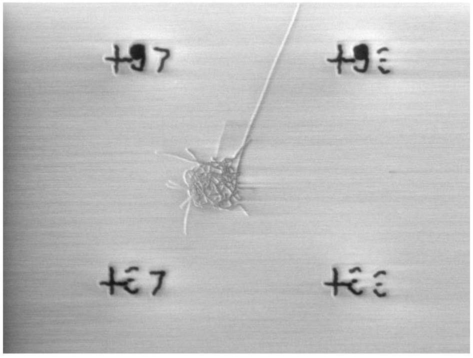

Figure 11.1: CNT growth obtained from well defined catalyst pads.

---

[1] Spot 1 corresponds typically to 20 pA and spot 5 to 2 nA of current for the electron beam.

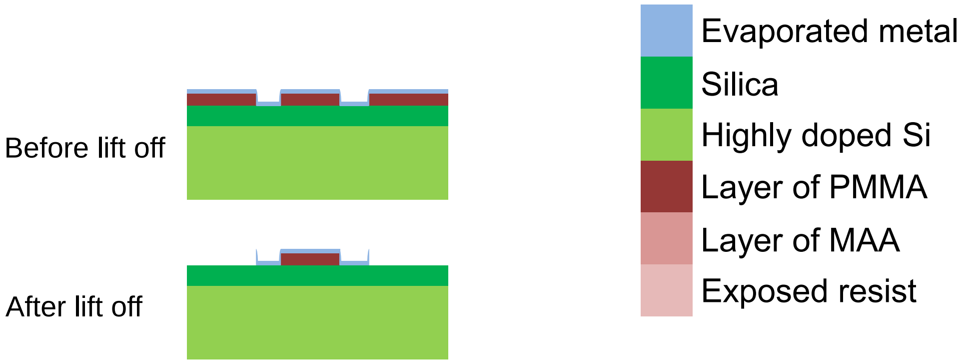

Figure 11.2: With a single layer of PMMA and after a metal evaporation, the mask may not lift properly or not at all if the resist cannot be reached by its solvent.

- Development for PMMA/MAA bilayer:

Development of a PMMA/MAA bilayer gives suspended masks of PMMA supported by MAA (see Fig. 10.2). We perform angle evaporation using this kind of mask. It can be also useful to make the lift off easier for small structures which may not lift properly otherwise (see Fig. 11.2).

With such mask, because of proximity effect, represented by a zigzag arrow in Fig. 10.2 (a), we need several iterations to obtain a correct mask.

Once a mask is done, we deposit either catalyst for CNTs growth, or metals with an electron beam evaporator for alignment marks and electrodes connecting CNTs. After deposition, the mask is removed by lift off in acetone. Technique of catalyst deposition and principle of metal evaporation are described respectively in section 11.3 and 11.4.

11.3 Catalyst preparation and deposition

11.3.1 Catalyst suspension preparation

The catalyst suspension is obtained by dispersion of the following ingredients in 15 ml of methanol:

- 20mg iron nonahydrate powder,

- 15mg aluminum oxide powder,
- 1mg bis(acetylaceto)-dioxomolybdenum (VI) powder.

The solution is sonicated during 15 minutes to homogenise suspension. The sonication has also to be performed 10 minutes before each deposition.

11.3.2 Catalyst deposition

Disposition of the catalyst on the chip influences dramatically the concentration of CNT grown on the substrate (see Fig. 11.1). We have determined empirically that we obtain the appropriate concentration by having on the chip 4 networks of 30 pads. Pads are distant of 40 μm from each other. The 4 networks will give 4 different potential samples after the 1×1 cm^2 chip has been cut up in four 5×5 mm^2 chips (see Fig. 10.4).

To obtain such networks, we dispense on the chip on the mask 2 drops of the catalyst suspension which has been freshly sonicated during 10 minutes. The methanol is evaporated from the chip slowly under a petri dish slightly tilted so that the vapor can escape. This process lets a thin layer of catalyst. After a lift off of 10 minutes in acetone at 65°C, only catalyst remains in the lithographically defined pads. The chip is then rinsed with acetone and isopropanol.

11.4 Metal deposition and lift-off

11.4.1 Description of the electron gun evaporator

We deposit gold (Au), titanium (Ti) and aluminum (Al) on our samples in two similar electron gun evaporators[2] . They are divided in two chambers: a loadlock and a main chamber (see Fig. 11.3).

In the main chamber are located crucibles in which are positioned the different available metals. Deposition is realized by heating the desired target with an electron beam gun. Deposition rate, typically between 0.1 and 1 nm/s, is computer controlled through a quartz microbalance.

In the loadlock, a sample holder is attached to an arm which can be tilted between - and +90° for angle evaporation. This sample holder can be heated by an electrical heater to 400°C, or cooled down to nearly -200°C by circulation of liquid nitrogen. Pressure in this chamber[3] is lower than 10^{-6} mbar after 30 minutes of pumping and reaches 3.10^{-8} mbar after one night.

---

[2] Electron gun evaporator fabricated by PLASSYS

[3] Pressure in the lower chamber is slightly lower.

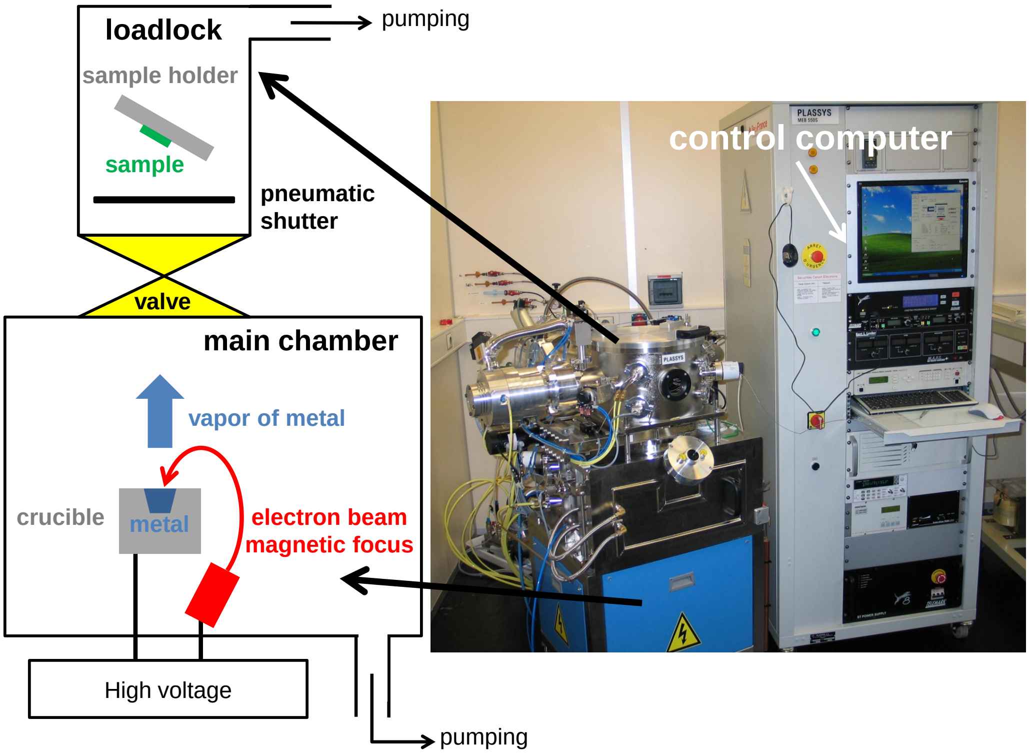

Figure 11.3: Schematic and picture of a PLASSYS e-gun

When we vent the loadlock, the main chamber remains isolated thanks to a valve to maintain its pressure low. Repumping after venting is then faster and there are less risks of pollution of the main chamber. This low pressure environment is crucial to obtain good metallic contacts by evaporation on nanotube.

11.4.2 Lift off

The last step of fabrication is the lift off. The resist on the chip is dissolved during 10 minutes in acetone heated on a hot plate at 65°C. Afterward, only metallic patterns and CNT remain on the chip (see Fig. 11.4).

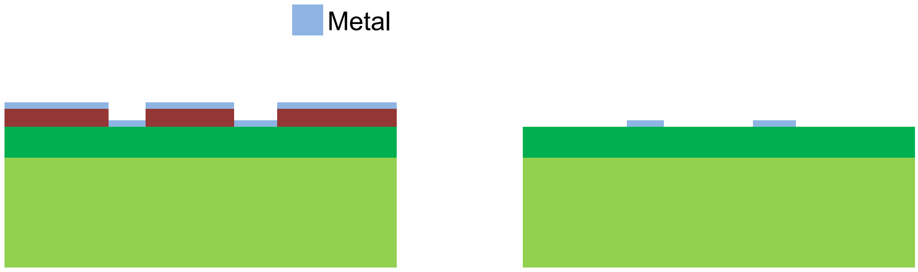

Figure 11.4: After metal deposition, the resist is removed by lift off and just metal and CNTs remain on the chip.

Part V

Appendices

Appendix A

Introduction to Quantum dots

The term of Quantum Dot (QD) designates systems such as molecules, small aggregates of semiconducting or metallic materials which are semi-isolated from bulk conducting materials and in which few-electron effects play a large role. The ab-initio physics of QD is a complicated many-body problem that cannot be solved exactly. However in some ranges of parameters, QD may be described by some fairly simple effective models, such as a independent particle-in-a-box model with interactions accounted for simply by a charging energy. In this case, when the dot is weakly connected to electrodes, one deals with simple Coulomb blockade physics, electrons being added one by one to the dot. On the other hand, when the dot is well coupled to some conducting reservoirs, many-body interaction effects lead to a variety of Kondo effects that require elaborate theoretical methods to capture them.

A.1 Energy quantization in QDs

Confined systems or QDs, such as those mentioned above, are first of all boxes or “pools” of electrons [17] whose electronic structures are quantized in discrete quantum states like in atoms. For that matter, they are often regarded as artificial atoms [142].

If we ignore for the moment Coulomb interactions, this quantization arises from boundary conditions of the box and, therefore, depends only on its geometry. For example, in nanopillars of semiconductor, the cylindrical geometry leads to orbital states with quantized radial and angular components [143]. When, as in our experiment, the QD is a quasi one-dimensional single walled CNT whose boundaries are marked by the leads, the system can be regarded as a quasi one-dimensional box. The CNT acquires thus a simple electronic structure whose levels form a ladder of discrete energies [144],

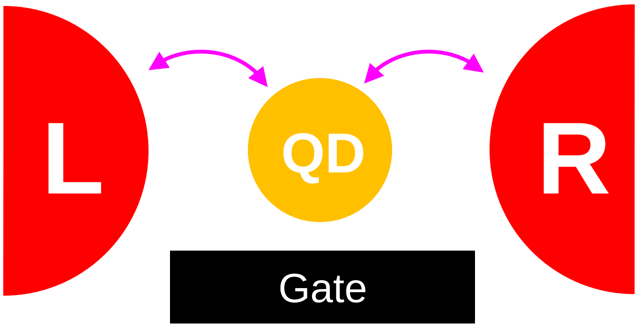

Figure A.1: Illustration of a QD connected to left (L) and right (R) electrodes through tunneling processes. An additional electrode called the gate is capacitively coupled to the QD in order to control its electro-chemical potential with a voltage. In such geometry, one can perform an electronic transport experiment which gives access to the energy spectrum of the latter in the weak coupling limit (see section A.3).

each of these levels being moreover fourfold degenerate [128, 145] because of the spin and the quantized orbital momentum[1] symmetries [146]. In absence of interaction, a QD can thus be adequately described by the following Hamiltonian:

$$H_{D0} = \sum_{n,\sigma} \epsilon_{n\sigma} d^\dagger_{n\sigma} d_{n\sigma}$$

where $d_{n\sigma}$ is a fermionic annihilation operator associated to a QD's eigenstate of energy $\epsilon_{n\sigma}$, orbital state n and spin σ.

To explore the energy spectrum of a QD, one can perform electronic transport experiments between a source and a drain, with an additional capacitively coupled gate electrode controlling the electro-chemical potential of the dot. The system is illustrated in Fig. A.1 with a left and right electrode that we respectively call from now on the source and the drain.

It is, however, crucial in this case to understand how the coupling to metallic electrodes affects the system and what will be the influence of Coulomb repulsion between electrons. In the following, we discuss these aspects in regimes of weak coupling to the leads and strong coupling to the leads. In QDs, the physics is actually dominated by these essential ingredients. But first, we explain how to describe the system of an interacting QD

---

[1] In dirty CNTs the orbital symmetry is generally broken and this fourfold degeneracy is lost.

connected to electrodes.

A.2 Hamiltonian description of the system

A QD can be modelled through the following Hamiltonian:

$$H = H_L + H_R + H_D + H_T \tag{A.1}$$

where H_L (resp. H_R) describes the left (resp. right) isolated leads, H_D the isolated dot itself and H_T the coupling between the dot and the leads.

H_L (resp. H_R) describes a normal non-interacting Fermi liquid[2]:

$$H_{L(R)} = \sum_{l(r),\sigma} \epsilon_{l(r)} c^{\dagger}_{l(r)\sigma} c_{l(r)\sigma}$$

with $c_{l(r)\sigma}$ a fermionic operator associated to the annihilation of an electron of spin σ in the eigenstate l (resp. r) of the isolated left (resp. right) lead.

The coupling H_T describes the hopping that takes place between states of the leads and the dot:

$$H_T = \sum_{n,l,\sigma} t_{n,l} d^{\dagger}_{n\sigma} c_{l\sigma} + t^{*}_{n,l} c^{\dagger}_{l\sigma} d_{n\sigma} + \sum_{n,r,\sigma} t_{n,r} d^{\dagger}_{n\sigma} c_{r\sigma} + t^{*}_{n,r} c^{\dagger}_{r\sigma} d_{n\sigma}$$

Finally, H_D concerns the QD and is composed of H_{D0}, describing electrons as independent particles occupying orbital eigenstates of the dot, and H_{int} which introduces correlations between them via interactions. The latter may include coupling of the electrons to mechanical vibrations of the QD's atomic lattice [147, 148] (electron-phonon interaction), spin-orbit coupling [149], exchange [98] (for a double QD) or Coulomb interaction between electrons.

In the following, we will consider only local Coulomb repulsion. In a QD containing many electrons, this type of interaction takes the universal form [150]:

$$H_{int} = \frac{E_C}{2} \left(N_D - \mathcal{N}\right)^2$$

with $N_D = \sum_{n,\sigma} d^{\dagger}_{n\sigma} d_{n\sigma}$ the particle number operator of the dot, $E_C = \frac{e^2}{C}$ the charging energy of the dot where C is the capacitance of the dot ($C = C_g + C_s + C_d$ with C_g the capacitance between the dot and the gate, C_s between the source and the dot, and C_d between the drain and the dot). $\mathcal{N}$ is a scalar, it gives the average number of electrons in the ground state and

---

[2] They may be replaced by BCS Hamiltonians for the case of superconducting leads.

depends on voltages applied on the gate and the source. This description, in which we parametrize the Coulomb interaction by a constant capacitor C, is actually fully justified only for large dots in which $\mathcal{N} \gg 1$. Validity of this approach is discussed in great details in Ref. [151, 152].

Physics of such system is governed by the interplay between the coupling of the QD to the leads which allows current to flow between L and R, and H_{int} which tends either to limit this flow, or to localize a spin in the QD driving the ground state in a highly correlated Kondo state. In the following discussion, we will distinguish two cases: weakly coupled QDs ($\langle H_T \rangle \ll \langle H_{int} \rangle$) and strongly coupled QDs ($\langle H_T \rangle \gg$ or $\approx \langle H_{int} \rangle$).

A.3 Weakly coupled QDs

For an interacting QD weakly coupled to its leads ($\langle H_T \rangle \ll \langle H_{int} \rangle$), we can address interactions in an essentially classical way (see for example Ref. [113]) where the physics is governed by the quantization of the charge. Indeed, in this case, the dot can be considered as isolated ($H \approx H_D$) and eigenstates of the system are given by the familiar classical state: one charge in the dot, two charges in the dot, etc... The number of charge can be regarded as a classical variable. This assumption is completely valid if the time spent by an electron in the dot is the largest time scale of the system including the coherence time: we will say that the system is in the classical regime.

In this regime and provided that energies $\epsilon_{n\sigma}$ are unaffected by interactions, the ground state energy of the system containing N electrons is given by [117]:

$$U(N) = \frac{1}{2C}\left[e(N - N_0) - C_g V_g - C_s V\right]^2 + \sum_N \epsilon_{n\sigma}$$

where V_g is the voltage applied on the gate, V the voltage applied on the source (the drain is grounded), N_0 the number of electrons[3] in the dot when $V = V_g = 0$, and the sum in the last term runs over all the occupied state.

From $U(N)$, we can deduce the electronic transport properties of the system. In particular, we can describe how the QD is sequentially filled when tuning the backgate, and also the so-called Coulomb blockade.

---

[3] We need to mention that in systems with a large number of electrons, we do not know N_0. We use as a variable the number of electrons in excess ($N - N_0$).

A.3.1 Sequential filling

In this regime, we can perform a sequential filling of the QD, electron by electron and orbital after orbital. Indeed, if μ is the common electrochemical-potential of the left and right leads, the condition for the QD to contain N electrons is:

$$\mu\,(N+1) > \mu > \mu\,(N)$$

with $\mu\,(N)$ the electro-chemical potential of the dot when it contains N electrons:

$$\mu\,(N) = U\,(N+1) - U\,(N)$$

Thereby, increasing the gate voltage, we can bring $\mu\,(N+1)$ below μ and add an extra electron in the dot.

This is illustrated in Fig. A.2 (adapted from figure 2. (b) of Ref. [117]) where orbitals are represented by black circles (whose radii indicate the relative magnitude of the orbital energies), electrons by blue dots, and the red dot symbolizes the center of the QD. At the beginning of this sequence, the QD is singly occupied with, in the lower orbital, an electron that is free to choose its spin. Increasing V_g, we add, in the same orbital, a second electron that, due to the Pauli principle, must be of exactly opposite spin. Despite the degeneracy of these two states, this process can only happen if the system is sufficiently lowered in energy (with the gate) to compensate the charging energy E_C. If we continue to increase V_g, we will add a third electron in the system but in the next orbital. The addition energy includes this time the charging energy plus the energy difference between orbitals $\Delta E = \epsilon_{n+1\sigma} - \epsilon_{n\sigma}$. The fourth electron will end in the same orbital but with a spin that is the exact opposite of the third one.

Note that this simple sequential filling of the orbitals is not always observed. For instance, in QDs with a reduced number of electrons [143], and with a shell of degenerate orbitals, this shell is first filled, by virtue of Hunds rule, with electrons of parallel spins until the shell is half full. After that, the filling continues with anti-parallel spins. Also, in QDs with reduced number of electrons, the charging energy may vary from one orbital to another.

A.3.2 Coulomb spectroscopy and Coulomb diamonds

The fact that the QD fills sequentially allows to perform a Coulomb spectroscopy of the QD. It can be realized through measurements of the differential conductance between the left source and the right drain at $V = 0$. Each time the QD's electro-chemical potential is equal to those of the left and right electrodes μ, electrons can flow through the QD and a peak of

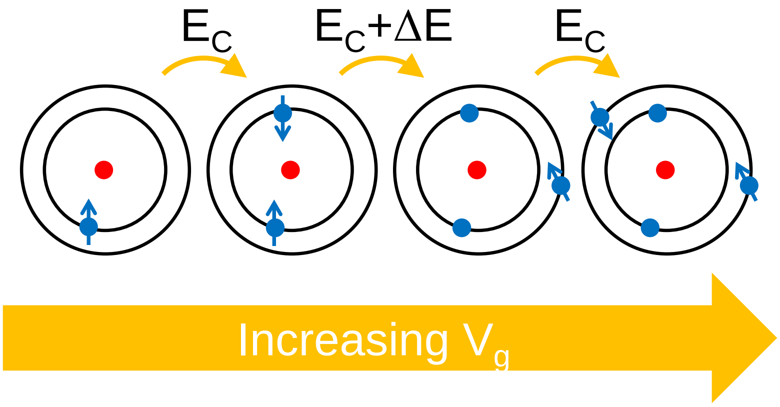

Schematic representation of electron additions in orbitals of a QD

Figure A.2: When a first electron is occupying an orbital, addition of a second electron costs an extra energy $E_C = e^2/C$. As the orbital can hold only two electrons, the second one is necessarily of opposite spin (by virtue of the Pauli principle), moreover addition of a third electron will take place in the next orbital and will cost $E_C + \Delta E$ with $\Delta E = \epsilon_{n+1\sigma} - \epsilon_{n\sigma}$ the energy difference between orbitals.

conductance develops whose width $\sim k_B T$ is imposed, in this regime, by the temperature (T is the temperature and k_B is the Boltzmann constant) [113]. As a consequence, provided that the charging energy E_C is constant and $k_B T < E_C$, we have a direct measurement of the relative orbital energies $\epsilon_{n\sigma}$. For example, in the sequence pictured in Fig. A.2, by increasing V_g we would observe three consecutive peaks of differential conductance with distance between them corresponding to $\Delta V_g = \frac{E_C + \Delta E}{C_g/C}$ between the first two peaks and only $\Delta V_g = \frac{E_C}{C_g/C}$ between the second and the third.

Extending this Coulomb spectroscopy to finite voltage bias, we obtain the so-called Coulomb diamonds. Indeed, when a voltage V is applied between the left and right leads, the condition for the QD to carry electrons from the left to right electrode (resp. from the right to left electrode) is $\mu_L \geq \mu(N) \geq \mu_R$ (resp. $\mu_L \leq \mu(N) \leq \mu_R$) with μ_L and μ_R the electrochemical potentials of the left and right leads (with $\mu_L - \mu_R = -eV$). These conditions define in the (V_g, V) plane, areas of blockade for each N, which take the shape of diamonds and where the charge in the QD is well defined.

In Fig. A.3, we have represented these diamonds for $N = 2n + 1$, $2n + 2$, $2n + 3$ and $2n + 4$ (n is an arbitrary integer). Widths and heights of these diamonds are directly related to their corresponding addition energies. Even diamonds (*i.e.* areas where the QD contains an even number of charge) are thus larger than odd diamonds: when N is even, addition of an electron necessarily takes place in the next orbital and the addition energy includes the charging energy plus the energy difference between orbital ΔE.

The Coulomb blockade has been observed extensively in CNTs and has allowed, for example, to observe the fourfold degeneracy through periodicity of the diamonds [153, 154, 145], electron-hole symmetry in semiconducting CNT [155], or spin-orbit coupling [149, 128]. Note that in these two last references the spectroscopy, though based on the same principle, was performed differently: in Ref. [149], the Coulomb spectroscopy was performed at fixed V_g and tuning V, whereas in Ref. [128] the spectroscopy was performed in the inelastic cotunneling regime (in this appendix, we will not address cotunneling events that are exchange of electrons occurring between the source and the drain at finite V through second order coherent tunneling processes).

Whereas the classical description we have presented so far is sufficient to understand physics related to the charge quantization, it cannot however describe phenomena that are of coherent nature like coherent exchange of electrons between the QD and its leads. It is indeed only valid under the assumptions that $\langle H_T \rangle \ll \langle H_{int} \rangle$ but also if particles systematically lose their coherence during the time spent in the QD. In the following, we present a phenomenological approach, from Ref. [16], which allows to address coherent

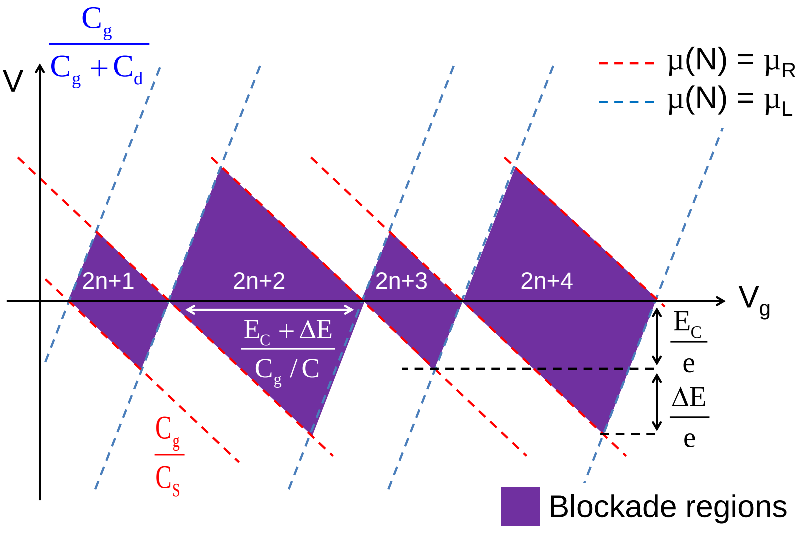

Coulomb diamonds

Figure A.3: Schematic representation of four Coulomb diamonds in the (V_g, V) plane. In regions of blockade (in violet), the charge in the QD is well defined and takes values $N = 2n + 1$, $2n + 2$, $2n + 3$ and $2n + 4$ (n is an arbitrary integer). Borders of this violet areas are defined by the conditions $\mu(N) = \mu_L$ (in blue) or $\mu(N) = \mu_L$ (in red) and, as indicated on the diagram, slopes of these borders are related to the capacitive couplings between the dot and the electrodes (including the gate). The height and the width of a diamond is related to the addition energy which is equal to the charging energy E_C for odd diamonds and the charging energy plus the energy difference between orbitals $E_C + \Delta E$ for even diamonds.

exchange of electrons between the QD and its leads in the weakly coupled regime.

A.4 Weakly coupled QDs in a coherent regime: a phenomenological approach

Whereas coherence of electrons in non-interacting QDs can be elegantly addressed with the scattering approach of Büttiker [56], and the interplay between charge and energy quantization can be correctly described with a semi-classical constant interaction model [113, 117], the simplest available model which brings together all these ingredients is the Anderson impurity model [63]. Unfortunately, and as mentioned before, there has been so far no exact solution found for this model. It has been yet analyzed using various approximations such as mean-field theory, perturbation expansion in the Coulomb interaction or in the tunnel coupling, but also exact numerical simulations based on the numerical renormalization group (NRG) (an exhaustive list of these methods can be found in Ref. [49] for the case of a QD connected to normal electrodes and Ref. [16, 71] and references therein for superconducting electrodes). However, all these methods either suffer of inaccuracy or are simply too much time-demanding.

A.4.1 A phenomenological approach

In Ref. [16], Vecino *et al.* have developed an effective and exactly solvable model which can correctly describe, for weakly coupled QDs, the coherent exchange of electrons between an interacting QD and its leads (in their work, the leads are actually superconducting and exchange electrons with the QD through Andreev reflections, but here we will only consider the case of normal electrodes in order to focus on the way they addressed interaction). This approach is based on a Hartree-Fock approximation. They describe the QD connected to its electrodes by means of a single-orbital Anderson model [63]:

$$H = H_L + H_R + \sum_{\sigma=\uparrow,\downarrow} \epsilon_0 d_\sigma^\dagger d_\sigma + E_C n_\uparrow n_\downarrow + \sum_{\sigma=\uparrow,\downarrow} \Big(t_L d_\sigma^\dagger c_{l\sigma} + t_R d_\sigma^\dagger c_{r\sigma} + h.c. \Big)$$

where ϵ_0 is the energy of the single orbital and $n_\sigma = d_\sigma^\dagger d_\sigma$. Then, the central approximation consists in replacing phenomenologically the repulsive interaction inside the QD by a local exchange field in such a way that:

$$\epsilon_\uparrow = \epsilon_0 - \frac{U}{2}$$

$$\epsilon_\downarrow = \epsilon_0 + \frac{U}{2}$$

with U a constant and $\epsilon_\uparrow$ (resp. $\epsilon_\downarrow$) the energy of a spin up (resp. down) electron in the QD. In absence of bias voltage between the leads, these energies can be related to the gate voltage as we have (with notations of previous section):

$$\epsilon_0 = \mu - e\frac{C_g}{C}V_g$$

We end up with an effective (non-interacting) Hamiltonian describing the system:

$$H_{eff} = H_L + H_R + \sum_{\sigma=\uparrow,\downarrow} \epsilon_\sigma d_\sigma^\dagger d_\sigma + \sum_{\sigma=\uparrow,\downarrow} \left(t_L d_\sigma^\dagger c_{l\sigma} + t_R d_\sigma^\dagger c_{r\sigma} + h.c. \right)$$

where d_σ is an annihilation operator for an electron of spin σ and the last term describes the coupling with the leads.

This model is formally equivalent to a mean field solution of Hamiltonian A.1, with the prescription $U = E_C \frac{\langle n_\downarrow - n_\uparrow \rangle}{2}$, except that here we will choose that U is a constant instead of calculating it self-consistently. It should be noted that, whereas in the classical approach of section A.3 spins of electrons were only taken into account through Pauli principle, here, an arbitrary spin is attributed to each level of the QD. If this can appear as an abusive symmetry breaking[4] introduced in the model, one has to keep in mind that the spin axis of quantization is actually not even specified. This choice just implies that if a second electron is added in the QD, it must have a spin opposite to that of the first one.

In the end, this model combines the advantages of a complete Hamiltonian treatment which allows to take into account the coherence of the system, and the ingredients of the classical approach: electrons take opposite spins within an orbital and fill sequentially the QD when increasing the gate. Except, here, the energies of the addition spectrum are replaced by single particle energy levels with the correspondence:

$$\mu(1) \leftrightarrow \epsilon_\uparrow \text{ and } \mu(2) \leftrightarrow \epsilon_\downarrow$$

In this thesis, we extensively used this phenomenological approach of Vecino *et al.*, to explain the formation of Andreev bound States in an interacting QD connected to superconducting leads.

---

[4] Broken symmetry is possible when the object that breaks the symmetry involves a macroscopic number of degrees of freedom, but here, we are dealing with a single spin.

A.4.2 Limits of this effective non-interacting model

This effective non-interacting model provides correct descriptions for mechanism based on single particle phenomena. It captures, for example, the broadening of the QD's levels caused by the coupling to leads with a continuum of states (reduction of quasiparticles' lifetime), or some aspects of the formation of Andreev Bound States when the leads are superconducting (see chapter 3 for comparison between exact NRG and phenomenological approach calculations).

There are however some shortcomings related to the fact that this approximation by essence completely ignores effects due to correlations between electrons. For example, as the spin operator:

$$S = d_\uparrow^\dagger d_\uparrow - d_\downarrow^\dagger d_\downarrow + \sum_l c_{l\uparrow}^\dagger c_{l\uparrow} - c_{l\downarrow}^\dagger c_{l\downarrow} + \sum_r c_{r\uparrow}^\dagger c_{r\uparrow} - c_{r\downarrow}^\dagger c_{r\downarrow}$$

commute with H_{eff}, spins of electrons are completely frozen and cannot fluctuate. Yet, in presence of interactions, electrons localized in the dot always have a certain quantum mechanical amplitude for their spin to flip by inversion with an electron of opposite spin from the electrodes. The corresponding spin flip rate τ_{sf} defines a temperature scale [17]:

$$k_B T_K = \frac{\hbar}{\tau_{sp}}$$

called the Kondo temperature above which these fluctuations are driven by thermal activation rather than quantum correlations. However for $T < T_K$, these fluctuations are quantum and lead to the formation of a many-body Kondo singlet state in which electrons of the leads screen the magnetic moment formed by electrons localized in the dot. In the following section, we discuss this phenomenon which arises when an interacting QD is strongly coupled to its leads

A.5 QDs with stronger coupling

For QDs which are more strongly coupled to their leads, the picture of a sequential filling with single electrons is generally not correct. One can mention the particular case of electronic devices made with single nanotubes which are so strongly coupled to their leads that charging effect becomes negligible. The CNTs thus act as coherent electron waveguides [7, 141] and electronic transport measurements can be understood within the Landauer-Büttiker formalism. This is called the Fabry-Perot regime. In this section, we focus on an intermediate case in which the coupling to the leads is strong and the Coulomb repulsion plays an important role driving the system into the Kondo regime in which electrons are highly correlated.

A.5.1 Spin-1/2 Kondo effect in nanostructures

The concept of Kondo state was originally introduced by Kondo to explain an anomalous increase of resistance which occurs in some metals at low temperature [49]. This phenomenon arises because of the formation, around residual magnetic impurities, of clouds of conduction electrons which scatter charge carriers near the Fermi level. In the ground state of the system, the magnetic moment and the conduction electrons form then a many-body singlet state.

The recent possibility to fabricate confined conductors has allowed to observe the Kondo effect on artificial magnetic impurities constituted by localized electrons [118, 126] and study this many-body phenomenon in a controlled way. The competition between coherent exchange of electrons with the leads and Coulomb repulsion inside the QD may indeed drive the system into a Kondo state. Because of Coulomb repulsion, a single electron can be trapped in the dot and form a localized magnetic moment. If the coupling to the leads is strong enough, the conduction electrons of the leads tends to screen this artificial magnetic impurity. This can be formally seen performing a Schrieffer-Wolff transformation on the Anderson Hamiltonian [65] which changes H_T+H_{int} into an antiferromagnetic interaction of the form $J \times \vec{S}_{cond}.\vec{S}_{QD}$ between the localized electron and the conduction electrons ($\vec{S}_{QD}$ is the spin of the QD, $\vec{S}_{cond}$ is the sum of the spins of the conduction electrons and J is the strength of the antiferromagnetic interaction).

In nanostructures, the Kondo effect manifests by the apparition of a peak of density of states at the Fermi level (or an enhancement of the conductivity, up to perfect transmission, at zero voltage bias in electronic transport experiment) for temperature below the so-called Kondo temperature. As a consequence, differential conductance measurements show, as in previous section, a Coulomb blockade pattern with Kondo ridge around $V = 0$ in areas of blockade corresponding to an odd number of charge in the QD (see Fig.A.4).

The Kondo temperature depends both on the strength of the Coulomb repulsion U and the coupling to the leads $\Gamma = \pi\rho_0 \left(t_L^2 + t_R^2\right)$ and takes the following form [49, 115, 119, 121]:

$$k_B T_K = \sqrt{\frac{\Gamma U}{2}} \exp\left(\frac{\pi\epsilon_0\left(\epsilon_0 - U\right)}{2\Gamma U}\right)$$

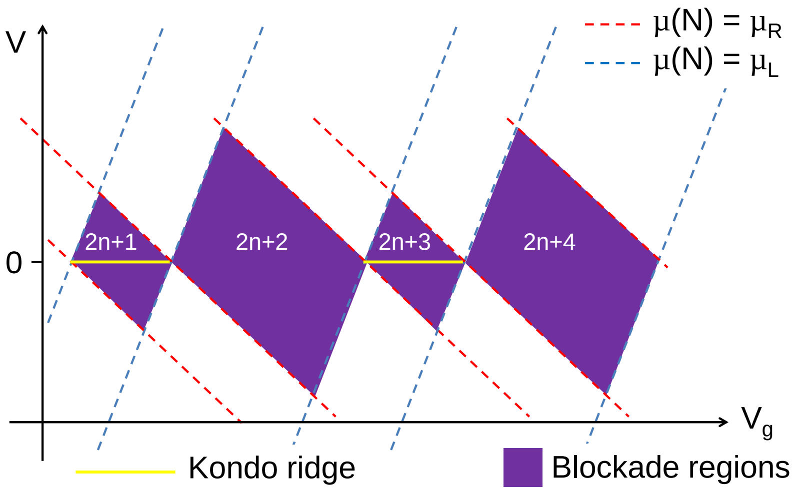

Figure A.4: Schematic representation of differential conductance measurements for a QD in the Kondo regime. The pattern is similar to the one of Fig. A.3 except that peaks of conductance, also called Kondo ridges, has appeared around $V = 0$ in diamonds corresponding to an odd number of electrons in the QD. These ridges appear at low temperature and their width is given by the Kondo temperature.

Note that since there is no analytic solution to the Kondo problem, this formula derived by Haldane is not expected to be exact. For increasing temperature, the zero-bias conductance amplitude in a quantum dot obeys a logarithmic dependence with T/T_K and completely disappears when T is far above T_K. When $T \ll T_K$, this energy scale also gives the HWHM of the conductance peaks through the relation:

$$\text{HWHM} \sim \frac{k_B T_K}{e}$$

A.5.2 Variety and universality of the Kondo effect

The Kondo effect has now been observed in a wide variety of man-made nanostructures: carbon nanotubes connected to normal [96], ferromagnetic [98] or superconducting contacts [9], molecular devices (see the review [119] and references therein) including fullerene [101] or adatoms deposited on a metallic surface [21, 156].

Moreover, it has also been seen in various type of situations: in double QDs [103], in systems with two degenerate orbitals [97], or in which the artificial magnetic impurities is not constituted by the spin of a single localized electron but rather by its orbital momentum [157] or the spins of two localized electrons in a triplet-state ($S = 1$). In the latter case, a major change with the spin-1/2 Kondo effect comes from the fact that the spin-1 Kondo effect happens for an even number of electrons localized in the QD [102] and involves two channels of screening.

In all these experiments, the various kind of many-body Kondo states differ in the details of their manifestation (double peak structure in double QDs, nonmonotonic temperature dependence of the Kondo ridge amplitude for $S = 1$ with much weaker Kondo temperature than for $S = 1/2$...), but share common robust universal features [158]: peaks of density of states at low energy, reduction of the zero-bias conductance with temperature, maximum transmission at $V = 0$, universal scaling with T/T_K...

Appendix B

Quantum dot Green's function

In this appendix we give some general definitions on Green's functions for system at equilibrium (section B.1 and B.2) and explain how to calculate the quantum dot's (QD) Green's function (GF) using equation of motion techniques (section B.3). In the last section, we show useful identities for calculation of the supercurrent and tunnel current, between lesser, greater, retarded and advanced GFs.

In all this appendix, Hamiltonian H is time-independent. In the particular case of a QD connected to superconducting electrodes, this supposes that none of the electrodes are voltage biased.

B.1 Definitions of the QD's GFs and TDOS

B.1.1 Green's functions in real time

The QD's GF is a causal correlation function from which can be calculated physical observables of the QD. In Nambu notation and time domain, it takes the form[1]:

$$\begin{aligned}\hat{\mathcal{G}}_{dd}\left(t\right) &= -i\langle T_t\psi_d\left(t\right)\psi_d^\dagger\left(0\right)\rangle \\ &= -i\begin{pmatrix} \langle T_t d_\uparrow\left(t\right)d_\uparrow^\dagger\left(0\right)\rangle & \langle T_t d_\uparrow\left(t\right)d_\downarrow\left(0\right)\rangle \\ \langle T_t d_\downarrow^\dagger\left(t\right)d_\uparrow^\dagger\left(0\right)\rangle & \langle T_t d_\downarrow^\dagger\left(t\right)d_\downarrow\left(0\right)\rangle \end{pmatrix}\end{aligned}$$

with t a time variable, $\psi_d\left(t\right) = e^{iHt}\psi_d e^{-iHt}$ the Heisenberg notation for the QD spinor field operator taking $\hbar = 1$ (we choose this convention for the

---

[1] We consider a problem with a time-independent Hamiltonian (or in other words a system invariant by translation in time) such that $\langle T_t\psi_d\left(t-t'\right)\psi_d^\dagger\left(0\right)\rangle = \langle T_t\psi_d\left(t\right)\psi_d^\dagger\left(t'\right)\rangle$. We can thus only consider correlation functions of the form $\langle T_t\psi_d\left(t\right)\psi_d^\dagger\left(0\right)\rangle$.

all appendix) and H the Hamiltonian. T_t is the time-ordering operator, it preserves causality of the Green's functions and is defined by:

$$T_t \psi_d(t)\,\psi_d^\dagger(0) = \theta(t)\,\psi_d(t)\,\psi_d^\dagger(0) - \theta(-t)\,\psi_d^\dagger(0)\,\psi_d(t)$$

with $\theta(t)$ the Heavyside function, and the brackets $\langle A\rangle$ symbolizes a thermal average of the quantum operator A. It can be expressed with the density matrix operator ρ:

$$\rho \equiv \frac{e^{-\beta H}}{Z} = \frac{1}{Z}\sum_\alpha |\alpha\rangle e^{-\beta E_\alpha}\langle\alpha|$$

with $\{|\alpha\rangle\}$ a complete basis set of the system, E_α the energy of state $|\alpha\rangle$, $\beta = 1/k_B T$ (with k_B the Boltzmann constant and T the temperature) and $Z = Tr\left[e^{-\beta H}\right]$ is the partition function. With this definition we have:

$$\langle A\rangle = \mathrm{Tr}\left[\rho A\right] = \frac{1}{Z}\sum_\alpha \langle\alpha\,|A|\,\alpha\rangle e^{-\beta E_\alpha} \tag{B.1}$$

At $T = 0$, this thermal average becomes an expectation value of A in the system ground state $|\psi_0\rangle$: $\langle\psi_0\,|A|\,\psi_0\rangle$.

B.1.2 Retarded and advanced Green's function in real time

We can also define the retarded and advanced GF of the QD by:

$$\hat{\mathcal{G}}^R_{dd}(t) = -i\theta(t)\,\langle\left\{\psi_d(t)\,,\psi_d^\dagger(0)\right\}\rangle \tag{B.2}$$

$$\hat{\mathcal{G}}^A_{dd}(t) = i\theta(-t)\,\langle\left\{\psi_d(t)\,,\psi_d^\dagger(0)\right\}\rangle \tag{B.3}$$

with:

$$\left\{\psi_d(t)\,,\psi_d^\dagger(0)\right\} = \begin{pmatrix} \left\{d_\uparrow(t)\,,d_\uparrow^\dagger(0)\right\} & \left\{d_\uparrow(t)\,,d_\downarrow(0)\right\} \\ \left\{d_\downarrow^\dagger(t)\,,d_\uparrow^\dagger(0)\right\} & \left\{d_\downarrow^\dagger(t)\,,d_\downarrow(0)\right\} \end{pmatrix}$$

and $\{A, B\} = AB + BA$ the anticommutator. They are useful for TDOS computation of the QD.

For supercurrent and tunnel current calculation, we need also to introduce the greater and lesser GF:

$$\hat{\mathcal{G}}^>_{id}(t) = -i\langle\psi_i(t)\,\psi_d^\dagger(0)\rangle$$

$$\hat{\mathcal{G}}^<_{id}(t) = i\langle\psi_d(0)^\dagger\,\psi_i(t)\rangle$$

where $i = l$ or r are index for the states of the left and right leads.

B.2 Matsubara formalism and equation of motion

The QD GF can be obtained by resolution of the equation of motion (EOM), a Heisenberg-like equation for GFs. This resolution is particularly simple in Matsubara formalism.

Here we introduce GFs in the Matsubara formalism and their EOM.

B.2.1 Notation in Matsubara imaginary time

For calculation of the QD's GF, it is convenient to introduce GFs in Matsubara formalism in which time and frequency arguments are imaginary quantities. They are defined by:

$$\begin{aligned} \hat{\mathcal{G}}_{dd}\left(\tau\right) &= -\langle T_\tau \psi_d\left(\tau\right)\psi_d^\dagger\left(0\right)\rangle \\ &= -\begin{pmatrix} \langle T_\tau d_\uparrow\left(\tau\right) d_\uparrow^\dagger\left(0\right)\rangle & \langle T_\tau d_\uparrow\left(\tau\right) d_\downarrow\left(0\right)\rangle \\ \langle T_\tau d_\downarrow^\dagger\left(\tau\right) d_\uparrow^\dagger\left(0\right)\rangle & \langle T_\tau d_\downarrow^\dagger\left(\tau\right) d_\downarrow\left(0\right)\rangle \end{pmatrix} \end{aligned} \tag{B.4}$$

with τ real, $\psi_d\left(\tau\right) = e^{H\tau}\psi_d e^{-H\tau}$ (the Heisenberg notation in imaginary time for the QD spinor field operator) and T_τ is a time-ordering operator acting on variable τ:

$$T_\tau \psi_d\left(\tau\right)\psi_d^\dagger\left(0\right) = \theta\left(\tau\right)\psi_d\left(\tau\right)\psi_d^\dagger\left(0\right) - \theta\left(-\tau\right)\psi_d^\dagger\left(0\right)\psi_d\left(\tau\right)$$

B.2.2 Fourier transform of the Matsubara GF

The imaginary time QD's GF can be expressed in frequency domain by Fourier transformation. And as we have the property $\hat{\mathcal{G}}_{dd}\left(\tau+\beta\right) = -\hat{\mathcal{G}}_{dd}\left(\tau\right)$ (this can be shown from expression $-\frac{1}{Z}Tr\left[e^{-\beta H}T_\tau\psi_d\left(\tau\right)\psi_d^\dagger\left(0\right)\right]$ of the GF, see for example [65]), the QD's GF $\hat{\mathcal{G}}_{dd}\left(i\omega_n\right)$ is then defined only on Matsubara frequencies ω_n taking discrete values:

$$\omega_n = \frac{2n+1}{\beta}\pi \text{ with } n \in \mathbb{Z} \text{ and } \beta = k_B T$$

with:

$$\hat{\mathcal{G}}_{dd}\left(\tau\right) = \frac{1}{\beta}\sum_{n=-\infty}^{+\infty} e^{-i\omega_n\tau}\hat{\mathcal{G}}_{dd}\left(i\omega_n\right) \text{ and } \hat{\mathcal{G}}_{dd}\left(i\omega_n\right) = \int_0^\beta e^{i\omega_n\tau}\hat{\mathcal{G}}_{dd}\left(\tau\right)d\tau$$

The Fourier transform $\hat{\mathcal{G}}_{dd}\left(i\omega_n\right)$ can be extended by analytical continuation everywhere in the complex plane into $\hat{\mathcal{G}}_{dd}\left(z\right)$.

The retarded and advanced GFs' Fourier transform are given by the value of this analytical continuation approaching the real axis from the upper and lower half of the complex plane (see section B.4), respectively[2] (here ω and η are real, and $\eta \to 0^+$):

$$\hat{\mathcal{G}}^R_{dd}(\omega) = \hat{\mathcal{G}}_{dd}(\omega + i\eta)$$

$$\hat{\mathcal{G}}^A_{dd}(\omega) = \hat{\mathcal{G}}_{dd}(\omega - i\eta)$$

They give access to every observable of the system at equilibrium [159].

B.2.3 Equation of motion

GFs can be calculated by resolution of the equation of motion (EOM). The latter is obtained by derivation of matrix B.4 with respect to time:

$$\frac{\partial \hat{\mathcal{G}}_{dd}(\tau)}{\partial \tau} = -\frac{\partial \theta(\tau)}{\partial \tau} \left\langle \psi_d(\tau)\psi_d^\dagger(0)\right\rangle + \frac{\partial \theta(-\tau)}{\partial \tau}\left\langle \psi_d^\dagger(0)\psi_d(\tau)\right\rangle - \langle T_\tau \frac{\partial \psi_d(\tau)}{\partial \tau}\psi_d^\dagger(0)\rangle$$

from which we can deduce the final form of the EOM:

$$\frac{\partial \hat{\mathcal{G}}_{dd}(\tau)}{\partial \tau} = -\delta(\tau)\left\langle \left\{\psi_d(0), \psi_d^\dagger(0)\right\}\right\rangle - \langle T_\tau \frac{\partial \psi_d(\tau)}{\partial \tau}\psi_d^\dagger(0)\rangle \tag{B.5}$$

In the following section, we solve this equation for a QD connected to superconducting leads.

B.3 Calculation of the QD's GF by resolution of the EOM

Here we calculate the QD's GF by resolution of the EOM.

We recall from section 3.1.1 that the QD is described by the following Hamiltonian:

$$H = \sum_{i=l,r} \psi_i^\dagger \mathcal{E}_i \psi_i + \psi_d^\dagger \mathcal{E}_{QD}\psi_d + \sum_l \left[\psi_d^\dagger \mathcal{E}_{T_L}\psi_l + h.c.\right] + \sum_r \left[\psi_d^\dagger \mathcal{E}_{T_R}\psi_r + h.c.\right]$$

with $\mathcal{E}_{QD} = \begin{pmatrix} \epsilon_\uparrow & 0 \\ 0 & -\epsilon_\downarrow \end{pmatrix}$, $\mathcal{E}_{l(r)} = \begin{pmatrix} \epsilon_{l(r)} & \Delta e^{i\phi_{L(R)}} \\ \Delta e^{-i\phi_{L(R)}} & -\epsilon_{l(r)} \end{pmatrix}$, and $\mathcal{E}_{T_{L(R)}} = \begin{pmatrix} t_{L(R)} & 0 \\ 0 & -t^*_{L(R)} \end{pmatrix}$.

---

[2] These expressions in the frequency domain are of course consistent with Eq. B.2 and B.3 where retarded and advanced GF are expressed in time-domain (see Ref. [65]).

B.3.1 Resolution of the EOM

The GF, that will give us access to the spectral density of the dot, $\hat{\mathcal{G}}_{dd}(\tau)$ is obtained by resolution of the EOM B.5. The latter starts by calculating the anticommutators $\left\{\psi_d(0), \psi_d^\dagger(0)\right\}$ and the derivative $\frac{\partial\hat{\psi}_d(\tau)}{\partial\tau}$:

$$\left\langle\left\{\psi_d(0), \psi_d^\dagger(0)\right\}\right\rangle = \begin{pmatrix} \left\langle\left\{d_\uparrow, d_\uparrow^\dagger\right\}\right\rangle & \left\langle\left\{d_\uparrow, d_\downarrow\right\}\right\rangle \\ \left\langle\left\{d_\downarrow^\dagger, d_\uparrow^\dagger\right\}\right\rangle & \left\langle\left\{d_\downarrow^\dagger, d_\downarrow\right\}\right\rangle \end{pmatrix} = \begin{pmatrix} 1 & 0 \\ 0 & 1 \end{pmatrix} = \mathbf{1}$$

$$\frac{\partial\hat{\psi}_d(\tau)}{\partial\tau} = \begin{pmatrix} \left[H, d_\uparrow(\tau)\right] \\ \left[H, d_\downarrow^\dagger(\tau)\right] \end{pmatrix} = -\mathcal{E}_{QD}\psi_d(\tau) - \sum_l \mathcal{E}_{T_L}\psi_l(\tau) - \sum_r \mathcal{E}_{T_R}\psi_r(\tau)$$

It can then be written in a Schrödinger like form:

$$\frac{\partial\hat{\mathcal{G}}_{dd}(\tau)}{\partial\tau} = -\delta(\tau)\,\mathbf{1} - \mathcal{E}_{QD}\hat{\mathcal{G}}_{dd}(\tau) - \sum_l \mathcal{E}_{T_L}\hat{\mathcal{G}}_{ld}(\tau) - \sum_r \mathcal{E}_{T_R}\hat{\mathcal{G}}_{rd}(\tau)$$

With the same method, we can also write the equations of motion followed by $\hat{\mathcal{G}}_{l(r)d}(\tau)$:

$$\frac{\partial\hat{\mathcal{G}}_{l(r)d}(\tau)}{\partial\tau} = -\mathcal{E}_{l(r)}\hat{\mathcal{G}}_{l(r)d}(\tau) - \mathcal{E}_{T_{L(R)}}\hat{\mathcal{G}}_{dd}(\tau)$$

Fourier transformations in Matsubara frequency of these equations provides the central linear system whose solutions are our quantities of interest:

$$\begin{cases} -i\omega_n\hat{\mathcal{G}}_{dd}(i\omega_n) & = -\mathbf{1} - \mathcal{E}_{QD}\hat{\mathcal{G}}_{dd}(i\omega_n) - \sum_l \mathcal{E}_{T_L}\hat{\mathcal{G}}_{ld}(i\omega_n) - \sum_r \mathcal{E}_{T_R}\hat{\mathcal{G}}_{rd}(i\omega_n) \\ -i\omega_n\hat{\mathcal{G}}_{l(r)d}(i\omega_n) & = -\mathcal{E}_{l(r)}\hat{\mathcal{G}}_{l(r)d}(i\omega_n) - \mathcal{E}_{T_{L(R)}}^\dagger\hat{\mathcal{G}}_{dd}(i\omega_n) \end{cases} \tag{B.6}$$

The second equation of B.6 gives the expression of $\hat{\mathcal{G}}_{l(r)d}(i\omega_n)$ as a function of $\hat{\mathcal{G}}_{dd}(i\omega_n)$:

$$\hat{\mathcal{G}}_{l(r)d}(i\omega_n) = \left[i\omega_n - \mathcal{E}_{l(r)}\right]^{-1}\mathcal{E}_{T_{L(R)}}^\dagger\hat{\mathcal{G}}_{dd}(i\omega_n) \tag{B.7}$$

This matrix is useful for Josephson current calculation. But for the moment by combining it with first equation of B.6 we can solve the system and extend the GF to all the complex plane by replacing $i\omega_n$ by z, where z can take any value in the complex plane:

$$\hat{\mathcal{G}}_{dd}(z) = \left[z - \mathcal{E}_{QD} - \hat{\Sigma}(z)\right]^{-1} \tag{B.8}$$

with:

$$\hat{\Sigma}(z) = \hat{\Sigma}_L(z) + \hat{\Sigma}_R(z)$$

$$\hat{\Sigma}_L(z) = \sum_l \mathcal{E}_{T_L}\left[z - \mathcal{E}_l\right]^{-1}\mathcal{E}_{T_L}^\dagger$$

$$\hat{\Sigma}_R(z) = \sum_r \mathcal{E}_{T_R} [z - \mathcal{E}_r]^{-1} \mathcal{E}^\dagger_{T_R}$$

To make this expression usable for further spectral density calculation, we need in a last step to evaluate the self-energy due to the coupling to the leads $\hat{\Sigma}(z)$.

B.3.2 Calculation of the QD's self-energy

The self-energy takes the form of two discrete sums over l and r:

$$\hat{\Sigma}_{L(R)}(z) = \sum_{l(r)} \frac{|t_{l(r)}|^2}{z^2 - \epsilon^2_{l(r)} - \Delta^2} \begin{pmatrix} z + \epsilon_{l(r)} & \Delta e^{i\phi_{L(R)}} \\ \Delta e^{-i\phi_{L(R)}} & z - \epsilon_{l(r)} \end{pmatrix}$$

To get rid of the discrete sum we need to make some assumptions, in order to replace it by an integral. As the superconducting gap Δ is generally orders of magnitude smaller than the bandwidth D ($\Delta \ll D$: Δ of aluminum is 210 μeV when bandwidth D is several eV large), we can reasonably approximate D as infinite and that the bands are flat. Within these assumptions, the self-energy becomes:

$$\hat{\Sigma}_{L(R)}(z) = \int_{-\infty}^{+\infty} \rho_F \frac{|t_{L(R)}|^2}{z^2 - \epsilon^2 - \Delta^2} \begin{pmatrix} z + \epsilon & \Delta e^{i\phi_{L(R)}} \\ \Delta e^{-i\phi_{L(R)}} & z - \epsilon \end{pmatrix} d\epsilon$$

with ρ_F the density of states for each spin population at the Fermi energy (in fact at any energies within our approximations) of the electrodes in their normal state.

Because $\frac{\epsilon}{z^2 - \epsilon^2 - |\Delta|^2}$ is an odd function with respect to ϵ, its integration from $-\infty$ to $+\infty$ is equal to zero and gives no contribution to $\Sigma(z)$.

By performing the variable change $x = \frac{\epsilon}{\sqrt{\Delta^2 - (i\omega_n)^2}}$, we obtain the final expression for $\hat{\Sigma}(z)$:

$$\begin{aligned} \hat{\Sigma}(z) &= \sum_{i=L,R} -\frac{\rho_F |t_i|^2}{\sqrt{\Delta^2 - z^2}} \begin{pmatrix} z & \Delta e^{i\phi_i} \\ \Delta e^{-i\phi_i} & z \end{pmatrix} \int_{-\infty}^{+\infty} \frac{1}{1+x^2} dx \\ &= \sum_{i=L,R} \frac{\pi \rho_F |t_i|^2}{\sqrt{\Delta^2 - z^2}} \begin{pmatrix} -z & -\Delta e^{i\phi_i} \\ -\Delta e^{-i\phi_i} & -z \end{pmatrix} \end{aligned}$$

With the introduction of functions $g(\omega) = \frac{-\omega}{\sqrt{|\Delta|^2 - \omega^2}}$ and $f(\omega) = \frac{\Delta}{\sqrt{\Delta^2 - \omega^2}}$, the self-energy adopts then the compact form:

$$\hat{\Sigma}(z) = \sum_{i=L,R} \Gamma_i \begin{pmatrix} g(z) & -f(z) e^{i\phi_i} \\ -f(z) e^{-i\phi_i} & g(z) \end{pmatrix}$$

where $\Gamma_{L(R)} = \pi \rho_F \left| t_{L(R)} \right|^2$.

B.3.3 Comment on the temperature dependence of the QD's GF

According to the final expression of $\hat{\mathcal{G}}_{dd}(z)$ and $\hat{\Sigma}(z)$, there is no temperature dependence of the TDOS $\mathcal{A}_{dd}(\omega)$, given by the imaginary part of the retarded GF (see section 3.1.2 in chapter 3). Even if nowhere in the calculation we have specified at which temperature we calculate expectation values of operators.

The reason is that Δ and U are considered, in our model, as fixed phenomenological parameters. They should however be calculated self-consistently, and in this case they would exhibit a temperature dependence (see for example [63] or [65]). A temperature variation would cause a redistribution of $\mathcal{A}_{dd}(\omega)$ over the energy spectrum. This is actually a general property of the strongly correlated system, but in our case we use an effective model of free quasiparticles, that's why there is no temperature dependence (the spectral density of a Fermi liquid for example has also no temperature dependence).

Yet, there are a temperature dependence of the tunnel current. Indeed the latter depends not only on the spectral density of the probe and the sample, but also on their thermal distributions (see appendix D).

B.3.4 Poles as roots of the inverse GF's determinant

The poles of the GF's diagonal elements are also the roots of the inverse GF's determinant.

Indeed, equation B.8 can also be written:

$$\hat{\mathcal{G}}_{dd}(z) = \frac{1}{\mathrm{Det}\left(z - \mathcal{E}_{\mathcal{QD}} - \hat{\Sigma}(z)\right)} \, {}^{t}\mathrm{com}\left[z - \mathcal{E}_{\mathcal{QD}} - \hat{\Sigma}(z)\right]$$

where ${}^{t}\mathrm{com}\left[z - \mathcal{E}_{\mathcal{QD}} - \hat{\Sigma}(z)\right]$ is the transposed comatrix of $\left[z - \mathcal{E}_{\mathcal{QD}} - \hat{\Sigma}(z)\right]$.

As elements of ${}^{t}\mathrm{com}\left[z - \mathcal{E}_{\mathcal{QD}} - \hat{\Sigma}(z)\right]$ have no pole except at $\pm\Delta$, poles of the diagonal element of $\hat{\mathcal{G}}_{dd}(z)$ are given by the roots of $D(z) = \mathrm{Det}\left(z - \mathcal{E}_{\mathcal{QD}} - \hat{\Sigma}(z)\right)$ or equivalently by $\mathrm{Det}\left(\hat{\mathcal{G}}_{dd}(z)^{-1}\right) = 0$.

B.3.5 Physical signification of a GF

Due to its physical signification, a GF is also called a propagator. Indeed, its diagonal elements contain information about the evolution of a bare particle (electron or hole) injected in the system, and its antidiagonal elements about the tendency for electrons to exist in pair in the ground state.

If we consider, for example, the case $t > 0$, the spin up diagonal elements of the GF is proportional to:

$$\langle\psi_0|e^{iHt}d_\uparrow e^{-iHt}d_\uparrow^\dagger|\psi_0\rangle \tag{B.9}$$

This function is the recovering between states:

$$e^{-iHt}d_\uparrow^\dagger|\psi_0\rangle$$

and:

$$d_\uparrow^\dagger e^{-iHt}|\psi_0\rangle$$

The first one gives the dynamic of a spin up electron injected in the ground state, through the QD, that we let evolve under H during a time t, whereas the second corresponds to a spin up electron injected in the system at t. Function B.9 compares this two states to test how much the injected electron has changed, and gives through its decaying time information on the electron's lifetime (infinite if the injected particle corresponds to an eigenstate of the system). For $t < 0$, the diagonal spin up element of the GF fulfils the same role but for a hole injected in the QD.

The non diagonal terms of the GF (or anomalous correlation functions), they contain information about pairing between electrons of opposite spin in the QD. For example:

$$\langle\psi_0|e^{iHt}d_\downarrow^\dagger e^{-iHt}d_\uparrow^\dagger|\psi_0\rangle$$

is the recovering product between states:

$$e^{-iHt}d_\uparrow^\dagger|\psi_0\rangle$$

and:

$$d_\downarrow e^{-iHt}|\psi_0\rangle$$

It gives therefore the probability amplitude to find, after a lapse time t, the time-reverse conjugated hole of an electron injected in the QD. In absence of induced superconductivity, these correlations functions would be equal to zero for charge conservation consideration. However, superconductivity authorizes charge fluctuations and these anomalous correlation functions can be different from zero.

B.4 Useful identities for calculation of the tunnel Density of states and supercurrent

In this section, we give demonstrations of the following relations (valid for any time-independent Hamiltonian):

$$f_{FD}\left(-\omega\right)\left[\hat{\mathcal{G}}^{R}_{ld}\left(\omega\right)-\hat{\mathcal{G}}^{A}_{ld}\left(\omega\right)\right]=\hat{\mathcal{G}}^{>}_{ld}\left(\omega\right)\text{ and }-f_{FD}\left(\omega\right)\left[\hat{\mathcal{G}}^{R}_{ld}\left(\omega\right)-\hat{\mathcal{G}}^{A}_{ld}\left(\omega\right)\right]=\hat{\mathcal{G}}^{<}_{ld}\left(\omega\right) \tag{B.10}$$

where $f_{FD}\left(\omega\right)$ is the Fermi-Dirac distribution. These relations are useful for calculation of the supercurrent (see section 3.1.5) and the tunnel current (it is done in section D.1.2.2).

First, we need to introduce the Lehmann representation of the advanced and retarded GF.

B.4.1 Lehmann representation

The Lehmann representation of a GF function is a decomposition on the eigenstates basis of H, noted $\{|\alpha\rangle\}$. To illustrate it, we consider a GF in real time:

$$\mathcal{G}\left(t\right)=-i\left\langle T_t a\left(t\right)b\right\rangle=\frac{-i}{Z}\sum_{\alpha}e^{-\beta E_\alpha}\left(\theta\left(t\right)\left\langle\alpha\left|a\left(t\right)b\right|\alpha\right\rangle-\theta\left(-t\right)\left\langle\alpha\left|ba\left(t\right)\right|\alpha\right\rangle\right)$$

where a and b are two operators creation or annihilation.

Using the property[3] $\sum_{\alpha'}|\alpha'\rangle\langle\alpha'|=\mathbb{I}$, we can write these GF:

$$\begin{array}{rcl}\mathcal{G}\left(t\right) & = & -\frac{i}{Z}\sum_{\alpha,\alpha'}e^{-\beta E_\alpha}(\theta\left(t\right)\left\langle\alpha\left|e^{iHt}ae^{-iHt}\left|\alpha'\right\rangle\left\langle\alpha'\right|b\right|\alpha\right\rangle\\ & & -\theta\left(-t\right)\left\langle\alpha\left|b\left|\alpha'\right\rangle\left\langle\alpha'\right|e^{iHt}ae^{-iHt}\right|\alpha\right\rangle)\end{array}$$

and as we have $H|\alpha\rangle=E_\alpha|\alpha\rangle$, it becomes:

$$\begin{array}{rcl}\mathcal{G}\left(t\right) & = & -\frac{i}{Z}\sum_{\alpha,\alpha'}e^{-\beta E_\alpha}(\theta\left(t\right)e^{i\left(E_\alpha-E_{\alpha'}\right)t}\left\langle\alpha\left|a\left|\alpha'\right\rangle\left\langle\alpha'\right|b\right|\alpha\right\rangle\\ & & -\theta\left(-t\right)e^{i\left(E_{\alpha'}-E_\alpha\right)t}\left\langle\alpha\left|b\left|\alpha'\right\rangle\left\langle\alpha'\right|a\right|\alpha\right\rangle)\end{array}$$

After Fourier transform, we end up with the Lehmann representation of $\mathcal{G}\left(t\right)$:

$$\mathcal{G}\left(\omega\right)=\frac{1}{Z}\sum_{\alpha,\alpha'}e^{-\beta E_\alpha}\left(\frac{\left\langle\alpha\left|a\left|\alpha'\right\rangle\left\langle\alpha'\right|b\right|\alpha\right\rangle}{\omega+i\eta+E_\alpha-E_{\alpha'}}+\frac{\left\langle\alpha\left|b\left|\alpha'\right\rangle\left\langle\alpha'\right|a\right|\alpha\right\rangle}{\omega-i\eta-E_\alpha+E_{\alpha'}}\right)$$

---

[3] $\mathbb{I}$ is the identity operator.

where the inverse and direct Fourier transform a of function h are respectively given by:

$$h\left(t\right)=\int h\left(\omega\right)e^{-i\omega t}\frac{d\omega}{2\pi}\text{ and }h\left(\omega\right)=\int h\left(t\right)e^{i\omega t}dt$$

and the Heaviside function Fourier transform (with $\eta\to0^{+}$)[4]:

$$\int\theta\left(t\right)e^{i\omega t}dt=i\frac{1}{\omega+i\eta}\text{ and }\int\theta\left(-t\right)e^{i\omega t}dt=-i\frac{1}{\omega-i\eta}$$

Following the same reasoning, we can find the Lehmann representation of the retarded ($\mathcal{G}^{R}\left(\omega\right)$) and advanced ($\mathcal{G}^{A}\left(\omega\right)$) GF:

$$\mathcal{G}^{R}\left(\omega\right)=\frac{1}{Z}\sum_{\alpha,\alpha'}e^{-\beta E_{\alpha}}\left(\frac{\left\langle\alpha\left|a\right|\alpha'\right\rangle\left\langle\alpha'\right|b\left|\alpha\right\rangle}{\omega+i\eta+E_{\alpha}-E_{\alpha'}}+\frac{\left\langle\alpha\left|b\right|\alpha'\right\rangle\left\langle\alpha'\right|a\left|\alpha\right\rangle}{\omega+i\eta-E_{\alpha}+E_{\alpha'}}\right)\tag{B.11}$$

$$\mathcal{G}^{A}\left(\omega\right)=\frac{1}{Z}\sum_{\alpha,\alpha'}e^{-\beta E_{\alpha}}\left(\frac{\left\langle\alpha\left|a\right|\alpha'\right\rangle\left\langle\alpha'\right|b\left|\alpha\right\rangle}{\omega-i\eta+E_{\alpha}-E_{\alpha'}}+\frac{\left\langle\alpha\left|b\right|\alpha'\right\rangle\left\langle\alpha'\right|a\left|\alpha\right\rangle}{\omega-i\eta-E_{\alpha}+E_{\alpha'}}\right)\tag{B.12}$$

B.4.2 Relation between lesser, greater, advanced and retarded GFs at equilibrium

Using Lehmann representations B.11 and B.12, we can find an expression for the greater and lesser GFs as a function of the retarded and advanced GFs. For this, we consider a greater GF with a general form (here again $\{|\alpha\rangle\}$ is the eigenstates basis of H):

$$\mathcal{G}^{>}\left(t\right)=-i\left\langle a\left(t\right)b\right\rangle=\frac{-i}{Z}\sum_{\alpha}e^{-\beta E_{\alpha}}\left\langle\alpha\left|a\left(t\right)b\right|\alpha\right\rangle$$

where a and b are two creation or annihilation operators. Using the property $\sum_{\alpha'}|\alpha'\rangle\langle\alpha'|=\mathbb{I}$, we can write:

$$\mathcal{G}^{>}\left(t\right)=-\frac{i}{Z}\sum_{\alpha,\alpha'}\left\langle\alpha\left|a\right|\alpha'\right\rangle\left\langle\alpha'\right|b\left|\alpha\right\rangle e^{i\left(E_{\alpha}-E_{\alpha'}\right)t}e^{-\beta E_{\alpha}}$$

After Fourier transform we find:

$$\mathcal{G}^{>}\left(\omega\right)=-2i\pi\frac{1}{Z}\sum_{\alpha,\alpha'}\left\langle\alpha\left|a\right|\alpha'\right\rangle\left\langle\alpha'\right|b\left|\alpha\right\rangle\delta\left(\omega+E_{\alpha}-E_{\alpha'}\right)e^{-\beta E_{\alpha}}\tag{B.13}$$

---

[4] This can be shown using residues theorem.

or thanks to the Dirac function:

$$\mathcal{G}^{>}(\omega) = -2i\pi \frac{1}{Z} \sum_{\alpha,\alpha'} \langle \alpha \left| a \right| \alpha' \rangle \langle \alpha' \right| b \left| \alpha \rangle \, \delta(\omega + E_\alpha - E_{\alpha'}) \, e^{-\beta E_{\alpha'}} e^{\beta\omega} \tag{B.14}$$

Moreover, as we have the equality $\frac{1}{x+i\eta} - \frac{1}{x-i\eta} = -2\pi i \delta(x)$, the difference between the retarded (B.11) and advanced (B.12) GFs gives:

$$\mathcal{G}^{R}(\omega) - \mathcal{G}^{A}(\omega) = -2i\pi \frac{1}{Z} \sum_{\alpha,\alpha'} \langle\alpha|a|\alpha'\rangle\langle\alpha'|b|\alpha\rangle \delta(\omega + E_\alpha - E_{\alpha'}) \left(e^{-\beta E_\alpha} + e^{-\beta E_{\alpha'}}\right)$$

This expression is actually also equal to the sum of Eq. B.13 and Eq. B.14 multiplied by $e^{-\beta\omega}$.

Therefore, we have the following relation between greater, advanced and retarded GF:

$$\mathcal{G}^{R}(\omega) - \mathcal{G}^{A}(\omega) = \mathcal{G}^{>}(\omega)\left(1 + e^{-\beta\omega}\right)$$

or by introducing the Fermi-Dirac distribution $f_{FD}(\omega)$, we end up with a relation between the greater, retarded and advanced GFs:

$$f_{FD}(-\omega)\left[\mathcal{G}^{R}(\omega) - \mathcal{G}^{A}(\omega)\right] = \mathcal{G}^{>}(\omega) \tag{B.15}$$

With the same method, we could also show:

$$-f_{FD}(\omega)\left[\mathcal{G}^{R}(\omega) - \mathcal{G}^{A}(\omega)\right] = \mathcal{G}^{<}(\omega) \tag{B.16}$$

Note that in an out-of-equilibrium situation, H would depend on time and the distribution would be different from the Fermi-Dirac distribution function.

Replacing a and b, by the appropriate operators we find indeed equations B.10, useful for calculations of the Josephson current flowing through a QD.

A particular case In the particular case $b = a^\dagger$ (useful for calculation of the tunnel current in section D.1.2.2), we have the relation $\mathcal{G}^{A}(\omega) = \mathcal{G}^{R}(\omega)^*$. Equations B.15 and B.16 thus becomes:

$$2\left(1 - f_{FD}(\omega)\right) i\mathrm{Im}\left[\mathcal{G}^{R}(\omega)\right] = \mathcal{G}^{>}(\omega)$$

$$-2 f_{FD}(\omega)\, i\mathrm{Im}\left[\mathcal{G}^{R}(\omega)\right] = \mathcal{G}^{<}(\omega)$$

or if we introduce the TDOS $\mathcal{A}(\omega) = -\pi\mathrm{Im}\left[\mathcal{G}^{R}(\omega)\right]$:

$$-2i\pi\left(1 - f_{FD}(\omega)\right)\mathcal{A}(\omega) = \mathcal{G}^{>}(\omega) \tag{B.17}$$

$$2i\pi f_{FD}(\omega)\,\mathcal{A}(\omega) = \mathcal{G}^{<}(\omega) \tag{B.18}$$

In appendix D, we will use Eq. B.17 and B.18 to calculate the tunnel current flowing between the tunnel probe and the QD in our experiment.

Appendix C

Relation between ABS's energies and Josephson current

In section 3.1.5, we have demonstrated that the Josephson current carried by a QD connected to two superconducting leads is equal to:

$$I_J = \frac{2e}{\hbar} \int f_{FD}\left(\omega\right) \mathrm{Re}\left[\mathrm{T}r_N \left(\hat{I}_L\left(-\omega - i\eta\right) - \hat{I}_L\left(-\omega + i\eta\right)\right)\right] \frac{d\omega}{2\pi} \tag{C.1}$$

with:

$$\hat{I}_L\left(z\right) = \hat{\Sigma}_L\left(z\right) \hat{\mathcal{G}}_{dd}\left(z\right)$$

We will call matrix $\hat{I}_L\left(z\right)$ the "current GF" in the following, $-e$ is the charge of electron, $\hbar$ the reduced Planck constant, $f_{FD}\left(\omega\right)$ the Fermi-Dirac distribution, $\mathrm{T}r_N$ the trace in Nambu space, $\Sigma_L\left(z\right)$ the self-energy of the left lead and $\hat{\mathcal{G}}_{dd}\left(z\right)$ the QD's GF.

Here we show how to relate this definition of the Josephson current with the phase derivative of the ABS's energies $\epsilon_\pm$. For this we first derive an expression of the Josephson current GF in terms of the parameters of the system Γ, U, etc... Then we separate this current in two contributions, one carried by the ABSs and the other by the continuum of the QD's TDOS. We will see that the first contribution is given by the phase derivative of $\epsilon_\pm$.

C.1 Josephson current carried by a S-QD-S junction

In this section, we derive an expression of the Josephson current expressed in terms of the system's parameters. For this, we first perform a symmetrization, based on current conservation, of the current GF with respect to the left and right leads. We take afterward its trace in Nambu space to end up with a simple form for the Josephson current.

C.1.1 Symmetrization of the current GF

Current conservation Expression C.1 was originally obtained in section 3.1.5 from:

$$I_J = \frac{ie}{\hbar} \langle [H_T, N_L] \rangle \tag{C.2}$$

We can however find a symmetric expression of the Josephson current with operator N_R. For this we start with an argument of current conservation: at equilibrium the charge in the QD, given by operator $N_D = \sum_\sigma d_\sigma^\dagger d_\sigma$, remains constant in average[1]. Therefore, if we write N_D in its Heisenberg representation we have:

$$\left\langle \frac{dN_D}{dt} \right\rangle = 0 \tag{C.3}$$

Then, using the fact that the QD's charge variation is given by $\left\langle \frac{dN_D}{dt} \right\rangle = \frac{i}{\hbar} \langle [H, N_D] \rangle$, we also have[2]:

$$\left\langle \frac{dN_D}{dt} \right\rangle = -\frac{i}{\hbar} \langle [H_T, N_L] \rangle - \frac{i}{\hbar} \langle [H_T, N_R] \rangle \tag{C.4}$$

Combining Eq. C.2, C.3 and C.4, we can finally write an expression of the Jospehson current with operator N_R:

$$I_J = -\frac{ie}{\hbar} \langle [H_T, N_R] \rangle \tag{C.5}$$

In the following, we will use both Eq. C.2 and C.5 to express the current, so we note for convenience $I_{JL} = \frac{ie}{\hbar} \langle [H_T, N_L] \rangle$ and $I_{JR} = \frac{ie}{\hbar} \langle [H_T, N_R] \rangle$, where I_{JL} (resp. I_{JR}) is the current going out of the left (resp. right) electrode. It is interesting to note that, combining Eq. C.3 and C.4, we can show that $I_{JL} = -I_{JR}$ and thus that the current is conserved along the circuit.

---

[1] In a real closed system, the charge is of course always constant. But in our model, it is only true in average as we describe the leads with mean-field BCS Hamiltonians which do not conserve the charge and induce fluctuations.

[2] This comes from the fact that, for our Hamiltonian: $[H, N_D] = -[H_T, N_L] - [H_T, N_R]$ which can be straightforwardly shown by calculating the commutators.

Symmetrization Using the relation between the Josephson current going out of the left and right electrode $I_{JL} = -I_{JR}$, we can write a more symmetric expression of the Josephson current I_J. Indeed, for any constant x, we have[3]:

$$I_J = xI_{JL} - (1-x)\, I_{JR}$$

If we choose $x = \frac{\Gamma_R}{\Gamma_L+\Gamma_R}$, this expression becomes:

$$I_J = \frac{2e}{\hbar} \int f_{FD}\left(\omega\right) \mathrm{Re}\left[\mathrm{Tr}_N \left(\hat{I}\left(-\omega - i\eta\right) - \hat{I}\left(-\omega + i\eta\right)\right)\right] \frac{d\omega}{2\pi} \tag{C.6}$$

with the following definition of symmetric current GF $\hat{I}\left(z\right)$:

$$\hat{I}\left(z\right) = \frac{\Gamma_R}{\Gamma_L+\Gamma_R} \hat{\Sigma}_L\left(z\right) \hat{\mathcal{G}}_{dd}\left(z\right) - \frac{\Gamma_L}{\Gamma_L+\Gamma_R} \hat{\Sigma}_R\left(z\right) \hat{\mathcal{G}}_{dd}\left(z\right) \tag{C.7}$$

This expression is more symmetric and will naturally simplify the following calculations.

C.1.2 Expression of the current GF

In order to express the current GF in terms of the parameters of the system, we need first to express $\hat{\Sigma}_L\left(z\right) \hat{\mathcal{G}}_{dd}\left(z\right)$ (and by deduction $\hat{\Sigma}_R\left(z\right) \hat{\mathcal{G}}_{dd}\left(z\right)$) explicitly.

The starting expression of the current GF is:

$$\hat{\Sigma}_L\left(z\right) \hat{\mathcal{G}}_{dd}\left(z\right) = \begin{bmatrix} g\left(z\right)\Gamma_L & f\left(z\right)\Gamma_L e^{i\phi_L} \\ f\left(z\right)\Gamma_L e^{-i\phi_L} & g\left(z\right)\Gamma_L \end{bmatrix} \begin{bmatrix} z - \epsilon_\uparrow - g\left(z\right)\Gamma & f\left(z\right)\sum_i \Gamma_i e^{i\phi_i} \\ f\left(z\right)\sum_i \Gamma_i e^{-i\phi_i} & z + \epsilon_\downarrow - g\left(z\right)\Gamma \end{bmatrix}^{-1}$$

where we remind that:

$$g\left(z\right) = -\frac{z}{\sqrt{\Delta^2 - z^2}} \text{ and } f\left(z\right) = \frac{\Delta}{\sqrt{\Delta^2 - z^2}}$$

After inversion of the second matrix, it becomes:

$$\begin{aligned} \hat{\Sigma}_L\left(z\right) \hat{\mathcal{G}}_{dd}\left(z\right) &= \begin{bmatrix} g\left(z\right)\Gamma_L & f\left(z\right)\Gamma_L e^{i\phi_L} \\ f\left(z\right)\Gamma_L e^{-i\phi_L} & g\left(z\right)\Gamma_L \end{bmatrix} \\ &\quad \times \frac{1}{D(z)} \begin{bmatrix} z + \epsilon_\downarrow - g\left(z\right)\Gamma & -f\left(z\right)\sum_i \Gamma_i e^{i\phi_i} \\ -f\left(z\right)\sum_i \Gamma_i e^{-i\phi_i} & z - \epsilon_\uparrow - g\left(z\right)\Gamma \end{bmatrix} \end{aligned} \tag{C.8}$$

---

[3] Indeed, as $I_{JL} = -I_{JR}$, then $xI_{JL} - (1-x)\, I_{JR} = (x+1-x)\, I_{JL} = I_{JL} = I_J$.

with $D\left(z\right)$ the determinant of the QD's GF inverse:

$$D\left(z\right)=\mathrm{Det}\left(\hat{\mathcal{G}}_{dd}\left(z\right)^{-1}\right)=\left(z-\epsilon_{\uparrow}-g\left(z\right)\Gamma\right)\left(z+\epsilon_{\downarrow}-g\left(z\right)\Gamma\right)-f\left(z\right)^{2}\left|\sum_{i}\Gamma_{i}e^{i\phi_{i}}\right|^{2}$$

From expression C.8 of $\hat{\Sigma}_{L}\left(z\right)\hat{\mathcal{G}}_{dd}\left(z\right)$ (and the equivalent expression of $\hat{\Sigma}_{R}\left(z\right)\hat{\mathcal{G}}_{dd}\left(z\right)$) and Eq. C.7, we can calculate the symmetric current GF (we take $\phi_{L}=-\phi_{R}=\delta/2$ in the following to get rid of a phase factor without any loss of generality):

$$\hat{I}\left(z\right)=i\frac{\Gamma_{L}\Gamma_{R}}{\Gamma_{L}+\Gamma_{R}}f\left(z\right)^{2}\sin\left(\frac{\delta}{2}\right)\frac{1}{D\left(z\right)}\begin{bmatrix}-\sum_{i}\Gamma_{i}e^{i\phi_{i}} & \frac{\left(z-\epsilon_{\uparrow}-g(z)\Gamma\right)}{f(z)}\\ \frac{\left(-z-\epsilon_{\downarrow}+g(z)\Gamma\right)}{f(z)} & \sum_{i}\Gamma_{i}e^{-i\phi_{i}}\end{bmatrix}$$

At this stage, it is more convenient to express $\hat{I}\left(z\right)$ as a function of $\Gamma=\Gamma_{L}+\Gamma_{R}$ and $\delta\Gamma=\Gamma_{L}-\Gamma_{R}$ rather than Γ_{L} and Γ_{R}. As we have $\Gamma_{L}e^{i\phi_{L}}+\Gamma_{R}e^{i\phi_{R}}=\Gamma\cos\left(\frac{\delta}{2}\right)+i\delta\Gamma\sin\left(\frac{\delta}{2}\right)$ and $\frac{\Gamma_{L}\Gamma_{R}}{\Gamma_{L}+\Gamma_{R}}=\frac{1}{2}\frac{\Gamma^{2}-\delta\Gamma^{2}}{\Gamma}$, we can write:

$$\begin{aligned}\hat{I}\left(z\right) &= \tfrac{i}{2}\tfrac{\Gamma^{2}-\delta\Gamma^{2}}{\Gamma}f\left(z\right)^{2}\sin\left(\tfrac{\delta}{2}\right)\\ &\times\tfrac{1}{D(z)}\begin{bmatrix}-\Gamma\cos\left(\frac{\delta}{2}\right)+i\delta\Gamma\sin\left(\frac{\delta}{2}\right) & \frac{\left(z-\epsilon_{\uparrow}-g(z)\Gamma\right)}{f(z)}\\ \frac{\left(-z-\epsilon_{\downarrow}+g(z)\Gamma\right)}{f(z)} & \Gamma\cos\left(\frac{\delta}{2}\right)+i\delta\Gamma\sin\left(\frac{\delta}{2}\right)\end{bmatrix}\end{aligned}$$

and by taking the trace in Nambu space, we obtain:

$$\begin{aligned}\mathrm{T}r_{N}\left(\hat{I}\left(\omega+i\eta\right)\right) &= \textstyle\sum_{\sigma}\frac{i}{2}\left(\Gamma^{2}-\delta\Gamma^{2}\right)f\left(\sigma\omega+i\eta\right)^{2}\\ &\times\tfrac{1}{D(\sigma\omega+i\eta)}\left(-\sigma\tfrac{\sin(\delta)}{2}+i\tfrac{\delta\Gamma}{\Gamma}\tfrac{1-\cos(\delta)}{2}\right)\end{aligned}\tag{C.9}$$

with $\sigma=\pm1$ respectively for the spin up part and the spin down part of $\hat{I}\left(z\right)$ (*i.e.* $\hat{I}^{11}\left(\omega+i\eta\right)$ and $\hat{I}^{22}\left(-\omega+i\eta\right)$).

Final expression of the Josephson current Now by inserting expression C.9 in C.6, I_{J} becomes:

$$I_{J}=-\frac{2e}{\hbar}\int\frac{d\omega}{2\pi}f_{FD}\left(\omega\right)\frac{1}{2}\left(\Gamma^{2}-\delta\Gamma^{2}\right)\sum_{\sigma}\mathrm{Im}\left[F\left(\omega\right)\left(-\sigma\frac{\sin\left(\delta\right)}{2}+i\frac{\delta\Gamma}{\Gamma}\frac{1-\cos\left(\delta\right)}{2}\right)\right]$$

where the factor $F\left(\omega\right)$:

$$F\left(\omega\right)=\left(f\left(-\sigma\omega-i\eta\right)^{2}\frac{1}{D\left(-\sigma\omega-i\eta\right)}-f\left(-\sigma\omega+i\eta\right)^{2}\frac{1}{D\left(-\sigma\omega+i\eta\right)}\right)$$

is purely imaginary because $\left[\frac{f(-\omega-i\eta)^2}{D(-\omega-i\eta)}\right]^* = \frac{f(-\omega+i\eta)^2}{D(-\omega+i\eta)}$.

This allows a simplification of the previous expression to:

$$\begin{array}{rcl} I_J & = & \frac{e}{\hbar}\int f_{FD}\left(\omega\right) \\ & & \times\sum_\sigma \mathrm{Im}\left[\left(\Gamma^2-\delta\Gamma^2\right)\left(\frac{\Delta^2}{\Delta^2-(-\sigma\omega+i\eta)^2}\frac{1}{D(-\sigma\omega+i\eta)}\right)\left(-\sigma\sin\left(\delta\right)\right)\right]\frac{d\omega}{2\pi} \end{array} \tag{C.10}$$

This expression is the one we use to compute the Josephson current in the following and the rest of this thesis.

C.2 Supercurrent carried by the ABSs

We can distinguish two contributions in the Josephson current (or supercurrent): one carried by the ABSs (I_{ABS}) which corresponds to $|\omega| < \Delta$, and another one carried by the continuum (I_{cont}) which corresponds to $|\omega| > \Delta$:

$$\int \to \int_{-\Delta}^{\Delta} + \int \theta\left(\Delta - |\omega|\right)$$

In this section we express the first contribution in terms of the phase derivative of the ABSs's energies $E_{ABS}^{\pm}$. We only treat the case $\eta_{inel} = 0$ for simplicity.

Evaluation of the integral with the residue theorem As $D\left(\epsilon_\pm\right) = 0$, for $\eta \to 0$ the integral in I_{ABS} has two real poles ϵ_+ and ϵ_- corresponding to the energies of the ABSs. We can thus evaluate I_{ABS} by applying, on this integral, the residue theorem.

The latter tells us that:

$$\int \theta\left(|\omega|-\Delta\right) f_{FD}\left(\omega\right)\left(\frac{\Delta^2}{\Delta^2-\omega^2}\frac{1}{D\left(\omega\right)}\right)\frac{d\omega}{2\pi} = \frac{1}{2}\sum_{\pm} f_{FD}\left(\epsilon_\pm\right)\frac{\Delta^2}{\Delta^2-\epsilon_\pm^2}\mathrm{Im}\left[i\,\underbrace{\frac{1}{D'\left(\epsilon_\pm\right)}}_{\text{purely real}}\right]$$

so that the current carried by the ABSs becomes:

$$I_{ABS} = \frac{e}{\hbar}\frac{1}{2}\sum_\sigma\sum_\pm f_{FD}\left(-\sigma\epsilon_\pm\right)\left(\Gamma^2-\delta\Gamma^2\right)\left(-\sigma\sin\left(\delta\right)\right)\frac{\Delta^2}{\Delta^2-\epsilon_\pm^2}\frac{1}{D'\left(\epsilon_\pm\right)} \tag{C.11}$$

Expression of $\frac{\partial \epsilon_\pm}{\partial \delta}$ as a function of $D'(\epsilon_\pm)$ The final step consists in expressing $\frac{\partial \epsilon_\pm}{\partial \delta}$ as a function of $D'(\epsilon_\pm)$. For this we take the derivative of the following equation (corresponding to $D(\epsilon_\pm) = 0$):

$$\left(\epsilon_\pm - \epsilon_\uparrow - g(\epsilon_\pm)\Gamma\right)\left(\epsilon_\pm + \epsilon_\downarrow - g(\epsilon_\pm)\Gamma\right) - f(\epsilon_\pm)^2 \frac{1}{2}\left[\Gamma^2 + \delta\Gamma^2 + \left(\Gamma^2 - \delta\Gamma^2\right)\cos(\delta)\right] = 0$$

with respect to the superconducting phase difference δ, and obtain:

$$\frac{\partial \epsilon_\pm}{\partial \delta} = -\frac{f(\epsilon_\pm)^2 \frac{\left(\Gamma^2 - \delta\Gamma^2\right)}{2}\sin(\delta)}{D'(\epsilon_\pm)} \tag{C.12}$$

Current carried by the ABSs If now we use relations C.12 to transform expression C.11, we end up with the final result:

$$I_{ABS} = \frac{e}{\hbar}\sum_\sigma \sum_\pm f_{FD}(-\sigma\epsilon_\pm)\left(\sigma \frac{\partial \epsilon_\pm}{\partial \delta}\right)$$

or:

$$I_{ABS} = -\frac{e}{\hbar}\sum_\pm \tanh\left(\frac{\beta\epsilon_\pm}{2}\right)\frac{\partial \epsilon_\pm}{\partial \delta}$$

This result is in agreement with Ref. [51] of Beenakker who treats the case where the two ABS are degenerated[4] and thus $\epsilon_+ = -\epsilon_-$.

It is interesting to note that this expression doesn't depend on the heights of the ABSs in the TDOS, and that both ABSs + and − carry supercurrent whatever the temperature consistent with the fact that their position above or below the Fermi level is arbitrary.

Furthermore if we consider the case where the spin degeneracy has not been broken ($U = 0$ in our phenomenological model), for a system at zero temperature, we recover the well-known formula:

$$I_{ABS} = -\frac{e}{\hbar}\sum_\pm \text{sign}(\epsilon_\pm)\frac{\partial \epsilon_\pm}{\partial \delta} = I_{ABS} = \frac{2e}{\hbar}\frac{\partial \epsilon_-}{\partial \delta}$$

The presence of a single ABS in this latter expression is due to the peculiar symmetry of the system.

---

[4] For us, this is only true when $\epsilon_\uparrow = \epsilon_\downarrow$ or equivalently when $U = 0$.

C.3 Supercurrent carried by the continuum

In the general case, the continuum carries supercurrent that is not always negligible compared to the contribution of the ABSs. We can say however, from Eq. C.10, that for large ω the continuum contribution decreases as $\frac{1}{\omega^4}$. Therefore, the part of the continuum that may carry significantly supercurrent is around $\omega \approx \pm\Delta$. Moreover, because of the factor $\frac{\Delta^2}{\Delta^2-\omega^2}$, the supercurrent carried by the continuum ($|\omega| > \Delta$) may flow in opposite direction than the one carried by the ABS ($|\omega| > \Delta$).

In this section, we compare the contribution of the continuum and the ABSs for three cases:

- non-interacting resonant QD with highly coupled symmetric contact ($U = 0$, $\epsilon = 0$, $\delta\Gamma = 0$ and $\Gamma \gg \Delta$),
- non-interacting out-of-resonance QD with weakly coupled symmetric contact ($U = 0$, $\epsilon \neq 0$, $\delta\Gamma = 0$ and $\Gamma \approx \Delta$),
- interacting resonant QD with weakly coupled symmetric contact ($U \approx \Delta$, $\epsilon = 0$, $\delta\Gamma = 0$ and $\Gamma \approx \Delta$).

In Fig. C.1, we have represented the phase dependence of the supercurrent I_J separating contributions of the ABSs (in red) and the continuum (in green) for these three different cases.

The first case, that concerns an experimental situation where the weak link connecting the two superconducting reservoirs is an atomic contact with perfect transmission, shows a completely negligible contribution of the continuum. The latter can thus be ignored to interpret experimental results obtained with an atomic contact. This is actually a general property of weak links where Γ is the largest characteristic energy of the system.

In the second case, the QD is driven out of resonance. This reduces the transmission of the weak link and suppresses the abrupt change at $\delta = \pi$ which occurs in the previous case (introducing an asymmetry $\delta\Gamma$ would have the same effect). Furthermore we have drastically reduced the coupling to the leads in order to raise the contribution of the continuum. Besides, the latter becomes comparable to the contribution of the ABSs and is in opposite direction. Therefore, if one wants to describe an experimental situation where a QD is coupled to the leads with a characteristic energy comparable to Δ (as it is typically the case for CNTs), the current carried by the continuum cannot be ignored.

The third case is interesting because, around $\delta = \pi$, it is an extreme case where the contribution of the ABSs becomes negligible compared to the supercurrent carried by the continuum. This is actually quite rare and may only happen when the system is in between a 0 state and a π state (see section 3.1.5.3).

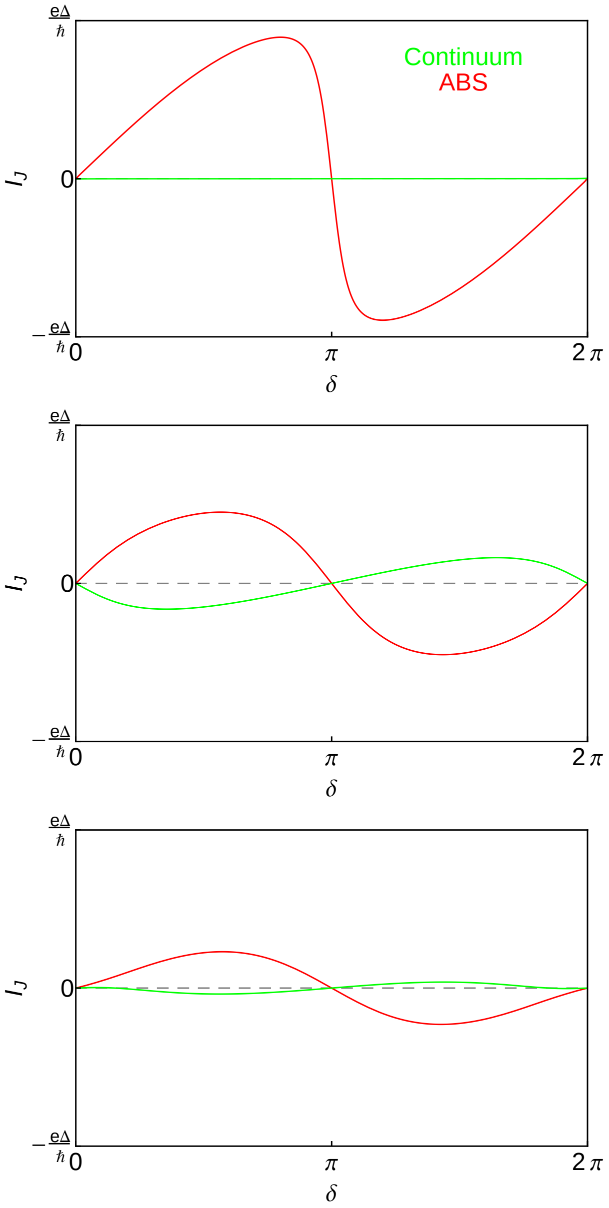

Comparison between contributions to the supercurrent of the ABSs (red) and the continuum (green)

Figure C.1: Josephson current I_J carried by the ABSs (red) and the continuum (green) respectively from top to bottom for the following parameters: $U = 0$, 0, and 2Δ, $\Gamma = 20000\Delta$, 2Δ, and 2Δ, $\delta\Gamma = 0$, 0, and 0, $\eta_{inel} = 0$, 0, and 0 and $\epsilon = 0$, $-\Delta$, and 0.

Appendix D

Tunneling spectroscopy

The tunneling spectroscopy is a technique aiming to explore the DOS of a sample by injecting or extracting electrons from a well characterized probe (we therefore talk about tunneling DOS (TDOS)). For this purpose, the sample is separated from the probe by a thin barrier which can be for example a few nanometers of vacuum or insulator. In this configuration, electrons can tunnel through the insulator (see Fig. D.1). If the probe and the sample are coupled weakly enough to be described by two independent sets of states, they are said to be in the tunnel regime. We can consider henceforth that the probe and the sample both remain at equilibrium.

In this regime, and provided that we know the probe DOS, measurements of the tunnel current flowing between the probe and the sample $I\left(V\right)$, with V the voltage applied on the probe, gives a direct access to the sample DOS. Indeed, under some hypotheses that we will detail below, the tunnel current is proportional to the following product of convolution:

$$I(V) \propto \int \mathcal{A}_{probe}(\omega + eV)\mathcal{A}_{sample}(\omega)\left(f_{sample}(\omega) - f_{probe}(\omega + eV)\right)d\omega \quad \text{(D.1)}$$

with $e = 1.6 \times 10^{-19}$C the charge of an electron, $\mathcal{A}_{probe}(\omega)$ and $\mathcal{A}_{sample}(\omega)$ the TDOS of the probe and the sample at energy ω, and $f_{sample}(\omega) = f_{probe}(\omega) = f_{FD}\left(\omega\right)$ the Fermi-Dirac distribution. With a deconvolution procedure that we describe in section D.3, we can thus extract $\mathcal{A}_{sample}(\omega)$ from the tunnel current.

In the following, we first show how Eq. D.1 which relates tunnel current and TDOS can be obtained by a perturbative approach. Afterward we discuss the impact of the tunnel probe on the ABSs linewidth, for the cases of a normal and a superconducting probe. In the last section, we explain how to perform the deconvolution procedure.

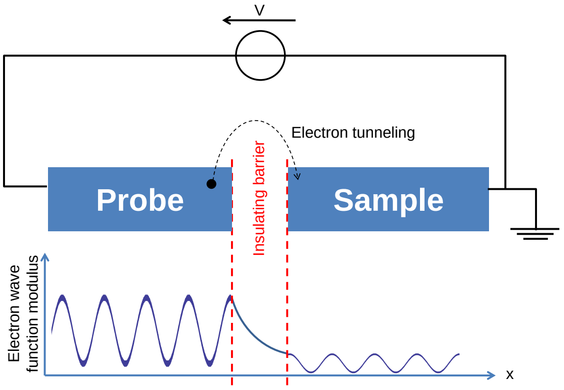

Figure D.1: The wave function of an electron in the left part decreases exponentially in the barrier and reach the right part. If the barrier is not too thick, the probability for an electron to "jump" from an electronic state of the left part to one of the right part is not negligible and a current can flow.

D.1 The tunnel current and tunnel density of states

In this section, we define the tunnel current and the tunnel density of states, and show how the latter is related to the imaginary part of the Green's function.

For this purpose, we introduce the Hamiltonian H describing the exchange of electrons between a tunnel probe biased with a voltage V and a sample connected to the ground. It contains in particular the "tunneling Hamiltonian" H_T of Ref. [70, 160]. Then we calculate the tunnel current, to the lowest order in H_T, by mean of a generalized Kubo formula [161], when a voltage V is applied on the probe.

D.1.1 Description of the system and tunneling Hamiltonian

Tunneling Hamiltonian To describe the coupling between a tunnel probe (L) and a sample (R), weakly connected together, we need to introduce, in addition to their respective Hamiltonian H_L and H_R, an Hamiltonian H_T so that the complete Hamiltonian H describing the system reads:

$$H = H_L + H_R + H_T$$

with the tunneling Hamiltonian:

$$H_T = \sum_{l,r} t_{lr} c_l^\dagger c_r + t_{lr}^* c_r^\dagger c_l$$

and H_L (resp. H_R) represents the Hamiltonian of the isolated probe L (resp. sample R) on the left (resp. right), as in Fig. D.1.

Operators $c_l^\dagger$ and $c_r^\dagger$ are creation operators of single-electron states of L and R. These states $|l\rangle$ and $|r\rangle$ constitute complete sets of eigenstates for L and R. The coupling H_T describes thus exchange of normal electrons between L and R (even if one of them is a BCS superconductor), by a hopping term like in a tight-binding model. The tunnel matrix elements t_{lr} represent overlap integrals of electronic wave functions between states $|l\rangle$ and $|r\rangle$, belonging respectively to L and R. In the following we will consider that matrix elements t_{lr} are energy independent and all equal to a constant t_{probe} (in Ref. [64], Bardeen showed that this assumption is plausible).

Voltage in the phase of the tunneling amplitude When a voltage is applied on the probe, the tunneling Hamiltonian becomes time-dependent (see Ref. [162]) and takes the form:

$$H_T(t) = T^\dagger(t) + T(t) \tag{D.2}$$

where:

$$T^\dagger(t) = \sum_{l,r} t_{probe} e^{-i\frac{eV}{\hbar}t} c_l^\dagger c_r$$

This time-dependence makes the problem very difficult to solve, but this difficulty can be circumvented by performing a perturbative calculation of the tunnel current to the first order in $H_T(t)$. This is explained in the following.

D.1.2 Calculation of the tunnel current

In this section, we briefly explain how to calculate the tunnel current following Ref. [65] where the readers can find all the details.

D.1.2.1 Definition of the tunnel current operator

In order to obtain the tunnel current, we need to define a tunnel current operator $I(t)$ as the time derivative of the number of particles operator of the probe:

$$I(t) = \frac{dN_L(t)}{dt}$$

where $N_L(t)$ is in Heisenberg representation:

$$N_L(t) = e^{iHt} \sum_l c_l^\dagger c_l e^{-iHt}$$

From this definition, we can show the following equality:

$$I(t) = \frac{ie}{\hbar} \left[H_T(t), N_L(t)\right] = \frac{ie}{\hbar} \left(T^\dagger(t) - T(t)\right) \tag{D.3}$$

The average value of this operator gives the current flowing between the probe and the sample. In the following, we calculate $\langle I(t) \rangle$ perturbatively by means of the Kubo formula which gives the expectation value of the current up to linear order in $H_T(t)$.

D.1.2.2 Calculation of the tunnel current using the Kubo formula

According to the Kubo formula (see chapter 8 of Ref. [65]), the tunnel current to first order in $H_T(t)$ is given by:

$$\langle I(t) \rangle = -\frac{i}{\hbar} \int_{-\infty}^{+\infty} \theta(t-t') \left\langle \left[I(t), H_T(t')\right] \right\rangle_0 dt' \tag{D.4}$$

where $\langle . \rangle_0$ is the thermal average in absence of tunnel coupling, *i.e.* with $H_T(t) = 0$.

Inserting equations D.3 and D.2 in the Kubo formula D.4, we get two terms and their complex conjugates so that the current reads:

$$\langle I(t) \rangle = \frac{2e}{\hbar^2} \times \mathrm{Re}\left[\int_{-\infty}^{+\infty} \theta(t-t') \left(\left\langle \left[T^\dagger(t), T(t')\right] \right\rangle_0 - \left\langle \left[T(t), T(t')\right] \right\rangle_0 \right) dt' \right]$$

The term $\langle [T(t), T(t')] \rangle_0$, involving the creation of an electron pair in R and the annihilation of another one in L, concerns the flow of Josephson current between L and R. In our experiment, we don't see this contribution. Indeed, at finite V, this current is oscillating at GHz frequency, whereas we perform experimentally DC measurements, and at $V = 0$, the branch of supercurrent is too small to be measured. We will therefore neglect this term from now on.

Expectation values are evaluated for operators governed by $H_0 = H_L + H_R$. As a consequence L and R are completely independent, and we can write $\left\langle \left[T^\dagger(t), T(t')\right] \right\rangle_0$ as the product of two correlation functions calculated respectively over states of L and R in such a way that $\langle I(t) \rangle$ becomes:

$$\begin{aligned}\langle I(t) \rangle = {} & \frac{2e}{\hbar^2} \left|t_{probe}\right|^2 \times \mathrm{Re}[\int_{-\infty}^{+\infty} e^{-i\frac{eV}{\hbar}(t-t')} \theta(t-t') \\ & \times \sum_{l,r,l',r'} \left(\left\langle c_l^\dagger(t) c_{l'}(t') \right\rangle_0 \left\langle c_r(t) c_{r'}^\dagger(t') \right\rangle_0 - \left\langle c_{l'}(t') c_l^\dagger(t) \right\rangle_0 \left\langle c_{r'}^\dagger(t') c_r(t) \right\rangle_0 \right) dt']\end{aligned}$$

For simplicity, we choose a basis set $\{|l\rangle, |r\rangle\}$ in which H_0 is diagonal, such that those correlation functions are different from 0 only if $r = r'$ and $l = l'$. After the variable change $t' \to t' + t$ and thanks to the fact that these correlation functions are invariant by time-translation[1], we can express the tunnel current with lesser and greater Green's functions of L and R (see section B.1 appendix B for definitions):

$$\begin{aligned}\langle I\left(t\right)\rangle &= \tfrac{2e}{\hbar^2}\left|t_{probe}\right|^2 \\ &\times \mathrm{Re}\left[\textstyle\int_{-\infty}^{+\infty} e^{-i\frac{eV}{\hbar}\left(-t'\right)}\theta\left(-t'\right)\sum_{l,r}\left(\mathcal{G}_{ll}^{<}\left(t'\right)\mathcal{G}_{rr}^{>}\left(-t'\right) - \mathcal{G}_{ll}^{>}\left(t'\right)\mathcal{G}_{rr}^{<}\left(-t'\right)\right)dt'\right]\end{aligned}$$

which is equal to[2]:

$$\langle I\left(t\right)\rangle = \frac{e}{\hbar}\left|t_{probe}\right|^2 \times \int_{-\infty}^{+\infty}\sum_{l,r}\left(\mathcal{G}_{ll}^{<}\left(\omega+eV\right)\mathcal{G}_{rr}^{>}\left(\omega\right) - \mathcal{G}_{ll}^{>}\left(\omega+eV\right)\mathcal{G}_{rr}^{<}\left(\omega\right)\right)\frac{d\omega}{2\pi}$$

As shown in section B.4, these lesser and greater GFs for a time-independent Hamiltonian can be related to the TDOS and the Fermi-Dirac distribution in the following way:

$$2\left(1 - f_{FD}\left(\omega\right)\right)i\mathrm{Im}\left[\mathcal{G}_{ll}^{R}\left(\omega\right)\right] = \mathcal{G}_{ll}^{>}\left(\omega\right)$$

$$-2f_{FD}\left(\omega\right)i\mathrm{Im}\left[\mathcal{G}_{ll}^{R}\left(\omega\right)\right] = \mathcal{G}_{ld}^{<}\left(\omega\right)$$

We thus end up with formula D.1:

$$\langle I\left(t\right)\rangle = \frac{2e}{\hbar}\left|t_{probe}\right|^2 \times \int_{-\infty}^{+\infty}\mathcal{A}_{probe}\left(\omega+eV\right)\mathcal{A}_{sample}\left(\omega\right)\left[f_{FD}\left(\omega\right) - f_{FD}\left(\omega+eV\right)\right]d\omega \tag{D.5}$$

where:

$$\mathcal{A}_{probe}\left(\omega\right) = -\pi\sum_{l}\mathrm{Im}\left[\mathcal{G}_{ll}^{R}\left(\omega\right)\right] \text{ and } \mathcal{A}_{sample}\left(\omega\right) = -\pi\sum_{r}\mathrm{Im}\left[\mathcal{G}_{rr}^{R}\left(\omega\right)\right]$$

At this point, we see that the tunnel current doesn't depend on time, as the time-variable does not appear in expression D.5. This formula can be interpreted as a balance of electrons exchange between L and R as it involves the product between the availability of states and the TDOS of the probe and the sample. By sweeping V and as we know the TDOS of the probe, we can explore the TDOS of the sample.

---

[1] This is true because H_0 does not depend on time.

[2] Here we have used the fact that the lesser and greater GFs are purely imaginary, see Eq. B.17 and B.18.

D.1.2.3 Tunnel differential conductance

Derivation with respect to V of equation D.5 gives access to the differential conductance $G\left(V\right)$, the quantity that we measure experimentally:

$$\begin{aligned} G\left(V\right) &= \tfrac{2e}{\hbar}\left|t_{probe}\right|^2 \\ &\times \int_{-\infty}^{+\infty} \mathcal{A}_{sample}\left(\omega\right) \tfrac{\partial}{\partial V}\left[\mathcal{A}_{probe}\left(\omega+eV\right)\left(f_{FD}\left(\omega\right)-f_{FD}\left(\omega+eV\right)\right)\right] d\omega \end{aligned} \tag{D.6}$$

D.2 Broadening of the ABSs due to the coupling to the tunnel probe

Theory predicts ABSs as infinitely thin peaks in the spectral density. In experiments however, we expect measurements to be smeared either by temperature or voltage fluctuations of the bias on the tunnel probe. These peaks should then appear experimentally as bell-shaped function with a characteristic width of $k_B T_{eff}$, with $T_{eff} = \sqrt{T^2 + 3\left(eV_{rms}/k_B\pi\right)}$ [163] where T is the temperature and V_{rms} is the rms amplitude of the voltage noise. Our apparatus was characterized in a previous experiment [79] and expected to have a limiting resolution of ~ 15 μeV. However we observe experimentally that ABSs are bell-shaped with a full-width at half-maximum between 30 and 40 μeV.

Here we show that broadening due to the coupling to the probe is sufficient to understand this experimental linewidth.

D.2.1 ABSs coupled to a normal tunnel probe

Self-energy of the normal probe If we take into account the coupling of the QD to a normal tunnel probe into the retarded GF $\hat{\mathcal{G}}^R_{dd}\left(\omega\right)$, we simply have to add the self-energy of the probe:

$$\hat{\Sigma}_P\left(\omega+i\eta\right) = \begin{bmatrix} -i\Gamma_P & 0 \\ 0 & -i\Gamma_P \end{bmatrix}$$

into the QD GF. Here $\Gamma_P = \pi\rho_F\left|t_P\right|^2$ is the strength of this coupling to the probe, with t_P the hopping term between the latter and the QD. The QD GF, initially given by Eq. 3.2 in chapter 3, thus becomes:

$$\hat{\mathcal{G}}^R_{dd}\left(\omega\right) = \left[\omega + i\eta - \mathcal{E}_{\mathcal{QD}} - \hat{\Sigma}\left(\omega+i\eta\right) - \hat{\Sigma}_P\left(\omega+i\eta\right)\right]^{-1}$$

Consequence on the ABSs When the QD is not coupled to the tunnel probe, the ABSs are real poles of the QD GF and consequently appear as infinitely thin peaks in the TDOS. If the QD is coupled to a continuum spectrum of energy (for example the normal tunnel probe), a quasiparticle lying in an ABS may escape from the QD and acquires thus a finite lifetime. It becomes a complex pole because of the imaginary part $i\Gamma_P$ and appears as a broaden peak in the QD TDOS[3].

In Fig. D.2, we show the TDOS of a QD in three cases:

- the QD is not coupled to the probe and there is no phenomenological loss introduced,
- the QD is not coupled to the probe and there is a phenomenological loss introduced,
- the QD is coupled to the probe and there is no phenomenological loss introduced.

We can see that the coupling to a normal tunnel probe has a very similar effect than the phenomenological inelastic loss.

There are however some differences. Whereas η_{inel} seems to give a Lorentzian shape to the ABSs, Σ_P gives them a bell-shaped which cannot be fitted by a Lorentzian. Furthermore the TDOS cancels to zero at $\pm\Delta$ whatever the value of Γ_P, but takes a finite value as soon as $\eta_{inel} \neq 0$.

Conductance between the tunnel probe and the superconducting loop The maximum conductance G_p between the tunnel probe and the superconducting loop (when $\epsilon_d = 0\Delta$) is of the order of[4]:

$$G_p = 2 \times \frac{4\Gamma\Gamma_P}{\left[\frac{U^2}{4} + (\Gamma + \Gamma_P)^2\right]} \frac{e^2}{h}$$

where we have supposed that the tunnel probe sees the left and right electrode in parallel and the factor 2 takes into account the spin. For typical parameters (those of Fig. D.2), G_p is of the order of $0.1\frac{e^2}{h}$. This corresponds to a tunnel resistance of about 250 kΩ in adequacy to our experimental values (see for example part IV).

---

[3] In Ref. [94], Chang and Bagwell demonstrate that ABSs also acquire a finite linewidth, in the case of a ballistic S-N-S junction where the N part is coupled to a normal side probe. This width increases with the coupling to the probe.

[4] We use here the Breit-Wigner formula (see for example [56] or Eq. 3.5 from chapter 3).

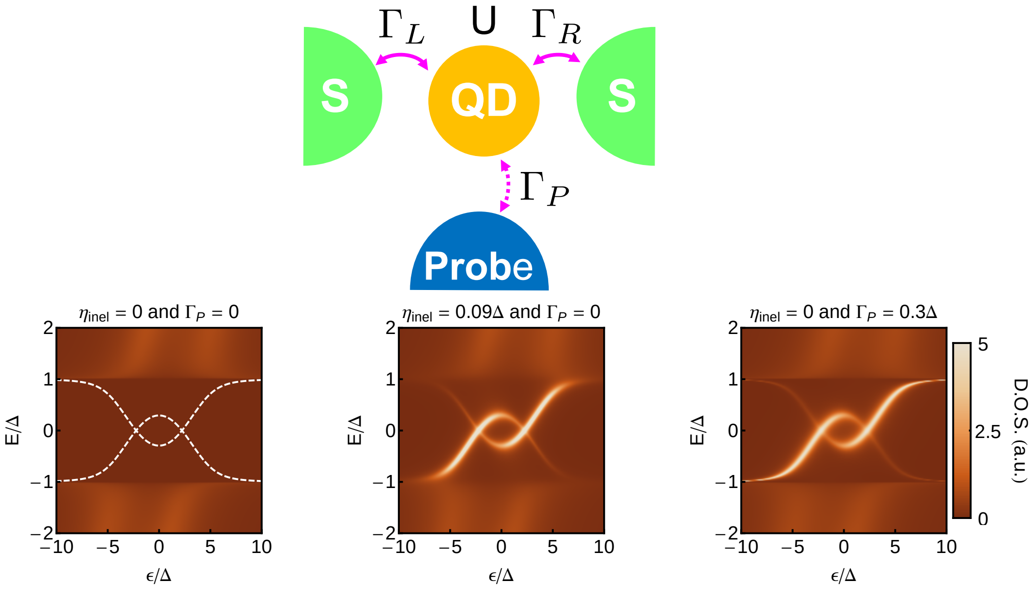

Effect of the coupling to a normal tunnel probe on the ABSs width

Figure D.2: TDOS of a QD connected to superconducting leads for three different cases. Common parameters are $\Gamma = 2\Delta$, $\delta\Gamma = 0$, $U = 6\Delta$ and $\delta = 0$. As they are not visible for $\eta_{inel} = \Gamma_P = 0$, the ABSs are indicated in white dashed line on the left.

D.2.2 ABSs coupled to a superconducting tunnel probe

When a system is coupled to a biased electrode, out-of-equilibrium processes (quasiparticle current, inelastic tunneling of Cooper pairs [164], multiple Andreev reflection (MAR) current [68]...) may happen such that the system cannot be described anymore by a thermal distribution function.

Here we suppose that the current between the tunnel probe and the left and right superconducting electrodes is sufficiently low to maintain them at thermal equilibrium. Under such approximations the tunnel probe can be taken into account in the QD GF by adding the self-energy $\Sigma_{SP}(z)$:

$$\Sigma_{SP}(z) = \sum_p \begin{bmatrix} \sqrt{\Gamma_P} & 0 \\ 0 & -\sqrt{\Gamma_P} \end{bmatrix} \begin{bmatrix} \epsilon_p - eV_{bias} & \Delta_P \\ \Delta_P & -\epsilon_p - eV_{bias} \end{bmatrix}^{-1} \begin{bmatrix} \sqrt{\Gamma_P} & 0 \\ 0 & -\sqrt{\Gamma_P} \end{bmatrix}$$

$$\Sigma_{SP}(z) = \begin{pmatrix} \Gamma_P g_P(z) & -\Gamma_P f_P(z) \\ -\Gamma_P f_P(z) & \Gamma_P g_P(z) \end{pmatrix}$$

with $g_P(z) = \frac{-(z-eV_{bias})}{\sqrt{\Delta_P^2-(z-eV_{bias})^2}}$ and $f_P(z) = \frac{\Delta_P}{\sqrt{\Delta_P^2-(z-eV_{bias})^2}}$. Here Γ_P is the coupling strength between the QD and the probe and Δ_P is the superconducting gap of the probe.

We have set the superconducting phase of the probe ϕ_P to zero, throwing away all the dynamics induced by the time-dependent nature of the Hamiltonian. Indeed, when the tunnel probe is biased, ϕ_P is actually equal to $\frac{2eV_{bias}t}{\hbar}$. This phase is generally important as it is the cause of the MAR processes (see [165, 166]). However as we are in the tunnel regime, these processes are negligible and we can neglect them by taking $\phi_P = 0$ (as in [167] for example).

Consequence on the ABSs If the QD is coupled to a superconducting probe, the latter doesn't broaden the ABSs when at equilibrium. Indeed when the voltage on the probe V_{bias} is equal to zero, the ABSs see only the superconducting gap of the tunnel probe and not its continuum. As a consequence quasiparticles lying in an ABS cannot escape and the ABS conserves its infinite lifetime. However, when the superconducting tunnel probe is biased, ABSs see the continuum spectrum of the tunnel probe and acquire a finite lifetime (see Fig. D.3).

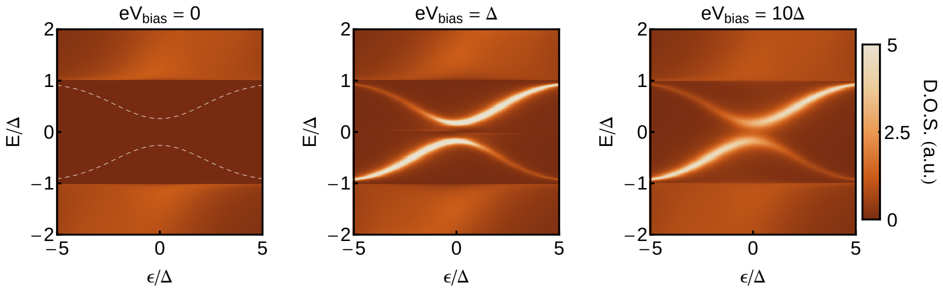

Evolution of the QD TDOS with the voltage applied on the superconducting tunnel probe

Figure D.3: TDOS of a QD connected to superconducting leads for different V_{bias} applied on the superconducting tunnel probe. Common parameters are $\Gamma = 2\Delta$, $\delta\Gamma = 0$, $U = 3\Delta$, $\Gamma_P = 0.3\Delta$, $\eta_{inel} = 0$ and $\delta = 0$.

D.3 Extracting the Density of States (DOS) from the differential conductance

In our experiment we measure the tunnel differential conductance between a BCS probe and a CNT. This differential conductance is given by expression (see Eq. D.6):

$$\begin{aligned} G(V) &= \tfrac{2e}{\hbar}\left|t_{probe}\right|^2 \\ &\times \textstyle\int_{-\infty}^{+\infty} \mathcal{A}_{sample}(\omega)\, \tfrac{\partial}{\partial V}\left[\mathcal{A}_{probe}(\omega+eV)\left(f_{FD}(\omega)-f_{FD}(\omega+eV)\right)\right] d\omega \end{aligned}$$

where $\mathcal{A}_{sample}(\omega)$ is the CNT TDOS. We note this TDOS $\mathcal{A}(\omega)$ in the following for compactness. To extract $\mathcal{A}(\omega)$ from $G(V)$ we need to perform a deconvolution procedure. Here we described this technique.

D.3.1 Principle of the deconvolution procedure

Discretization of the integral The normalized differential conductance:

$$g(V) = G(V)\,\frac{1}{\left|t_{probe}\right|^2}\frac{\hbar}{2e^2}$$

can be expressed as the integral of convolution:

$$g(V) = \int_{-\infty}^{+\infty} h(\omega, V)\,\mathcal{A}(\omega)\, d\omega \tag{D.7}$$

where $h(\omega, V)$ is defined as:

$$\begin{aligned} h(\omega, V) &= \tfrac{\partial}{\partial V}\left[\mathcal{A}_{probe}(\omega+eV)\right]\left(f_{FD}(\omega)-f_{FD}(\omega+eV)\right) \\ &+\mathcal{A}_{probe}(\omega+eV)\,\tfrac{\partial}{\partial V}\left[f_{FD}(\omega+eV)\right] \end{aligned}$$

with $\mathcal{A}_{probe}(\omega)$ the TDOS of the tunnel probe and $f_{FD}(\omega)$ the Fermi-Dirac distribution function.

Since convolution is a linear operation, its implementation on a discretized set of data $[g(V)]$ can be expressed as a matrix operation:

$$[g(V)] = M.\left[\mathcal{A}(\omega)\right] \tag{D.8}$$

with $[\mathcal{A}(\omega)]$ a discretized DOS.

Here, $[g(V)]$ is a vector containing $2N+1$ experimental points of differential conductance measured between $-V_0$ and V_0 with a step $s = \frac{V_0}{N}$:

$$[g(V)] = \begin{bmatrix} g(-V_0) \\ g(-V_0+s) \\ g(-V_0+2s) \\ \vdots \\ g(V_0) \end{bmatrix}$$

$[\mathcal{A}(\omega)]$ is a vector of $2P+1$ points of the CNT TDOS from energy $-P \times s$ to $P \times s$ expressed in eV:

$$[\mathcal{A}(\omega)] = \begin{bmatrix} \mathcal{A}\left(-\frac{P}{N} \times V_0\right) \\ \mathcal{A}\left(-\frac{P}{N} \times V_0 - +s\right) \\ \vdots \\ \mathcal{A}(0) \\ \vdots \\ \vdots \\ \mathcal{A}\left(\frac{P}{N} \times V_0\right) \end{bmatrix}$$

M is thus a matrix of dimensions $(2N+1) \times (2P+1)$ just depending on $\mathcal{A}_{probe}$ and f_{FD}, with its coefficients given by:

$$M_{ij} = h\left((j-1) \times s - \frac{P}{N} \times V_0, (i-1) \times s - V_0\right) \times s$$

Equation D.8 then reads:

$$[g(V)]_i = \sum_j h\left((j-1) \times s - \frac{P}{N} \times V_0, (i-1) \times s - V_0\right) [\mathcal{A}(\omega)]_j \times s$$

which corresponds indeed to the discretization of integral D.7, except that boundaries of the integral $\pm\infty$ are replaced by finite boundaries $\pm\frac{P}{N} \times V_0$ for pratical purpose.

Deconvolution by multiplication to a fixed matrix $[\mathcal{A}(\omega)]$ is obtained by multiplying $[g(V)]$ by the "inverse" of M. Yet M is not necessarily an inversible matrix, and is generally not even a square matrix.

There exists though a unique Moore-Penrose pseudo-inverse (see Wikipedia) M^{-1} so that, for any vector b with the appropriate length, the vector $x = M^{-1}.b$ gives the minimum of:

$$\|Mx - b\|^2$$

This pseudoinverse can be obtained in Mathematica with the command: *"M^{-1}"=Pseudoinverse[M]*, or in MatLab with the command: *"M^{-1}"=$M\backslash I_{2N+1}$*.

We obtain the least-square error estimate of the DOS in the nanotube by left-multiplying the measured differential conductance $[g(V)]$ by the Moore-Penrose pseudo-inverse of M. The differential conductance can thus be deconvolved to get CNT DOS simply by multiplying it by a fixed matrix.

D.3.2 Introduction of a Dynes parameter

To smooth the BCS singularity that may be responsible of divergences in the numerical calculation of M, we assume that the probe have a BCS DOS with a Dynes "depairing" imaginary part $i\gamma\Delta_p$ (γ is a dimensionless parameter and Δ_p the superconducting gap of the probe) added to ω:

$$\mathcal{A}_{probe}\left(\omega\right)=n_{LF}\mathrm{Re}\left[\frac{\left|\omega\right|}{\sqrt{\left(\omega+i\gamma\Delta_p\right)^2-\Delta_p^2}}\right]$$

with n_F the DOS of the probe in its normal state at the Fermi level. This avoids to obtain unphysical TDOS after deconvolution (negative TDOS, oscillations, divergences...), but also to take into account the finite differential conductance measured, in the energy range $[-\Delta_p, \Delta_p]$, that should be equal to zero for a perfect BCS tunnel probe.

During data treatments, we chose Dynes parameters lying between 0.5 and 2% of the superconducting gap. A value of about 150 eV for Δ_p gave us generally the best overall consistency and was compatible with the estimated gap of our Ti/Al bilayers.

D.3.3 Influence of the finite measurement range

The integration bounds of integral D.7 are infinite. We should therefore measure $g\left(V\right)$ between $-\infty$ and $+\infty$ in order to perform the deconvolution procedure properly. Similarly P should be also infinite (as it corresponds to the integration bounds) and we should pseudo-inverse an infinite matrix.

However as we are almost at zero temperature, f_{FD} becomes a step function and the bounds are effectively 0 and $-eV$. Therefore in Eq. D.7, ω takes values only in the interval $[-eV_0, eV_0]$ and the knowledge of $g\left(V\right)$ in this interval is sufficient to deduce $\mathcal{A}\left(\omega\right)$ for the interval $\left[-e\left(V_0-\Delta\right), e\left(V_0-\Delta\right)\right]$. The latter is smaller because, within the gap of the tunnel probe, we do not extract information about the TDOS.

Appendix E

Calculation of Coulomb blockade peaks for a DQD

In this thesis, we model the DQD structure of our sample's CNTs with an Anderson-type Hamiltonian where Coulomb interaction has been phenomenologically replaced by a Zeeman splitting. The latter mimics indeed quite reasonably the effect of repulsion between electrons which compels to pay a charging energy to add a second electron of opposite spin in an orbital. This allows us to understand in detail how ABSs form in our system and to fit our data with a good qualitative agreement.

However, we are experimentally confronted to some situations (not to mention the Kondo effect) where this approach completely falls apart. For example, in Fig. 7.3, we can observe experimental data taken in the normal state in which four levels of two different orbitals, each one belonging to a different QD, form avoided crossings. This four avoided crossings cannot be rendered by our phenomenological approach as we have assigned a spin to each level and levels of opposite spin are not coupled together.

Here we adopt a slightly different approach, based on self-consistent calculation of the DQD occupancy. We use the Anderson model's equations of motion (EOM) in which we neglect terms responsible of the Kondo effect. With this approach, we can describe patterns such as the one of Fig. 7.3 missed by the phenomenological approach. The method we present in this appendix is an extension of the Coulomb blockade peaks calculation in QD explained in chapter 10 of Ref. [65] but for a DQD connected to normal leads.

E.1 GF of an interacting DQD connected to normal leads

E.1.1 DQD Anderson-type Hamiltonian

Here we consider an Anderson-type Hamiltonian with a left and right QDs, in series, that have on site Coulomb repulsion (we neglect interdot Coulomb repulsion) and a hopping term that couples them together:

$$H_{DQD}^{int}=\sum_{\sigma,\alpha=L,R}\epsilon_\alpha d_{\alpha\sigma}^\dagger d_{\alpha\sigma}+\sum_{\alpha=L,R}U_\alpha n_{\alpha\uparrow}n_{\alpha\downarrow}+\sum_{\sigma}\left(t'd_{L\sigma}^\dagger d_{R\sigma}+t'd_{R\sigma}^\dagger d_{L\sigma}\right)$$

with $n_{\alpha\sigma}=d_{\alpha\sigma}^\dagger d_{\alpha\sigma}$ and with notation of section 3.1.4. This DQD is coupled to normal electrodes described by:

$$\begin{array}{c}H_L=\sum_l\sum_\sigma \epsilon_l c_{l\sigma}^\dagger c_{l\sigma}\\ H_R=\sum_r\sum_\sigma \epsilon_r c_{r\sigma}^\dagger c_{r\sigma}\end{array}$$

through the terms[1]:

$$\begin{array}{c}H_{T_L}=\sum_{l,\sigma}\left(t_L d_{L\sigma}^\dagger c_{l\sigma}+t_L c_{l\sigma}^\dagger d_{L\sigma}\right)\\ H_{T_R}=\sum_{r,\sigma}\left(t_R d_{R\sigma}^\dagger c_{r\sigma}+t_R c_{l\sigma}^\dagger d_{R\sigma}\right)\end{array}$$

The complete Hamiltonian is thus equal to:

$$H=H_L+H_R+H_{DQD}^{int}+H_{T_L}+H_{T_R}$$

To calculate the DQD's TDOS $\mathcal{A}_{DQD}(\omega)$, we need to find the DQD's GF. As in this model there are no superconducting correlations and no breaking of spin degeneracy, we just need to calculate the normal spin up GFs of each QD:

$$\mathcal{G}_{L\uparrow L\uparrow}(\tau)=-\left\langle T_\tau d_{L\uparrow}(\tau)\,d_{L\uparrow}^\dagger\right\rangle \text{ and } \mathcal{G}_{R\uparrow R\uparrow}(\tau)=-\left\langle T_\tau d_{R\uparrow}(\tau)\,d_{R\uparrow}^\dagger\right\rangle$$

from which we can deduce the spin down GFs by symmetry:

$$\mathcal{G}_{L\uparrow L\uparrow}(\tau)=\mathcal{G}_{L\downarrow L\downarrow}(\tau) \text{ and } \mathcal{G}_{R\uparrow R\uparrow}(\tau)=\mathcal{G}_{R\downarrow R\downarrow}(\tau) \tag{E.1}$$

The DQD's TDOS is obtained just by taking the imaginary part of those GFs's Fourier transform:

$$\mathcal{A}_{DQD}(\omega)=-\frac{1}{\pi}\text{Im}\left[\mathcal{G}_{L\uparrow L\uparrow}^R(\omega)+\mathcal{G}_{R\uparrow R\uparrow}^R(\omega)+\mathcal{G}_{L\downarrow L\downarrow}^R(\omega)+\mathcal{G}_{R\downarrow R\downarrow}^R(\omega)\right]$$

where the superscript R means that these GFs are the retarded ones.

---

[1] Note that we have considered t', t_L and t_R real for simplicity.

E.1.2 Interacting DQD's GF calculation

Those GFs in Matsubara frequencies are obtained by resolution of the EOM as done in appendix B:

$$\frac{\partial}{\partial \tau}\mathcal{G}_{\alpha\sigma\alpha\sigma}\left(\tau\right) = -\delta\left(\tau\right)\left\langle\left\{d_{\alpha\sigma}, d_{\alpha\sigma}^{\dagger}\right\}\right\rangle - \left\langle T_{\tau}\left[H, d_{\alpha\sigma}\left(\tau\right)\right] d_{\alpha\sigma}^{\dagger}\right\rangle$$

where $\alpha = L$ or R and $\sigma =\uparrow$ or $\downarrow$.

EOM for the left QD For the left QD and after Fourier transform in Matsubara frequency and extension to all the complex plane, these equations read:

$$\begin{cases} -\left(z-\epsilon_L\right)\mathcal{G}_{L\uparrow L\uparrow}\left(z\right) & = -1 - t'\mathcal{G}_{R\uparrow L\uparrow}\left(z\right) - \sum_l t_L \mathcal{G}_{l\uparrow L\uparrow}\left(z\right) - U\mathcal{D}_{L\uparrow L\uparrow}\left(z\right) \\ -z\mathcal{G}_{l\uparrow L\uparrow}\left(z\right) & = -\epsilon_l \mathcal{G}_{l\uparrow L\uparrow}\left(z\right) - t_L \mathcal{G}_{L\uparrow L\uparrow}\left(z\right) \end{cases} \tag{E.2}$$

where we have introduced the Fourier transform of additional GFs:

$$\mathcal{G}_{R\uparrow L\uparrow}\left(\tau\right) = -\left\langle T_{\tau} d_{R\uparrow}\left(\tau\right) d_{L\uparrow}^{\dagger}\right\rangle$$

$$\mathcal{G}_{l\uparrow L\uparrow}\left(\tau\right) = -\left\langle T_{\tau} c_{l}\left(\tau\right) d_{L\uparrow}^{\dagger}\right\rangle$$

and a two-particles correlation function due to the Coulomb repulsion:

$$\mathcal{D}_{L\uparrow L\uparrow}\left(\tau\right) = -\left\langle T_{\tau} n_{L\downarrow}\left(\tau\right) d_{L\uparrow}\left(\tau\right) d_{L\uparrow}^{\dagger}\right\rangle \tag{E.3}$$

related to the evolution of a spin up electron in the left QD already occupied by a spin down electron.

Higher order correlation functions This function is also solution of its own equation of motion that we obtain by deriving Eq. E.3 with respect to the time variable (in the same way than in section B.2.3):

$$\frac{\partial}{\partial \tau}\mathcal{D}_{L\uparrow L\uparrow}\left(\tau\right) = -\delta\left(\tau\right)\left\langle\left\{n_{L\downarrow} d_{\uparrow}, d_{\uparrow}^{\dagger}\right\}\right\rangle - \left\langle T_{\tau}\left[H, n_{L\downarrow}\left(\tau\right) d_{L\uparrow}\left(\tau\right)\right] d_{\uparrow}^{\dagger}\right\rangle \tag{E.4}$$

The anti-commutator introduces the mean value of the left QD spin up occupancy that we will evaluate self-consistently:

$$\left\langle\left\{n_{L\downarrow} d_{\uparrow}, d_{\uparrow}^{\dagger}\right\}\right\rangle = \left\langle n_{L\downarrow}\right\rangle$$

whereas the commutator is equal to:

$$\begin{aligned} \left[H, n_{L\downarrow} d_{L\uparrow}\right] = & -\epsilon_L n_{L\downarrow} d_{L\uparrow} - U n_{L\downarrow} d_{L\uparrow} - t' n_{L\downarrow} d_{R\uparrow} - \textstyle\sum_l t_L n_{L\downarrow} c_{l\uparrow} \\ & - \left[t' d_{L\downarrow}^{\dagger} d_{R\downarrow} d_{L\uparrow} - \textstyle\sum_l t_L d_{L\downarrow}^{\dagger} c_{l\downarrow} d_{L\uparrow}\right] \end{aligned} \tag{E.5}$$

where we have used the fact that $(n_{L\downarrow})^2 = n_{L\downarrow}$.

The first two terms of Eq. E.5 just give correlation functions proportional to $\mathcal{D}_{L\uparrow L\uparrow}(\tau)$. The third and fourth term give correlation functions related to the possibility for an interacting electron of the left QD to go respectively in the right QD or the left electrode and come back in the left QD. The last terms in brackets introduce higher order correlations where the spin of the left QD flips by exchange with an electron of the right QD or the left lead. These processes are responsible for the Kondo effect. Our first approximation is to ignore them in the following, but they should be taken into account if one wants to see all the effects of on-site Coulomb interaction.

After Fourier transform Eq. E.4 becomes:

$$(-z + \epsilon_L + U)\,\mathcal{D}_{L\uparrow L\uparrow}(z) = -\langle n_{L\downarrow}\rangle - t'\mathcal{D}_{R\uparrow L\uparrow}(z) - \sum_l t_L \mathcal{D}_{l\uparrow L\uparrow}(z) \qquad \text{(E.6)}$$

where we have defined:

$$\mathcal{D}_{l\uparrow L\uparrow}(\tau) = -\left\langle T_\tau n_{L\downarrow}(\tau)\, c_{l\uparrow}(\tau)\, d^\dagger_{L\uparrow}\right\rangle$$

and:

$$\mathcal{D}_{R\uparrow L\uparrow}(\tau) = -\left\langle T_\tau n_{L\downarrow}(\tau)\, d_{R\uparrow}(\tau)\, d^\dagger_{L\uparrow}\right\rangle$$

Using the same method that we have used for $\mathcal{D}_{L\uparrow L\uparrow}(\tau)$ (EOM with omission of terms responsible for the Kondo effect), we can evaluate $\mathcal{D}_{l\uparrow L\uparrow}(\tau)$ and find its Fourier transform:

$$(z - \epsilon_l)\,\mathcal{D}_{l\uparrow L\uparrow}(z) = t_L \mathcal{D}_{L\uparrow L\uparrow}(z)$$

On $\mathcal{D}_{R\uparrow L\uparrow}(\tau)$ we perform a Hartree-Fock approximation, this avoids to introduce higher order correlation functions with six fermions operators:

$$\mathcal{D}_{R\uparrow L\uparrow}(\tau) = \langle n_{L\downarrow}\rangle\, \mathcal{G}_{R\uparrow L\uparrow}(\tau)$$

This is our second approximation.

GF of the left QD If we introduce the left electrode self-energy that we calculate with the same approximation than in section B.3.2:

$$\Sigma_L(z) = \sum_l \frac{t_L^2}{(z - \epsilon_l)} = -i\Gamma \mathrm{sign}\left[\mathrm{Im}(z)\right]$$

we can rewrite system E.2 and Eq. E.6 in the following form:

$$\begin{cases} (z - \epsilon_L + \Sigma_L(z))\,\mathcal{G}_{L\uparrow L\uparrow}(z) & = 1 + t'\mathcal{G}_{R\uparrow L\uparrow}(z) + U\mathcal{D}_{L\uparrow L\uparrow}(z) \\ (z - \epsilon_L - U + \Sigma_L(z))\,\mathcal{D}_{L\uparrow L\uparrow}(z) & = \langle n_{L\downarrow}\rangle + t'\langle n_{L\downarrow}\rangle\, \mathcal{G}_{R\uparrow L\uparrow}(\tau)(z) \end{cases}$$

And by combining them we find:

$$\mathcal{G}_{L\uparrow L\uparrow}\left(z\right)=\mathcal{G}^{t'=0}_{L\uparrow L\uparrow}\left(z\right)\left(1+t'\mathcal{G}_{R\uparrow L\uparrow}\left(z\right)\right)$$

with $\mathcal{G}^{t'=0}_{L\uparrow L\uparrow}\left(z\right)$ the GF of the left QD for $t'=0$:

$$\mathcal{G}^{t'=0}_{L\uparrow L\uparrow}\left(z\right)=\left[\frac{1-\langle n_{L\downarrow}\rangle}{\left(z-\epsilon_L+\Sigma_L\left(z\right)\right)}+\frac{\langle n_{L\downarrow}\rangle}{\left(z-\epsilon_L-U+\Sigma_L\left(z\right)\right)}\right]$$

And following exactly the same calculations (from the beginning) for $\mathcal{G}_{R\uparrow L\uparrow}\left(z\right)$, we end up with:

$$\mathcal{G}_{R\uparrow L\uparrow}\left(z\right)=\mathcal{G}^{t'=0}_{R\uparrow R\uparrow}\left(z\right)t'\mathcal{G}_{L\uparrow L\uparrow}\left(z\right)$$

As a conclusion of this calculation, we obtain the left QD's GF for spin up:

$$\mathcal{G}_{L\uparrow L\uparrow}\left(z\right)=\frac{\mathcal{G}^{t'=0}_{L\uparrow L\uparrow}\left(z\right)}{1-t'^2\mathcal{G}^{t'=0}_{L\uparrow L\uparrow}\left(z\right)\mathcal{G}^{t'=0}_{R\uparrow R\uparrow}\left(z\right)}$$

and by symmetry the right QD's GF for spin up:

$$\mathcal{G}_{R\uparrow R\uparrow}\left(z\right)=\frac{\mathcal{G}^{t'=0}_{R\uparrow R\uparrow}\left(z\right)}{1-t'^2\mathcal{G}^{t'=0}_{R\uparrow R\uparrow}\left(z\right)\mathcal{G}^{t'=0}_{L\uparrow L\uparrow}\left(z\right)}$$

Again using an argument of symmetry we can deduce the spin down GFs using Eq. E.1.

E.2 Self-consistent calculation of the DQD's occupancy and TDOS

E.2.1 Self-consistency

Once we have the DQD's GF, its imaginary part gives us the DQD's TDOS. From now on, we can define the left QD's TDOS:

$$\mathcal{A}_{LQD}\left(\omega\right)=-\frac{1}{\pi}\mathrm{Im}\left[\mathcal{G}_{L\uparrow L\uparrow}\left(\omega\right)+\mathcal{G}_{L\downarrow L\downarrow}\left(\omega\right)\right]=-\frac{2}{\pi}\mathrm{Im}\left[\mathcal{G}_{L\uparrow L\uparrow}\left(\omega\right)\right]$$

the right QD's TDOS:

$$\mathcal{A}_{RQD}\left(\omega\right)=-\frac{2}{\pi}\mathrm{Im}\left[\mathcal{G}_{R\uparrow R\uparrow}\left(\omega\right)\right]$$

and the DQD's TDOS:

$$\mathcal{A}_{DQD}\left(\omega\right)=\mathcal{A}_{LQD}\left(\omega\right)+\mathcal{A}_{RQD}\left(\omega\right)$$

These TDOS depend on the DQD's occupancy numbers $\langle n_L \rangle = \langle n_{L\uparrow} \rangle + \langle n_{L\downarrow} \rangle$ and $\langle n_R \rangle = \langle n_{R\uparrow} \rangle + \langle n_{R\downarrow} \rangle$ which themselves depend on these TDOS as we have:

$$\langle n_L \rangle = \int f_{FD}(\omega)\, \mathcal{A}_{LQD}(\omega)\, d\omega \tag{E.7}$$

$$\langle n_R \rangle = \int f_{FD}(\omega)\, \mathcal{A}_{RQD}(\omega)\, d\omega \tag{E.8}$$

where $f_{FD}(\omega)$ is the Fermi-Dirac distribution. occupancies $\langle n_L \rangle$ and $\langle n_R \rangle$ depend thus on temperature. However, in the following, we take the temperature equal to zero for simplicity.

Eq. E.7 and E.8 constitute a self-consistent system that we can easily solve numerically and from which we can deduce the DQD's TDOS.

E.2.2 DQD's TDOS

Here we show some results of calculation based on the self-consistent system defined above. We show that we have indeed obtained as expected the avoided crossings that were missing in our previous model where the Coulomb repulsion was replaced by a Zeeman splitting.

DQD's occupancy In Fig. E.1, we have plotted in three dimensions the DQD's occupancy as a function of ϵ_L and ϵ_R for a set of parameters that are given in the figure's legend. We can see that when we increase ϵ_L and ϵ_R the occupancy number decreases taking the shape of a staircase. Each intermediate plateau has a width approximately equal to the charging energy of the DQD but limited by the coupling to the leads which rounds this plateau on the edge.

DQD's TDOS and avoided crossings If we compare the DQD's occupancy with its TDOS represented in Fig. E.2, we see that there is a complete correspondence between occupancy and TDOS. This is expected as a peak in the TDOS corresponds to a configuration where it is possible to inject or extract an electron in the system (see appendix D).

We see that we obtain, with these calculations, the four avoided crossings which appear experimentally when four levels of two orbitals meet each other, contrary to the phenomenological model. This allows us to make a better estimation of parameter t' which couples the two QDs.

Another interesting aspect of this approach is that the coupling t' introduces some asymmetry in the peaks of the TDOS in the vicinity of the

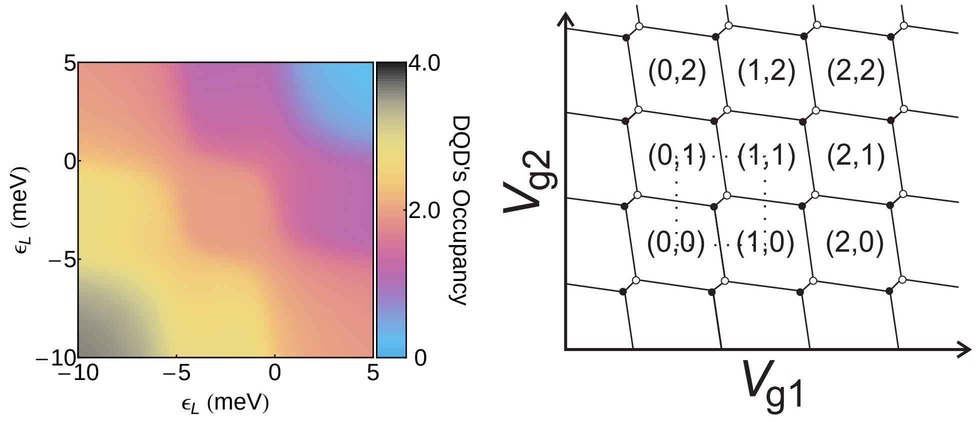

DQD's occupancy

Figure E.1: Color plot of the DQD's occupancy (left) calculated within the approach described in this appendix. Parameters: $U_L = U_R = 5$meV, $\Gamma_L = \Gamma_R = 1$ meV, $t' = 1.75$ meV. For comparison, we also show on the right a figure from Ref. [112] which represents a DQD's occupancy calculated within an electrostatic approach as a function of the gate voltages applied on the two dots. We can see that the boundaries between areas of different occupancies are rather smooth in our approach and angular within the electrostatic approach.

avoided crossings (see cuts of Fig. E.2), this may explain some asymmetries that we observe sometimes experimentally for certain Coulomb peaks.

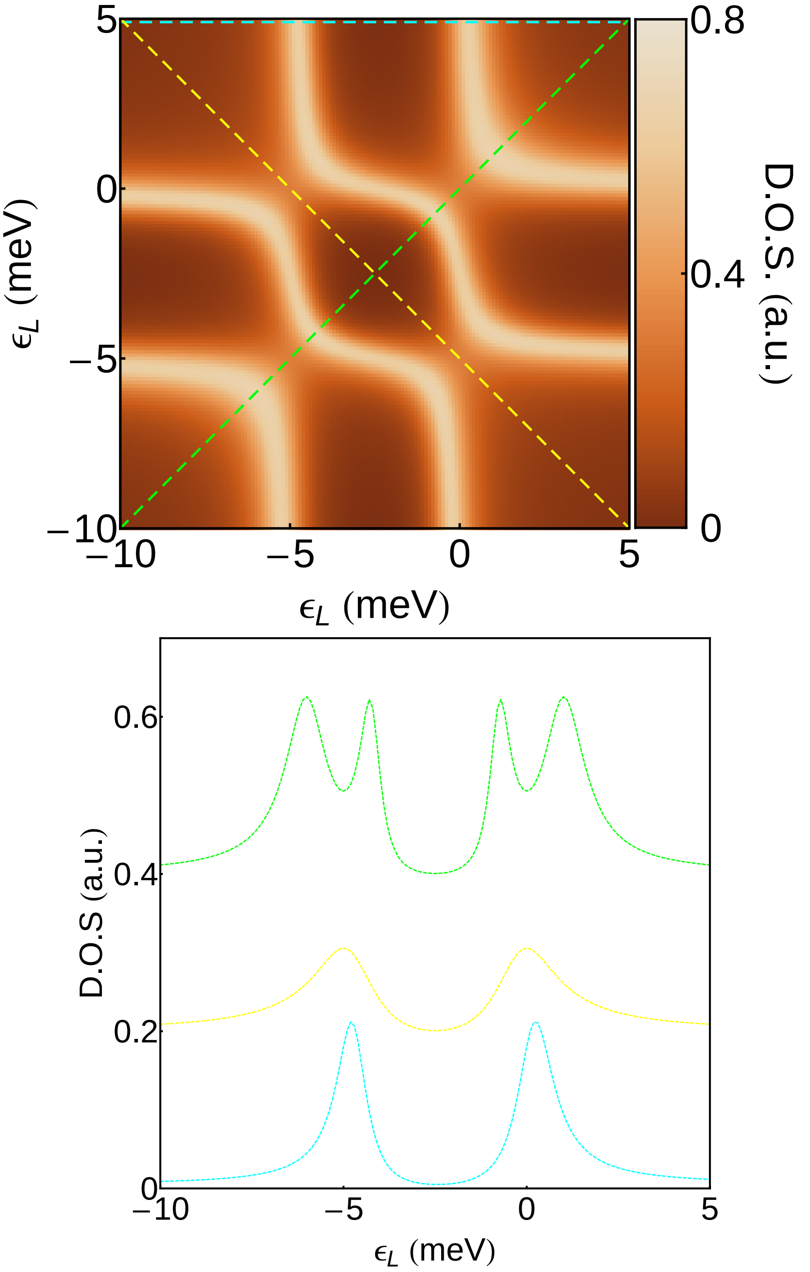

Figure E.2: Colorplot and cuts (shifted for clarity) of the TDOS calculated within the approach explained in this appendix. Parameters: $U_L = U_R =$ 5meV, $\Gamma_L = \Gamma_R = 1$ meV, $t' = 1.75$ meV

Appendix F

Bogoliubov de Gennes equations formalism

The Bogoliubov-de Gennes (BdG) equations formalism provides a compact theoretical description of mesoscopic systems with inhomogeneous superconductivity.

In this appendix, we first introduce the basic principles of this formalism and explain how it can be interpreted as "one particle" wave equations (see also Ref. [168] for more details). We also discuss why this description contains some arbitrariness that does not however change the physics described. Then we will see that these equations have evanescent solutions with energies smaller than the superconducting gap. These evanescent waves form bound states in presence of an interface with a non-superconducting material. In the next appendix, we will study a simple case where hybridization of such evanescent states allows the formation of the ABSs: the infinitely short one dimensional single channel.

F.1 Inhomogeneous superconductivity

F.1.1 Effective Hamiltonian describing an inhomogeneous superconductors

A system with inhomogeneous superconductivity can be described by an effective Hamiltonian H_{eff} obtained by mean-field approximation on the BCS Hamiltonian[1]. This Hamiltonian is composed of a "normal" term H_N and a

---

[1] We consider a problem in one dimension along x for simplicity. Furthermore a constant term $\int \frac{|\Delta|^2}{g} dr + \int \frac{U^2}{4g} dr$ ($-g$ is the interaction constant of the BCS theory of superconductivity and U a Zeeman energy) that plays no role in the discussion has been dropped

pairing interaction H_S, source of superconductivity through the formation of Cooper pairs. They read [44, 47]:

$$H_N = \sum_{k,\sigma=\uparrow,\downarrow} \xi_{k\sigma} c^\dagger_{k\sigma} c_{k\sigma}$$

$$H_S = \sum_k \Delta_k c^\dagger_{k\uparrow} c^\dagger_{-k\downarrow} + \Delta^*_k c_{-k\downarrow} c_{k\uparrow}$$

where $\{k, \sigma\}$ constitutes a complete states basis in which H_N is diagonal with σ the spin and k a quantum number that we do not need to specify here. $c_{k\sigma}$ (resp. $c^\dagger_{k\sigma}$) is an annihilation (resp. creation) operator for an electron in state (k, σ). The latter has a kinetic energy[2] $\xi_{k\sigma}$ and is paired with its time-reverse conjugated state $(-k, -\sigma)$. The strength of this pairing is given by the potential Δ_k:

$$\Delta_k = \int \phi_{k\uparrow}(x)^* \, \Delta(x) \, \phi_{-k\downarrow}(x)^* \, dx$$

with $\Delta(x) = |\Delta(x)| \, e^{i\phi(x)}$ the inhomogeneous superconducting complex order parameter and $\phi_{k\uparrow}(x)$ (resp. $\phi_{-k\downarrow}(x)$) the wave function of state $(k, \uparrow)$ (resp. $(-k, \downarrow)$).

For a system with inhomogeneous superconductivity, H_S contains normally terms of pairing between states that are not time-reverse conjugated (for example $\Delta_{pq} c^\dagger_{p\sigma} c^\dagger_{q\sigma}$ with $q \neq -p$). However as they are generally smaller, and to simplify the discussion, we drop them in this appendix.

F.1.2 Bogoliubov-de Gennes equations

The BdG equations are obtained by diagonalization of H_{eff} in Nambu space in which eigenstates of the system are expressed in term of electron-hole superposition.

In order to perform this diagonalization, we introduce spinors ψ_k that have two components: a spin up k-electron component and spin down $(-k)$-hole component:

$$\psi_k = \begin{pmatrix} c_{k\uparrow} \\ c^\dagger_{-k\downarrow} \end{pmatrix}$$

(see Ref. [54, 168]). It appears when one does the mean field approximation on the BCS Hamiltonian [47]. Without this term the interaction energy is counted twice and therefore the condensation energy is wrong, but the physics we are looking here does not depend on this condensation energy.

[2] For a Fermi liquid in presence of a magnetic field, we would have $\xi_{k\sigma} = \hbar^2 k^2/2m - E_F + \epsilon_\sigma U/2$ with $\hbar$ the Planck constant, m the electron effective mass, E_F the Fermi level and U the Zeeman energy. This term can also contain a contribution due to a static potential caused by disorder.

Hamiltonian H_{eff} can hence be written:

$$H_{eff} = \sum_k \psi_k^\dagger \begin{pmatrix} \xi_{k\uparrow} & \Delta_k \\ \Delta_k^* & -\xi_{-k\downarrow} \end{pmatrix} \psi_k + \sum_k \xi_{-k\downarrow} \tag{F.1}$$

and its diagonalization reduces to the diagonalization of 2 × 2 matrices of the first term. We thus have to solve the following system, with u_k and v_k unknown variables that are known as the "coherence factors":

$$\begin{pmatrix} \xi_{k\uparrow} & \Delta_k \\ \Delta_k^* & -\xi_{-k\downarrow} \end{pmatrix} \begin{pmatrix} u_k \\ v_k \end{pmatrix} = E \begin{pmatrix} u_k \\ v_k \end{pmatrix} \tag{F.2}$$

System F.2 constitutes the BdG equations of the system. It has two eigenvectors, that we can note $|k_+\rangle = \begin{pmatrix} u_{k+} \\ v_{k+} \end{pmatrix}$ and $|k_-\rangle = \begin{pmatrix} u_{k-} \\ v_{k-} \end{pmatrix}$, with eigenenergies ϵ_{k+} and ϵ_{k-}. Factor $u_{k\pm}$ (resp. $v_{k\pm}$) represents the electron (resp. hole) part of state $|k_\pm\rangle$ and energies $\epsilon_{k\pm}$ may be positive or negative.

F.1.3 Interpretation of the BdG equations as 'one-particle' wave equations

Equations F.2 can be interpreted as 'one-particle' wave equations, as the Schrödinger equation of a normal metal. In this interpretation, eigenstates (or Bogoliubons) fill a "vacuum" $|V\rangle$, very much like the electrons of a normal metal fill the vacuum of electron $|0\rangle$ until the Fermi level.

Bogoliubons $|k_+\rangle$ and $|k_-\rangle$ can thus be seen as "particles" to which we can associate creation operators $\gamma_{k+}^\dagger$ and $\gamma_{k-}^\dagger$:

$$\gamma_{k+}^\dagger = u_{k+} c_{k\uparrow}^\dagger + v_{k+} c_{-k\downarrow} \text{ and } \gamma_{k-}^\dagger = u_{k-} c_{k\uparrow}^\dagger + v_{k-} c_{-k\downarrow} \tag{F.3}$$

These "particles" may have positive or negative energy, as electrons in a normal metal. To simplify the discussion with no loss of generality, let's consider a particular case where, for all k, $\epsilon_{k+} \geq 0$ and $\epsilon_{k-} \leq 0$ (this is true for example in a spin degenerate system, and, for the case of a QD, in absence of local Coulomb repulsion).

Within the new algebra F.3, we can write H_{eff}:

$$H_{eff} = \sum_k \epsilon_{k+} \gamma_{k+}^\dagger \gamma_{k+} + \epsilon_{k-} \gamma_{k-}^\dagger \gamma_{k-} + \underbrace{\sum_k \xi_{k\downarrow}}_{\text{energy of the vacuum } |V\rangle}$$

In this form, the Hamiltonian is made of three terms: the first and second terms concern respectively Bogoliubons of positive and negative energy, whereas the third concerns the energy of the "vacuum" $|V\rangle$, mentioned above, constituted by an empty band of spin up and a full band of spin down (see Fig. F.1 (a)):

$$|V\rangle = \prod_k c^\dagger_{-k\downarrow}|0\rangle$$

The term $\sum_k \xi_{k\downarrow}$ comes from the anti-commutation rule for fermions: we have replaced $c^\dagger_{-k\downarrow}c_{-k\downarrow}$ by $1 - c_{-k\downarrow}c^\dagger_{-k\downarrow}$, an operation which corresponds to the inversion of the spin down band.

Eigenstates $|k_+\rangle$ and $|k_-\rangle$ can thus be seen as "particles" of wave functions:

$$\begin{pmatrix} u_{k+}\phi_{k\uparrow}(x) \\ v_{k+}\phi_{-k\downarrow}(x)^* \end{pmatrix} \text{ and } \begin{pmatrix} u_{k-}\phi_{k\uparrow}(x) \\ v_{k-}\phi_{-k\downarrow}(x)^* \end{pmatrix}$$

that propagates into $|V\rangle$.

In this context, the ground state of the system $|G\rangle$ is obtained by populating this "vacuum" with Bogoliubons of negative energies[3]:

$$|G\rangle = \prod_k \gamma^\dagger_{k-}|V\rangle = \prod_k \left(v_{k-} + u_{k-}c^\dagger_{k\uparrow}c^\dagger_{-k\downarrow}\right)|0\rangle$$

whereas the excitations $\gamma_{k-}|G\rangle$ and $\gamma^\dagger_{k+}|G\rangle$, that have always positive energies $|\epsilon_{k-}|$ and $|\epsilon_{k+}|$, correspond to the creation of a quasi-hole with operator γ_{k-} and the creation of a quasi-electron with operator $\gamma^\dagger_{k+}$ (in complete analogy with the normal metal which has hole or electron excitations of positive energy respectively below an above the Fermi level).

F.1.4 Arbitrariness of the description and diagonalization with a different spinor

F.1.4.1 Arbitrariness of the description

This description contains some arbitrariness due to the choice of the spinor. Indeed, if we diagonalize the Hamiltonian, for example, using spinor $\overline{\psi_k} = \begin{pmatrix} c^\dagger_{k\uparrow} \\ c_{-k\downarrow} \end{pmatrix}$, we can show that equation F.1 becomes:

$$H_{eff} = \sum_k \overline{\psi_k}^\dagger \begin{pmatrix} -\xi_{k\uparrow} & -\Delta^*_k \\ -\Delta_k & \xi_{-k\downarrow} \end{pmatrix} \overline{\psi_k} + \sum_k \xi_{k\uparrow} \tag{F.4}$$

---

[3] In particular, in a system with homogeneous superconductivity $|G\rangle$ corresponds to the well-known BCS ground state $|G\rangle = |\psi_{BCS}\rangle = \prod_k(u_k - v^*_k c^\dagger_{k\uparrow}c^\dagger_{-k\downarrow})|0\rangle$ with the "coherence factors" $u_k = \frac{1}{\sqrt{2}}\sqrt{1+\frac{\xi_k}{E_k}}$ and $v_k = \frac{e^{-i\phi}}{\sqrt{2}}\sqrt{1-\frac{\xi_k}{E_k}}$, where $\xi_k = \xi_{k\uparrow} = \xi_{-k\downarrow}$, $E_k = \sqrt{\xi_k^2 + |\Delta|^2}$ and ϕ is the phase of the superconducting order parameter.

and after diagonalization H_{eff} reads:

$$H_{eff} = \sum_k -\epsilon_{k+}\overline{\gamma}^\dagger_{k+}\overline{\gamma}_{k+} - \epsilon_{k-}\overline{\gamma}^\dagger_{k-}\overline{\gamma}_{k-} + \sum_k \xi_{k\uparrow}$$

with[4]:

$$\overline{\gamma}^\dagger_{k+} = \gamma_{k+} \text{ and } \overline{\gamma}^\dagger_{k-} = \gamma_{k-} \tag{F.5}$$

and energies $\epsilon_{k\pm}$ are the same than before.

We see that we have inverted the role of spin up and down, the "vacuum" $|\overline{V}\rangle$ in particular is now constituted by a full band of spin up and an empty band of spin down (as can be seen with the third term giving the energy of the vacuum). Moreover the new "particles" $|\overline{k_+}\rangle$ and $|\overline{k_-}\rangle$ are the "antiparticles" of $|k_+\rangle$ and $|k_-\rangle$, and therefore have the opposite energies $-\epsilon_{k+}$ and $-\epsilon_{k-}$.

The signs of these energies is thus arbitrary and depend on the spinor chosen.

F.1.4.2 Same physics described

However, despite the apparent differences with the description of section F.1.3, the physics described is the same, *i.e.* the ground state and its excitations have not changed.

Indeed, the new ground state $|\overline{G}\rangle$ is:

$$|\overline{G}\rangle = \prod_k \overline{\gamma}^\dagger_{k+}|\overline{V}\rangle = \prod_k \left(u^*_{k+} - v^*_{k+}c^\dagger_{k\uparrow}c^\dagger_{-k\downarrow}\right)|0\rangle$$

but, as $|k_+\rangle$ and $|k_-\rangle$ are orthogonal, we have $u^*_{k+} = v_{k-}$ and $-v^*_{k+} = u_{k-}$, so that[5]:

$$|\overline{G}\rangle = |G\rangle \tag{F.6}$$

The ground states are the same whatever the choice of the spinor, and this is expected as we start from exactly the same Hamiltonian.

Concerning the new excitations, they include the quasiholes $\overline{\gamma}_{k+}|\overline{G}\rangle$ of energy $|\epsilon_{k+}|$ and the quasielectrons $\overline{\gamma}^\dagger_{k-}|\overline{G}\rangle$ of energy $|\epsilon_{k-}|$. They are the same than in section F.1.3, as we can show the following equalities:

$$\overline{\gamma}_{k+}|\overline{G}\rangle = \gamma^\dagger_{k+}|G\rangle \text{ and } \overline{\gamma}^\dagger_{k-}|\overline{G}\rangle = \gamma_{k-}|G\rangle$$

combining equations F.6 and F.5.

---

[4] This comes simply from the fact that the 2×2 matrix in F.4 is the opposite of the complex conjugate of the matrix in F.1: $-\begin{pmatrix} -\xi_{k\uparrow} & -\Delta^*_k \\ -\Delta_k & \xi_{-k\downarrow} \end{pmatrix}^* = \begin{pmatrix} \xi_{k\uparrow} & \Delta_k \\ \Delta^*_k & -\xi_{-k\downarrow} \end{pmatrix}$.

[5] To obtain $u^*_{k+} = v_{k-}$ and $-v^*_{k+} = u_{k-}$, we actually use the orthogonality $\langle k_+|k_-\rangle = u^*_{k+}u_{k-} + v^*_{k+}v_{k-} = 0$, but also the normalizations $|u_{k\pm}|^2 + |v_{k\pm}|^2 = 1$ of the vectors.

F.1.4.3 Diagonalization using a spinor with equivalence between the spins

The spinor used to diagonalize H_{eff} can be adapted to the symmetry of the system. A clever choice provides solutions with clearer physical meanings. For example in graphene a four-dimensional spinor [169] is suitable to solve BdG equations because of the spin and valley degeneracies. The two valleys are indeed time-reversal conjugated and thus coupled by superconductivity.

The spinor ψ_k, that we chose above for diagonalization of H_{eff}, is an interesting option when the spin symmetry is broken. Otherwise this choice remains purely arbitrary and another one can be made leading to a different vacuum and different solutions to fill it. The previous "vacuum" $|V\rangle$ (resp. $|\overline{V}\rangle$) contains a distinction between spins because we choose to diagonalize H_{eff} in Nambu space in which solutions are described in terms of electrons (resp. holes) of spin up and holes (resp. electrons) of spin down.

However, to diagonalize H_{eff}, we could perfectly choose a spinor with equivalence between spins. For example if k is the momentum, we can consider a spinor $\widetilde{\psi}_{k\sigma} = \begin{pmatrix} c_{k\sigma} \\ c^{\dagger}_{-k-\sigma} \end{pmatrix}$ with $k > 0$, and write H_{eff} differently than F.1 and F.4:

$$H_{eff} = \sum_{\sigma} \sum_{k>0} \widetilde{\psi}^{\dagger}_{k\sigma} \begin{pmatrix} \xi_{k\sigma} & \epsilon_{\sigma}\Delta_k \\ \epsilon_{\sigma}\Delta^{*}_{k} & -\xi_{-k-\sigma} \end{pmatrix} \widetilde{\psi}_{k\sigma} + \sum_{\sigma} \sum_{k>0} \xi_{-k\sigma}$$

with $\epsilon_{\sigma} = 1$ (resp. -1) for $\sigma =\uparrow$ (resp. $\downarrow$).

Within the Nambu space defined by $\widetilde{\psi}_{k\sigma}$, excitations are described in terms of electron of positive momentum and hole of negative momentum, propagating in a new vacuum $|\widetilde{V}\rangle$:

$$|\widetilde{V}\rangle = \prod_{\sigma} \prod_{k>0} c^{\dagger}_{-k-\sigma}|0\rangle$$

This vacuum corresponds to an empty band of $k > 0$ and a full band of $k < 0$ (see Fig. F.1 (b)) and Bogoliubons are described in terms of electron with positive momentum and hole with negative momentum.

But in the end, as we start from the same Hamiltonian than in section F.1.3, this description with no spin symmetry breaking will bring the same physics than a diagonalization of H_{eff} with ψ_k or $\overline{\psi_k}$. The broken spin symmetry, introduced when we use spinor ψ_k or $\overline{\psi_k}$ is thus purely apparent and has no influence on the physics described.

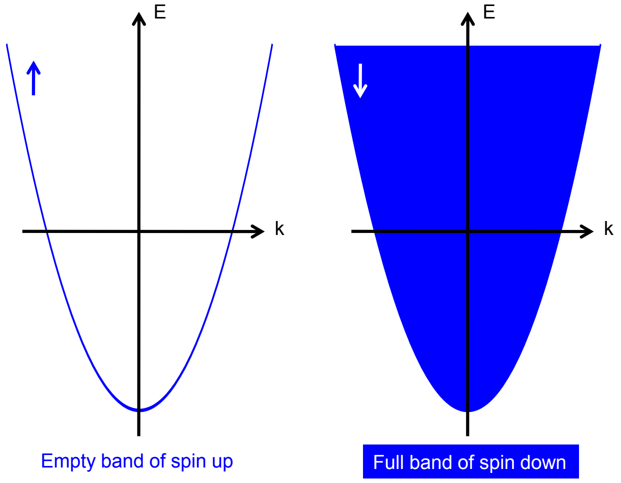

(a) Vacuum after inversion of a spin down band

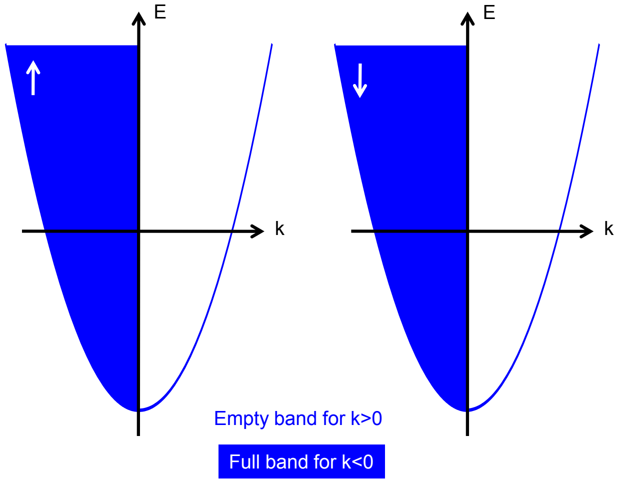

(b) Vacuum after inversion of the $k < 0$ band

Figure F.1: Depending on the choice of the spinor used to diagonalize the Hamiltonian, solutions of the BdG equations fill different kinds of vacuum. When solutions of the BdG equations are expressed in terms of electron of spin up and holes of spin down, the vacuum is constituted by an empty band of spin up and a full band of spin down because of a spin down band inversion. But if they are expressed in terms of electron of positive momentum and hole of negative momentum, the vacuum is an empty band for positive momentum and a full band for negative momentum.

F.1.4.4 Excitation picture

The excitation picture (see Ref. [168]) provides a different way (but completely equivalent) to describe a system with superconductivity. In this picture, we arrange the states of the system according to their total energy. From the ground state, one can only create positive-energy excitations (see Fig. F.2 on the left). Our system has thus excitations at energy $|\epsilon_+|$ and $|\epsilon_-|$ which correspond to emptying a negative-energy ABS or filling a positive-energy ABS (see Fig. F.2 on the right). However, the energies of these excitations do not depend on the initial convention regarding electrons and holes.

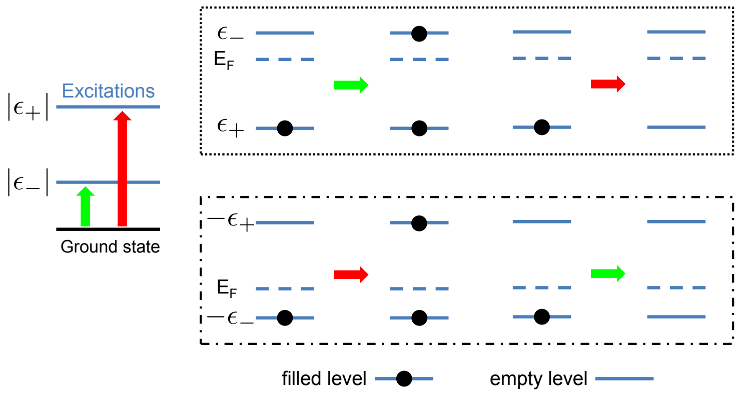

Representation of the system’s excitations with two different conventions

Figure F.2: Diagrammatic representation of system’s excitations from the ground state, for two different conventions: description in terms of electron of spin up and hole of spin down (top diagram with dotted frame), or description in terms of electron of spin down and hole of spin up (bottom diagram with dashed-dotted frame). Depending on the chosen convention, excitation of energy $|\epsilon_+|$ (thick red arrows) corresponds either to emptying an ABS of energy $-|\epsilon_+|$ below the Fermi level E_F or filling one of energy $|\epsilon_+|$ above E_F, whereas excitation of energy $|\epsilon_-|$ (thick green arrows) corresponds either to emptying an ABS of energy $-|\epsilon_-|$ below the Fermi level or filling one of energy of energy $|\epsilon_-|$ above the Fermi level.

The fact that we talk about positive and negative energies is just a convenient way to describe BCS superconductor’s eigenstates, it corresponds to the so-called semiconductor model [47, 167, 168]. But, contrarily to a real semiconductor, it is impossible to distinguish states of positive and negative energies, as they depend of an arbitrary choice made when defining the Nambu space.

F.2 States in gap

In section F.1, we have expressed the eigenenergies and eigenvectors of the mean field BCS Hamiltonian using a parametrization of the states in k, and introducing the "coherence factors" $u_{k\pm}$ and $v_{k\pm}$. If we parametrize these eigenstates by their energy, we can see that some of these solutions are evanescent waves with energy smaller than the superconducting gap (in a bulk superconductor there are no quasiparticle state between $-|\Delta|$ and $|\Delta|$, see Ref. [47]).

Let's consider the case of an homogeneous spin degenerate BCS superconductor [47] ($\xi_{k\uparrow} = \xi_{-k\downarrow} = \xi_k = \frac{\hbar^2 k^2}{2m} - \mu$ with $\hbar$ the reduced Planck constant, m the mass of electron and E_F the Fermi level) with a superconducting order parameter $\Delta = |\Delta| e^{i\phi}$. We have the eigenstates:

$$\begin{pmatrix} u_k \\ v_k \end{pmatrix} \text{ and } \begin{pmatrix} -v_k^* \\ u_k \end{pmatrix}$$

with:

$$u_k = \frac{1}{\sqrt{2}} \sqrt{1 + \frac{\xi_k}{\sqrt{\xi_k^2 + |\Delta|^2}}} \text{ and } v_k = \frac{e^{-i\phi}}{\sqrt{2}} \sqrt{1 - \frac{\xi_k}{\sqrt{\xi_k^2 + |\Delta|^2}}}$$

that have eigenenergies $\epsilon_{k\pm} = \pm\sqrt{\xi_k^2 + |\Delta|^2}$ roots of the equation in ϵ:

$$\text{Det} \begin{pmatrix} \xi_k - \epsilon & \Delta \\ \Delta^* & -\xi_k - \epsilon \end{pmatrix} = 0$$

The kinetic energy ξ_k reads then:

$$\xi_k^2 = \epsilon^2 - |\Delta|^2$$

and can take real or complex values:

$$\xi_k = \begin{cases} \pm\sqrt{\epsilon^2 - |\Delta|^2} \text{ for } |\epsilon| > |\Delta| \\ \pm i\sqrt{|\Delta|^2 - \epsilon^2} \text{ for } |\epsilon| < |\Delta| \end{cases}$$

Therefore, as around the Fermi level $\xi_k \simeq 2E_F(\frac{k}{k_F} - 1)$, eigenstates' momentum are given by:

$$k_\pm(\epsilon) = \begin{cases} k_F \left(1 \pm \frac{\sqrt{\epsilon^2 - |\Delta|^2}}{2E_F}\right) \text{ for } |\epsilon| > |\Delta| \\ k_F \left(1 \pm i\frac{\sqrt{|\Delta|^2 - \epsilon^2}}{2E_F}\right) \text{ for } |\epsilon| < |\Delta| \end{cases}$$

We hence have solutions corresponding to waves that decay or rise slowly ($|\mathrm{Im}\,[k_\pm]| \ll \mathrm{Re}\,[k_\pm] = k_F$) while propagating. They must necessarily be bounded in space on the side where they grow (for instance by reaching an interface), otherwise the wavefunction is not normalized.

In this parametrization, the eigenvectors[6] can be written as:

$$\frac{e^{ik_+(\epsilon)x}}{\sqrt{1+\left|a\left(\frac{\epsilon}{|\Delta|}\right)\right|^2}}\begin{bmatrix} 1 \\ a\left(\frac{\epsilon}{|\Delta|}\right)e^{-i\phi} \end{bmatrix} \quad ; \quad \frac{e^{ik_-(\epsilon)r}}{\sqrt{1+\left|a\left(\frac{\epsilon}{|\Delta|}\right)\right|^2}}\begin{bmatrix} a\left(\frac{\epsilon}{|\Delta|}\right)e^{+i\phi} \\ 1 \end{bmatrix} \tag{F.7}$$

where $a(\varepsilon)$ is given by the ratio between the coherence factor parametrized in energy:

$$a(\varepsilon) = \begin{cases} \mathrm{sign}(\varepsilon)\left|\varepsilon - \sqrt{\varepsilon^2-1}\right| & \text{for } |\varepsilon| > 1 \\ \varepsilon - i\sqrt{1-\varepsilon^2} = e^{-i\arccos(\varepsilon)} & \text{for } |\varepsilon| < 1 \end{cases}$$

The function $a(\varepsilon)$ has the properties:

$$\begin{aligned} \forall\varepsilon \quad -a(-\varepsilon) &= (a(\varepsilon))^* \text{ (for } |\varepsilon| > 1, a \text{ is real and thus simply odd)} \\ |\varepsilon| < 1 \quad \frac{1}{a(\varepsilon)} &= (a(\varepsilon))^* \Leftrightarrow |a(\varepsilon)| = 1 \end{aligned}$$

and is represented in Fig. F.3.

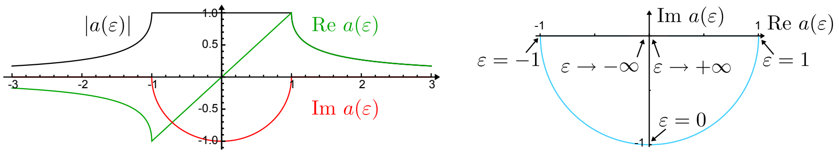

Figure F.3: Plot of the modulus, real part and imaginary part (l.h.s.), and parametric plot in the complex plan (r.h.s.) of the function $a(\varepsilon)$ as a function of ε.

---

[6] Note that these vectors are orthogonal because of their different k vectors, not their e-h components.

Appendix G

Andreev Bound States in a well-known system

In this appendix, we analyze the formation of Andreev Bound States (ABSs) in well-known model systems. We address cases where the weak link connecting two superconducting reservoirs is an infinitely short one dimensional single channel (achievable experimentally in a superconducting atomic-size quantum point contact). It has been proposed [170] for the realization of a new type of superconducting qubit where a two-level system is constituted by the ABS.

We analyze first a system with a weak link of perfect transmission, and then a system with a weak link of finite transmission.

G.1 ABSs in an infinitely short perfectly transmitted one dimensional single channel

In Fig. G.1, we have sketched an infinitely short single channel in one dimension with a perfect transmission connected on both side to superconducting leads. In such system, for electrons with an energy smaller than the superconducting gap Δ, superconducting electrodes act as perfect mirrors where electrons are reflected as their time reversal conjugated holes propagating in opposite direction. This constitutes therefore a kind of Fabry-Perot for electrons with infinite finesse and phase-conjugated mirrors [52].

In this "Fabry-Perot", a right moving electron, with energy $|\epsilon| < \Delta$, is reflected on the right mirror as a left moving hole with opposite spin, while a Cooper pair of charge 2e is transferred in the superconductor. The reflected hole acquired a phase $\arg[a(\epsilon/\Delta)e^{-i\phi_R}]$ with respect to the electron, this phase depending on the energy of the electron and the superconducting phase

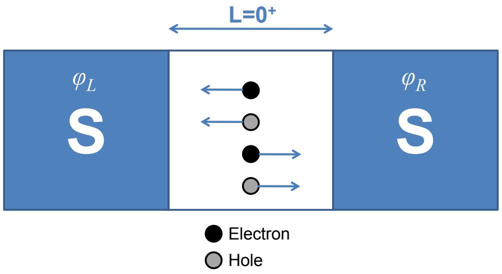

Figure G.1: Schematic representation of a S-N-S junction based on an infinitely short unidimensional single channel. A S-N-S junction acts as Fabry-Perot resonator with phase-conjugating mirrors for electrons and holes.

of the lead ϕ_R (see section F.2). As it propagates in opposite direction, this hole is reflected on the left mirror as right moving electron, while a Cooper pair is extracted from the left superconductor. The electron acquires an additional phase of $\arg[a(\epsilon/\Delta)e^{i\phi_L}]$ with respect to the hole.

The resonant condition of this Fabry-Perot is reached if the total phase acquired is a multiple of 2π. Or in other words if:

$$a(\epsilon/\Delta)^2 e^{i(\phi_L-\phi_R)} = 1$$

two ABSs, responsible of the supercurrent flow, form with energies, represented in Fig. G.2), that are 2π periodic:

$$\epsilon_\pm = \mp\Delta\cos\left(\frac{\delta}{2}\right)\mathrm{sign}\left[\sin\left(\frac{\delta}{2}\right)\right]$$

where $\delta = \phi_L - \phi_R$.

Each of these two states carry supercurrent in opposite direction. As explained in Ref. [171], the latter is given by the following current-phase relationship:

$$I_\pm = \frac{1}{\phi_0}\frac{\partial\epsilon_\pm}{\partial\phi} = \pm 2\frac{e\Delta}{2\hbar}\left|\sin\left(\frac{\delta}{2}\right)\right|$$

where ϕ_0 is the flux quantum.

G.2 ABSs in an infinitely short one dimensional single channel with finite transmission

If the weak link connecting the superconducting reservoirs has a finite transmission, these two ABSs are hybridized and form an avoided crossing around

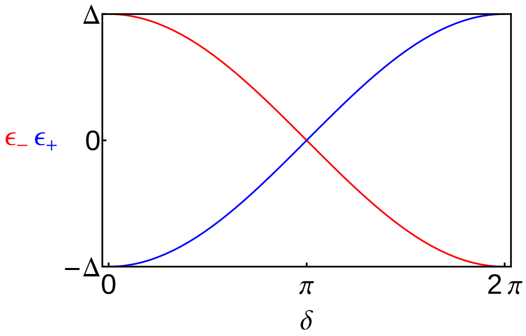

Figure G.2: Energies of the two Andreev Bound States $\epsilon_\pm$, as a function of the superconducting phase difference δ, in an infinitely short perfectly transmitted weak link with a single channel.

$\delta = \pi$. Describing the weak link by the following scattering matrix for electrons (with r and t real numbers):

$$S^e = \begin{pmatrix} -ir & t \\ t & -ir \end{pmatrix}$$

ABSs' energies can be found using Eq. 2.1. This leads the expression:

$$\epsilon_\pm = \pm\Delta\sqrt{1 - \tau \sin^2\left(\frac{\delta}{2}\right)} \tag{G.1}$$

where $\tau = |t|^2 = 1 - |r|^2$ is the transmission probability of the weak link. A gap is thus open around $\delta = \pi$, and increases with a decreasing transmission of the weak link.

In Fig. G.3, we have traced, in red, ϵ_+ and ϵ_- for $\tau = 1$, 0.8 and 0.6 using expressions G.1. The dashed green lines are also ϵ_+ and ϵ_- but obtained from the GF formalism (chapter 3) for a single non-interacting QD ($U = 0$), highly coupled to its leads ($\Gamma \gg \Delta$), at resonance with the Fermi level ($\epsilon_0 = 0$) and with $\delta\Gamma$ chosen in such way that the QD transmission obtained from the Breit-Wigner formula [56]:

$$\tau = 1 - \left(\frac{\delta\Gamma}{\Gamma}\right)^2$$

is equal to 1, 0.8 and 0.6. Let's point out that we could have decrease the transmission of the QD, keeping $\delta\Gamma = 0$, but driving the QD out of resonance ($\epsilon_0 \neq 0$). We can see that the two formalisms yield completely equivalent results.

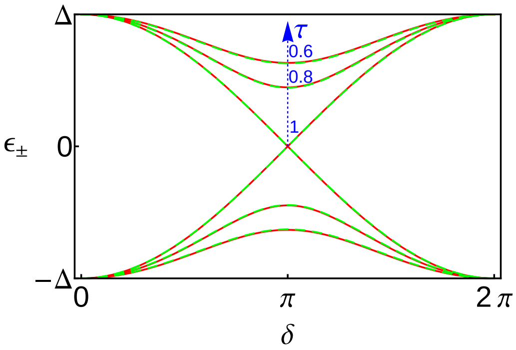

Figure G.3: Energies of the two Andreev Bound States $\epsilon_\pm$, as a function of the superconducting phase difference δ, in an infinitely short weak link with a single channel with transmission $\tau = 1$, 0.8 and 0.6, calculated from the scattering formalism of chapter 2 (red). In green, $\epsilon_\pm$ are calculated, within the GF formalism of chapter 3, for a QD with transmission 1, 0.8 and 0.6 obtained respectively with $\Gamma_R = 100\Delta$, $\sim 38.2\Delta$, $\sim 22.5\Delta$ and the following common parameters: $\Gamma_L = 100\Delta$, $U = 0$ and $\epsilon_0 = 0$. The two formalisms yields completely equivalent results.

Bibliography

[1] Y-J. Doh, J. A. van Dam, A. L. Roest, E. P. A. M. Bakkers, L. P. Kouwenhoven, and S. De Franceschi. Tunable Supercurrent Through Semiconductor Nanowires. *Science*, 309(5732):272 –275, July 2005. 13

[2] J. Xiang, A. Vidan, M. Tinkham, R. M. Westervelt, and C. M. Lieber. Ge/Si nanowire mesoscopic Josephson junctions. *Nat Nano*, 1(3):208–213, December 2006. 13

[3] J. A. van Dam, Y. V. Nazarov, E. P. A. M. Bakkers, S. De Franceschi, and L. P. Kouwenhoven. Supercurrent reversal in quantum dots. *Nature*, 442(7103):667–670, 2006. 13, 40, 57

[4] A. Y. Kasumov, R. Deblock, M. Kociak, B. Reulet, H. Bouchiat, I. I. Khodos, Y. B. Gorbatov, V. T. Volkov, C. Journet, and M. Burghard. Supercurrents Through Single-Walled Carbon Nanotubes. *Science*, 284(5419):1508–1511, 1999. 13, 14

[5] M. R. Buitelaar, T. Nussbaumer, and C. Schönenberger. Quantum Dot in the Kondo Regime Coupled to Superconductors. *Physical Review Letters*, 89(25):256801, December 2002. 13, 17, 131, 141, 164

[6] M. Buitelaar, W. Belzig, T. Nussbaumer, B. Babić, C. Bruder, and C. Schönenberger. Multiple Andreev Reflections in a Carbon Nanotube Quantum Dot. *Physical Review Letters*, 91(5):1–4, August 2003. 13

[7] P. Jarillo-Herrero, J. A. van Dam, and L. P. Kouwenhoven. Quantum supercurrent transistors in carbon nanotubes. *Nature*, 439(7079):953–956, February 2006. 13, 14, 114, 213

[8] J-P. Cleuziou, W. Wernsdorfer, V. Bouchiat, T. Ondarçuhu, and M. Monthioux. Carbon nanotube superconducting quantum interference device. *Nature nanotechnology*, 1(1):53–9, October 2006. 13, 14, 57, 114, 119

[9] A. Eichler, R. Deblock, M. Weiss, C. Karrasch, V. Meden, C. Schönenberger, and H Bouchiat. Tuning the Josephson current in carbon nanotubes with the Kondo effect. *Physical Review B*, 79(16):161407, 2009. 13, 17, 114, 131, 141, 164, 215

[10] A. Eichler, M. Weiss, S. Oberholzer, C. Schönenberger, A. Levy Yeyati, J. C. Cuevas, and A. Martín-Rodero. Even-odd effect in Andreev transport through a carbon nanotube quantum dot. *Physical review letters*, 99(12):126602, 2007. 13, 131, 141, 157, 164

[11] A. Eichler, M. Weiss, and C. Schönenberger. Gate-tunable split Kondo effect in a carbon nanotube quantum dot. *Nanotechnology*, 22:265204, July 2011. 13, 131, 157, 159

[12] D. C. Ralph, C. T. Black, and M. Tinkham. Spectroscopic Measurements of Discrete Electronic States in Single Metal Particles. *Physical Review Letters*, 74(16):3241–3244, April 1995. 13

[13] C. T. Black, D. C. Ralph, and M. Tinkham. Spectroscopy of the Superconducting Gap in Individual Nanometer-Scale Aluminum Particles. *Physical Review Letters*, 76(4):688–691, January 1996. 13

[14] C. Buizert, A. Oiwa, K. Shibata, K. Hirakawa, and S. Tarucha. Kondo universal scaling for a quantum dot coupled to superconducting leads. *Physical review letters*, 99(13):136806, 2007. 13, 17, 131, 141, 164

[15] C. B. Winkelmann, N. Roch, W. Wernsdorfer, V. Bouchiat, and F. Balestro. Superconductivity in a single-C60 transistor. *Nat Phys*, 5(12):876–879, December 2009. 13

[16] E. Vecino, A. Martín-Rodero, and A. Levy Yeyati. Josephson current through a correlated quantum level: Andreev states and pi junction behavior. *Physical Review B*, 68(3):035105, July 2003. 16, 17, 35, 39, 57, 114, 115, 116, 209, 211

[17] P. Coleman. Local moment physics in heavy electron systems. *arXiv:cond-mat/0206003*, May 2002. 17, 203, 213

[18] T. Sand-Jespersen, J. Paaske, B. M. Andersen, K. Grove-Rasmussen, H. I. Jørgensen, M. Aagesen, C. B. Sørensen, P. E. Lindelof, K. Flensberg, and J. Nygård. Kondo-Enhanced Andreev Tunneling in InAs Nanowire Quantum Dots. *Physical Review Letters*, 99(12):126603, 2007. 17, 131, 141

[19] K. Grove-Rasmussen, H. Ingerslev Jørgensen, and P. E. Lindelof. Kondo resonance enhanced supercurrent in single wall carbon nanotube Josephson junctions. *New Journal of Physics*, 9:124–124, May 2007. 17, 131, 141

[20] R. Maurand. *Carbon nanotube based nanoSQUIDs : quantum dot Josephson Pi-junction, Kondo effect, and magnetic detection of molecular nanomagnets*. PhD thesis, February 2011. 17, 57, 114, 131

[21] K. J. Franke, G. Schulze, and J. I. Pascual. Competition of Superconducting Phenomena and Kondo Screening at the Nanoscale. *Science*, 332(6032):940, 2011. 17, 131, 141, 215

[22] L. I. Glazman and K. A. Matveev. Resonant Josephson current through Kondo impurities in a tunnel barrier. *JETP LETTERS*, 49(10):659–662, May 1989. 17, 34, 141

[23] M-S. Choi, M. Lee, K. Kang, and W. Belzig. Kondo effect and Josephson current through a quantum dot between two superconductors. *Physical Review B*, 70(2):020502, July 2004. 17, 141

[24] J. Bauer, A. Oguri, and A. C. Hewson. Spectral properties of locally correlated electrons in a Bardeen Cooper Schrieffer superconductor. *Journal of Physics: Condensed Matter*, 19:486211, December 2007. 17, 56, 141, 151

[25] R. Žitko, M. Lee, R. López, R. Aguado, and M-S. Choi. Josephson Current in Strongly Correlated Double Quantum Dots. *Physical Review Letters*, 105(11):116803, September 2010. 17, 141

[26] A. F. Andreev. Thermal conductivity of the intermediate state of superconductors. *Sov. Phys. JETP*, 19:1228, 1964. 18, 23

[27] D. Saint-James. Elementary excitations in the vicinity of the surface separating a normal metal and a superconducting metal. Excitations élémentaires au voisinage de la surface de séparation d'un métal normal et d'un métal supraconducteur. *Journal de Physique*, 25(10):7, 1964. 18, 23

[28] A. F. Andreev. Electron spectrum of the intermediate state of superconductors. *Sov. Phys. JETP*, 22:455, 1966. 18, 23

[29] A. Golub, I. Kuzmenko, and Y. Avishai. Kondo Correlations and Majorana Bound States in a Metal to Quantum-Dot to Topological-Superconductor Junction. *Physical Review Letters*, 107(17):176802, October 2011. 18

[30] F. Deon, V. Pellegrini, F. Giazotto, G. Biasiol, L. Sorba, and F. Beltram. Quantum dot spectroscopy of proximity-induced superconductivity in a two-dimensional electron gas. *Applied Physics Letters*, 98:132101, 2011. 20

[31] F. Deon, V. Pellegrini, F. Giazotto, G. Biasiol, L. Sorba, and F. Beltram. Proximity effect in a two-dimensional electron gas probed with a lateral quantum dot. *Physical Review B*, 84(10):100506, 2011. 20

[32] J. Alicea. Majorana fermions in a tunable semiconductor device. *Physical Review B*, 81(12):125318, March 2010. 20, 81

[33] C. Altimiras, H. le Sueur, U. Gennser, A. Cavanna, D. Mailly, and F. Pierre. Non-equilibrium edge-channel spectroscopy in the integer quantum Hall regime. *Nat Phys*, 6(1):34–39, January 2010. 20

[34] P. G. de Gennes and D. Saint-James. Elementary excitations in the vicinity of a normal metal-superconducting metal contact. *Physics Letters*, 4(2):151–152, March 1963. 23

[35] P. G. de Gennes. Boundary Effects in Superconductors. *Reviews of Modern Physics*, 36(1):225, January 1964. 23

[36] Y. M. Blanter and M. Büttiker. Shot Noise in Mesoscopic Conductors. *Physics Reports*, 336(1-2):1–166, 2000. 23, 29, 34, 126

[37] C. W. J. Beenakker. Random-matrix theory of quantum transport. *Reviews of Modern Physics*, 69(3):731, July 1997. 23

[38] Y. V. Nazarov. Circuit Theory of Andreev Conductance. *Physical Review Letters*, 73(10):1420, 1994. 23

[39] R. S. Keizer, S. T. B. Goennenwein, T. M. Klapwijk, G. Miao, G. Xiao, and A. Gupta. A spin triplet supercurrent through the half-metallic ferromagnet CrO2. *Nature*, 439(7078):825–7, February 2006. 23

[40] T. S. Khaire, M. A. Khasawneh, W. P. Pratt, and N. O. Birge. Observation of Spin-Triplet Superconductivity in Co-Based Josephson Junctions. *Physical Review Letters*, 104(13):137002, March 2010. 23

[41] F. Bergeret, A. Volkov, and K. Efetov. Long-Range Proximity Effects in Superconductor-Ferromagnet Structures. *Physical Review Letters*, 86(18):4096–4099, April 2001. 23

[42] L. Fu and C. L. Kane. Superconducting Proximity Effect and Majorana Fermions at the Surface of a Topological Insulator. *Physical Review Letters*, 100(9):096407, March 2008. 23, 81

[43] I. O. Kulik. Macroscopic quantization and the proximity effect in SNS junctions. *Soviet Journal of Experimental and Theoretical Physics*, 30(5):944, 1969. 23, 53

[44] P. G. de Gennes. *Superconductivity of Metals and Alloys.* Addison-Wesley, New York, 1989. 23, 260

[45] J. Bardeen, L. N. Cooper, and J. R. Schrieffer. Microscopic theory of superconductivity. *Physical Review*, 106(1):162–164, April 1957. 23

[46] J. Bardeen, L. N. Cooper, and J. R. Schrieffer. Theory of superconductivity. *Physical Review*, 108(5):1175, December 1957. 23

[47] M. Tinkham. *Introduction to superconductivity (Second Edition).* Dover Publications, Inc. Mineola, NY, 1996. 23, 46, 85, 260, 266, 267

[48] S. De Franceschi, L. Kouwenhoven, C. Schonenberger, and W. Wernsdorfer. Hybrid superconductor-quantum dot devices. *Nat Nano*, 5(10):703–711, October 2010. 24, 40, 57, 114

[49] A. C. Hewson. *The Kondo Problem to Heavy Fermions.* Cambridge University Press, April 1997. 24, 39, 148, 155, 211, 214

[50] C. J. Lambert. Generalized Landauer formulae for quasi-particle transport in disordered superconductors. *Journal of Physics: Condensed Matter*, 3(34):6579–6587, August 1991. 25

[51] C. W. J. Beenakker. Universal limit of critical-current fluctuations in mesoscopic Josephson junctions. *Physical review letters*, 67(27):3836, December 1991. 25, 29, 32, 56, 234

[52] H. van Houten and C. W. J. Beenakker. Andreev reflection and the Josephson effect in a quantum point contact: An analogy with phase-conjugating resonators. *Physica B: Condensed Matter*, 175(1-3):187–197, December 1991. 32, 269

[53] P. W. Anderson. Special effects in superconductivity. In ER Caianiello, editor, *Ravello Lectures on the Many-Body Problem*, volume 2, pages 113–135. Academic Press, New York, 1964. 32, 53

[54] C. W. J. Beenakker and H. van Houten. The Superconducting Quantum Point Contact. *cond-mat/0512610*, December 2005. 32, 53, 260

[55] G. Breit and E. Wigner. Capture of Slow Neutrons. *Physical Review*, 49(7):519, April 1936. 33

[56] M. Buttiker. Coherent and sequential tunneling in series barriers. *IBM Journal of Research and Development*, 32(1):63–75, January 1988. 33, 34, 50, 135, 211, 245, 271

[57] N. R. Claughton, M. Leadbeater, and C. J. Lambert. Theory of Andreev resonances in quantum dots. *Journal of Physics: Condensed Matter*, 7(46):8757–8784, November 1995. 33

[58] C. W. J. Beenakker. Three "universal" mesoscopic Josephson effects. *Arxiv preprint cond-mat/0406127*, June 2004. 33, 56

[59] C. W. J. Beenakker and H. Van Houten. Resonant Josephson current through a quantum dot. *Arxiv preprint cond-mat/0111505*, November 2001. 34

[60] D. Fisher and P. Lee. Relation between conductivity and transmission matrix. *Physical Review B*, 23(12):6851–6854, June 1981. 39

[61] A. Levy Yeyati and M. Büttiker. Scattering phases in quantum dots: An analysis based on lattice models. *Physical Review B*, 62(11):7307–7315, September 2000. 39

[62] L. Szunyogh. Introduction to Multiple Scattering Theory. 39

[63] P. W. Anderson. Localized Magnetic States in Metals. *Physical Review*, 124(1):41, October 1961. 41, 211, 223

[64] J. Bardeen. Tunnelling from a Many-Particle Point of View. *Physical Review Letters*, 6(2):57–59, January 1961. 41, 241

[65] H. Bruus and K. Flensberg. *Many-Body Quantum Theory in Condensed Matter Physics: An Introduction.* OUP Oxford, September 2004. 44, 45, 46, 137, 214, 219, 220, 223, 241, 242, 251

[66] A. Damascelli, Z-X. Shen, and Z. Hussain. Angle-resolved photoemission studies of the cuprate superconductors. *Reviews of Modern Physics*, 75(2):473–541, April 2003. 46

[67] R. C. Dynes, V. Narayanamurti, and J. P. Garno. Direct Measurement of Quasiparticle-Lifetime Broadening in a Strong-Coupled Superconductor. *Physical Review Letters*, 41(21):1509, November 1978. 47

[68] M. Chauvin. *Effet Josephson dans les contacts atomiques / The Josephson Effect in Atomic Contacts*. PhD thesis, November 2005. 53, 116, 246

[69] M. L. Della Rocca, M. Chauvin, B. Huard, H. Pothier, D. Esteve, C. Urbina, and M. Della Rocca. Measurement of the Current-Phase Relation of Superconducting Atomic Contacts. *Physical Review Letters*, 99(12):1–4, September 2007. 53, 54, 81, 116

[70] M. H. Cohen, L. M. Falicov, and J. C. Phillips. Superconductive Tunneling. *Physical Review Letters*, 8(8):316, April 1962. 54, 240

[71] T. Meng, S. Florens, and P. Simon. Self-consistent description of Andreev bound states in Josephson quantum dot devices. *Physical Review B*, 79(22), June 2009. 56, 114, 211

[72] B. I. Spivak and S. A. Kivelson. Negative local superfluid densities: The difference between dirty superconductors and dirty Bose liquids. *Physical Review B*, 43(4):3740, February 1991. 57

[73] V. Ryazanov, V. Oboznov, A. Rusanov, A. Veretennikov, A. Golubov, and J. Aarts. Coupling of Two Superconductors through a Ferromagnet: Evidence for a π Junction. *Physical Review Letters*, 86(11):2427–2430, March 2001. 57

[74] T. Kontos, M. Aprili, J. Lesueur, F. Genêt, B. Stephanidis, and R. Boursier. Josephson Junction through a Thin Ferromagnetic Layer: Negative Coupling. *Physical Review Letters*, 89(13):1–4, September 2002. 57

[75] J. J. A. Baselmans, A. F. Morpurgo, B. J. van Wees, and T. M. Klapwijk. Reversing the direction of the supercurrent in a controllable Josephson junction. *Nature*, 397(6714):43–45, January 1999. 57

[76] H. Ingerslev Jorgensen, T. Novotny, K. Grove-Rasmussen, K. Flensberg, and P.E. E. Lindelof. Critical Current 0-Pi Transition in Designed Josephson Quantum Dot Junctions. *Nano Letters*, 7(8):2441–2445, 2007. 57

[77] A. Martin-Rodero and A. Levy Yeyati. The Andreev states of a superconducting quantum dot: mean field versus exact numerical results. *Journal of Physics: Condensed Matter*, 24:385303, 2012. 72

[78] M. F. Goffman, R. Cron, A. Levy Yeyati, P. Joyez, M. H. Devoret, D. Esteve, and C. Urbina. Supercurrent in Atomic Point Contacts and Andreev States. *Physical Review Letters*, 85(1):170, July 2000. 81

[79] H. Le Sueur, P. Joyez, H. Pothier, C. Urbina, and D. Esteve. Phase Controlled Superconducting Proximity Effect Probed by Tunneling Spectroscopy. *Physical Review Letters*, 100(19):1–4, May 2008. 81, 244

[80] Travis Dirks, Yung-fu Chen, Norman O Birge, and Nadya Mason. No Title. pages 1–12. 81

[81] M. Zgirski, L. Bretheau, Q. Le Masne, H. Pothier, D. Esteve, and C. Urbina. Evidence for long-lived quasiparticles trapped in superconducting point contacts. *Physical Review Letters*, 106(25):257003, June 2011. 81

[82] M. Covington, M. Aprili, E. Paraoanu, L. H. Greene, F. Xu, J. Zhu, and C. A. Mirkin. Observation of Surface-Induced Broken Time-Reversal Symmetry in YBa_{2}Cu_{3}O_{7} Tunnel Junctions. *Physical Review Letters*, 79(2):277, July 1997. 81

[83] A. Yazdani, C. M. Howald, C. P. Lutz, A. Kapitulnik, and D. M. Eigler. Impurity-Induced Bound Excitations on the Surface of Bi2Sr2CaCu2O8. *Physical Review Letters*, 83(1):176, July 1999. 81

[84] L. Alff, A. Beck, R. Gross, A. Marx, S. Kleefisch, Th. Bauch, H. Sato, M. Naito, and G. Koren. Observation of bound surface states in grain-boundary junctions of high-temperature superconductors. *Physical Review B*, 58(17):11197, November 1998. 81

[85] Z. Q. Mao, K. D. Nelson, R. Jin, Y. Liu, and Y. Maeno. Observation of Andreev Surface Bound States in the 3-K Phase Region of Sr2RuO4. *Physical Review Letters*, 87(3):037003, June 2001. 81

[86] L. Shan, Y. L. Wang, B. Shen, B. Zeng, and Y. Huang. Observation of ordered vortices with Andreev bound states in Ba0.6K0.4Fe2As2. *Nature Physics*, 7(4):325–331, April 2011. 81

[87] J. Nilsson, A. R. Akhmerov, and C. W. J. Beenakker. Splitting of a Cooper Pair by a Pair of Majorana Bound States. *Physical Review Letters*, 101(12):120403, 2008. 81

[88] A. R Akhmerov, J. P Dahlhaus, F. Hassler, M. Wimmer, and C. W. J Beenakker. Quantized conductance at the Majorana phase transition in a disordered superconducting wire. *1009.5542*, September 2010. 81

[89] J. C. Y. Teo and C. L. Kane. Majorana Fermions and Non-Abelian Statistics in Three Dimensions. *Physical Review Letters*, 104(4):046401, January 2010. 81

[90] H. Le Sueur. *Cryogenic AFM-STM for mesoscopic physics.* PhD thesis, 2007. 85, 86

[91] H. Le Sueur. Microfabricated electromagnetic filters for millikelvin experiments. *Review of scientific instruments*, 77(11):115102–115102, 2006. 86

[92] J-D. Pillet, C. H. L. Quay, P. Morfin, C. Bena, A. Levy Yeyati, and P. Joyez. Andreev bound states in supercurrent-carrying carbon nanotubes revealed. *Nature Physics*, 6(12):965–969, November 2010. 89, 114, 115, 116, 151, 184, 185, 186

[93] V. Ambegaokar and A. Baratoff. Tunneling Between Superconductors. *Physical Review Letters*, 10(11):486–489, June 1963. 114

[94] L. F. Chang and P. F. Bagwell. Control of Andreev-level occupation in a Josephson junction by a normal-metal probe. *Physical Review B*, 55(18):12678, 1997. 115, 245

[95] F. Giazotto, J. T. Peltonen, and M. Meschke. Superconducting quantum interference proximity transistor. *Nature Physics*, 6(4):254–259, April 2010. 119

[96] J. Nygård, D. H. Cobden, and P. E. Lindelof. Kondo physics in carbon nanotubes. *Nature*, 408(6810):342–346, November 2000. 131, 164, 171, 215

[97] T. Delattre, C. Feuillet-Palma, L. G. Herrmann, P. Morfin, J.-M. Berroir, G. Fève, B. Plaçais, D. C. Glattli, M.-S. Choi, C. Mora, and T. Kontos. Noisy Kondo impurities. *Nature Physics*, 5(3):208–212, January 2009. 131, 164, 215

[98] J. R. Hauptmann, J. Paaske, and P. E. Lindelof. Electric-field-controlled spin reversal in a quantum dot with ferromagnetic contacts. *Nat Phys*, 4(5):373–376, May 2008. 131, 157, 159, 205, 215

[99] L. Hofstetter, A. Geresdi, M. Aagesen, J. Nygård, C. Schönenberger, and S. Csonka. Ferromagnetic Proximity Effect in a FerromagnetQuantum-DotSuperconductor Device. *Physical Review Letters*, 104(24):246804, June 2010. 131

[100] F. Wu, R. Danneau, P. Queipo, E. Kauppinen, T. Tsuneta, and P. J. Hakonen. Single-walled carbon nanotube weak links: from Fabry-Pť erot to Kondo regime. *Nature*, 1:2–5, 2009. 131

[101] N. Roch, S. Florens, V. Bouchiat, W. Wernsdorfer, and F. Balestro. Quantum phase transition in a single-molecule quantum dot. *Nature*, 453(7195):633–637, May 2008. 131, 147, 166, 215

[102] S. Florens, A. Freyn, N. Roch, W. Wernsdorfer, F. Balestro, P. Roura-Bas, and A. A. Aligia. Universal transport signatures in two-electron molecular quantum dots: gate-tunable Hunds rule, underscreened Kondo effect and quantum phase transitions. *Journal of Physics: Condensed Matter*, 23:243202, June 2011. 131, 166, 216

[103] H. Jeong, A.M. Chang, and M.R. Melloch. The Kondo effect in an artificial quantum dot molecule. *Science*, 293(5538):2221, 2001. 131, 157, 215

[104] A. W. Holleitner, R. H. Blick, A. K. Hüttel, K. Eberl, and J. P. Kotthaus. Probing and Controlling the Bonds of an Artificial Molecule. *Science*, 297(5578):70 –72, July 2002. 131

[105] N. Mason, M. J. Biercuk, and C. M. Marcus. Local Gate Control of a Carbon Nanotube Double Quantum Dot. *Science*, 303(5658):655 –658, January 2004. 131, 133, 137, 157

[106] J. C. Chen, A. M. Chang, and M. R. Melloch. Transition between Quantum States in a Parallel-Coupled Double Quantum Dot. *Physical Review Letters*, 92(17):176801, April 2004. 131, 157

[107] G. A. Steele, G. Gotz, and L. P. Kouwenhoven. Tunable few-electron double quantum dots and Klein tunnelling in ultraclean carbon nanotubes. *Nature Nanotechnology*, 4(6):363–367, April 2009. 131, 135

[108] L. G. Herrmann, F. Portier, P. Roche, A. Levy Yeyati, T. Kontos, and C. Strunk. Carbon Nanotubes as Cooper Pair Beam Splitters. *Physical Review Letters*, 104(2):026801. 131, 133, 135

[109] J. Nygård, W. F Koehl, N. Mason, L. DiCarlo, and C. M Marcus. Zero-field splitting of Kondo resonances in a carbon nanotube quantum dot. *arXiv:cond-mat/0410467*, October 2004. 131, 157

[110] A. Cottet and T. Kontos. Spin Quantum Bit with Ferromagnetic Contacts for Circuit QED. *Physical Review Letters*, 105(16):160502, October 2010. 133

[111] H. Pothier, P. Lafarge, C. Urbina, D. Esteve, and M. H. Devoret. Single-Electron Pump Based on Charging Effects. *Europhysics Letters (EPL)*, 17(3):249–254, January 1992. 135, 137, 138

[112] W. van der Wiel, S. De Franceschi, J. Elzerman, T. Fujisawa, S. Tarucha, and L. Kouwenhoven. Electron transport through double quantum dots. *Reviews of Modern Physics*, 75(1):1–22, December 2002. 135, 137, 138, 257

[113] C. W. J. Beenakker. Theory of Coulomb-blockade oscillations in the conductance of a quantum dot. *Physical Review B*, 44(4):1646, July 1991. 135, 206, 209, 211

[114] J. S. Lim and M-S. Choi. Andreev bound states in the Kondo quantum dots coupled to superconducting leads. *Journal of Physics: Condensed Matter*, 20:415225, October 2008. 141

[115] A. Martín-Rodero and A. Levy Yeyati. Josephson and Andreev transport through quantum dots. *Advances in Physics*, 60:899–958, December 2011. 141, 148, 214

[116] H. Jørgensen, K. Grove-Rasmussen, T. Novotný, K. Flensberg, and P. Lindelof. Electron Transport in Single-Wall Carbon Nanotube Weak Links in the Fabry-Perot Regime. *Physical Review Letters*, 96(20):207003, May 2006. 141

[117] L. P. Kouwenhoven, D. G. Austing, and S. Tarucha. Few-electron quantum dots. *Reports on Progress in Physics*, 64(6):701–736, June 2001. 146, 206, 207, 211

[118] W. G. van der Wiel, S. De Franceschi, T. Fujisawa, J. M. Elzerman, S. Tarucha, and L. P. Kouwenhoven. The Kondo Effect in the Unitary Limit. *Science*, 289(5487):2105 –2108, 2000. 147, 214

[119] G. D. Scott and D. Natelson. Kondo Resonances in Molecular Devices. *ACS Nano*, 4(7):3560–3579, September 2011. 147, 148, 164, 214, 215

[120] D. Goldhaber-Gordon, J. Göres, M. A. Kastner, Hadas Shtrikman, D. Mahalu, and U. Meirav. From the Kondo Regime to the Mixed-Valence Regime in a Single-Electron Transistor. *Physical Review Letters*, 81(23):5225, December 1998. 147, 164, 165

[121] F. D. M. Haldane. Scaling Theory of the Asymmetric Anderson Model. *Physical Review Letters*, 40(6):416, February 1978. 148, 214

[122] J. Simonin. Looking for the Kondo cloud. *arXiv:0708.3604*, August 2007. 153

[123] I. Affleck and P. Simon. Detecting the Kondo Screening Cloud Around a Quantum Dot. *Physical Review Letters*, 86(13):2854, March 2001. 153

[124] J. Mravlje, A. Ramšak, and T. Rejec. Kondo effect in double quantum dots with interdot repulsion. *Physical Review B*, 73(24):241305, June 2006. 157

[125] H. B. Heersche, Z. de Groot, J. A. Folk, L. P. Kouwenhoven, H. S. J. van der Zant, A. A. Houck, J. Labaziewicz, and I. L. Chuang. Kondo Effect in the Presence of Magnetic Impurities. *Physical Review Letters*, 96(1):017205, January 2006. 157, 159, 166

[126] D. Goldhaber-Gordon, Hadas Shtrikman, D. Mahalu, David Abusch-Magder, U. Meirav, and M. A. Kastner. Kondo effect in a single-electron transistor. *Nature*, 391(6663):156–159, January 1998. 159, 214

[127] L. Vaugier, A. A. Aligia, and A. M. Lobos. Spectral density of an interacting dot coupled indirectly to conducting leads. *Physical Review B*, 76(16):165112, October 2007. 166

[128] T. S. Jespersen, K. Grove-Rasmussen, and J. Paaske. Gate-dependent spin-orbit coupling in multielectron carbon nanotubes. *Nature Physics*, 7(4):348–353, 2011. 166, 204, 209

[129] M. Lee, M.S. Choi, R. López, R. Aguado, and J. Martinek. Two-impurity Anderson model revisited: Competition between Kondo effect and reservoir-mediated superexchange in double quantum dots. *Physical Review B*, 81(12):121311, 2010. 166, 171

[130] R. López, R. Aguado, and G. Platero. Nonequilibrium Transport through Double Quantum Dots: Kondo Effect versus Antiferromagnetic Coupling. *Physical Review Letters*, 89(13):136802, 2002. 166, 171

[131] C. M. Varma and Y. Yafet. Magnetic susceptibility of mixed-valence rare-earth compounds. *Physical Review B*, 13(7):2950, April 1976. 169

[132] A. Georges and Y. Meir. Electronic Correlations in Transport through Coupled Quantum Dots. *Physical Review Letters*, 82(17):3508, April 1999. 171

[133] R. Aguado and D. C. Langreth. Out-of-Equilibrium Kondo Effect in Double Quantum Dots. *Physical Review Letters*, 85(9):1946, 2000. 171

[134] T. Aono and M. Eto. Kondo resonant spectra in coupled quantum dots. *Physical Review B*, 63(12):125327, 2001. 171

[135] J. Kong, H. T. Soh, A. M. Cassell, C. F. Quate, and H. Dai. Synthesis of individual single-walled carbon nanotubes on patterned silicon wafers. *Nature*, 395(6705):878–881, October 1998. 178, 179

[136] C-H. Kiang, W. A. III Goddard, R. Beyers, J. R. Salem, and D. S. Bethune. Catalytic Synthesis of Single-Layer Carbon Nanotubes with a Wide Range of Diameters. *The Journal of Physical Chemistry*, 98:6612–6618, June 1994. 178

[137] X. Lin, X. K. Wang, V. P. Dravid, R. P. H. Chang, and J. B. Ketterson. Large scale synthesis of single-shell carbon nanotubes. *Applied Physics Letters*, 64:181, 1994. 178

[138] V. Krstic, G. T. Kim, J. G. Park, D. S. Suh, Y. W. Park, S. Roth, and M. Burghard. Role of the metal in contacting Single-Walled Carbon Nanotubes. In *Electronic Properties of Novel Materials - Molecular Nanostructures. 14th International Winterschool/Euroconference Kirchberg, Austria, 4-11 March 2000*, volume 544, pages 367–370. AIP, USA, 2000. 187

[139] D. Mann, A. Javey, J. Kong, Q. Wang, and H. Dai. Ballistic Transport in Metallic Nanotubes with Reliable Pd Ohmic Contacts. *Nano Letters*, 3(11):1541–1544, November 2003. 187

[140] S. Gueron. *Quasiparticles in a diffusive conductor: Interactions and pairing.* PhD thesis, 1997. 187

[141] W. Liang, M. Bockrath, D. Bozovic, J. H. Hafner, M. Tinkham, and H. Park. Fabry - Perot interference in a nanotube electron waveguide. *Nature*, 411(6838):665–9, June 2001. 190, 213

[142] M. R. Delbecq, V. Schmitt, F. D. Parmentier, N. Roch, J. J. Viennot, G. Fève, B. Huard, C. Mora, A. Cottet, and T. Kontos. Coupling a quantum dot, fermionic leads and a microwave cavity on-chip. *arXiv:1108.4371*, August 2011. 203

[143] L. P. Kouwenhoven, T. H. Oosterkamp, M. W. S. Danoesastro, M. Eto, D. G. Austing, T. Honda, and S. Tarucha. Excitation Spectra of Circular, Few-Electron Quantum Dots. *Science*, 278(5344):1788 –1792, December 1997. 203, 207

[144] C. Cohen-Tannoudji, B. Diu, and F. Laloë. *Quantum mechanics.* Wiley, 1977. 203

[145] R. Leturcq, C. Stampfer, K. Inderbitzin, L. Durrer, C. Hierold, E. Mariani, M. G. Schultz, F. von Oppen, and K. Ensslin. Franck-Condon blockade in suspended carbon nanotube quantum dots. *Nat Phys*, 5(5):327–331, May 2009. 204, 209

[146] H. Ajiki and T. Ando. Electronic States of Carbon Nanotubes. *Journal of the Physical Society of Japan*, 62:1255–1266, 1993. 204

[147] G. A. Steele, A. K. Hüttel, B. Witkamp, M. Poot, H. B. Meerwaldt, L. P. Kouwenhoven, and H. S. J. van der Zant. Strong coupling between single-electron tunneling and nanomechanical motion. *Science (New York, N.Y.)*, 325(5944):1103–1107, August 2009. 205

[148] B. Lassagne, Y. Tarakanov, J. Kinaret, D. Garcia-Sanchez, and A. Bachtold. Coupling Mechanics to Charge Transport in Carbon Nanotube Mechanical Resonators. *Science*, 325(5944):1107 –1110, 2009. 205

[149] F. Kuemmeth, S. Ilani, D. C. Ralph, and P. L. McEuen. Coupling of spin and orbital motion of electrons in carbon nanotubes. *Nature*, 452(7186):448–52, March 2008. 205, 209

[150] M. Pustilnik and L. I. Glazman. Kondo Effect in Real Quantum Dots. *Physical Review Letters*, 87(21):216601, November 2001. 205

[151] I. L. Aleiner, P. W. Brouwer, and L. I. Glazman. Quantum effects in Coulomb blockade. *Physics Reports*, 358(5-6):309–440, March 2002. 206

[152] M. Pustilnik and L. Glazman. Kondo effect in quantum dots. *Journal of Physics: Condensed Matter*, 16:R513–R537, April 2004. 206

[153] W. Liang, M. Bockrath, and H. Park. Shell Filling and Exchange Coupling in Metallic Single-Walled Carbon Nanotubes. *Physical Review Letters*, 88(12):126801, March 2002. 209

[154] D. H. Cobden and J. Nygård. Shell Filling in Closed Single-Wall Carbon Nanotube Quantum Dots. *Physical Review Letters*, 89(4):046803, July 2002. 209

[155] P. Jarillo-Herrero, S. Sapmaz, C. Dekker, L. P. Kouwenhoven, and H. S. J. Van Der Zant. Electron-hole symmetry in a semiconducting carbon nanotube quantum dot. *Nature*, 429(6990):389–92, May 2004. 209

[156] H. C. Manoharan, C. P. Lutz, and D. M. Eigler. Quantum mirages formed by coherent projection of electronic structure. *Nature*, 403(6769):512–515, February 2000. 215

[157] P. Jarillo-Herrero, J. Kong, H.S.J. Van Der Zant, C. Dekker, L.P. Kouwenhoven, S. De Franceschi, and T V Superfluid. Orbital Kondo effect in carbon nanotubes. *Nature*, 434(7032):484–488, 2005. 216

[158] L. Kouwenhoven and L. Glazman. Revival of the Kondo effect. *arXiv:cond-mat/0104100*, April 2001. 216

[159] A. L. Fetter and J. D. Walecka. *Quantum Theory of Many-Particle Systems*. Dover Publications, June 2003. 220

[160] J. Bardeen. Tunneling Into Superconductors. *Physical Review Letters*, 9(4):147, 1962. 240

[161] R. Kubo. Statistical-Mechanical Theory of Irreversible Processes. I. General Theory and Simple Applications to Magnetic and Conduction Problems. *Journal of the Physical Society of Japan*, 12:570–586, 1957. 240

[162] H. Grabert and M. H. Devoret. *Single Charge Tunneling: Coulomb Blockade Phenomena in Nanostructures.* Springer, 1 edition, June 1992. 241

[163] H. Le Sueur and P. Joyez. Room-temperature tunnel current amplifier and experimental setup for high resolution electronic spectroscopy in millikelvin scanning tunneling microscope experiments. *Review of scientific instruments*, 77(12):123701, 2006. 244

[164] M. Hofheinz, F. Portier, Q. Baudouin, P. Joyez, D. Vion, P. Bertet, P. Roche, and D. Esteve. Bright Side of the Coulomb Blockade. *Physical Review Letters*, 106(21):217005, May 2011. 246

[165] J. C. Cuevas, A. Martín-Rodero, A. Levy Yeyati, and A. López-Dávalos. Resonant tunneling through a small quantum dot coupled to superconducting leads. *Physical Review B*, 55(10):R6137, March 1997. 247

[166] J. C. Cuevas, A. Martín-Rodero, and A. Levy Yeyati. Hamiltonian approach to the transport properties of superconducting quantum point contacts. *Physical review. B, Condensed matter*, 54(10):7366–7379, September 1996. 247

[167] G. E. Blonder, M. Tinkham, and T. M. Klapwijk. Transition from metallic to tunneling regimes in superconducting microconstrictions: Excess current, charge imbalance, and supercurrent conversion. *Physical Review B*, 25(7):4515, April 1982. 247, 266

[168] S. Datta and Philip F. Bagwell. Can the Bogoliubov-de Gennes equation be interpreted as a 'one-particle' wave equation? *Superlattices and Microstructures*, 25(5-6):1233–1250, May 1999. 259, 260, 266

[169] C. W. J. Beenakker. Specular Andreev Reflection in Graphene. *Physical Review Letters*, 97(6):067007, April 2006. 264

[170] A. Zazunov, V. S. Shumeiko, E. N. Bratus', J. Lantz, G. Wendin, and E. N Bratus\char39. Andreev Level Qubit. *Physical Review Letters*, 90(8):087003, February 2003. 269

[171] C. W. J. Beenakker and H. van Houten. Josephson current through a superconducting quantum point contact shorter than the coherence length. *Physical Review Letters*, 66(23):3056, June 1991. 270